

Development and Modelling of a Passively Q-switched Ytterbium Doped
Calcium Fluoride Laser

by

Travis Robert Schoepp

A thesis submitted in partial fulfillment of the requirements for the degree of

Master of Science

in

Photonics and Plasmas

Department of Electrical and Computer Engineering
University of Alberta

© Travis Robert Schoepp, 2014

Abstract

A longitudinally diode-pumped, passively Q-switched Yb:CaF₂ laser has been developed and characterised using a Cr:YAG saturable absorber. A peak average output power of 914 mW at a repetition rate of 1314 Hz was obtained with a slope efficiency of 20%. The output pulse energy was 0.62 mJ with a pulse width of 78.6 ns FWHM giving a peak power of 7.9 kW. Laser threshold pump power was 8.6 W. CW laser operation has also been achieved with a peak power of 6.0 W, a laser threshold pump power of 3.8 W, and a slope efficiency of 28%. At identical pump powers the maximum ratio of Q-switched to CW average output power was 0.42.

The thermal response of the laser medium was also studied. Crystal face temperature profiles were recorded using a thermal camera in both CW and Q-switched configurations. Measurements were made with increasing pump power from below to above laser threshold. Temperatures were seen to rise nearly linearly with pump power except at and just above threshold where additional dynamics play a role in heat generation and transport within the crystal. The thermal simulations were found to match the experiment to within 2% for the CW configuration and within 4% for the Q-switched configuration in terms of absolute temperatures.

Rate equation modelling was performed for the Q-switched Yb:CaF₂ laser. Output characteristics generally matched with experiment with the largest discrepancy observed of 30%. The laser rate equation modelling took into account the temperature variation in the gain medium with changing pump power through the use of the thermal simulations.

With appropriate optimisation it was found that the Q-switched peak output power could potentially be improved to the order of 200 kW with possible applications in x-ray generation for water window x-ray microscopy. Optimisation of the laser crystal cooling was also determined to be feasible with a simulated reduction in peak temperature rise of 72%.

To my parents
for believing in me always.

Acknowledgements

Research and scholarship are never completed in isolation and so with sincere gratitude I would like to thank those who have helped me towards completion of my MSc studies.

First, I owe my supervisor, Professor Robert Fedosejevs, many thanks in granting me a place in his laboratory at the University of Alberta. Dr. Fedosejevs' support has been evident in many ways through guidance, scholarly encouragement, commitment to excellence, and financial support. Without his keen observations I would not be at the point I am today. He fostered an environment where the freedom to learn and develop in many ways, not only academically, was encouraged.

I am profoundly grateful to have had the opportunity to work with many different people from the university over the years. In particular I would like to thank Dr. Renee Polziehn for taking me on as an FGSR Outreach coordinator and providing me with significant and profound guidance in my studies and personal life. My passion for sharing knowledge and teaching may never have been realized without her involvement.

I would like to express my gratitude to Professor Ying Tsui, Dr. Henry Tiedje, and Dr. Ilya Utkin for their guidance and suggestions throughout my MSc program. Many invaluable discussions were had and I am better because of them. I would like to thank Mr. Blair Harwood for being a source of inspiration and great technical knowledge. I would also like to thank Dr. Jörg Körner for his insights.

I must thank my lab colleagues for the many fruitful discussions, collaborations, and the shared understanding of the struggles we faced. Especially Yang, Raj, Mianzhen, Shaun, Zhijiang, and Shyama, thank you for sharing your time with me.

I am truly appreciative of the funding I have received from the Natural Sciences and Engineering Research Council of Canada (NSERC) and Alberta Innovates Technology Futures (AITF).

I would like to thank the congregation at St. John's Lutheran Church and especially my pastor Rev. Roland Kubke for the significant support and encouragement they provided me. To the Creator I owe everything and thank Him for the blessings in my life and the motivation to complete my studies.

In the most sincere way I must thank my family and friends for the encouragement throughout my program. I would like to thank my girlfriend Katherine for believing in me when I did not and supporting me in so many ways. A special thanks to my parents and brother for their unwavering support and love. I could not be where I am if not for all the little things, and of course the big things, that they have done and sacrificed for me.

Table of Contents

Introduction	1
1.1 Motivation	1
1.2 Background.....	3
1.3 Previous Work with Yb:CaF ₂	5
1.4 Modelling of Yb:CaF ₂ and Similar Systems	11
1.5 Outline	15
Theoretical Background.....	16
2.1 Longitudinally-Pumped Quasi-Three-Level Lasers	16
2.2 Heat Deposition and Thermal Distribution in Laser Crystals	19
2.3 Water Window X-ray Generation Techniques	24
Experimental Procedure.....	28
3.1 CW Laser Design and Measurement	28
3.2 Q-switched Laser Design and Measurement	31
3.3 Thermal Measurements	34
Simulations.....	41
4.1 Rate Equation Modelling.....	41
4.1.1 Solver Method and Verification.....	41
4.1.2 Modelling Parameters and Assumptions.....	42
4.1.3 Limitations	46
4.2 Thermal Modelling.....	48
4.2.1 Model Configuration and Geometry	48

4.2.2	Modelling Parameters and Assumptions.....	51
4.2.3	Configuration Specific Modelling Adjustments	55
4.2.4	Model Verification	58
4.2.5	Limitations	63
Results	67
5.1	Experimental Results.....	67
5.1.1	Pump Characterisation	67
5.1.2	CW Output Characteristics.....	70
5.1.3	Q-switching Output Characteristics	75
5.1.4	CW Thermal Measurement.....	82
5.1.5	Q-switching Thermal Measurement.....	86
5.2	Simulation Results.....	90
5.2.1	Q-switching Rate Equation Simulations	90
5.2.2	CW Thermal Simulations.....	101
5.2.3	Q-switching Thermal Simulations	109
Discussion	119
6.1	CW Output Results.....	119
6.1.1	Comparison with Theory.....	119
6.1.2	Further Improvements	123
6.2	Q-switching Output Results and Simulations.....	124
6.2.1	Comparison of Results and Simulations	124
6.2.2	Further Model Improvements.....	128
6.2.3	Experimental Optimisation	130

6.3	Thermal Results and Simulations	132
6.3.1	Comparison of Results and Simulations	132
6.3.2	Further Model Improvements.....	140
6.3.3	Experimental Optimisation	141
6.4	Feasibility for X-ray Generation.....	143
	Conclusion	149
7.1	Summary of Experiments	149
7.2	Summary of Simulations	150
7.3	Future Work.....	152
	References	154
	Appendix A	165
	Appendix B	176

List of Tables

Table 4.1-1: Room temperature effective cross-section values used in rate equation simulations.	44
Table 4.1-2: Constant parameter values for rate equation modelling. The parameters are defined above and in Section 2.1.	46
Table 4.2-1: Pump propagation and absorption parameters for FEA analysis. The parameters are defined in Sections 2.2 and 4.2.1.	52
Table 4.2-2: Material properties for thermo-mechanical FEA analysis.	55
Table 4.2-3: Boundary condition parameters for FEA analysis.	55
Table 4.2-4: Thermal load properties for thermomechanical FEA analysis.	57
Table 4.2-5: Mesh dependency study parameters.	59
Table 4.2-6: Comparison of modelling parameters for the original model and the modified model used to evaluate error created by parameter variation at high temperatures.	66
Table 4.2-7: Comparison of simulated temperatures for the original model and the modified model used to evaluate error created by parameter variation at high temperatures.	66
Table 5.2-1: Comparison of experimental and simulated QS output results.	92
Table 5.2-2: Parameter range for QS optimisation parametric study.	95
Table 5.2-3: Comparison of peak temperatures in the measured and simulated CW laser temperature profiles.	107
Table 5.2-4: Changes in CW thermal simulation peak and average beam axis temperatures under different simulation configurations.	109
Table 5.2-5: Comparison of peak temperatures in the measured and simulated QS laser temperature profiles.	114

Table 5.2-6: Changes in QS thermal simulation peak and average beam axis temperatures under different simulation configurations..... 116

Table 5.2-7: QS output performance under different simulation configurations..... 116

Table 6.4-1: QS rate equation input parameters for peak output power optimisation with and without the effect of thermal lensing. 145

Table 6.4-2: QS output performance for peak output power optimisation with and without the effect of thermal lensing..... 146

List of Figures

Figure 1.2-1: Effective emission cross-sections of 2.2 at.% Yb:CaF ₂ at 77 K and 2 at.% Yb:YAG at 80 K.	4
Figure 1.2-2: Energy levels of Yb:CaF ₂ at 77 K. ²⁸	5
Figure 2.1-1: Energy level diagram for a simple quasi-3-level laser and 4-level SA with energy levels, population densities, fluorescence lifetimes, and spectroscopic cross-sections shown. Fast, non-radiative transitions are shown by a dashed arrow.	19
Figure 2.3-1: The basic configurations for a) transmission full-field x-ray microscopy and b) scanning transmission x-ray microscopy. An order sorting aperture (OSA) is used to filter out zero and higher order radiation in the STXM scheme. ⁹¹	25
Figure 2.3-2: Absorption edges of water and protein in a range from 1 to 5 nm. Also shown are the emission lines from an ethanol plasma. ¹³	26
Figure 2.3-3: Emission spectra of nitrogen under laser excitation. ⁹²	27
Figure 3.1-1: CW laser experimental setup. OC is output coupler and ROC is radius of curvature.....	29
Figure 3.1-2: Diagram of the laser crystal installed in the water-cooled, aluminum mount and clamp.....	29
Figure 3.1-3: Measurement setup for CW characterisation. a) Power and spectral measurement, b) stability measurement, and c) beam size measurement. OC: output coupler, SM: spectrometer, LPF: long-wave pass filter, PM: power meter, PD: photodiode, W: wedge, ND: neutral density filter, and CCD: charge-coupled device.	31
Figure 3.2-1: QS laser experimental setup. OC is output coupler and ROC is radius of curvature.....	33

Figure 3.2-2: Measurement setup for Q-switching characterisation. a) Pulse energy measurement, b) repetition rate and pulse width measurement, and c) beam size measurement. OC: output coupler, LPF: long-wave pass filter, CM: calorimeter, PD: photodiode, W: wedge, ND: neutral density filter, and CCD: charge-coupled device. 34

Figure 3.3-1: Measurement setup for CW lasing thermal imaging. LPF stands for long-wave pass filter. 35

Figure 3.3-2: Transmission curves for the Spectrogon 11 μm long-wave pass filter (LPF), a typical uncoated Ge sample, and the combination of both. The extinction coefficient, κ , for CaF_2 is also included where κ is the imaginary component of the complex refractive index ($n = n - i\kappa$).¹⁰³⁻¹⁰⁵ 36

Figure 3.3-3: a) NTC thermistor calibration in a temperature regulated bath and b) crystal placement and temperature measurement in the laser cavity. OC: output coupler, SA: saturable absorber, LPF: long-wave pass filter, and DM: dichroic mirror. 38

Figure 3.3-4: Cubic regression of pixel value with respect to temperature for three different pixels. Measurements are taken from the QS laser thermal calibration. 39

Figure 3.3-5: Pixel locations chosen to demonstrate the temperature calibration cubic regression. 39

Figure 3.3-6: Measurement setup for QS lasing thermal imaging. LPF stands for long-wave pass filter. 40

Figure 4.2-1: COMSOL model laser crystal orientation. In the top view the edge domains have been omitted and the central pump region has been highlighted for ease of viewing. Directions for x, y, and z are shown as well. 49

Figure 4.2-2: Peak temperature, peak exit face temperature, and absorbed pump power dependence on cylindrical interaction region mesh element size (case one). 60

Figure 4.2-3: Peak temperature, peak exit face temperature, and absorbed pump power dependence on body and sides mesh element size (case two).	60
Figure 4.2-4: Back face FEA mesh used for thermal simulations.	61
Figure 4.2-5: Simulated Yb:GdCOB, back face, transverse temperature profile.	63
Figure 5.1-1: Changes in pump power and wavelength with pump current inside laser cavity.	68
Figure 5.1-2: Typical pump spectrum at 1.2 W output power.	68
Figure 5.1-3: M^2 fit to the measured pump beam radius in the y and z directions. Inset shows the focussed beam profile at its beam waist.	69
Figure 5.1-4: Output power versus pump power under CW operation.	71
Figure 5.1-5: Optical laser efficiency under CW operation.	72
Figure 5.1-6: Change in peak CW output wavelength with changing output power.	73
Figure 5.1-7: Photodiode measurement of laser power stability with 1000 Ω termination. Time scale: 100 μ s/div. Voltage scale: 500 mV/div. DC coupling.	73
Figure 5.1-8: Sub-nanosecond photodiode measurement of laser power stability with 50 Ω termination. Time scale: 1 ns/div. Voltage scale: 10 mV/div.	74
Figure 5.1-9: M^2 fit to the measured CW output beam radius in the y and z directions. Inset shows the focussed beam profile at its beam waist.	75
Figure 5.1-10: Repetition rate and average output power for QS operation as a function of pump power.	77
Figure 5.1-11: Pulse energy and FWHM pulse width for QS operation as a function of pump power.	78
Figure 5.1-12: Ratio of average QS output power to CW output power for the same pump power.	78

Figure 5.1-13: Change in peak QS output wavelength with changing output power. 79

Figure 5.1-14: Typical QS output spectrum at 11.3 W pump current. 80

Figure 5.1-15: QS pulse shape at 12.0 W pump power. 81

Figure 5.1-16: M^2 fit to the measured QS output beam radius in the y and z directions. Inset shows the focussed beam profile at its beam waist. 81

Figure 5.1-17: Thermal images captured at different pump powers below CW threshold. a) 0 W, b) 1.5 W, c) 2.6 W, and d) 3.8 W. Temperature scale is in degrees Celsius. 83

Figure 5.1-18: Thermal images captured at different pump powers at and above CW threshold. a) 4.0 W, b) 5.0 W, c) 9.6 W, and d) 19.0 W. Temperature scale is in degrees Celsius. 84

Figure 5.1-19: Crystal orientation as displayed in the thermal images used in the simulations and experiment. 84

Figure 5.1-20: Experimental evolution of temperatures at specific pixel locations as pump power increases for the CW laser case. 85

Figure 5.1-21: Pixel locations for plot of experimental CW pixel temperatures. 86

Figure 5.1-22: Thermal images captured at different pump powers below Q-switching threshold. a) 0 W, b) 2.6 W, c) 6.1 W, and d) 8.9 W. Temperature scale is in degrees Celsius. 87

Figure 5.1-23: Thermal images captured at different pump powers at and above Q-switching threshold. a) 9.4 W, b) 10.8 W, c) 14.3 W, and d) 19.0 W. Temperature scale is in degrees Celsius. 88

Figure 5.1-24: Experimental evolution of temperatures at specific pixel locations as pump power increases for the QS laser case. 89

Figure 5.1-25: Pixel locations for plot of experimental QS pixel temperatures. 89

Figure 5.2-1: Repetition rate and average output power for simulated QS operation as a function of pump power.	91
Figure 5.2-2: Pulse energy and FWHM pulse width for simulated QS operation as a function of pump power.	91
Figure 5.2-3: Population inversion, photon density, and SA transmission dynamics for a single QS pulse with 19.0 W pump power.....	93
Figure 5.2-4: Population inversion, photon density, and SA transmission dynamics in a QS pulse train.	94
Figure 5.2-5: Change in QS output parameters for changing OC reflectivity.	95
Figure 5.2-6: Change in QS output parameters for changing SA unsaturated transmission. .	96
Figure 5.2-7: Change in repetition rate and average output power for changing Yb ³⁺ doping concentration. Simulations run for laser crystal lengths (l) of 0.2-0.8 cm as indicated in the legend.	97
Figure 5.2-8: Change in output pulse energy and FWHM pulse width for changing Yb ³⁺ doping concentration. Simulations run for laser crystal lengths (l) of 0.2-0.8 cm as indicated in the legend.	97
Figure 5.2-9: Change in QS output parameters for changing laser crystal length.	98
Figure 5.2-10: Change in QS output parameters for changing laser cavity length.	99
Figure 5.2-11: Change in QS output parameters for changing laser mode radius. Pump to laser mode area ratio was fixed at one.	99
Figure 5.2-12: Change in QS output parameters for changing passive cavity loss.	100
Figure 5.2-13: Thermal images from simulations run at different pump powers below CW threshold. a) 1.45 W, b) 2.62 W, and c) 3.79 W. Temperature scale is in degrees Kelvin.	102

Figure 5.2-14: Thermal images from simulations run at different pump powers at and above CW threshold. a) 4.00 W, b) 4.95 W, c) 9.62 W, and d) 18.96 W. Temperature scale is in degrees Kelvin..... 103

Figure 5.2-15: Simulated evolution of temperatures at specific pixel locations as pump power increases for the CW laser case. Inset detail shows a comparison of simulation and experimental data points from 2.5 to 6 W..... 104

Figure 5.2-16: Pixel locations for plot of simulated CW pixel temperatures. 105

Figure 5.2-17: CW laser simulated distribution of temperature in Kelvin along the pump axis at a) 4.00 W, b) 7.29 W, c) 14.29 W, and d) 28.30 W pump power. The pump enters from the right side and exits the crystal at $x' = 0$, i.e. the back face of the crystal. The pump beam waist location is indicated in each figure. 106

Figure 5.2-18: CW laser thermal images from simulations run with different optimised parameters, all pumped at 18.96 W. a) lowered cooling temperature of 16.0°C, b) increased heat transfer coefficient of $1.0 \text{ W}\cdot\text{cm}^{-2}\cdot\text{K}^{-1}$, c) increased pump and radiative quantum efficiencies of 0.99 respectively, and d) all of the above (a – c). Temperature scale is in degrees Kelvin..... 108

Figure 5.2-19: Thermal images from simulations run at different pump powers below Q-switching threshold. a) 1.45 W, b) 2.62 W, c) 6.12 W, and d) 8.92 W. Temperature scale is in degrees Kelvin..... 110

Figure 5.2-20: Thermal images from simulations run at different pump powers at and above Q-switching threshold. a) 9.39 W, b) 10.79 W, c) 14.29 W, and d) 18.96 W. Temperature scale is in degrees Kelvin..... 111

Figure 5.2-21: Simulated evolution of temperatures at specific pixel locations as pump power increases for the QS laser case. Inset detail shows a comparison of simulation and experimental data points from 8 to 11 W..... 112

Figure 5.2-22: QS simulated distribution of temperature in Kelvin along the pump axis at a) 9.39W, b) 14.29 W, c) 18.96 W, and d) 28.30 W pump power. The pump enters from the right side and exits the crystal at $x' = 0$, i.e. the back face of the crystal. The pump beam waist location is indicated in each figure. 113

Figure 5.2-23: QS thermal images from simulations run with different optimised parameters, all pumped at 18.96 W. a) lowered cooling temperature of 16.0°C, b) increased heat transfer coefficient of $1.0 \text{ W}\cdot\text{cm}^{-2}\cdot\text{K}^{-1}$, c) increased pump and radiative quantum efficiencies of 0.99 respectively, and d) all of the above (a – c). Temperature scale is in degrees Kelvin..... 115

Figure 5.2-24: Stress distribution in constrained QS configuration at 100 s with 18.96 W incident pump power. Stress scale is in units of Pa. 117

Figure 5.2-25: Stress distribution in constrained QS configuration at 100 s with 18.96 W incident pump power. Colour bar is reduced in scale to show detail. Stress scale is in units of Pa. 118

Figure 5.2-26: Stress distribution in unconstrained QS configuration at 100 s with 18.96 W incident pump power. Stress scale is in units of Pa. 118

Figure 6.1-1: Mode matching efficiency for a top-hat pump distribution as a function of $a = wpwl$ for different values of reabsorption loss to passive cavity loss ratio, B . Plots are given for pump fluence (F) 10 times greater than threshold.¹¹⁹ 121

Figure 6.3-1: Comparison of simulated and experimental thermal images at 19 W pumping. a) CW thermal measurement, b) CW thermal simulation, c) QS thermal measurement, and d) QS thermal simulation. Temperatures are in degrees Celsius. 137

List of Abbreviations

AR	Anti-reflective
CCD	Charge-coupled Device
CM	Calorimeter
CPA	Chirped-pulse Amplifier
CW	Continuous Wave
DC	Direct Current
DM	Dichroic Mirror
ESA	Excited State Absorption
FEA	Finite Element Analysis
FWHM	Full-width Half-maximum
HR	High Reflectivity
HT	High Transmission
HTC	Heat Transfer Coefficient
IR	Infrared
LPF	Long-wave Pass Filter
LPP	Laser Produced Plasma
MOPA	Master Oscillator Power Amplifier
NA	Numerical Aperture
ND	Neutral Density
NIR	Near-Infrared

OC	Output Coupler
ODE	Ordinary Differential Equation
OPCPA	Optical Parametric Chirped-pulse Amplifier
OSA	Order Sorting Aperture
PCX	Plano-convex
PD	Photodiode
PDE	Partial Differential Equation
PM	Power Meter
PTFE	Polytetrafluoroethylene
QS	Q-switched
RK	Runge-Kutta
ROC	Radius of Curvature
SA	Saturable Absorber
SESAM	Semi-conductor Saturable Absorber Mirror
SM	Spectrometer
STXM	Scanning Transmission X-ray Microscopy
TFP	Thin-film Polariser
TL	Thermal Lensing
TXM	Transmission X-ray Microscopy
W	Wedge
WW	Water Window

Chapter 1

Introduction

1.1 Motivation

With the advent of high brightness diode laser pumping, quasi-three level laser materials have undergone somewhat of a resurgence. Previously with flash-lamp pumping, the significant population of active species in the lower laser level made quasi-three level lasers impractical because pump brightness was too low to greatly exceed threshold and initiate lasing. New quasi-three level gain materials have the benefit of lower quantum defects compared to four level laser systems which can lead to better efficiencies.¹ The reduced quantum defect can also decrease the thermal load in the crystal. Both of these aspects are important for high power laser systems. High power, quasi-three level laser systems have already been developed and have shown great promise. Many of the world's high power diode-pumped solid-state laser systems are currently using quasi-three level crystals such as Yb:YAG and Yb:S-FAP.²

The uses of high power laser systems are numerous. Ultrafast lasers have been utilised for micro-machining,³ micro- and nano-structuring,⁴ nano-ablation,^{5,6} 3D material processing,^{7,8} and many different sensing applications.⁹ Intermediate and high energy systems with pulse durations ranging from 10's of femtoseconds to 10's of nanoseconds have been used for the study of laser-plasma interactions such as wakefield particle acceleration,¹⁰ EUV nano-lithography,¹¹ x-ray micro-machining,¹² and x-ray microscopy;¹³ and as building blocks for inertial confinement nuclear fusion drivers.¹⁴⁻¹⁶ Developing laser systems based on new laser materials is of great interest in order to determine which materials will work best for different applications. Ytterbium-doped calcium fluoride has been suggested as a potential candidate for new high power laser systems because of its high damage threshold, low quantum defect,

and relatively large tunable bandwidth. But to succeed its various properties and capabilities must be understood.

In this thesis the experimental development of a longitudinally-pumped, passively Q-switched (QS), Yb:CaF₂ laser was undertaken. To my knowledge this is the first Cr:YAG, passively QS, Yb:CaF₂ laser demonstrated. In addition, a detailed rate equation model of the QS laser operation allowed for further optimisation for peak performance. Nanosecond pulsed lasers are useful for a variety of applications including pulsed laser annealing,¹⁷ machining,¹⁸ welding,^{19,20} and medical procedures.²¹ Of particular interest is the generation of soft x-rays in the water window (WW) between 2.3 nm and 4.4 nm. These x-rays can be used to image hydrated biological cells of thicknesses up to 10 μm and with resolutions down to 10's of nanometers.²² It is possible that a QS Yb:CaF₂ laser could generate powers high enough to achieve WW x-ray production from plasmas. In the last few years laser-based WW x-ray sources have been developed but they are generally based on actively QS lasers. The only other option is to use x-rays generated at large, expensive synchrotron facilities. A passively QS laser that could achieve the necessary pulse power for x-ray generation would have the benefit of being low cost and compact because there is no need for electro-optic or acousto-optic components. This would be a potentially valuable WW x-ray source.

As mentioned earlier, the thermal properties of the laser crystal are very important for applications in high power lasers and also play a role in the operation of a QS laser. The temperature profiles at the pump exit face of the laser crystal were measured in both CW and QS operation for various pump powers. This information was used to build a finite element, numerical model of heat transport for the CW pumped laser crystal under lasing and non-lasing operation. The combination of numerical rate equation modelling and 3D thermal modelling are not often mentioned in the literature but provide valuable insight into the operation of the laser.

1.2 Background

In terms of solid-state gain materials, Yb-doped crystals have become well studied over the past several years due to the ion's excellent spectroscopic properties. Trivalent Yb-doped laser materials have a simple energy level structure that consists of only two manifolds in the near-infrared (NIR). This simple structure precludes excited state absorption and up-conversion energy transfer effects from occurring.²³ In addition, Yb-doped materials have low quantum defects that reduce the heat generation from optical pumping and low concentration quenching leading to long fluorescence lifetimes.²⁴ This long fluorescence lifetime enables efficient energy storage and extraction. The Yb³⁺ ion was also found to have smooth and broad optical spectra with relatively large emission and absorption cross-sections for a variety of host materials.²

Yb:YAG has specifically become one of the most ubiquitous laser materials because it combines the qualities of the Yb³⁺ ion with the excellent thermomechanical properties of the YAG host. It has both high thermal conductivity and strong thermal shock resistance.²⁵ This becomes important when operating at high power and/or high repetition rate. However, it is worthwhile to consider Yb:CaF₂ as an alternative to Yb:YAG for several reasons. CaF₂ has a thermal conductivity only slightly lower than YAG when un-doped.² When doped the thermal conductivity drops faster than YAG but not significantly so. With cryogenic cooling the conductivity is improved further. The optical damage threshold is larger than that of Yb:YAG, and CaF₂ crystals can be manufactured in much larger sizes than YAG which is of importance for scaling to high energy systems. The fluorescence lifetime of Yb:CaF₂ is also longer than Yb:YAG at 2.4 ms versus 0.95 ms. Of significant importance is the wider emission spectrum of Yb:CaF₂ as compared to Yb:YAG. The cryogenic emission spectrum of Yb:CaF₂ doped at 2.2 at.% and Yb:YAG doped at 2 at.% are compared in Figure 1.2-1. The spectrum of Yb:CaF₂ is significantly wider which can lead to a theoretically shorter pulse width when mode-locked and to the development of tuneable sources. On the negative side of things, Yb:CaF₂ has a considerably lower absorption and emission cross section (in

large part due to its greater bandwidth) which means there is reduced gain from that of Yb:YAG. Finally, the mechanical properties of CaF₂ are not as robust as YAG with a higher coefficient of thermal expansion and lower hardness, fracture toughness, and thermal shock parameter. This means care must be used when handling the CaF₂ crystals.

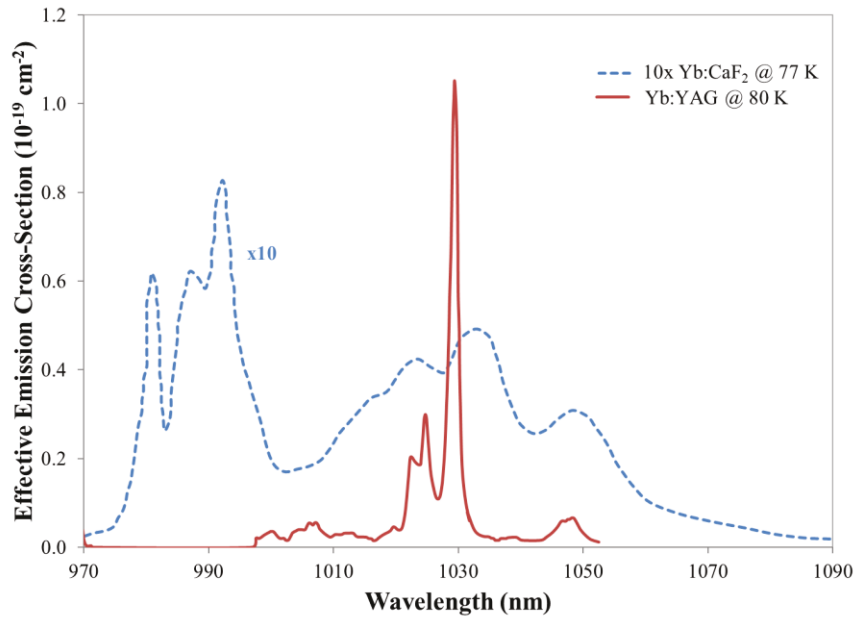


Figure 1.2-1: Effective emission cross-sections of 2.2 at.% Yb:CaF₂ at 77 K and 2 at.% Yb:YAG at 80 K.^{26,27}

The main energy levels for a Yb:CaF₂ crystal are shown in Figure 1.2-2, the lower ²F_{7/2} manifold consists of four Stark levels and the upper ²F_{5/2} manifold consists of three Stark levels. Stark levels are created when electric crystal-fields, manifested from the local crystal structure, cause the degenerate manifold energy levels to split.²⁸ Depending on the host crystal structure surrounding the dopant ions the crystal-field can be higher or lower leading to greater or lesser splitting, respectively. Lesser Stark level splitting can be useful when attempting to lase with a low quantum defect, but it also causes the thermal population in the lower lasing level to rise thus usually requiring cryogenic cooling. The broad emission and absorption cross-sections of Yb:CaF₂ come from a combination of Stark splitting and a rich multisite structure caused by the charge compensation required to substitute Ca²⁺ ions with

Yb^{3+} ions in the crystal lattice.²⁴ In this way, $\text{Yb}:\text{CaF}_2$ crystals act somewhat like doped glasses but with better thermal properties.

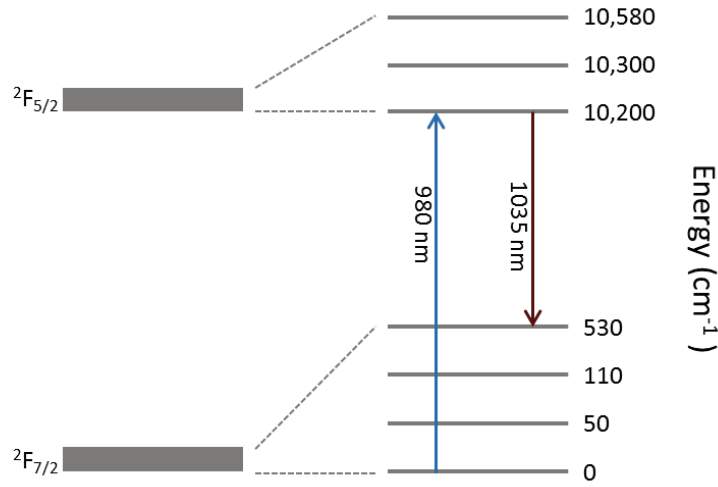


Figure 1.2-2: Energy levels of $\text{Yb}:\text{CaF}_2$ at 77 K.²⁸

1.3 Previous Work with $\text{Yb}:\text{CaF}_2$

Calcium fluoride has been known as a host crystal since some of the earliest days of the laser but the success of Nd^{3+} in other host crystals caused CaF_2 to be ignored to a large extent.² The first known demonstration of a $\text{Yb}:\text{CaF}_2$ laser was achieved by V. Petit et al.²³ in 2004. The 1.7 at.% Yb^{3+} doped crystal was pumped with a CW Ti:Sapphire laser at 920 nm and achieved a maximum output power of around 155 mW with a slope efficiency of 50%. Shortly following this A. Lucca et al.²⁴ produced a diode-pumped 5 at.% doped $\text{Yb}:\text{CaF}_2$ laser. This laser produced 5.8 W of power when pumped by a 15 W laser diode emitting at 980 nm. From the results of both authors the tuning range for $\text{Yb}:\text{CaF}_2$ lasers was found to lie between 1000 and 1072 nm. This broad emission spectrum indicated that $\text{Yb}:\text{CaF}_2$ could be a very good candidate for femtosecond lasers. Since these first results were produced, many monocrystalline $\text{Yb}:\text{CaF}_2$ laser systems have been developed in CW, mode-locked, regenerative amplifier, multi-pass, and QS configurations. The outcomes from this work have lead researchers to utilise $\text{Yb}:\text{CaF}_2$ in terawatt level systems.

CW lasers have been the most studied since they are the easiest laser to design and can help elucidate other results pertinent to the laser crystal. Slight improvements were made by some groups following the first CW results but only the most significant results will be presented here. In 2007 M. Siebold et al.²⁹ produced a 7.6 mm long, 3.3 at.% Yb-doped quasi-CW laser with diode stack pumping at 940 nm and achieved tunability from 1008-1090 nm with a peak output of 340 mW. J. Boudeile et al.³⁰ in 2008 improved on the maximum output power achieved at that point with 10.2 W output at an input pump power of 64 W at 980 nm. The laser utilised a 4 mm long, 2.6 at.% doped Yb:CaF₂ crystal and achieved a laser slope of 21.6%. In 2009 A. Pirri et al.³¹ reached a very high slope efficiency of 72.3% when diode laser pumping at 940 nm. The 2 mm long 5 at.% Yb-doped crystal produced the best overall efficiency of 52% at 2.7 W output and 4.7 W absorbed pump power. The best operation occurred for 20% duty cycle, quasi-CW lasing but CW lasing was very close.

Yb:CaF₂ was cryogenically cooled to 77 K by S. Ricaud et al.²⁶ in 2011 which enabled several gains. The 5 mm long, 2.2 at.% Yb-doped crystal produced 62 W at an absorbed pump power of 135 W. A very high input to output efficiency of 65% was achieved by decreasing the output coupler (OC) loss from 20% to 10%. The laser was diode pumped at 979 nm and found to be tunable from 992-1050 nm. Again in 2011 S. Ricaud et al.,²⁸ using the same laser crystal at 77 K, managed to lase with 35% input to output efficiency at 993 nm, producing 33 W of power. Since pumping was at 981 nm this low quantum defect of 1.2% led to a very low thermal load in the crystal. An even lower quantum defect of 0.7% was obtained when the crystal was operated at 993 nm while being pumped at 986 nm.

The first mode-locked oscillator based on Yb:CaF₂ was developed by A. Lucca et al.³² in 2004. They used a 4 mm long, 5 at.% Yb:CaF₂ sample and a semiconductor saturable absorber mirror (SESAM) to generate pulse widths down to 150 fs with an average power of 880 mW. The laser was pumped using a 15 W fibre-coupled diode laser at a wavelength of 979 nm and could achieve lasing from 1040 – 1053 nm. F. Friebel et al.,³³ in 2009,

demonstrated a sub-100 fs laser. This Yb:CaF₂ laser, pumped with a 7 W fibre-coupled laser diode at a wavelength of 979 nm, generated 99 fs pulses with an average power of 380 mW. Mode-locking was achieved with the 6.1 mm long, 2.6 at.% Yb:CaF₂ crystal through the use of a SESAM in conjunction with the Kerr-lens effect. In 2013 G. Machinet et al.³⁴ reported a Kerr-lens mode-locked Yb:CaF₂ laser. The Kerr-lens effect was produced within a 6 mm long, 4.5 at.% doped Yb:CaF₂ crystal. A very high quality single-mode Yb-doped fibre source was required to pump the crystal. The laser produced 68 fs pulses with a 2.3 W average power under a 7 W pump. They have since improved upon their results by generating 48 fs pulses with an average power of 2.7 W.³⁵

In order to develop terawatt systems the study of regenerative and multi-pass amplifiers is necessary. The first regenerative amplifier with Yb:CaF₂ was demonstrated by M. Siebold et al.²⁹ in 2007. The 7.6 mm long, 3.3 at.% Yb-doped laser crystal was pumped with a power up to 1.3 kW over 1.5 ms by a laser diode stack operating at 940 nm and 1 Hz. An approximately 10 μJ, 2.2 ns, 1030 nm centre wavelength seed pulse was amplified to 17.3 mJ after 32 round trips giving a final, recompressed pulse width of 215 fs at 1032.5 nm. In 2010 S. Ricaud et al.³⁶ designed a regenerative amplifier capable of amplifying seed pulses with 100 Hz to 10 kHz repetition rates. The 5 mm long, 2.6 at.% doped Yb:CaF₂ was pumped with a 980 nm fibre-coupled diode laser. When using a seed pulse stretched to 260 ps at 1043 nm the shortest amplified, recompressed pulse duration of 178 fs was achieved at a 500 Hz repetition rate. Peak energy occurred at a 300 Hz repetition rate with an uncompressed energy of 1.6 mJ. They improved on this result later that year with a 1.8 mJ uncompressed pulse at 100 Hz repetition rate.³⁷ T. Balčiunās et al.³⁸ developed a Yb:CaF₂, cryogenically cooled, regenerative amplifier for future use as a pump pulse in an optical parametric chirped-pulse amplifier (OPCPA) in 2014. Using diode pumping at 976 nm the regenerative amplifier increased the energy of the >500 ps pulse from approximately 100 μJ to 6.5 mJ at a 1 kHz repetition rate. These pulses are capable of being recompressed to less

than 150 fs but they used an acousto-optic programmable dispersion filter to create a top hat temporal pulse that was then compressed down to 1 ps.

Most multi-pass systems have been created as part of a larger laser system. However, in 2014 F. Friebe et al.³⁹ developed a multi-pass architecture that utilised two 2 mm long, 2.2 at.% Yb:CaF₂ crystals in an active mirror configuration. A 1.5 ns stretched pulse centred at 1030 nm with an energy of 1.1 mJ was amplified at a 20 Hz repetition rate to 57 mJ after 18 passes. Operation at 100 Hz was possible too but with amplification of only up to 32 mJ.

Regenerative amplifiers and multi-pass systems are good to study in isolation to develop understanding of their operation but ideally they are developed in conjunction with mode-locked oscillators and chirped-pulse amplifiers (CPAs) for the development of high power laser systems at the terawatt level. M. Siebold et al.⁴⁰ produced the first Yb:CaF₂ terawatt laser in 2008. Using a 20 mm long, 2.0-2.2 at.% doped Yb:CaF₂ multi-pass amplifier with a Ti:Sapphire oscillator and Yb:glass preamplifiers the system produced recompressed pulses of 192 fs in duration at 197 mJ of pulse energy. The Yb:CaF₂ multi-pass amplifier increased the energy of 1 Hz, 2 ns pulses centred at 1031 nm from 40 mJ to 420 mJ after 10 passes. The crystal was pumped with 7.4 kW of power over 4 ms from two diode stacks lasing at 940 nm. In 2014 A. Kessler et al.⁴¹ discussed the improvements to this system with an additional 34 mm long, 2.3 at.% doped Yb:CaF₂ based multi-pass amplifier. This amplifier was capable of being pumped with 810 J of total energy over 2.7 ms at a repetition rate of 1/120 Hz from 120 diode laser stacks emitting at 940 nm producing a circular spot diameter on the crystal of 32 mm. After 9 passes the 2.5 ns long, 2.7 J seed pulse was amplified to 16.6 J with possible compression down to 150 fs at a wavelength of 1034 nm.

Specifically important to the research presented in this thesis is the previous development of Yb:CaF₂ QS lasers. In 2005 L. Su et al.⁴² developed a self-QS laser based on a Yb³⁺ co-doped with Na⁺:CaF₂ crystal. The 6 mm long crystal was placed in a v-shaped laser cavity with a flat dichroic mirror on one end to enable diode pumping, a flat OC at the other end, and a 100 mm radius of curvature (ROC) mirror in the middle of the cavity. The pump was

focussed to a radius of 40 μm in the crystal. With pumping of 5 W at 976 nm the laser produced 1050 nm pulses, 1.5 μs in duration, at a repetition rate of 28 kHz and an average output power of approximately 390 mW when using a 2% transmission OC. The slope efficiency was 20.3%. They found that the laser was tunable between 1036 nm and 1059 nm. Demonstration of pure Yb:CaF₂ active Q-switching was achieved by M. Siebold et al.²⁹ in 2007. A DKDP Pockels cell and a thin-film polariser (TFP) were used to create the pulse via cavity dumping with a 2.6 ns Pockels cell switching time. The 95 cm cavity was designed with a flat dichroic mirror on one end and a 300 cm ROC mirror at the other. The 7.6 mm long, 3.3 at.% Yb:CaF₂ crystal was pumped with a 1.3 kW diode stack at 940 nm and the beam was focussed to a 1.4 mm x 1.9 mm elliptical spot. After a build-up time of 540 ns, 44 mJ pulses were generated with pulse durations of 6.4 ns at a repetition rate of 1 Hz. In the same year, output energy was improved to 60 mJ but with a decrease in peak power due to a longer pulse width of 23 ns.⁴³ In 2009 F. Friebel et al.,³³ while attempting to achieve mode-locking, produced passively QS pulses with peak output power of 9 W at 3 μs pulse durations and repetition rates between 13-14 kHz. The cavity was designed with a 1% saturable absorption SESAM at one end, a 400 mm ROC curved mirror followed by a 100 mm ROC curved mirror, then a 6.1 mm long 2.6 at.% doped Yb:CaF₂ crystal, then another 100 mm ROC curved mirror, followed by two SF10 prisms, and ending with an OC with a reflectivity of 98.7%. The laser crystal was pumped with a laser diode emitting at 979 nm and focussed down to approximately a 50 μm radius.

In 2010 S. Ricaud et al.^{36,37} operated their regenerative amplifier in actively QS mode. The 1.5 m cavity included a 5 mm long, 2.6 at.% doped Yb:CaF₂ crystal that was pumped through a dichroic mirror by a 10 W, CW, fibre-coupled laser diode at 978 nm with a spot diameter in the crystal of approximately 200 μm . The resonator was in a five mirror arrangement with two flat end mirrors, a flat dichroic mirror in the middle near the crystal, and two curved mirrors with ROCs of 300 mm. A BBO Pockels cell and a TFP were utilised for Q-switching. At a 100 Hz repetition rate 1.8 mJ pulses were generated though the peak average output

power of 850 mW was achieved at 800 Hz. The output spectrum was centred at 1040 nm. The latest Q-switching result was demonstrated by V. Clet et al. in 2012.⁴⁴ They used a 4 mm long, 4.5 at.% Yb-doped crystal pumped at 981 nm with a fibre-coupled laser diode producing a spot diameter in the crystal of approximately 200 μm . The cavity was configured nearly identically to S. Ricaud et al.'s QS laser above but with 500 mm ROC mirrors and an unspecified cavity length. They achieved tunable laser operation continuously from 1028-1065 nm with a maximum energy of 3 mJ at 1050 nm and a repetition rate of 300 Hz. They found that the pulse build-up time was 3.5 μs with pulse widths in the nanosecond regime and that continuous wave pumping produced better pulse-to-pulse stability than quasi-CW pumping.

Many groups have studied the spectroscopic and crystal structure properties of Yb^{3+} -doped CaF_2 crystals to aid in the development of better lasers. The first study of CaF_2 crystals doped with greater than 0.5 at.% Yb^{3+} was conducted by Y. Voron'ko et al.⁴⁵ in 1969 where they discovered the existence of hexameric clusters and attempted to map some of the Stark shifted energy levels. A more thorough examination of the lasing centre energy levels was completed by M. Ito et al.⁴⁶ in 2004. In 2008 V. Petit et al.⁴⁷ also produced highly cited results regarding the energy levels in $\text{Yb}:\text{CaF}_2$ and the two results differed but V. Petit et al. had good reasoning to believe their results were more accurate. From 2004 on there have been several attempts to measure and assign or calculate the energy levels with no significant agreement between authors.⁴⁸⁻⁵² In fact, the latest result presented in 2014 by B. Lacroix et al.⁵³ postulated that the hexameric Yb^{3+} clusters, originally thought to be the primary active laser sites, do not become prominent until greater than 20 at.% doping. This is much higher than laser crystal doping concentrations. They believe that a combination of dimeric, trimeric, and tetrameric Yb^{3+} clusters give rise to lasing. Fortunately, even though the clusters may be different they still exhibit similar energy level schemes. In short, there is still much debate regarding the true crystal structure and its effect on laser operation.

Many studies on fluorescence lifetimes, radiation trapping, Yb^{2+} impurities, absorption and emission cross-sections, and thermal properties have been undertaken. In 2004 V. Petit et al.²³ along with demonstrating the first $\text{Yb}:\text{CaF}_2$ laser also measured its spectroscopic and emission lifetime properties. In the same year M. Ito et al.⁴⁶ measured similar properties but also discussed the role that energy transfers between Yb^{3+} ions, and to impurities, had on the spectra. This study included looking at the effects concentration had on radiation trapping and radiative lifetimes. In 2008 V. Petit et al.⁴⁷ spent significant time discussing the emission and absorption spectra while attempting to determine the energy levels. Additionally, they reviewed many of the past studies done on $\text{Yb}:\text{CaF}_2$ by other researchers. An excellent review of the history and properties of $\text{Yb}:\text{CaF}_2$ was written by M. Siebold et al.² in 2009. F. Druon et al.⁵⁴ wrote a review paper in 2011 regarding the spectroscopic and thermal properties of $\text{Yb}:\text{CaF}_2$ which discussed the cross-sections, thermal conductivity, and possible effects of Yb^{2+} impurities. In 2012 J. Körner et al.⁵⁵ produced new absorption and emission cross-sections from 20-200°C that differed somewhat from previous results. They also calculated a shorter radiative lifetime than previous authors by minimising radiation trapping. J. Körner et al.⁵⁶ measured the same properties but at cryogenic temperatures in 2014. A means to estimate the concentration of Yb^{2+} ions in a Yb^{3+} -doped CaF_2 crystal was presented by A. Shcheulin et al.⁵⁷ in 2013. They converted the Yb^{3+} ions to Yb^{2+} and determined the absorption cross-section of $\text{Yb}^{2+}:\text{CaF}_2$.

1.4 Modelling of $\text{Yb}:\text{CaF}_2$ and Similar Systems

The rate equation modelling of $\text{Yb}:\text{CaF}_2$ QS lasers is absent from the literature but the means by which the modelling occurs is well defined. The first Q-switching rate equation models were developed and solved by W. Wagner and B. Lengyel,⁵⁸ and R. Kay and G. Waldman⁵⁹ in the mid-sixties. Around this time modifications were made to the rate equations to include the possibility of a saturable absorber (SA) acting as the switching mechanism by A. Szabo and R. Stein.⁶⁰ In 1976 W. Koechner⁶¹ provided an engineering approach to the problem by developing some approximate expressions for the output

parameters as long as the initial and final population inversions were known. Analytical solutions and optimisations for many of the output parameters such as pulse energy, power, and duration in an actively QS laser were given by J. Degnan⁶² in 1989. He also provided a new way of considering the inversion reduction factor, γ , showing that it can be between 0 and 2 depending on the laser crystal and the laser pulse duration. Then in 1994 C. Nabors⁶³ introduced a theoretical model for longitudinally-pumped quasi-three level QS lasers with the inclusion of reabsorption where the pump beam is assumed to be a plane wave. In 1995 J. Degnan⁶⁴ applied the same techniques as before to develop analytical solutions and optimisations for a passively, rather than actively, QS laser. He then went on in 1998 to consider the effects of thermalisation times within the Stark level manifolds on the performance of a QS laser when the pulse durations are greater than 20 ns.⁶⁵ This work was developed further by S. Voitkov et al.⁶⁶ in 2005 by considering pulses that are on the order of, or shorter than, the thermalisation times such as is the case for sub-nanosecond pulses.

In 2007 G. Xiao and M. Bass⁶⁷ took Degnan's 1995 work on passively QS lasers and generalised the formulas to include excited state absorption (ESA) in the SA. X. Zhang et al.⁶⁸ studied the implication of a transverse Gaussian pump and mode profile on the output parameters of a passively QS laser in 2000 and found it made a significant difference, especially in the pump to mode coupling efficiency. S. Li et al.⁶⁹ then took this work and expanded on it in 2007 by considering flat-top pumping profiles. In 2003 J. Dong⁷⁰ studied numerically a passively QS Yb:YAG laser with a Cr:YAG SA using rate equations. The rate equations included the influence of the pump power on the output pulse characteristics. M. Lu et al.⁷¹ took this further in 2009 and solved some relations analytically for the influence of pump power on the population inversion. Additionally, the finite recovery time of the SA was included in the model and the rate equations were solved numerically to study the relationship between finite recovery time and pump power. To include the effect of longitudinal temperature distribution on QS operation, C. Li et al.⁷² in 2004 developed a

model and looked at the differences in laser optimisation introduced by a non-uniform temperature distribution.

The analysis of heat generation in laser crystals has been of interest since the early days of the laser. It is especially important in quasi-three level laser systems due to a thermally populated lower laser level. S. Chénais et al.^{73,74} provided a review in 2004 on the relevant solutions to the cylindrical heat equation for axial heat sources with distributions ranging from Gaussian to super-Gaussian to top-hat. They also discuss the sources of heat generation, thermal lensing, and quantum efficiencies in Yb^{3+} -doped materials. The analysis was enhanced by experimental measurement of the thermal lens, thermo-optic coefficients, and quantum efficiencies for several crystals. This work was done following F. Augé et al.⁷⁵ in 2000 who studied the thermal effects on Yb:GdCOB. They theoretically and experimentally analysed the effect heat had on absorption saturation, M^2 factor, and fluorescence quenching when the pump and mode profiles were transversely Gaussian but also longitudinally dependent. Some of the original work on heat generation in Yb:YAG was done by T. Fan⁷⁶ in 1993 where he looked at the fractional thermal loading of laser crystals and compared Yb:YAG to Nd:YAG.

In 2004 S. Chénais et al.⁷⁷ specifically measured the surface temperature map of a Yb:YAG crystal under longitudinal diode pumping with a thermal camera and computed the heat transfer coefficient between the crystal and mount with various heat transfer materials in-between. Following the same method as S. Chénais et al., in 2005 J. Didierjean et al.⁷⁸ measured the temperature map of Nd-doped crystals and compared them to finite element analysis (FEA) simulations. In the same year H. Yu, G. Bourdet, and S. Ferre⁷⁹ undertook significant numerical modelling of the population inversion, gain, wavefront distortion, and thermal stress dependent on the average temperature of the laser crystal for a high energy multi-pass Yb:YAG laser. In 2008 J. Didierjean et al.⁸⁰ developed a method to measure thermal conductivity of a laser crystal while under CW laser operation using a thermal camera. Though the results were presented for Nd:YAG, in the same year J. Boudeile et al.³⁰

used the method to discuss Yb:CaF₂ crystals under high power pumping. This was the first thermal study for lasing Yb:CaF₂ crystals and they measured the crystal face thermal gradients, the thermal lens, and the absorption coefficients. These results were utilised in the determination of the crystal's thermal conductivity, fractional thermal load, thermo-optic coefficient, and radiative quantum efficiency.

A. Pirri et al.³¹ in 2010 investigated the temperature influence of CW and quasi-CW operation on a Yb:CaF₂ laser. They found some performance degradation with increasing duty cycle but not a significant amount. Thermal modelling was done, ignoring pump absorption saturation, to determine the approximate temperatures reached in the laser crystal. The latest results with Yb:CaF₂ come from F. Friebel et al.³⁹ in 2014 where the thermal response times of the crystal were measured on a time scale of seconds with a thermal camera and milliseconds with a pump-probe thermal lensing setup. The thermal effects were measured for a quasi-CW diode pumped, multi-pass configuration under non-lasing conditions. To understand the delay found between the pump pulse and the thermal lens effect an FEA simulation was run and determined that the thermal load was intimately linked to the fluorescence.

Specific thermal measurements based on QS lasers have not been carried out for Yb:CaF₂. As previously mentioned, C. Li et al.⁷² in 2004 produced active Q-switching simulations based on a non-uniform temperature distribution in Yb:YAG. More recently, in 2013, S. Zhang and X. Wang⁸¹ numerically solved a model that included the passive Q-switching rate equations and the heat equation for an Nd:YVO₄ laser. This simulation showed that instantaneous changes in the population inversion caused thermal fluctuations, which modulated the thermal diffraction loss in the gain crystal, leading to instability in the output characteristics of the laser. This analysis did not take into account any quasi-three level behaviour.

1.5 Outline

In Chapter 2 the theoretical background of Q-switching for longitudinally-pumped quasi-three level lasers is outlined and the creation and distribution of heat in a laser crystal is discussed. A brief introduction to water window x-ray generation is also given.

The criteria used in the design of the Yb:CaF₂ laser cavity, for both CW and QS operation, is presented in Chapter 3. The procedures used to measure the laser output parameters and thermal distributions in the laser crystal are provided. Then in Chapter 4 the simulation method, setup, and limitations are discussed with respect to the rate equation modelling and thermal modelling. Verification of the thermal model through comparison to other results in the literature is given.

Chapter 5 reports the results from the experiments. These include the pump characterisation, CW and QS output performance, and CW and QS thermal measurements. Following this, the simulation results for the Q-switching rate equations and thermal models are presented.

In Chapter 6 the results from the experiments and simulations are discussed. The CW laser results are compared to theory and the QS laser results are compared to the simulations. The thermal results for both CW and QS cases are compared to each other and to the simulations. Overall, results are equated to previous results in the literature. In both the laser performance and thermal results, possible model improvements and experimental optimisation are considered. Finally, the applicability of such lasers for the generation of soft x-rays is considered.

Chapter 7 summarizes the work and discussions detailed in the thesis. Conclusions are drawn and possible future directions are also presented.

Chapter 2

Theoretical Background

2.1 Longitudinally-Pumped Quasi-Three-Level Lasers

In many types of gain media, and specifically in Yb:CaF₂, the traditional three-level and four-level laser schemes do not accurately describe the laser dynamics taking place. These laser media have a small but significant thermal population of electrons in the lower laser level and are known as quasi-three-level lasers.⁸² There are two main features of quasi-three-level gain media that, in general, decrease the performance versus a four-level laser. The first is the reduction of the population inversion $N_2 - N_1$, where N_2 is the upper laser level population and N_1 is the lower laser level population. The second is the reabsorption of the emitted laser radiation by a transition from level one back to level two.

Models can be developed to explain quasi-three-level laser systems. In a CW pumping and lasing case the approximation of instantaneous thermalisation of the laser manifolds is assumed. In this situation energy is extracted from the entire upper manifold as the upper laser level is repopulated much faster than changes in the optical field.⁸³ Thermalisation times are not well known but are anticipated to be in the range of several hundred picoseconds to a few nanoseconds.^{65,66,84} The upper, lower, and ground laser population densities are given by:

$$N_2 = g_2 f_2 N_u \quad (2.1-1)$$

$$N_2^p = g_2^p f_2^p N_u \quad (2.1-2)$$

$$N_1 = g_1 f_1 N_l \quad (2.1-3)$$

$$N_g = g_g f_g N_l \quad (2.1-4)$$

Where N_g and N_2^p are the ground level and upper pump level population densities respectively in m^{-3} ; N_l and N_u are the lower and upper manifold population densities respectively in m^{-3} ; g_2 , g_2^p , g_1 , and g_g are the upper laser, upper pump, lower laser, and ground level degeneracies respectively; and f_2 , f_2^p , f_1 , and f_g are the upper laser, upper pump, lower laser, and ground level Boltzmann factors respectively.

The Boltzmann factors are calculated in the following way:

$$f_2 = g_2 \frac{\exp(-\frac{E_2}{kT})}{\sum_j g_j \exp(\frac{-E_j}{kT})} \quad (2.1-5)$$

$$f_2^p = g_2^p \frac{\exp(-\frac{E_2^p}{kT})}{\sum_j g_j \exp(\frac{-E_j}{kT})} \quad (2.1-6)$$

$$f_1 = g_1 \frac{\exp(-\frac{E_1}{kT})}{\sum_i g_i \exp(\frac{-E_i}{kT})} \quad (2.1-7)$$

$$f_g = g_g \frac{\exp(-\frac{E_g}{kT})}{\sum_i g_i \exp(\frac{-E_i}{kT})} \quad (2.1-8)$$

Where E_2 , E_2^p , E_1 , and E_g are the upper laser, upper pump, lower laser, and ground state energy levels respectively; E_j and E_i are the upper and lower manifold energy levels respectively; k is the Boltzmann constant; and T is the temperature.

In the Q-switched (QS) laser model, the instantaneous thermalisation of the laser manifolds are again assumed since thermalisation occurs faster than the changes in the optical field.⁸⁵ This allows the CW rate equations to be modified to accurately describe a QS laser. Passively QS lasers can be thought of as the most general case since actively QS lasers are essentially a passive Q-switch with a saturable absorber (SA) that bleaches extremely easily.⁶⁹ The rate equations for a laser diode end-pumped QS laser are given in Equations (2.1-9) to (2.1-11).⁸⁶

$$\frac{d\phi}{dt} = \frac{l_l c}{Ln_l} \left[\sigma_e^l N_2 \left(\phi + \frac{1}{Ls_2} \right) - \sigma_a^l N_1 \phi \right] - \frac{l_a c \phi}{Ln_s} [\sigma_{gs} N_{gs} + \sigma_{es} N_{es}] - \frac{\phi}{\tau_c} \quad (2.1-9)$$

$$\frac{dN_l}{dt} = \frac{c}{n_l} \phi [\sigma_e^l N_2 - \sigma_a^l N_1] + \frac{N_u}{\tau_l} - \frac{W_p}{l_l s_1 h \nu_p} \left[1 - e^{-(\sigma_a^p N_g - \sigma_e^p N_2) l_l} \right] \quad (2.1-10)$$

$$\frac{dN_{gs}}{dt} = -\sigma_{gs} \frac{c}{n_a} \phi N_{gs} + \frac{N_{es}}{\tau_2} \quad (2.1-11)$$

Where ϕ is the total photon number in the laser mode in m^{-3} , l_l and l_a are the length of the laser crystal and SA respectively in m, L is the length of the cavity in m, σ_e^l and σ_e^p are the spectroscopic emission transition cross-sections for the laser and pump wavelengths respectively in m^2 , σ_a^l and σ_a^p are the spectroscopic absorption transition cross-sections for the laser and pump wavelengths respectively in m^2 , σ_{gs} and σ_{es} are the absorption cross-sections for the SA ground and excited states respectively in m^2 , s_1 and s_2 are the areas of the pump beam and laser mode in the laser crystal respectively in m^2 , N_{gs} and N_{es} are the SA ground and excited state population densities respectively in m^{-3} , τ_l and τ_2 are the fluorescence lifetimes of the excited state in the laser crystal and SA respectively in s, W_p is the pump power in W, n_a is the refractive index of the SA, ν_p is the pump frequency in Hz, h is Plank's constant in $\text{m}^2 \cdot \text{kg} \cdot \text{s}^{-1}$, c is the speed of light in free space in $\text{m} \cdot \text{s}^{-2}$, and τ_c is the cavity photon lifetime in s defined in Equation (2.1-12). Equations (2.1-13) and (2.1-14) describe the relationship between laser and SA energy level population densities respectively.

$$\tau_c = \frac{L + (n_l - 1)l_l + (n_a - 1)l_a}{\frac{c}{2} [L_i - \ln(R_1 R_2)]} \quad (2.1-12)$$

$$N_l + N_u = N_0 \quad (2.1-13)$$

$$N_{gs} + N_{es} = N_{s0} \quad (2.1-14)$$

Where L_i is the internal resonator loss per round trip, n_l is the refractive index of the laser crystal, R_1 and R_2 are the end mirror and output coupler reflectivities respectively, and N_0 and N_{s0} are the dopant concentrations in the laser medium and SA respectively in m^{-3} . The various energy levels, population densities, fluorescence lifetimes, and spectroscopic cross-

sections for a simple quasi-3-level laser and 4-level saturable absorber are shown in Figure 2.1-1.

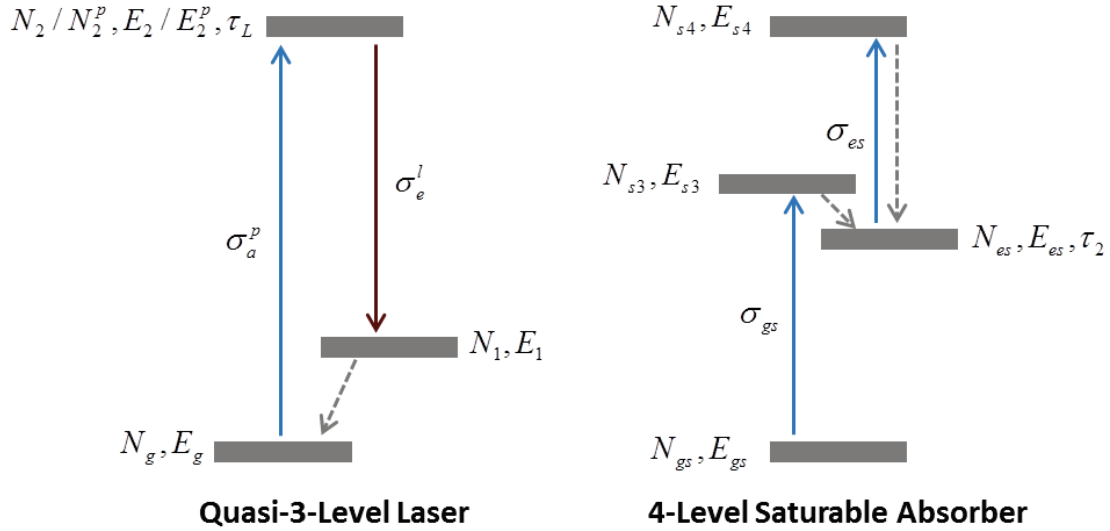


Figure 2.1-1: Energy level diagram for a simple quasi-3-level laser and 4-level SA with energy levels, population densities, fluorescence lifetimes, and spectroscopic cross-sections shown. Fast, non-radiative transitions are shown by a dashed arrow.

Some modifications to the equations given in Reference [86] were required to suit a laser where the gain medium and saturable absorber medium are separate. Specifically, the refractive indices and medium lengths have been separated. In addition, passive resonator losses have been added to τ_c . This model does not take into account spatial or temporal variations in temperature within the gain medium nor does it address spatial variations of the pump or laser mode in the cavity. Relating to the latter, the model presented here is a plane-wave approximation where the pump and laser fields are assumed to be uniform through the cross-section.⁶⁹

2.2 Heat Deposition and Thermal Distribution in Laser Crystals

In order to determine the thermal distribution in a material, first the sources of heat and heat extraction must be known and then the heat equation must be solved using material parameters. Heat deposited in an absorbing dielectric such as Yb:CaF₂ is characterised by the

amount of light absorbed per unit length and the percentage of this absorbed energy that is not re-emitted due to fluorescence or stimulated emission, i.e. becomes heat.

The heat equation is given by:

$$\rho c_p \frac{\partial T(x, y, z, t)}{\partial t} - \nabla \cdot (K_c \nabla T(x, y, z, t)) = Q_{th}(x, y, z, t) \quad (2.2-1)$$

Where ρ is density in $\text{kg}\cdot\text{m}^{-3}$, c_p is the specific heat capacity at constant pressure in $\text{J}\cdot\text{kg}^{-1}\cdot\text{K}^{-1}$, $T(x, y, z, t)$ is the temperature in K, K_c is the thermal conductivity in $\text{W}\cdot\text{m}^{-1}\cdot\text{K}^{-1}$, and Q_{th} is the thermal load per unit volume in $\text{W}\cdot\text{m}^{-3}$.

Heat transfer from the laser crystal to its surroundings is an important characteristic when determining absolute crystal temperature. Heat can transfer out of the crystal by conduction, convection, and radiation; with conduction being the primary method of heat extraction when using a cooled crystal mount. For the contact between the mount and crystal the most relevant boundary condition is the Newton Law of cooling which is often also used to represent convection.⁷³ Mathematically the boundary condition is:

$$-K_c \frac{\partial T}{\partial n} = H(T(x, y, z) - T_c) \quad (2.2-2)$$

Where $\frac{\partial T}{\partial n}$ is the derivative of temperature in the normal direction in $\text{K}\cdot\text{m}^{-1}$, H is the heat transfer coefficient (HTC) in $\text{W}\cdot\text{m}^{-2}\cdot\text{K}^{-1}$, and T_c is the temperature of the mount in K. Equation (2.2-2) is also used as a boundary condition for natural convective cooling on the sides of the crystal that are not in direct contact with the mount; this includes the faces of the crystal. Finally, the radiation boundary condition is:⁸⁷

$$-K_c \frac{\partial T}{\partial n} = \epsilon \sigma (T(x, y, z)^4 - T_c^4) \quad (2.2-3)$$

Where ϵ is the emissivity of the material and σ is the Stefan-Boltzmann constant in $\text{W}\cdot\text{m}^{-2}\cdot\text{K}^{-4}$.

When modelling temperature distributions analytically, simplifications are often made to enable ease of calculation. Since the heat transfer due to conduction is several orders of magnitude greater than the heat transfer due to convection and radiation it is often the only factor taken into account. However, using finite element analysis (FEA) it is possible to consider all of these conditions.

In order to determine the thermal load per unit volume due to fibre-coupled diode end-pumping, the pump intensity, I_p , absorbed in the crystal must be calculated. The amount of absorbed pump intensity in an infinitesimally thin cross-section dx is equal to $-\frac{dI_p}{dx} \cdot dx$, or the negative of the change in pump intensity passing through the cross-section times the width of the cross-section. The following equations can be used to calculate this change under steady-state lasing conditions.⁸⁸

$$\frac{dI_p(r, x)}{dx} = \frac{-\left(\alpha_0^p + \alpha_0^l \frac{I_l(x)e^{-(2r^2/w_l(x)^2)}}{I_{min}}\right)}{1 + \frac{I_p(r, x)}{I_{psat}} + \frac{I_l(x)e^{-(2r^2/w_l(x)^2)}}{I_{lsat}}} I_p(r, x) \quad (2.2-4)$$

$$I_{lsat} = \frac{h\nu_l}{\left(\sigma_{a_{eff}}^l + \sigma_{e_{eff}}^l\right) \tau_L} \quad (2.2-5)$$

$$I_{psat} = \frac{h\nu_p}{\left(\sigma_{a_{eff}}^p + \sigma_{e_{eff}}^p\right) \tau_L} \quad (2.2-6)$$

$$I_{min} = \frac{h\nu_p}{\left(\sigma_{a_{eff}}^p \cdot \frac{\sigma_{e_{eff}}^l}{\sigma_{a_{eff}}^l} - \sigma_{e_{eff}}^p\right) \tau_L} \quad (2.2-7)$$

Where α_0^l and α_0^p are the unsaturated absorption coefficients at the laser and pump wavelengths (λ_l and λ_p) respectively in m^{-1} , I_{min} is the minimum pump intensity required to reach transparency at the laser wavelength in $W \cdot m^{-2}$, I_{lsat} and I_{psat} are the laser and pump saturation intensity respectively in $W \cdot m^{-2}$, I_l is the intracavity laser intensity in W , w_l is the

laser mode radius, $r = \sqrt{y^2 + z^2}$ is the radial coordinate in m; ν_l and ν_p are the laser and pump frequencies respectively in Hz; $\sigma_{a_{eff}}^l$ and $\sigma_{a_{eff}}^p$ are the effective absorption cross-sections for the laser and pump wavelengths respectively in m^2 , and $\sigma_{e_{eff}}^l$ and $\sigma_{e_{eff}}^p$ are the effective emission cross-sections for the laser and pump wavelengths respectively in m^2 . The effective cross-sections are related to the transition cross-sections by the Boltzmann occupation factors defined in Equations (2.1-5) to (2.1-8), i.e. $\sigma_{e_{eff}}^l = f_2 \sigma_e^l$, $\sigma_{a_{eff}}^l = f_1 \sigma_a^l$, $\sigma_{e_{eff}}^p = f_2^p \sigma_e^p$, and $\sigma_{a_{eff}}^p = f_1^p \sigma_a^p$. It is also possible to calculate pump power absorbed in the gain medium below laser threshold by setting I_l to 0 in Equation (2.2-4).

Equation (2.2-4) can be found from the solution of the CW rate equations by assuming the population inversion is constant with time. The numerator describes the contributions to pump absorption from the pump and laser beams and the denominator describes the saturation of absorption due to the pump and laser intensities. The initial pump intensity is assumed to be top-hat and the laser intensity is assumed to be Gaussian.

The upper state lifetime can be related to the radiative and non-radiative lifetimes of the gain material. The upper state lifetime, or fluorescence lifetime, is temperature dependent due to the non-radiative lifetime's dependence.⁷⁵

$$\frac{1}{\tau_l(T)} = \frac{1}{\tau_{NR}(T)} + \frac{1}{\tau_R} \quad (2.2-8)$$

Where τ_R is the radiative lifetime in s or equivalently the upper state lifetime at 0 K and $\tau_{NR}(T)$ is the non-radiative lifetime in s.

Both the laser and pump modes are not constant within the gain crystal though the laser mode is very nearly constant for short crystals. Both modes can be calculated using the Gaussian beam evolution formula with an M^2 correction factor; where for the laser mode M^2 is very nearly one.

$$w(x) = w_0 \sqrt{1 + \left(\frac{M^2 \lambda (x - x_0)}{n \pi w_0^2} \right)^2} \quad (2.2-9)$$

Where w_0 is the beam waist in m and M^2 is the beam propagation factor. The laser mode radius in the cavity can be calculated even if the beam waist position, x_0 , is located outside of the cavity.

Once Equation (2.2-4) is solved, the change in pump power through the crystal can be used to determine the absorbed power's contribution to the heating of the crystal, Q_{th} .^{30,73}

$$Q_{th}(r, x) = -\eta_h \cdot \frac{dI_p(r, x)}{dx} \quad (2.2-10)$$

The fractional thermal load, η_h , is given by:

$$\eta_h = 1 - \eta_p \left[(1 - \eta_l) \eta_r \frac{\lambda_p}{\lambda_f} + \eta_l \frac{\lambda_p}{\lambda_l} \right] \quad (2.2-11)$$

Where η_p is the pump quantum efficiency defined as the fraction of absorbed pump photons that add to the upper laser manifold population and is often approximated as unity in crystals without significant defects or impurities, η_l is the laser extraction efficiency or the fraction of excited electrons that decay due to stimulated emission, and η_r is the radiative quantum efficiency of the upper manifold which is the fraction of excited electrons that decay by spontaneous emission. η_l and η_r are given by:

$$\eta_l = \frac{\frac{I_l}{h\nu_l} [(\sigma_e^l + \sigma_a^l)N_2 - \sigma_a^l N_0]}{\frac{I_l}{h\nu_l} [(\sigma_e^l + \sigma_a^l)N_2 - \sigma_a^l N_0] + \frac{N_2}{\tau_R} + \frac{N_2}{\tau_{NR}}} \quad (2.2-12)$$

$$\eta_r = \frac{\tau_{NR}}{\tau_{NR} + \tau_R} \quad (2.2-13)$$

The radiative quantum efficiency is equal to the ratio of the spontaneous emission rate to the sum of the spontaneous and non-radiative relaxation rates and similarly the laser extraction efficiency is equal to the ratio of the stimulated emission rate to the sum of the

stimulated, spontaneous, and non-radiative emission/relaxation rates. In order to simplify the laser extraction efficiency and remove the dependency on the upper laser manifold population, laser reabsorption can be neglected if $\sigma_e^l N_2 \gg \sigma_a^l N_1$; in that case η_l is given by Equation (2.2-14).

$$\eta_l \approx \frac{\frac{\sigma_e^l I_l}{h\nu_l}}{\frac{\sigma_e^l I_l}{h\nu_l} + \frac{1}{\eta_r \tau_R}} \quad (2.2-14)$$

The fractional thermal load given above takes into account the major processes inside the pump gain medium that can lead to heat generation. This includes fluorescence and laser quantum defects, non-radiative relaxation, concentration quenching, and the presence of non-radiative sites in the host crystal. The value of η_h is anisotropic during laser operation due to radially dependent laser intensity and temperature gradients in the crystal.

2.3 Water Window X-ray Generation Techniques

There have been several x-ray microscopy schemes developed over the years to study biological cells. Of particular interest for the imaging of hydrated cells using table-top x-ray sources are transmission full-field x-ray microscopy (TXM) and scanning transmission x-ray microscopy (STXM).⁸⁹ These methods can also be extended to full 3D tomographic imaging which is even more valuable. A typical setup for TXM and STXM can be seen in Figure 2.3-1. In order to modify these methods for 3D imaging the specimen must be fixed to a rotating holder so that 180 degrees of imaging is possible. Generally an image is taken every one degree.

The water window (WW) consists of x-rays with energies between the K absorption edges of carbon and oxygen, 284 eV and 543 eV respectively. This corresponds to a wavelength between 2.28 and 4.36 nm. Figure 2.3-2 shows the absorption coefficient values for water (oxygen) and proteins (carbon) in this wavelength region.

X-ray microscopy finds itself between optical and electron microscopy in terms of its resolution. The best performance of a WW x-ray microscope was 10 nm resolution using a synchrotron x-ray source.⁹⁰ Synchrotron facilities have achieved the best results for TXM and STXM both in resolution and in imaging time. Imaging time relates to the duration of x-ray exposure. Shorter imaging times lead to better images because there are less thermal-mechanical distortions in the samples and in the mounting mechanism. Synchrotron facilities are capable of achieving these results due to the monochromaticity of the x-rays and the high brightness (large photon flux).⁸⁹ The greatest issue with the synchrotron facilities are they cannot be used in the laboratory in a bench-top setup. The facilities are very large, have wait times, and are not necessarily geographically close to the biology laboratory.

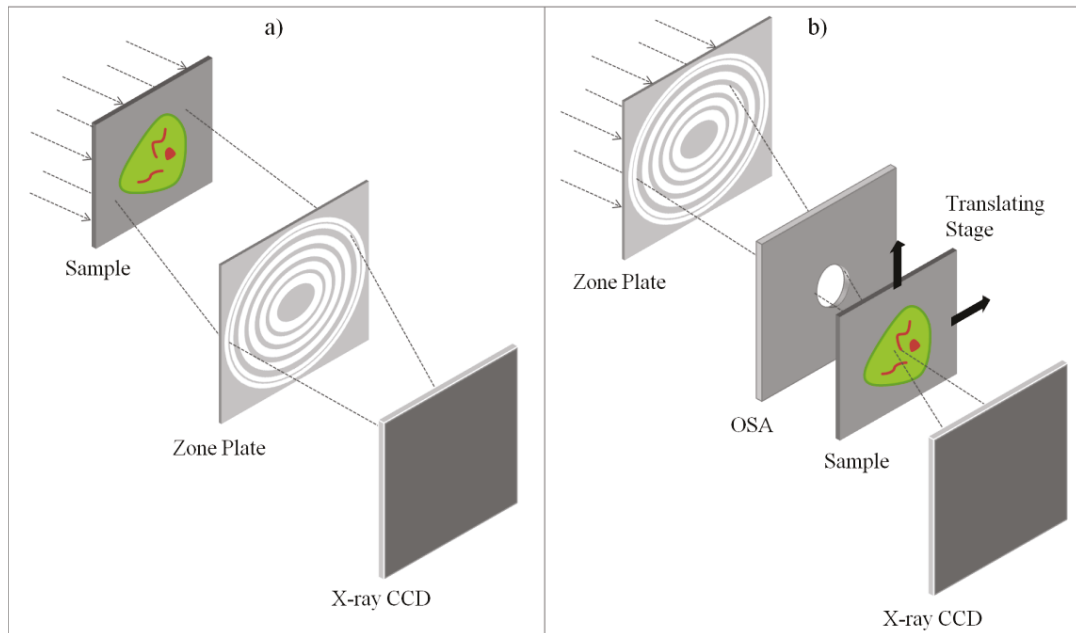


Figure 2.3-1: The basic configurations for a) transmission full-field x-ray microscopy and b) scanning transmission x-ray microscopy. An order sorting aperture (OSA) is used to filter out zero and higher order radiation in the STXM scheme.⁹¹

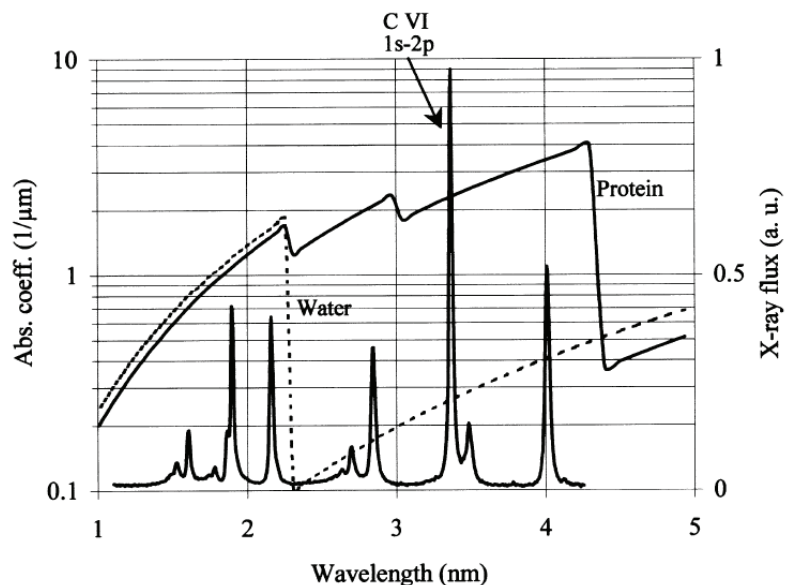


Figure 2.3-2: Absorption edges of water and protein in a range from 1 to 5 nm. Also shown are the emission lines from an ethanol plasma.¹³

A compact source would have great benefit for use in individual laboratories at universities or companies. This source would not be capable, currently, of producing the image quality of a synchrotron source, but it would provide a tool for researchers that is readily available, convenient, and could even be used as an inexpensive test before sending samples to a large facility.⁹² Compact sources are available in the form of laser produced plasmas (LPPs). It has been found that the most efficient method of generating x-rays in the WW are with nano- and pico-second laser pulses.⁸⁹ These laser pulses are focussed onto a target consisting of a solid, liquid, or gas, ionizing it in the process. The hot plasma produced by this interaction contains many free electrons. The electrons then produce x-ray radiation from bremsstrahlung or from free electron collisions with inner shell electrons resulting in excitation and recombination processes.⁹²

Typical targets used in a LPP based x-ray source are carbon and nitrogen containing materials such as ethanol,¹³ solid carbon,⁹³ boron-nitride,⁸⁹ nitrogen gas,^{94,95} and liquid nitrogen.^{90,92,96} In these materials some of the dominant K-shell emission lines lie in the WW. The emission spectrum from an ethanol plasma is shown in Figure 2.3-2. The line of

particular interest is marked C IV 1s-2p. This represents the x-ray emission for a 2p to 1s orbital transition in a C^{+3} ion (hydrogen-like carbon). Figure 2.3-3 shows the emission spectrum from a nitrogen plasma. The emission lines of particular interest for nitrogen are the N VI 1s2p-1s² and N VII 2p-1s transitions. These emissions represent the He- α (helium-like) 1s2p to 1s² transition in an N^{+5} ion and the Ly- α (hydrogen-like) 2p to 1s orbital transition in an N^{+6} ion respectively.

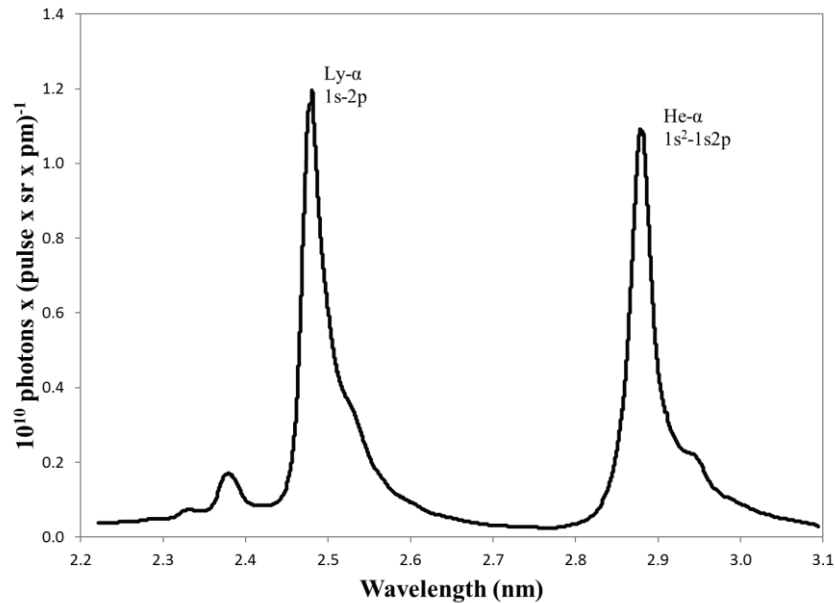


Figure 2.3-3: Emission spectra of nitrogen under laser excitation.⁹²

Nitrogen plasma emissions are particularly of interest because they emit x-rays in the WW in relatively low temperature plasmas. Optimum plasma temperatures range between 40-100 eV for nitrogen WW emission.⁹⁵ This means that x-rays can be produced with lower laser intensities; for example, laser pulses with 10^{11} - 10^{13} W/cm² intensities at 1064 nm have excited x-ray lines in nitrogen.⁸⁹ The most valuable spectral line from nitrogen is the Ly- α transition which produces 2.478 nm photons. This is beneficial because it has a theoretically better resolution than the 2.879 nm line produced by the He- α transition and it is closer to the oxygen absorption edge leading to less absorption of the x-rays in carbon based matter and subsequently the ability to image thicker samples.

Chapter 3

Experimental Procedure

3.1 CW Laser Design and Measurement

The CW laser resonator designed for study is shown in Figure 3.1-1. It consisted of a 10 mm x 10 mm x 5 mm thick, uncoated, 2.0 at.% Yb-doped CaF₂ crystal at Brewster's angle pumped by a 100 W (LIMO 100-F200-DL980-AV5-A) fibre-coupled diode laser. The pump beam was coupled into a 200 µm diameter fibre with a numerical aperture (NA) of 0.22 and then focussed with a 50:50 mm achromatic doublet pair (ThorLabs MAP105050-B) onto the crystal. The laser crystal was purchased from Korth Kristalle GmbH. The laser resonator was a simple linear design, 99.1 mm ± 0.2 mm in length with a flat dichroic mirror (DM) and a concave, 100 mm radius of curvature (ROC) output coupler (OC) with a transmission of 95.0% ± 0.2% at 1050 nm. The DM was coated for high transmission (HT) >99.8% side one and >98% side two from 800-1000 nm and high reflectivity (HR) >99.9% side two from 1020-1200 nm. The Yb:CaF₂ crystal was temperature controlled with a custom built, water-cooled, aluminum mount contacting on two sides using silicone heat transfer compound (M. G. Chemicals). The crystal was mounted at 45° and clamped along the top two sides. The mount design is shown in Figure 3.1-2. To reduce the chance of fracture, a 125 µm thick piece of indium foil was placed between the crystal and the clamp. The 4-40 clamping screws were made of nylon and were both tightened to a torque of 1.5 N·cm which corresponded to a combined downward force of 53.4 N and a pressure on the crystal surface of 216 N·cm⁻².

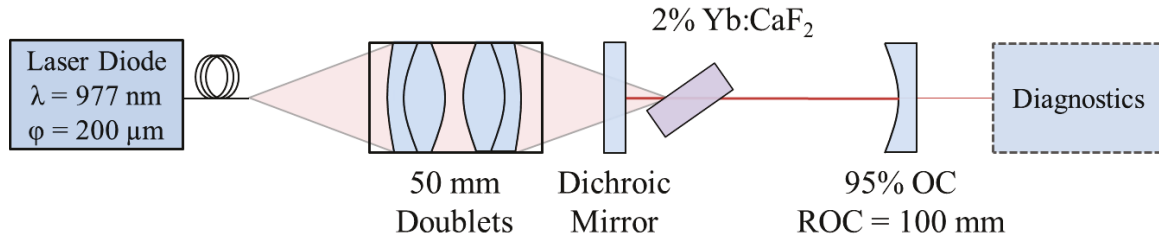


Figure 3.1-1: CW laser experimental setup. OC is output coupler and ROC is radius of curvature.

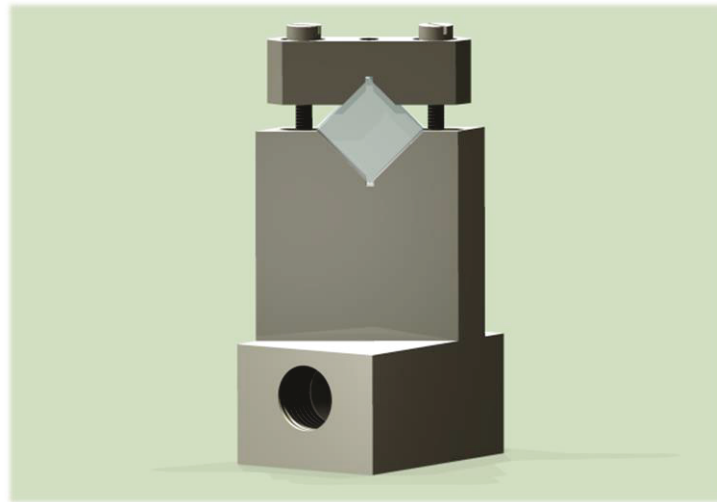


Figure 3.1-2: Diagram of the laser crystal installed in the water-cooled, aluminum mount and clamp.

In order to characterise the CW performance of the laser, measurements were taken of the average power, beam stability, wavelength, and laser mode quality. Measurements were made with the setups shown in Figure 3.1-3. Power was measured with a Spectra-Physics 407A power meter, wavelength with an Ocean Optics USB2000 spectrometer, stability with both a nanosecond photodiode (Thorlabs DET10A) and a sub-ns photodiode, and mode quality with a CCD camera (Point Grey Chameleon[®]). This CCD camera was employed as it produces low noise images, can be operated without automatic gain or exposure settings, and has good pixel linearity with increasing light intensity. A 1000 nm long-wave pass filter (LPF) (ThorLabs FEL1000) was used in the measurements to block visible and pump

light. For the CCD measurements a neutral density (ND) filter (ThorLabs NE60B-B) with an optical density of 6.0 along with a glass wedge at 45° were employed to attenuate the laser signal. A piece of polytetrafluoroethylene (PTFE) Seal Tape was placed in front of the photodiode as a diffuser. When measuring laser beam quality an anti-reflective (AR) coated, 200 mm focal length, plano-convex (PCX) lens (ThorLabs LA1708) was used to focus the beam.

Beam width ($D4\sigma$) measurements for the beam quality, or M^2 , calculation required extra care in order to produce accurate results. Many of the methods employed came from the ISO 11146-1 standard though it was not rigorously followed. A minimum of ten beam width measurements were taken inside the Rayleigh range and another ten outside twice the Rayleigh range of the focussed beam. Background noise can cause large errors in the $D4\sigma$ method of calculating beam size due to the greater weighting of pixel values the further from the beam centroid they are located.⁹⁷ In order to reduce this effect, image summation and background subtraction was used. A minimum of five measurement images and five background images were taken and summed. The background was then subtracted pixel for pixel with negative values retained. This unfortunately left a DC bias possibly resulting from camera baseline drift and non-linearity. The DC bias was removed by averaging the four corners of the resultant image, still outside of the beam location, and subtracting this value from the entire image.

Following this, the outlier pixels were normalized by setting them to the median of the pixels surrounding them. To finish, the beam width was calculated iteratively by creating an artificial aperture (i.e. setting the pixels to zero) twice the diameter of the calculated beam diameter each iteration and comparing the current beam diameter value to the previous one. Once the relative error between beam sizes was less than 1% the calculation was terminated. The aperture method was described by Ophir/Spiricon engineers to reduce the beam width measurement error significantly from <10% to <1%.⁹⁸ To calculate the M^2 factor, the locations and beam widths were fit to Equation (2.2-9) using least-squares regression.

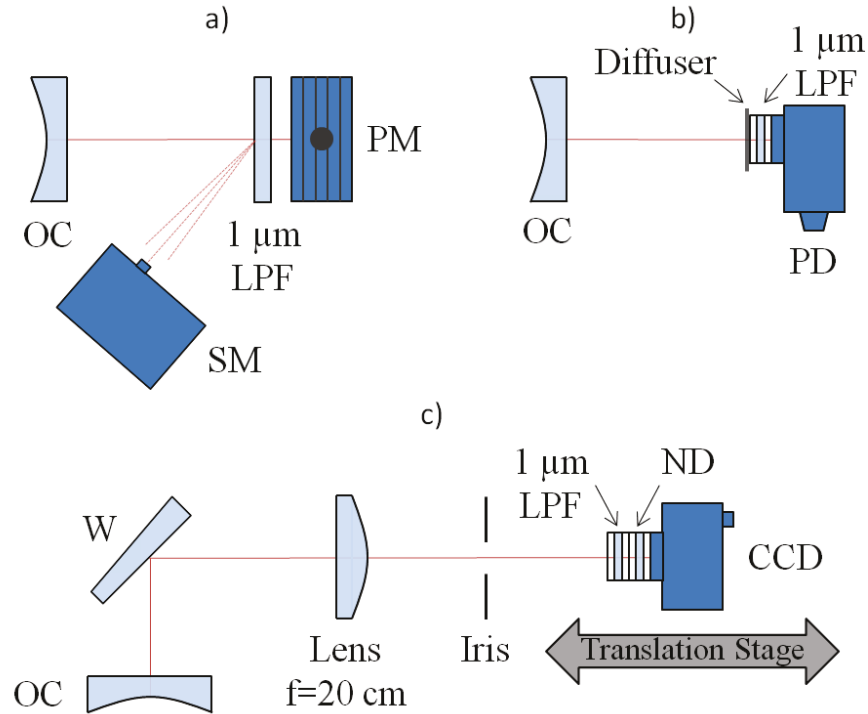


Figure 3.1-3: Measurement setup for CW characterisation. a) Power and spectral measurement, b) stability measurement, and c) beam size measurement. OC: output coupler, SM: spectrometer, LPF: long-wave pass filter, PM: power meter, PD: photodiode, W: wedge, ND: neutral density filter, and CCD: charge-coupled device.

3.2 Q-switched Laser Design and Measurement

The Q-switched (QS) laser cavity was identical in length and mirror configuration to that of the CW resonator. A saturable absorber was introduced to the cavity in order to initiate passive Q-switching. Due to its broad absorption bandwidth from 800 nm to nearly 1200 nm, Cr-doped YAG was used as the solid-state saturable absorber. Cr:YAG has a suitable absorption cross-section for saturable absorption and indeed peaks from 1000-1050 nm which is ideal for a Yb:CaF₂ gain medium.⁹⁹ Cr:YAG has a ground state absorption cross-section value high enough to make its saturation intensity lower than Yb:CaF₂ over the wavelength range of interest which enables QS pulses to be produced. In addition, the excited state absorption cross-section is lower than the ground-state absorption cross-section which reduces the SA saturated loss – a major factor affecting QS laser output efficiency.¹⁰⁰ The

second characteristic of Cr:YAG that makes it an excellent Q-switching saturable absorber is its excited state, or 2nd energy level, spontaneous lifetime on the order of microseconds and its 4th energy level spontaneous lifetime on the order of picoseconds; see Figure 2.1-1 for the energy level diagram.¹⁰¹ The excited state lifetime should be short enough to only allow a single QS pulse through before decaying to the ground state but long enough so that excited state saturation can occur and the QS pulse has enough time to build-up and be ejected from the cavity. The 4th level lifetime needs to be fast in order to both maintain a large saturation population in the excited state and to enable recovery on the order of the excited-state lifetime. By assuming the saturable absorber 4th level lifetime is shorter than the pulse duration, the approximation that the populations of the ground and excited state together equal the total dopant concentration, i.e. $N_{s0} = N_{gs} + N_{es}$, is valid.¹⁰⁰

Uncoated Cr:YAG has a damage threshold of greater than 500 MW·cm⁻² at 1064 nm for 10 ns pulses and so was expected to handle high intracavity intensities. The first saturable absorber placed in the cavity at normal incidence, with an unsaturated transmission of 95%, was burned repeatedly and was only capable of producing a repetitive pulse train under specific pumping powers and crystal orientation. This issue was caused by an AR coating applied to the Cr:YAG with a significantly lower damage threshold than the crystal itself. New uncoated crystals were ordered from Altechna (90% and 95% unsaturated transmission) and Newlight Photonics Inc. (98% unsaturated transmission) in order to rectify the issue. These new crystals were then placed at Brewster's angle in the cavity to significantly reduce Fresnel losses. Q-switching was achieved with the uncoated 98% SA but the uncoated 95% SA caused an intense intracavity fluence that damaged the DM.

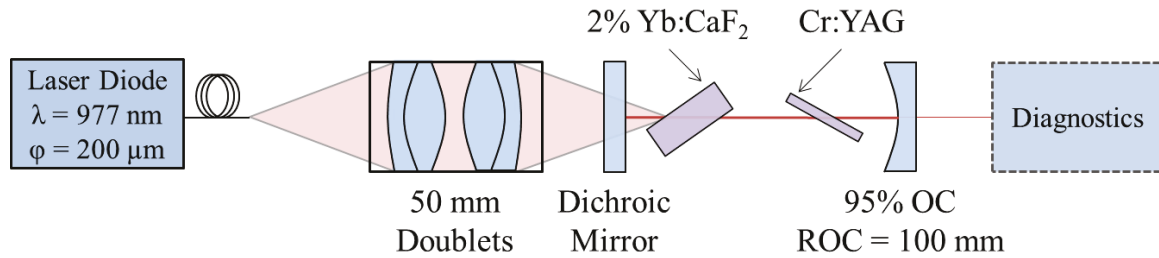


Figure 3.2-1: QS laser experimental setup. OC is output coupler and ROC is radius of curvature.

The Q-switching cavity configuration can be seen in Figure 3.2-1. The saturable absorber was placed $24 \text{ mm} \pm 1 \text{ mm}$ from the OC. Placing the Cr:YAG closer to the OC would minimize thermal effects on the crystal due to the larger cavity and pump mode sizes incident on it, while placing it further away would increase absorption and therefore speed of saturation. The Cr:YAG was positioned closer to the OC to lessen the potential to burn the surface as it was deemed that the faster speed of absorption saturation was not necessary.

Measurements were taken to characterise the individual QS pulses and the pulse train. The pulse energy was measured using a pyroelectric calorimeter (Gentec ED-200). This pulse energy was corroborated with average power measurements using the power meter (Spectra-Physics 407A) and repetition rate measurements with the nanosecond photodiode (ThorLabs DET10A). The results differed by no more than 12%. Pulse width was also determined using the photodiode. Wavelength was measured with the spectrometer (Ocean Optics USB2000). Beam quality was measured with the camera (Point Grey Chameleon[®]). Power and spectral measurements were taken with the same configuration as in the CW case, shown in Figure 3.1-3a. To reduce the average beam intensity on the photodiode the beam was attenuated with an optical chopper wheel (Stanford Research Systems Inc. SR540) and a folded optical tissue as a diffuser. The chopper wheel attenuated the beam by blocking it for portions of the wheel's rotation, effectively reducing the duty cycle of the laser pulses. The beam quality measurement employed the chopper for attenuation in addition to the glass wedge at 45° , the 1000 nm LPF, and the ND 6.0 filter as discussed above for CW lasing.

When measuring pulse energy, the chopper, with the addition of an optical shutter (Vincent Associates UNIBLITZ[®] VS-25), were used to select as few pulses as possible. The 1000 nm LPF to block pump light and a -25 mm focal length bi-concave lens (Newport KBC046) to expand the beam in order to reduce intensity were also employed. The QS laser measurement setups are shown in Figure 3.2-2. Once these measurements were taken it was possible to analyse the performance of the laser and compare it to the CW case.

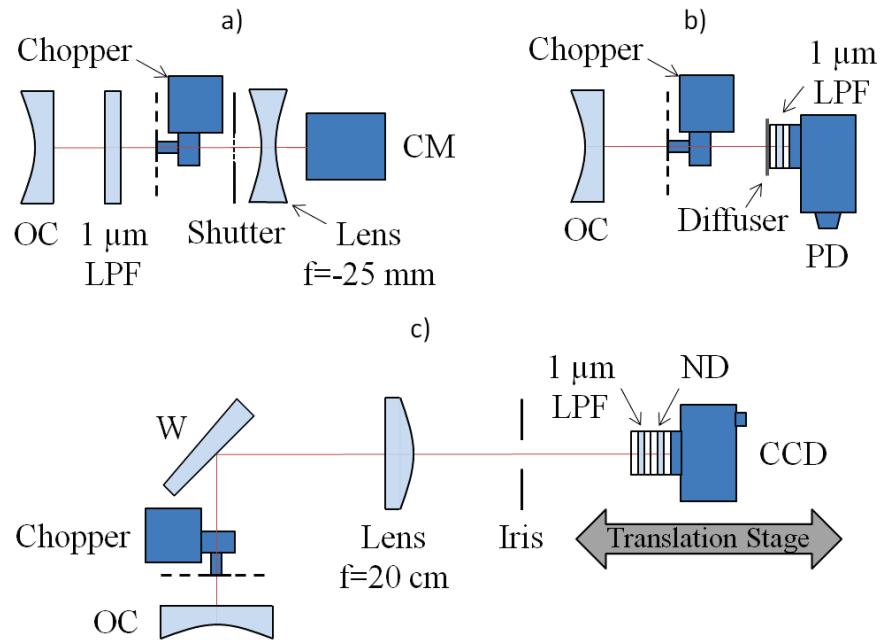


Figure 3.2-2: Measurement setup for Q-switching characterisation. a) Pulse energy measurement, b) repetition rate and pulse width measurement, and c) beam size measurement. OC: output coupler, LPF: long-wave pass filter, CM: calorimeter, PD: photodiode, W: wedge, ND: neutral density filter, and CCD: charge-coupled device.

3.3 Thermal Measurements

In addition to the characterisation of the laser output, the thermal profile of the laser crystal was recorded and analysed. By doing so, thermal models of the laser system could be validated and used to optimize the system. The thermal image was recorded from the back of the crystal, or in other words the surface from which the pump exits. The measurement arrangement is shown in Figure 3.3-1. The thermal camera was an uncooled, pyroelectric

thermal imager with a germanium lens optimized for 8-12 μm wavelengths (Electrophysics PV-320LR). Because the camera itself has a sensitivity range from 2-14 μm and the germanium lens is transmissive from 4 μm and longer it was necessary to add an additional filter. An 11 μm cut-on LPF (Spectrogon LP-11000) was placed in-between the camera and the laser crystal in order to block out wavelengths that pass through the laser crystal with appreciable transmission. CaF_2 has a transmission of at least 35% from 4-10 μm .¹⁰² Conversely, from 11-14 μm $\text{Yb}:\text{CaF}_2$ is highly absorbing. This means that the mid-IR light that the thermal camera collects will have been emitted very close to the surface of the crystal as the penetration depth in this wavelength region is on the order of 95-200 μm .¹⁰³ The transmission curves for the 11 μm LPF, uncoated Ge, and the combination of both along with the extinction coefficient for CaF_2 are shown in Figure 3.3-2.

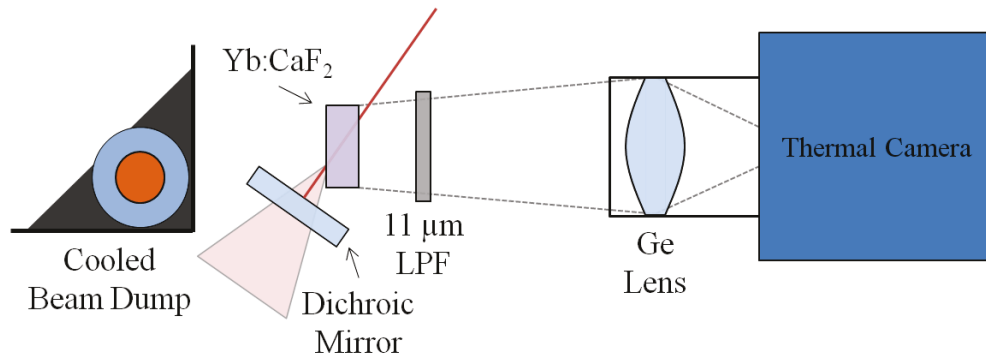


Figure 3.3-1: Measurement setup for CW lasing thermal imaging. LPF stands for long-wave pass filter.

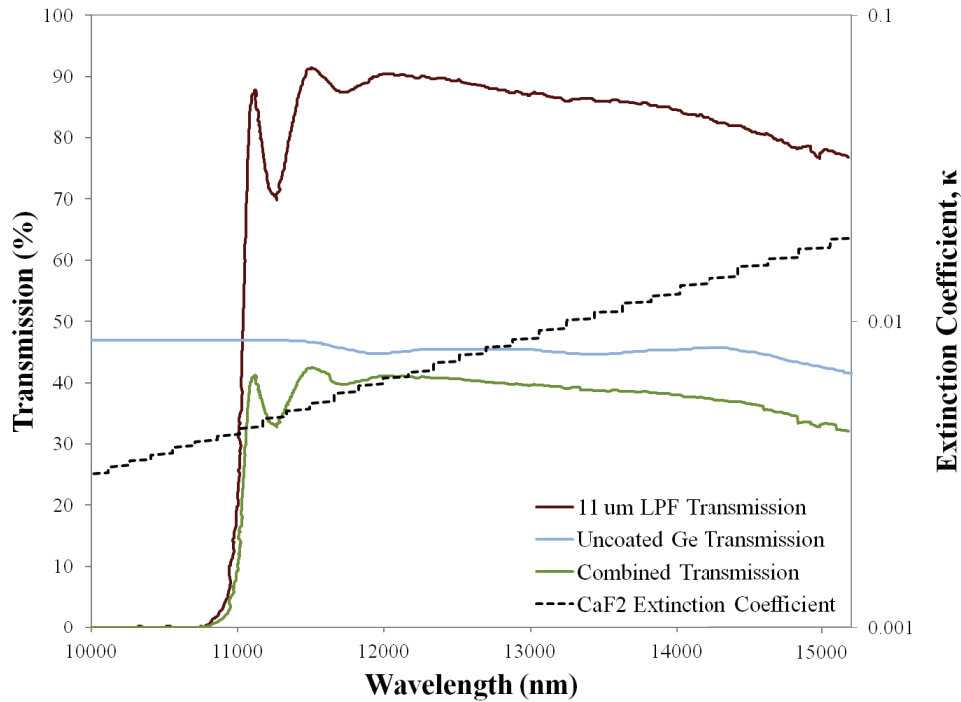


Figure 3.3-2: Transmission curves for the Spectrogon 11 μm long-wave pass filter (LPF), a typical uncoated Ge sample, and the combination of both. The extinction coefficient, κ , for CaF_2 is also included where κ is the imaginary component of the complex refractive index ($\tilde{n} = n - i\kappa$).¹⁰³⁻¹⁰⁵

Images from the thermal camera were captured on an EPIX PIXCI SV5 video capture card and saved using the EPIX proprietary software, XCAP. This video capture card is designed to be used in scientific environments and allows control over the image acquisition parameters. Once captured the images were analysed using Matlab scripts.

In order to ensure quantitative temperature readings it was imperative to first calibrate the thermal camera with known temperatures. The water-cooled mount could not be assumed to be the exact same temperature as the refrigerated bath circulator's (Fisher Scientific IsoTemp 1006D) reservoir as there is a temperature change along the cooling line; thus there were several steps in this calibration. First, a thermistor was calibrated to known crystal mount temperatures by submerging the aluminum mount in the circulator's reservoir and affixing the thermistor into a drilled hole in the mount with silicon thermal paste and electrical tape as

shown in Figure 3.3-3a. As the circulator's water temperature was varied the thermistor resistance was measured and tabulated.

Subsequently, the thermistor was affixed to the crystal mount within the resonator using thermal paste and electrical tape in the same way, as can be seen from Figure 3.3-3b. The thermal camera was then focussed onto the crystal and images were recorded as temperature was varied. The temperature was adjusted between 16°C and 65°C. Higher temperatures were not available as the cooling lines were only rated to 65°C. The gain and reference settings on the thermal camera, used to control contrast between low and high intensity pixels, was set to a constant value that enabled measurement over the range of temperatures of interest. The aperture of the lens could have been modified to enable an even higher contrast ratio over the crystal temperature range and to help avoid saturation of the pixel values at higher temperatures but the process of changing the aperture shifted the image which was not desirable for ease and accuracy of temperature calibration and calculation. An aluminum laser beam dump, cooled by conduction simply with a plastic water bottle from the freezer, was set behind the laser crystal to ensure the background radiation level was of a low temperature.

Following the calibration measurements, the thermistor temperature values were associated with the image intensity of the laser crystal to build a relationship between temperature and pixel value. The temperature of the laser crystal was known at the bottom edge via contact with the aluminum; however, a gradient was expected across the crystal due to radiative and convective heat transfer. To estimate this gradient, and subsequently the pixel to pixel change in calibration temperature, a simplified COMSOL model was used that calculated the temperature distribution of the laser crystal with the appropriate heat transfer boundary conditions. A two-dimensional, general quadratic, least-squares regression was done on the calculated temperatures to create an equation relating pixel location to the appropriate temperature. Finally, a cubic, least-squares regression was completed for each individual pixel to relate pixel value to any temperature within the range of calibrated values.

An example of the regression on three different pixel values over the temperature range can be seen in Figure 3.3-4. The pixel locations on the crystal face are shown in Figure 3.3-5.

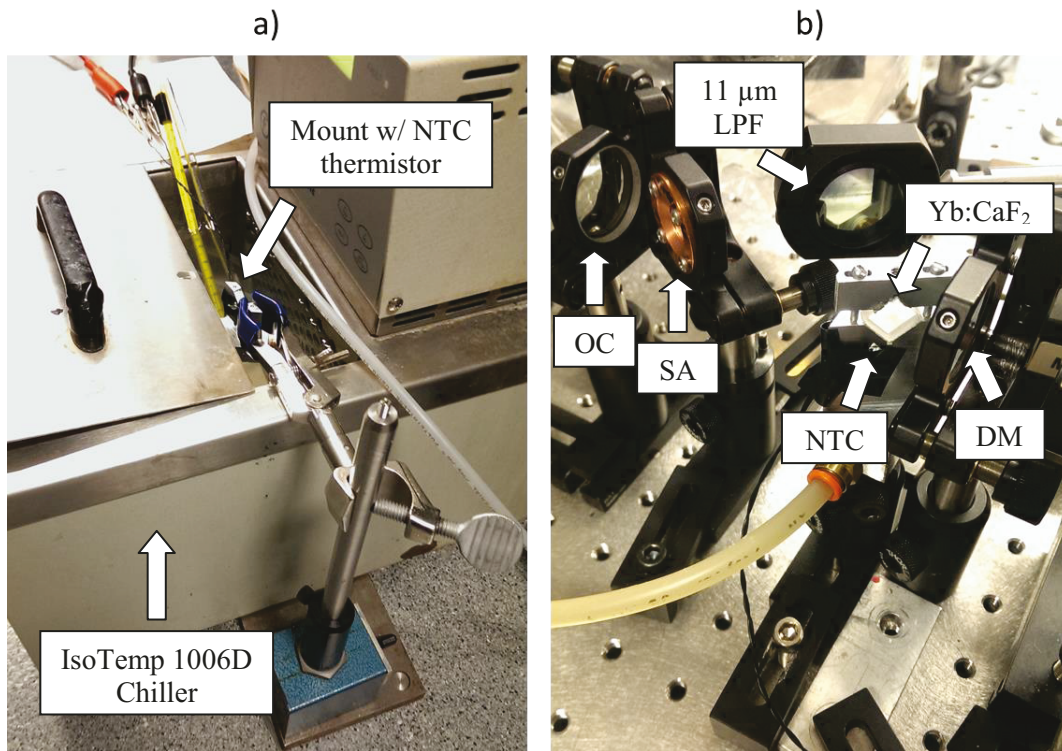


Figure 3.3-3: a) NTC thermistor calibration in a temperature regulated bath and b) crystal placement and temperature measurement in the laser cavity. OC: output coupler, SA: saturable absorber, LPF: long-wave pass filter, and DM: dichroic mirror.

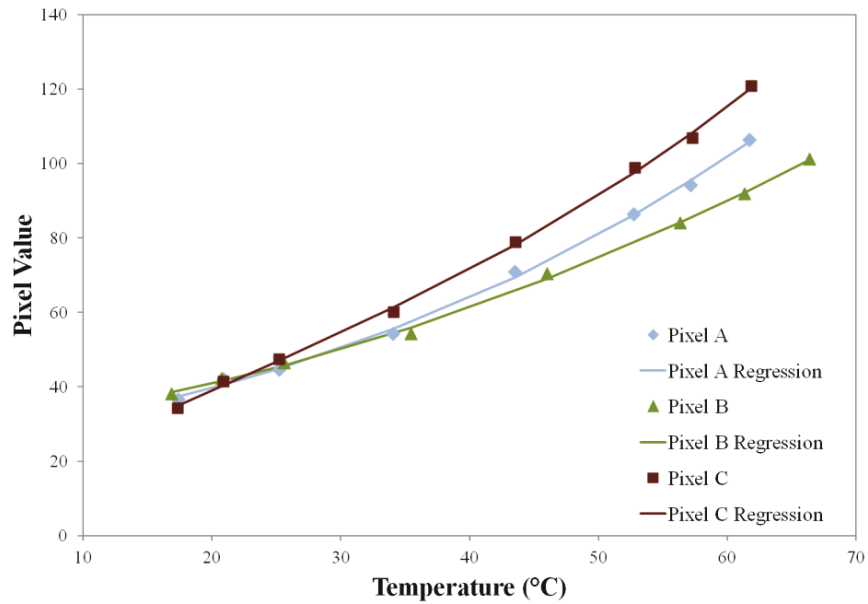


Figure 3.3-4: Cubic regression of pixel value with respect to temperature for three different pixels. Measurements are taken from the QS laser thermal calibration.

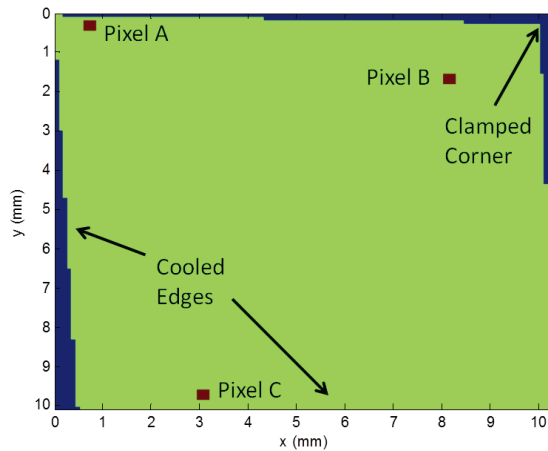


Figure 3.3-5: Pixel locations chosen to demonstrate the temperature calibration cubic regression.

Once calibration of the thermal imager was completed the thermal measurements were carried out. Care was taken to maintain the same setup and lens focus and aperture throughout the experiment. First, thermal measurements were taken with the Yb:CaF₂ gain medium in CW operation. Again, a cold water cooled aluminum beam dump was used as a

background. Pump power was increased from 0 to 29 W and the thermal images were taken. It was found that the field of view of the thermal imager was too large and caused a loss of detail. It was not possible to see the central hotspot created by the absorbed pump. Thermal modelling had to be used to fill in the details.

In order to combat the large field of view a 10.6 μm AR coated, 7.63" focal length, ZnSe, plano-convex lens (Laser Research Optics LX-1576-Z-ET7.6) was used in conjunction with the Ge lens to magnify the face of the laser crystal onto the thermal detector. The experimental setup can be seen in Figure 3.3-6. The experiment was repeated under Q-switching operation with a pump power of 0 to 19 W. Higher pump powers were not attempted due to concerns about DM damage.

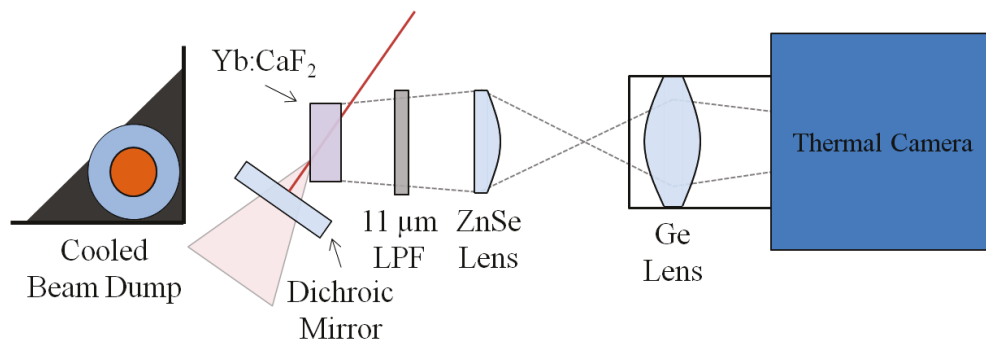


Figure 3.3-6: Measurement setup for QS lasing thermal imaging. LPF stands for long-wave pass filter.

Chapter 4

Simulations

When designing a laser system it is valuable to know several characteristics about the laser before even physically constructing it. This can be difficult in some cases as all parameters are not always known about the gain medium and other cavity components. In our case the Yb:CaF₂ gain material had several unknowns and parameters that change from crystal to crystal so in order to properly analyse the laser it was fabricated and operated under fixed conditions and then the modelling was carried out to match the performance under these conditions. The output characteristics such as pulse duration, pulse energy, average output power, and repetition rate were simulated using rate equation modelling. Additional information regarding the heat generated in the crystal under different configurations was also deemed important. Understanding the temperatures reached in laser materials and how to mitigate them are vital for high power laser systems and can be related to our own terawatt laser development. The rate equation and thermal models, in fact, build on each other by providing information that each require. Temperature was taken from the thermal model and used in the rate equation model and the population inversion value from the rate equations was used to calculate the pump absorption in the thermal model.

4.1 Rate Equation Modelling

4.1.1 Solver Method and Verification

The rate equations used to simulate Q-switching output performance were given previously in Equations (2.1-9) – (2.1-11). Since these equations are coupled, first order, ordinary differential equations (ODEs) they can be solved with the Runge-Kutta (RK) method. The RK method is a means of solving ODEs that requires only the values at the previous time step to compute the current value but to higher orders of accuracy than other

single-step methods.¹⁰⁶ Matlab was used for the model calculations carried out. It has functionality for a 5th order, variable time-step solver that satisfies the requirements for solving coupled ODEs. When solving the rate equations, 3rd order RK results were compared to 5th order results and there was essentially no difference; therefore, a higher order solver is not required.

The Q-switching rate equation solver was verified by modelling the quasi-three-level Nd:YAG laser described by Q. Li et al.⁸⁶ All of the model parameters were kept identical to that paper and the only difference was possibly the time step employed as the RK solver details were not discussed. Results were nearly identical with the relative error approximately 1% for pulse width and repetition rate determinations. There were changes introduced to the rate equation model for our laser system that were not present in Q. Li's paper in order to take into account physically separate gain and SA media, and cavity loss in addition to the output coupler (OC) loss. These changes are discussed in Section 2.1 as well.

4.1.2 Modelling Parameters and Assumptions

Determination of the modelling parameters for a passively QS, Yb:CaF₂ laser were not as straightforward as might be expected. Due to the quasi-three level nature of Yb³⁺ it is important to know the Boltzmann occupation factors and the detailed spectroscopic transition cross-sections to properly model the laser when temperatures differ from the assumptions of other publications. Fluorescence and radiative lifetimes were also important in the modelling. The energy level determination for Yb:CaF₂ has been undertaken several times with significant difference in the values of some of the energy levels. V. Petit et al.⁴⁷ mentioned that the crystal growth procedure and doping concentration can play a role in modifying the crystal structure leading to changes to the energy levels, cross-sections, and also to the emission lifetimes. The energy levels determined by V. Petit et al., and shown in Figure 1.2-2, were used in the model. The changes in energy levels due to temperature would have been small and should not have affected the results.

The fluorescence lifetime of Yb:CaF₂ can be derived with Equation (2.2-8) if radiative and non-radiative lifetimes are known. Radiative lifetime has been stated to be between 1.9 and 2.4 ms in the literature.^{46,55,107,108} Non-radiative lifetime is not known but would act to decrease the fluorescence lifetime. An additional mechanism that modifies the fluorescence lifetime by increasing it is radiation trapping. This becomes more significant for larger dopant concentrations as it is only an important effect if reabsorption occurs within the mode volume. The relationship between the trapped fluorescence lifetime, τ'_f , and the fluorescence lifetime is:⁴⁶

$$\tau'_f = \tau_f(1 + \sigma_a N_0 l) \quad (4.1-1)$$

Where l is the length of the interaction region. The value of fluorescence lifetime used in the model was 1.66 ms as this produced reasonable results for both the rate equation simulations and the thermal simulations. This was derived based on a radiative lifetime of 1.9 ms. Since the fluorescence lifetime was reduced from the radiative lifetime it was possible that the Yb:CaF₂ crystal was not of the highest quality and non-radiative relaxations dominated over reabsorption.

Cross-section is another parameter where the value is not known to great accuracy for both Yb:CaF₂ and Cr:YAG. Individual crystals are slightly different from one another and, for proper determination, parameters should be measured for each individual crystal. From the literature a range of values can be extracted for both crystals. This provided some leeway in determining modelling parameters. The Yb:CaF₂ effective cross-section values for the pump and laser wavelengths were chosen from literature and verified first from the thermal simulations and then by the rate equation simulations. Room temperature effective absorption cross-sections ranged from 4.07 – 5.26 ($\times 10^{-21}$) cm⁻¹ for the pump wavelength of 977 nm and 5.00 – 7.68 ($\times 10^{-23}$) cm⁻¹ for the laser wavelength of 1047 nm.^{2,55,108-110} Room temperature effective emission cross-sections are determined using the McCumber relations and ranged from 3.62 – 5.83 ($\times 10^{-21}$) cm⁻¹ for the pump wavelength and 1.68 – 2.14 ($\times 10^{-21}$) cm⁻¹ for the laser wavelength.^{2,55,108,109} The Cr:YAG ground state and excited state effective cross-

sections at the laser wavelength were chosen directly from literature. The important factor for Cr:YAG acting as a SA is the ratio of ground state to excited state absorption cross-sections. These values have been measured to lie between 3.5 and 7.2.¹⁰¹ Values of effective cross-sections used in the model are given in Table 4.1-1. The actual Yb:CaF₂ cross-sections used in the model for computation were the spectroscopic transition cross-sections as this allowed the values to represent any temperature. The relationship between effective and spectroscopic cross-sections is discussed in Section 2.2 but of note is that the Boltzmann occupation factors allow the spectroscopic transition cross-sections to be approximated in the limit where only one energy level transition influences the emission or absorption of a specific wavelength of light. I.e. the absorption transition at 977 nm is assumed to only occur by a transition from the 1st energy level to the 5th energy level. This assumption is not perfectly accurate but provides a close approximation and allows modelling of the temperature dependency.

Table 4.1-1: Room temperature effective cross-section values used in rate equation simulations.

Parameter	Value	Wavelength	Reference
σ_{eff}^l	$2.14 \times 10^{-21} \text{ cm}^2$	1047 nm	[55]
σ_{eff}^p	$5.83 \times 10^{-21} \text{ cm}^2$	977 nm	[55]
$\sigma_{a_{eff}}^l$	$5.37 \times 10^{-23} \text{ cm}^2$	1047 nm	[55]
$\sigma_{a_{eff}}^p$	$5.26 \times 10^{-21} \text{ cm}^2$	977 nm	[55]
σ_{gs}	$9.55 \times 10^{-19} \text{ cm}^2$	1047 nm	[101]
σ_{es}	$1.54 \times 10^{-19} \text{ cm}^2$	1047 nm	[101]

Table 4.1-2 contains the remaining parameters that stay constant under changing pump power. Certain parameters were measured directly from the laser or found from product literature which included the cavity length, crystal lengths, mirror reflectivities, the pump and laser frequencies, gain medium and SA angles of incidence (θ_l and θ_a), and the pump power. The average mode area in the laser crystal was calculated using the Gaussian ray matrix method. The output coupler reflectivity (R_2) was given from the manufacturer as

$95.0 \pm 0.2\%$ so it was not modified. The SA saturated transmission (T_a), and consequently the SA dopant density, was provided by the manufacturer as $98\% \pm 2\%$ which was modified in the model to produce appropriate results. Additional parameters were taken directly from literature and well known references, and that includes the refractive indices of both crystals and the excited state emission lifetime for Cr:YAG.

The average pump area in the crystal was one parameter that had only bounds on it but no clear value. This was because pump divergence was very large but divergence could not be modelled in the rate equations. Thus, the vertical and horizontal beam radii were free parameters that were modified to produce the proper repetition rate and pulse energy to match experiment. The selected radii were located between the measured beam waist radii (see Section 3.1) and the integrated average pump radii within the crystal. They were chosen to be $384 \mu\text{m}$ and $541 \mu\text{m}$ for vertical and horizontal respectively. The horizontal beam radius was larger due to the propagation through the crystal at Brewster's angle. Scattering losses in the cavity were added to the rate equations via L_i and were varied to obtain a good agreement between the modelling results and measured data. A loss of 6% was determined which is slightly high for only scattering losses but there would also be residual absorption and loss in the laser crystal due to the drop in the population inversion density along the crystal length. This spatially varying inversion density is not taken into account in the QS laser modelling and thus was approximately added to the scattering loss term.

One final parameter was required to complete the model but could not be directly obtained from measurement. The temperature in the mode volume of the crystal was determined in conjunction with the thermal simulations. The variation in the population inversion with time was needed to simulate appropriate pump absorption in the thermal model and was provided by the rate equation solutions. Correspondingly, in order to properly simulate the population inversion the average mode temperature was taken from the solution of the thermal model. The models were run iteratively until the solutions converged. More detail is given in Section 4.2.2.

Table 4.1-2: Constant parameter values for rate equation modelling. The parameters are defined above and in Section 2.1.

Parameter	Value	Reference
n_l	1.429	[111]
n_a	1.815	[112]
l_l	0.5 cm	
l_a	0.048 cm	
L	9.91 cm	
s_1	$7.508 \times 10^{-4} \text{ cm}^2$	
s_2	$4.624 \times 10^{-4} \text{ cm}^2$	
ν_l	$2.863 \times 10^{14} \text{ Hz}$	
ν_p	$3.069 \times 10^{14} \text{ Hz}$	
T_a	0.975	
R_1	0.999	
R_2	0.95	
τ_l	1.66 ms	[55]
τ_2	3.5 μs	[113]
N_0	$5.15 \times 10^{20} \text{ cm}^{-3}$	
N_{s0}	$5.52 \times 10^{17} \text{ cm}^{-3}$	
θ_l	55.0°	
θ_a	61.2°	

4.1.3 Limitations

As discussed in Section 2.1, this model did not take into account the changing pump and mode radii through the crystal nor the Gaussian shape of the laser mode. Spatial variations in temperature along the crystal were not included; instead the temperature within the mode volume was averaged. Spatial fluctuations in inversion and photon density were not modelled but treated as bulk values for the entire cavity. Thermal lensing (TL), which can be significant at high pump powers and temperatures, was also not included. The thermal dioptric power is given by:⁷³

$$D_{th} = \frac{\eta_h \left(\frac{dn}{dt} \right)}{2\pi K_c} \int_0^L -\frac{1}{w_p^2(x)} \frac{dP_p(x)}{dx} dx \quad (4.1-2)$$

Where D_{th} is the thermal dioptric power in m^{-1} , $\frac{dn}{dt}$ is the change in refractive index with temperature in K^{-1} , K_c is the thermal conductivity in $W \cdot m^{-1} \cdot K^{-1}$, η_h is the thermal load, P_p is the pump power in W, and w_p is the pump beam radius in m. The strength of the thermal lens is simply the inverse of the dioptric power. This formula is valid for situations where the thermal lens is mainly affected by changes in refractive index from temperature rather than dilation of the end faces and changes in the refractive index due to the photoelastic effect. In CaF_2 the two stress related components nearly cancel each other out as they are opposite in sign; hence, the refractive index change from temperature does dominate and is equal to $-10.6 \times 10^{-6} K^{-1}$.³⁰ It was estimated that the strength of the thermal lens would range from an effective focal length of -1.7 m to, at the most extreme case, -0.13 m. At -0.13 m thermal lens the mode size in the cavity changed by only 2.5% and the de-focussing of the pump over the 5 mm crystal would also be negligible. Thus, it was deemed that TL at our pump powers was not a concern.

There remained several uncertainties in the various parameters used in the model. Spectroscopic cross-sections, fluorescence lifetimes, energy levels, and absorption coefficients of the $Yb:CaF_2$ and $Cr:YAG$ were not explicitly known and there exists a relatively broad range of values in the literature. The measurement of certain aspects of the crystals such as unsaturated transmission, absorption coefficient, effective cross-sections, and fluorescence lifetimes would add great value to the accuracy of the modelling. Experimental confirmation of the resonator passive losses would also be an asset. There exists a temperature dependence on certain parameters such as the spectroscopic cross-sections (to some extent), fluorescence lifetimes, energy levels, and refractive indices and this was not modelled. The wavelength of both the pump and laser are kept constant in the model even

though there are slight changes with increasing pump power in the experiment. Regardless of these facts the model is still capable of producing reasonably accurate results.

4.2 Thermal Modelling

4.2.1 Model Configuration and Geometry

With the purpose of developing a model to simulate the heat evolution in the laser crystal under CW pumping and various lasing conditions, COMSOL Multiphysics finite element analysis (FEA) was chosen as the computational platform. This platform enabled the modelling of the pump absorption in the crystal, the conversion of the absorbed power to heat, the transfer of heat through the crystal, the removal of the heat via appropriate boundary conditions, and the structural deformation incurred by such heating.

One challenge in modelling the actual experimental configuration of the laser crystal in the software was that the beam path of the light travelled at an angle through the crystal. To model this correctly a cylinder was created at the angle of transmission (34.98°) through the crystal and located on the input, or front, face where the pump beam entered the crystal in the experimental setup. The back face is labelled in Figure 4.2-1. The crystal itself was created as a block matching the experimental size of 10 mm x 10 mm x 5 mm thick. Around the outside edges of the 10 mm x 10 mm face several regions were created as can be seen in Figure 4.2-1. These regions, or domains, were used to separate the boundaries of the crystal for application of different cooling boundary conditions. They also served to allow regions with smaller mesh sizes to more accurately model the sharp corners. Figure 4.2-1 shows the orientation of the model with respect to the crystal orientation in the experiment. The top was the clamped boundary and the bottom was the cooled boundary. Once the direction of the cylinder was determined the modelling equations for beam propagation had to be modified. With the axis orientation as shown in Figure 4.2-1 corresponding to unit vector directions \hat{x} , \hat{y} , and \hat{z} , the new unit vectors \hat{x}' , \hat{y}' , and \hat{z}' for the modelling equations became:

$$\hat{x}' = 0.81935\hat{x} + 0.40538\hat{y} - 0.40538\hat{z} \quad (4.2-1)$$

$$\hat{y}' = 0.57330\hat{x} - 0.57937\hat{y} + 0.57937\hat{z} \quad (4.2-2)$$

$$\hat{z}' = 0.70711\hat{y} + 0.70711\hat{z} \quad (4.2-3)$$

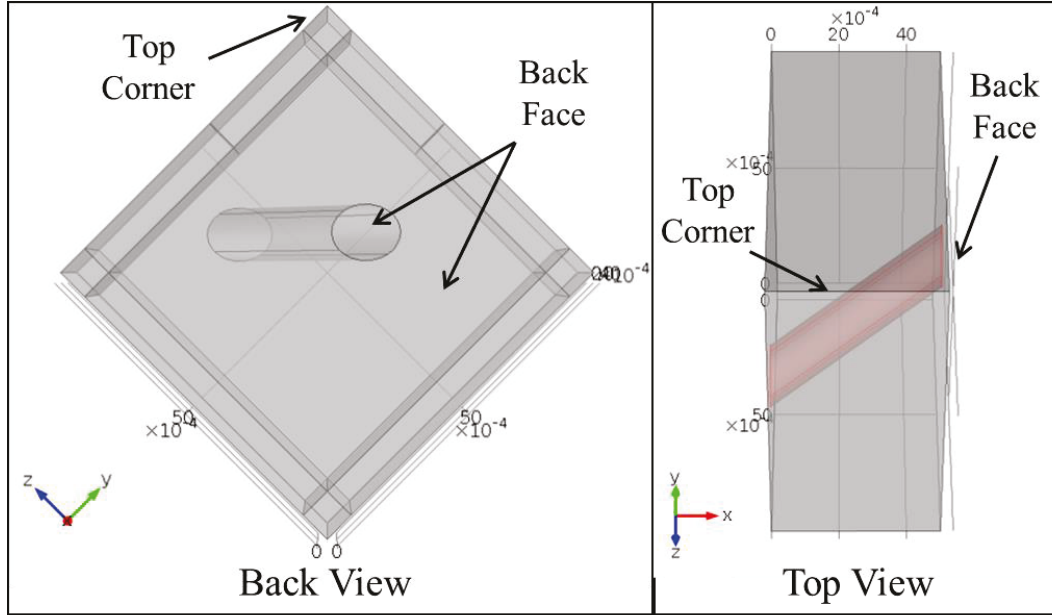


Figure 4.2-1: COMSOL model laser crystal orientation. In the top view the edge domains have been omitted and the central pump region has been highlighted for ease of viewing. Directions for x, y, and z are shown as well.

Pump absorption in the crystal was modelled using a partial differential equation (PDE) where the temporal differentials were set to zero because the pump did not change with time. The spatial first derivatives were computed vectorially in the direction of beam propagation. The initial condition was simply defined on the front face of the cylindrical volume as the incident pump power. The incident pump power is the pump power multiplied by the transmission of the crystal entrance face at Brewster's angle for the laser wavelength (55.0°). Knowing that the pump light was randomly polarized the transmission was equal to $1 - \frac{R_{c_s}}{2}$, where R_{c_s} is the s polarised reflectivity at Brewster's angle. Heat generation from absorbed power was given by Equation (2.2-10) and was directly included as a volumetric heat source coincident with the pumped volume. The pump absorption was evaluated over the entire

cylinder and this would lead to overestimation of the crystal temperature if used directly as the heat source; therefore, the heat source was radially limited by a high-order super-Gaussian function approximating a top-hat distribution. The extents of the function were given by the horizontal and vertical pump beam widths where the horizontal beam width is in the y' direction and the vertical beam width is in the z' direction. The beam widths were a function of distance along the propagation axis (x' direction) and were given by Equation (2.2-9).

The heat distribution and thermo-mechanical stress were modelled using the thermal stress module in COMSOL. The thermo-mechanical stress was only of secondary importance but did provide information about where stress was concentrated in the crystal. For thermal modelling the crystal was mounted at a 45° angle and the two lower edges of the crystal adjacent to the aluminum mount were treated as fixed surfaces and the portion of the upper two edges that were clamped had a distributed normal force applied. The upper and lower edges here correspond to the upper and lower edges in Figure 4.2-1. Of primary importance was the heat distribution which was modelled with Equation (2.2-1). The boundary conditions for each side of the crystal were modelled in the form of Equation (2.2-2). Both convective and radiative heat transfer can be combined together to produce an effective heat transfer coefficient (HTC) for the open faces that is reasonably accurate over the desired temperature range.

During the experiment the laser crystal was cooled on the two bottom sides by a water-cooled aluminum mount where the thermal contact was made with silicon thermal paste. The faces and additional two sides were primarily open to the air with a small portion of the top two sides contacting an aluminum clamp. This clamp was in thermal contact with the crystal through a $125\ \mu\text{m}$ thick piece of indium foil. Due to the extra surface area the clamp added some slight additional cooling. A diagram of the mount and clamp can be seen in Figure 3.1-2.

4.2.2 Modelling Parameters and Assumptions

To model pump propagation and absorption through the crystal it was important to know the physical properties of the pump and laser beam and the saturable absorption characteristics of the gain medium. The horizontal and vertical pump beam waists were determined from the experiment along with the M^2 factor for each which enabled the beam widths to be modelled using Equation (2.2-9). Mode radii in the cavity were found as in Section 4.1.2. Of particular difficulty was determining accurate values for the fluorescence lifetime, transition cross-sections for 977 nm and 1047 nm wavelengths, and subsequently the absorption coefficients. Since literature values showed a spread of data, the best values were found by simulating pump absorption and matching it to the measured pump absorption from the experiment. The transition cross-sections were taken from J. Körner et al.⁵⁵ The absorption coefficient for 977 nm was set to 2.71 cm^{-1} which indicates a doping concentration of $5.15 \times 10^{20} \text{ cm}^{-3}$ or 2.1 at.% doping. This value is slightly larger than expected as the crystal is specified for 2 at.%. Using the literature cross-section for 1047 nm and the determined doping concentration, the absorption coefficient for 1047 nm was calculated to be 0.028 cm^{-1} . Finally, the fluorescence lifetime was modified so as to change the saturation intensities. A value of 1.66 ms was found which is in line with theory as discussed in Section 4.1.2. Laser propagation and absorption modelling parameters are given in Table 4.2-1. Cross-sections are given as spectroscopic transition cross-sections.

Table 4.2-1: Pump propagation and absorption parameters for FEA analysis. The parameters are defined in Sections 2.2 and 4.2.1.

Parameter	Definition	Value	Reference
n_l	Refractive Index	1.429	[111]
w_{py0}	Horiz. Pump Beam Waist	93.6 μm	
w_{pz0}	Vert. Beam Waist	95.0 μm	
w_{ly0}	Horiz. Laser Beam Waist	85.3 μm	
w_{lz0}	Vert. Laser Beam Waist	73.1 μm	
M_y^2	Horiz. Pump M^2 Factor	50.1	
M_z^2	Vert. Pump M^2 Factor	53.9	
ν_p	Pump Frequency	3.069×10^{14} Hz	
ν_l	Laser Frequency	2.863×10^{14} Hz	
σ_a^l	1047 nm Absorption Cross-section	1.77×10^{-21} cm^2	[55]
σ_a^p	977 nm Absorption Cross-section	1.28×10^{-20} cm^2	[55]
σ_e^l	1047 nm Emission Cross-section	3.76×10^{-21} cm^2	[55]
σ_e^p	977 nm Emission Cross-section	1.04×10^{-20} cm^2	[55]
α_0	Pump Absorption Coefficient	2.71 cm^{-1}	
α_{l0}	Laser Absorption Coefficient	0.028 cm^{-1}	
R_2	OC Reflectivity	0.95	
R_{cs}	Crystal Face Reflectivity	0.0586	
τ_l	Laser Fluorescence Lifetime	1.66 ms	
N_0	Doping Density	5.15×10^{20} cm^{-3}	
$x0$	Pump Focal Position*	2.03 mm	
$x0l$	Laser Focal Position*	-13.1 mm	

* Focal position is referenced to the pump input face of the crystal.

The mechanical properties of CaF_2 were of less importance in the model but were still valuable for determining deformation and stress in the laser crystal. In the experiments some specimens of the $\text{Yb}:\text{CaF}_2$ crystal were cracked on a couple of occasions and it was in the interest of reducing the likelihood of another stress fracture that the mechanical parameters were found with some degree of accuracy. The Young's modulus, Poisson's ratio, coefficient of thermal expansion, and density were determined from various references as given in Table 4.2-2. In contrast to the mechanical properties, the thermal properties were critical.

Heat capacity is of primary importance for transient behaviour, which was not modelled, whereas thermal conductivity is the single most important factor in the thermal model. Under doping, the thermal conductivity changes and so Gaumé's model¹¹⁴ is often used to determine the proper value. In the case of Yb:CaF₂, Gaumé's model underestimates the thermal conductivity so instead a quadratic function was fit to the existing experimental data.⁵⁴ Once again, the true thermal conductivity value is hard to determine due to numerous values quoted in literature but all fall within a range of 6.2-7.3 W·m⁻¹·K⁻¹.^{30,54,115} Both thermal and mechanical properties are listed in Table 4.2-2 along with references.

The most conservative mechanical boundary conditions on the crystal were simple to determine. The edges adjacent to the mount had fixed constraints applied to them and the clamped portion of each top edge was assumed to be under a load of 215.8 N·cm⁻², derived from the load present in the experiment. Due to the extreme constraint of two fixed sides, the model produced very high stresses. A second simulation with all boundaries free of constraints was completed to get a more accurate picture of the internal stresses. These two results should be considered as only relative stress magnitudes due to the inaccuracies in the model.

The thermal boundary conditions were more challenging to develop. For surfaces with free convection in still air, HTC's were taken from the ASHRAE Handbook for the approximate average emissivities of 0.9 for CaF₂ and 0.05 for Al.^{116,117} The top corner HTC was more involved to determine and was calculated by adding the thermal resistances of CaF₂ to In, through the In, In to Al, spreading through the Al, and finally Al to air.

The most critical factor was the HTC for the Yb:CaF₂ to Al through the silicone heat paste as this was much larger than the other heat transfer processes. To begin with, the value determined by S. Chénais et al.⁷⁷ for the HTC from Yb:YAG to Cu through heat paste was used. They found a HTC of 2 W·cm²·K⁻¹. This value, however, produced simulation results far from the experimental ones. The HTC was reduced to 0.15 W·cm²·K⁻¹ for the CW model at which point the results became reasonable. A lower HTC makes sense due to the reduced

thermal conductivities of Yb:CaF₂ and Al to that of Yb:YAG and Cu respectively. Additionally, the heat paste used in the experiment had dried to some extent which may have led to a decrease in effectiveness. The value was also corroborated by an investigation into the thermal images. The thermal gradient was linearly estimated close to the crystal edge by taking the slope of temperature versus distance. The value for H could then be determined from Equation (2.2-2). The HTC approximations determined by this method averaged to $0.2 \text{ W}\cdot\text{m}^{-2}\cdot\text{K}^{-1}$. Considering the low precision of this method a value of $0.15 \text{ W}\cdot\text{m}^{-2}\cdot\text{K}^{-1}$ is quite reasonable. When running simulations for the QS model the results produced better matching to experiment with a decreased HTC of $0.13 \text{ W}\cdot\text{m}^{-2}\cdot\text{K}^{-1}$. Since the QS laser measurements were taken at a later date from the CW ones it is possible that the heat paste had dried further and the crystal may have been shifted during the cavity reconfiguration. HTCs utilized in the model are shown in Table 4.2-3.

For the sake of simplicity the actual Al mount was not modelled in COMSOL. The issue inherent with this was that the mount, in the vicinity of the laser crystal as shown in Figure 3.1-2, could not be assumed to be the same temperature as the circulating water because the Al finger that the crystal was set on gained heat from both the air and the laser crystal itself. To address this issue, the effective external temperature when considering the thermal boundary condition from the crystal to the mount was increased as the pump power increased. It was possible to determine the appropriate temperature as it was measured with a thermistor drilled into the mount directly below the contacting edge for each thermal measurement.

Table 4.2-2: Material properties for thermo-mechanical FEA analysis.

Parameter	Definition	Value	Reference
E	Young's Modulus	89.6 GPa	[54]
P	Density	3181 kg·m ⁻³	[30]
α	Coeff. of Thermal Expansion	1.887x10 ⁻⁵ K ⁻¹	[118]
ν	Poisson's Ratio	0.21	[54]
c_p	Heat Capacity Const. Pressure	854 J·kg ⁻¹ ·K ⁻¹	[118]
K_c	Thermal Conductivity	6.87 W·m ⁻¹ ·K ⁻¹	[54]

Table 4.2-3: Boundary condition parameters for FEA analysis.

Parameter	Definition	Value
F_A	Boundary Load	215.8 N·cm ⁻²
H_v	Vert. Effective HTC in Still Air ($\epsilon=0.9$)	8.29 W·m ⁻² ·K ⁻¹
H_{45}	45° Effective HTC in Still Air ($\epsilon=0.9$)	9.08 W·m ⁻² ·K ⁻¹
H_c	Al Clamp Effective HTC in Still Air ($\epsilon=0.05$)	38.9 W·m ⁻² ·K ⁻¹
H_{mC}	Al Mount Effective HTC (CW case)	1500 W·m ⁻² ·K ⁻¹
H_{mQ}	Al Mount Effective HTC (QS case)	1300 W·m ⁻² ·K ⁻¹

4.2.3 Configuration Specific Modelling Adjustments

In addition to the above modelling parameters, there were also specific changes required for the modelling of lasing and non-lasing pumping in the CW and QS cavity configurations. In the case of the CW experimental setup, the pump reflected off the OC and passed back through the crystal with an expanded beam radius. To account for this, a second ODE was modelled in COMSOL for the reflected pump power. The ODE was modified from Equation (2.2-4) to reflect the two counter-propagating pump beams. The form of Equation (4.2-4) has been modified from that of Equation (2.2-4) by converting intensities to power over area and removing any fractions in the numerator and denominator.

$$\frac{dP_{pr}}{dx} = \frac{-(\pi\alpha_0^p w_l^2 I_{min} + \alpha_0^l P_l(r))A_{pprpl}P_{pr}}{\pi w_l^2 A_{pprpm} I_{lsat} + A_{prllm}P_p + A_{pllm}P_{pr} + A_{pprpm}P_l(r)} \quad (4.2-4)$$

$$P_l(r) = 2P_l \cdot e^{-2\left(\frac{r^2}{w_l^2}\right)} \quad (4.2-5)$$

$$A_{abcd} = w_a^2 w_b^2 I_b I_c \quad (4.2-6)$$

Where a and b are p , pr , or l , and c and d are p ($psat$), l ($lsat$), or m (min); w_r and w_{pr} are the initial and reflected pump radii respectively in m; w_l is the laser mode radius in m; and P_{pr} is the reflected pump power. The variable dependencies on x and r have been omitted from some variables in the above equations to be concise. P_p , P_{pr} , A_{abcd} , w_l , w_p , and w_{pr} are dependent on x ; and P_p and P_{pr} are dependent on r .

The propagation of the initial pump beam must also be modified to fit the form of Equation (4.2-4) so the differential term and numerator occurrences of P_{pr} in Equation (4.2-4) were exchanged for P_p . Additional parameters that were necessary for the modification were the reflected pump beam widths and the incident reflected pump power. The reflected horizontal and vertical beam widths were calculated directly using matrix methods and were found to be 6.92 mm and 7.36 mm respectively. This value did not change significantly over the length of the crystal so it was assumed a constant. The incident reflected pump power was the initial transmitted pump power multiplied by the OC reflectivity. For the QS configuration there was very little back reflected pump; therefore, it was not added to the model.

One of the most important factors in determining crystal temperature was the value of the fractional thermal load. In the simple case of non-lasing operation the fractional thermal load becomes $\eta_h = 1 - \eta_p \eta_r \frac{\lambda_p}{\lambda_f}$. Where η_p and η_r are defined as the pump and radiative quantum efficiencies respectively as discussed in Section 2.2. This was true in both CW and QS configurations. Once all other model parameters had been set, the fractional thermal load for CW configuration was varied until the temperature distribution was close in value to the experimental results. This gave a value of 0.23 for η_h which means the product $\eta_p \eta_r$, assuming a mean fluorescence wavelength of 1008 nm, was 0.79. To then find η_p and η_r

individually the model for CW lasing was utilized. At high intracavity laser intensity the lasing efficiency approaches one which means the influence of η_r on the fractional thermal load becomes nearly negligible. By varying η_p , once again the simulation could be matched to experimental data. η_p was found to be 0.94 which leads to an η_r of 0.88. One issue to be careful of was the fact that the fractional thermal load's dependence on lasing was only within the laser mode volume; outside of this the heat load was still governed by the non-lasing fractional thermal load. The values for the thermal load parameters, constant for all simulations, are shown in Table 4.2-4.

Table 4.2-4: Thermal load properties for thermomechanical FEA analysis.

Parameter	Value
η_r	0.88
η_p	0.94

The final situation to take into account was for QS lasing. The absorption of pump power is influenced by the populations of the upper and lower pump energy levels, and within the laser mode volume, under QS operation, the population cannot be described by Equation (2.2-4). The population of the upper level increases as it is pumped and then suddenly decreases once a pulse is generated. Due to the short time scales of this phenomenon it is not reasonable to simulate it exactly. Since the laser pulses were produced many times a second and the thermal diffusion process occurred over several seconds it was possible to assume a constant population density that produced the average pump absorption in the crystal. The average pump absorption was determined by solving Equation (4.2-7) for several time steps where the ground state and upper manifold population variations with time were determined from the rate equation modelling.

$$\frac{dP_p}{dx} = -(\sigma_a^p N_g - (\sigma_a^p f_g + \sigma_a^l f_2) N_{um}) P_p \quad (4.2-7)$$

In order to use both the thermal model to determine the average mode volume temperature and the rate equation model to produce the proper population densities over time it was necessary to iterate the solutions between the two until convergence was reached. The pump power absorbed in the crystal was then a combination of the modified absorption within the laser mode volume and the original steady-state absorption over the remainder of the pumped volume. Because the lasing duty cycle was on the order of 0.005-0.02% it was not necessary to include the laser extraction efficiency in the fractional thermal load. Therefore, η_h was again 0.23.

Every QS pulse generated in the laser cavity would have a portion reabsorbed from the finite population in the lower laser level. Because QS model temperatures were slightly low compared to the experiment, reabsorption was modelled using the average upper manifold population, $N_{um_{ave}}$, generated by the rate equation modelling to provide an approximate additional heating. Equation (4.2-8) was utilised to find the fractional laser reabsorption, η_{re} . This value was then substituted into Equation (4.2-9) to find the average heat generated from reabsorbed photons within the laser mode volume, $Q_{th_{re}}$.

$$\eta_{re} = \sigma_a^l f_1 (N_0 - N_{um_{ave}}) \cdot e^{-\sigma_a^l f_1 (N_0 - N_{um_{ave}}) x} \quad (4.2-8)$$

$$Q_{th_{re}} = \eta_{re} (1 - \eta_r) \frac{E_{out} \cdot RR}{\pi w_l^2 (1 - R_2)} \quad (4.2-9)$$

Where E_{out} is the QS output pulse energy in J and RR is the repetition rate in Hz.

4.2.4 Model Verification

To determine the effect of the mesh on the model accuracy a mesh dependency study was undertaken. There were three “zones” within the model with different mesh sizes. It is easiest to see them by looking at the crystal in the x direction as shown on the left in Figure 4.2-1. There is the cylinder region, the four corners, and the body and sides of the crystal. The cylinder that defined the interaction region of the pump and laser modes within the crystal

used a finer mesh than the body and sides of the crystal. So too did the corner edges along the x direction due to the stress concentrations in the corners. Two studies were run as tabulated in Table 4.2-5; one where the body, sides, and corner mesh sizes remained constant while the cylindrical interaction region mesh size was varied, and another where the cylindrical region and corner mesh sizes remained constant while the body and sides mesh sizes were varied. As can be seen in Figures 4.2-2 and 4.2-3, the peak crystal temperature, peak pump exit face temperature, and absorbed power values all converged quickly as the mesh sizes were reduced.

Table 4.2-5: Mesh dependency study parameters.

Case	Cylinder Max Element Size	Corner Max Element Size	Body and Sides Max Element Size	Total # of Mesh Elements
One	0.55 mm	0.35 mm	1.00 mm	12352
	0.38 mm	0.35 mm	1.00 mm	15320
	0.28 mm	0.35 mm	1.00 mm	23019
	0.22 mm	0.35 mm	1.00 mm	36483
	0.20 mm	0.35 mm	1.00 mm	59876
Two	0.28 mm	0.35 mm	1.90 mm	16702
	0.28 mm	0.35 mm	1.50 mm	18509
	0.28 mm	0.35 mm	1.00 mm	23019
	0.28 mm	0.35 mm	0.80 mm	33062
	0.28 mm	0.35 mm	0.60 mm	49602

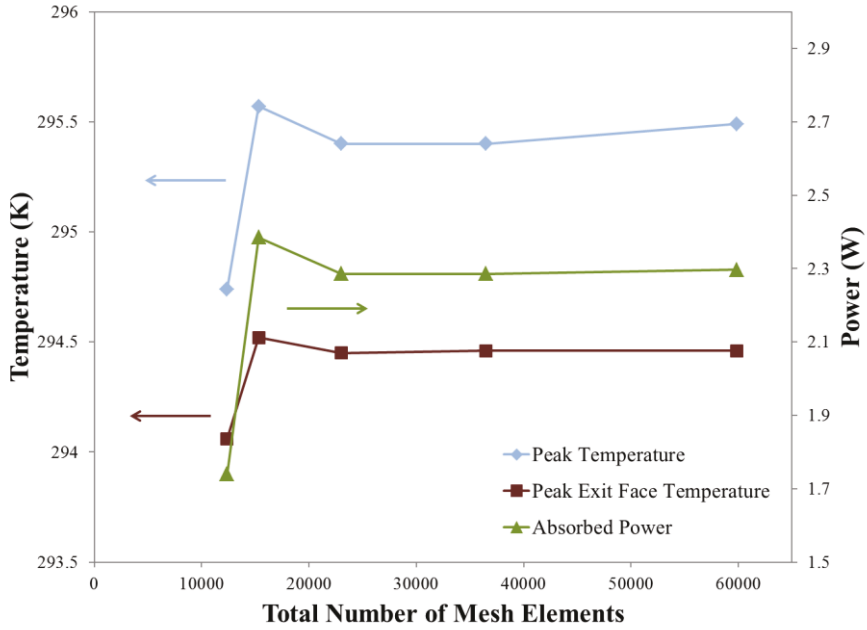


Figure 4.2-2: Peak temperature, peak exit face temperature, and absorbed pump power dependence on cylindrical interaction region mesh element size (case one).

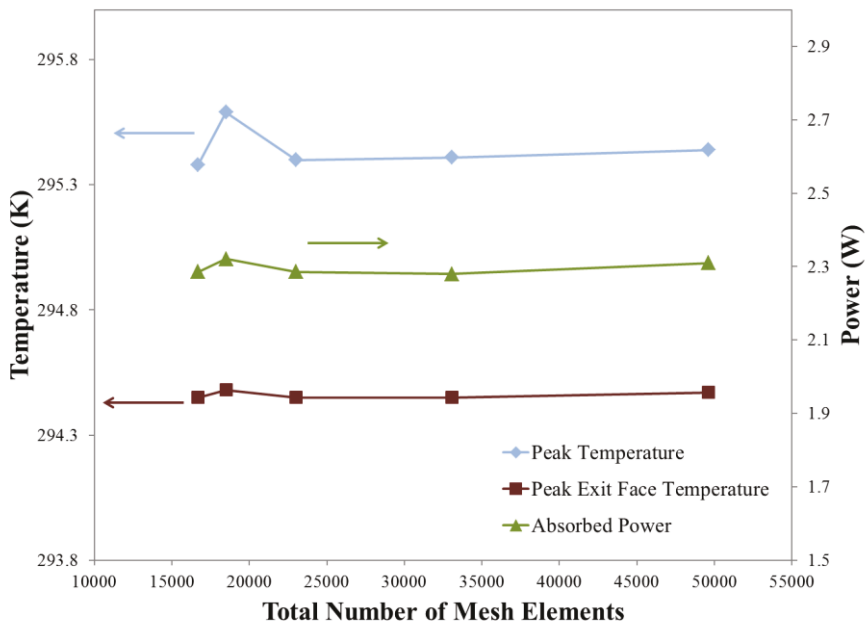


Figure 4.2-3: Peak temperature, peak exit face temperature, and absorbed pump power dependence on body and sides mesh element size (case two).

The point at which the model converged was related to the COMSOL maximum element sizes of 1.0 mm for the body and sides and 0.28 mm for the cylindrical interaction region. The corner maximum element size was set to be 0.35 mm. An illustration of the mesh on the back face can be seen in Figure 4.2-4.

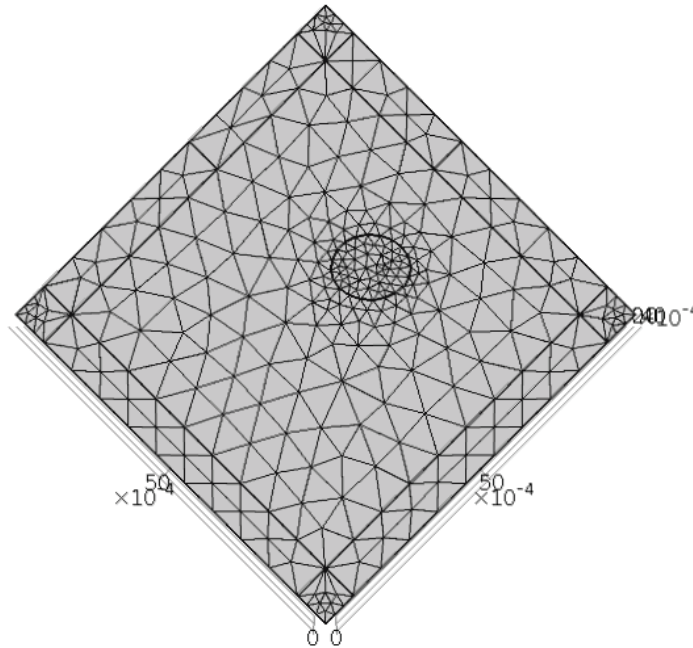


Figure 4.2-4: Back face FEA mesh used for thermal simulations.

It was also of value to compare the COMSOL FEA model with other literature to assess the accuracy of the simulations. A comparison for the case of no lasing was made with S. Chénais et al.^{77,88} for Yb:GdCOB and Yb:YAG, and J. Boudeile et al.³⁰ for Yb:CaF₂. For lasing comparison the paper by J. Boudeile et al.³⁰ for Yb:CaF₂ was once again used. In the instance of Yb:GdCOB the paper presented a theoretical model for the temperature distribution. This model calculated the transverse temperature elevation from one edge of the crystal to the other, assuming a cylindrical form. To compare, the FEA model was simulated with equivalent parameters. The peak temperature difference from the edge to the center of the crystal was found, just as in the paper, to be located on the back face. To understand the form of the transverse temperature profile, Figure 4.2-5 gives the result from my simulation

of Yb:GdCOB on the back face of the crystal. The simulated temperature difference was 29 K and the theoretical value was approximately 30 K. This difference likely originated from the approximations used in the paper such as a cylindrical crystal cross-section and the dropping of both the longitudinal spatial derivative and time derivative of temperature. The change in crystal from a cylinder to a rectangle adds significant additional volume that lowers the peak temperature in the simulation.

For the papers discussing both Yb:YAG and Yb:CaF₂ laser crystals, actual experimental results were presented. In the case of Yb:YAG my simulated temperature difference on the front face from peak to minimum was 22 K and the experimental temperature difference was 20 K. The variation here can likely be attributed to the measured and theoretical parameters given in the publication differing slightly from the experimental laser crystal's true characteristics. For the non-lasing Yb:CaF₂ results my front face simulated temperature difference was 15 K and the experimental temperature difference was 13 K. Under CW laser operation the front face temperature difference for my simulation was 34 K and for the experiment it was also 34 K. The paper on Yb:CaF₂ had several important aspects of the laser setup missing such as M² factor, double-pass pump configuration, and heat transfer coefficient. Additionally, there are inconsistencies in the reporting of the temperatures in the non-lasing case. The differences are likely due to the uncertainty of some model parameters and the inconsistencies in the paper.

As can be seen from the percent error, the FEA model was reasonably close to both theoretical and experimental results. The distributions, both longitudinal and transverse, also match with what is expected for a divergent pump beam absorbed in a radially cooled crystal with a moderate to low saturation intensity. These two details verify the accuracy of the model.

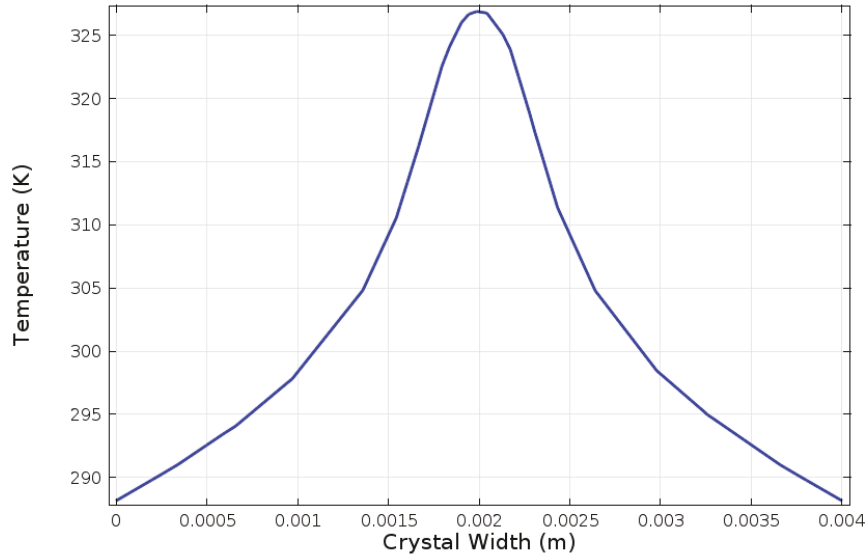


Figure 4.2-5: Simulated Yb:GdCOB, back face, transverse temperature profile.

4.2.5 Limitations

With the care taken to estimate the relevant parameters for the model and to accurately calculate the amount of heat deposited in the crystal the model was expected to be reasonably accurate. The largest source of error was from the uncertainty in physical parameters; specifically, cross-sections, absorption coefficients, heat transfer coefficients, and thermal conductivity. In addition, the actual intracavity laser intensity was only approximated from the output power and output coupler reflectivity. Wavelength of pump and laser were also assumed constant even though they changed slightly with increasing pump power.

There was also a source of error introduced in the QS lasing model from the averaging of the energy level population densities. Just as in the rate equation modelling, the population inversion would be spatially and temporally dependent and would affect the distribution of heat generated in the QS model. The lack of spatial dependence would also be relevant for the CW lasing and the general non-lasing cases as Equation (2.2-4) for pump absorption was generated from rate equations with the assumption of a spatially independent population

inversion. Thermal lensing was not considered either due to the small effect it would have on the mode sizes as discussed in Section 4.1.3.

The boundary conditions and physical thermomechanical properties also introduced error as the temperature increased to higher levels. The HTC for radiation will change depending on temperature and the emissivity will also vary. The thermal paste would change consistency as the temperature rose leading to a change in the effective HTC. Within the laser crystal itself the thermal conductivity, spectroscopic cross-sections, fluorescence lifetime, energy levels, and refractive index all change with temperature. Due to the modelled temperatures only ranging from around 290 K to 400 K the room temperature values for coefficients were used and it was assumed that the changes in the values would not cause a significant error for the temperatures of interest.

To test this assumption, the HTCs, fluorescence lifetime, radiative quantum efficiency, and heat load were modified to values representative of the actual crystal temperature at 19 W pump power in the QS laser configuration. The average crystal temperature and the average pumped region temperature used to calculate parameter modifications were assumed to be 344 K and 365 K respectively. Values for thermal conductivity, spectroscopic cross-section, energy levels, and refractive index were deliberately left unchanged because they would cause negligible changes to the model. Thermal conductivity for Yb:CaF₂ remains nearly constant for temperatures above 150 K. The energy levels and spectroscopic cross-sections are not significantly affected by temperature, especially in the wavelength region of interest, where the major changes from temperature are taken into account by the Boltzmann distribution functions already present in the model. Finally, refractive index changes slowly at these temperatures and does not have any effect on the model. The HTCs for the un-cooled faces of the crystal would increase as temperature rose because the radiative component was calculated based on the assumption demonstrated in Equation (4.2-10). This assumption is valid if the difference between the temperature of the crystal, T , and the external temperature, T_e , is small.

$$T^4 - T_e^4 \cong T_{e0}^3 \cdot (T - T_e) \quad (4.2-10)$$

Where T_{e0} is the temperature at which the HTC was defined. In the model this temperature was 294.2 K. With this relationship in mind it was found that the HTCs would increase by a factor of 5 approximately. The effective HTC from the crystal to the cooled aluminum would increase as well because the silicon heat grease would become more fluid and improve contact with the two surfaces. An increase of 1.4 times was assumed.

The second major change to occur with increasing temperature would be a decrease in fluorescence lifetime due to the increased non-radiative decays at higher temperatures. Using Yb:GdCOB as a reference for the relative magnitude of the shift,⁷⁵ for a temperature change from 293 K to 365 K, a decrease of 0.11 ms was determined. With a decrease of fluorescence lifetime comes a decrease in the radiative quantum efficiency and subsequently an increase in the fractional heat load. The new radiative quantum efficiency became 0.816 and the fractional heat load became 0.257. Table 4.2-6 shows the differences between the original model and the modified one. The simulation results from the new configuration produced an overall decrease in the average crystal temperature but with a higher peak crystal temperature occurring near the pump beam waist. A comparison of the two cases is shown in Table 4.2-7. From the size of the difference it can be seen that the original assumption of temperature independent parameters was valid.

Table 4.2-6: Comparison of modelling parameters for the original model and the modified model used to evaluate error created by parameter variation at high temperatures.

Parameter	Original Model	Modified Model
P_p	19.0 W	19.0 W
H_v	8.29 W·m ⁻² ·K ⁻¹	41.45 W·m ⁻² ·K ⁻¹
H_{45}	9.08 W·m ⁻² ·K ⁻¹	45.4 W·m ⁻² ·K ⁻¹
H_c	38.9 W·m ⁻² ·K ⁻¹	194.5 W·m ⁻² ·K ⁻¹
H_{mQ}	0.13 W·m ⁻² ·K ⁻¹	0.185 W·m ⁻² ·K ⁻¹
τ_l	1.66 ms	1.55 ms
η_r	0.878	0.816
η_h	0.23	0.257

Table 4.2-7: Comparison of simulated temperatures for the original model and the modified model used to evaluate error created by parameter variation at high temperatures.

Description	Original Model	Modified Model	Percent Difference
Maximum Temperature	380.5 K	386.2 K	1.5%
Minimum Temperature	307.8 K	303.2 K	1.5%
Average Temperature	334.0 K	327.4 K	2.0%
Average Temperature along Pump Axis	370.7 K	369.8 K	0.2%

Chapter 5

Results

5.1 Experimental Results

There were four main experiments undertaken to develop and characterise the Q-switched (QS) laser. To begin, the pump beam quality and pump power within the cavity were determined to make subsequent laser output analysis possible. Next, the output characteristics of the CW laser cavity were used to determine the best output efficiency and laser slope for that layout and to later compare with the QS output in terms of extraction efficiency. The output of the QS laser was then measured since the primary goal of this work was to produce laser pulses with the desired properties. Finally, temperature profiles under increasing pump power for both CW and QS lasers were taken. This information provided an understanding of the quality of the laser crystals and the effectiveness of the cooling system. These two aspects should be optimized to produce the best possible laser system.

5.1.1 Pump Characterisation

The three most important aspects of the pump beam within the laser cavity were the power transmitted through the dichroic mirror (DM) (see Figure 3.1-1), the wavelength, and the beam profile (waist and divergence). The pump power and wavelength versus input current is shown in Figure 5.1-1. Pump wavelength fluctuated for pump power less than 1.3 W, which explains the relatively large uncertainty, but generally followed an increasing trend as power increased. Pump output power with input current becomes linear, as expected, for output power greater than 1.3 W. A typical pump spectrum is shown in Figure 5.1-2. The spectrum was taken with an integration time of 10 ms thus the true spectrum is likely somewhat narrower. The pump power for the measurement was 1.2 W.

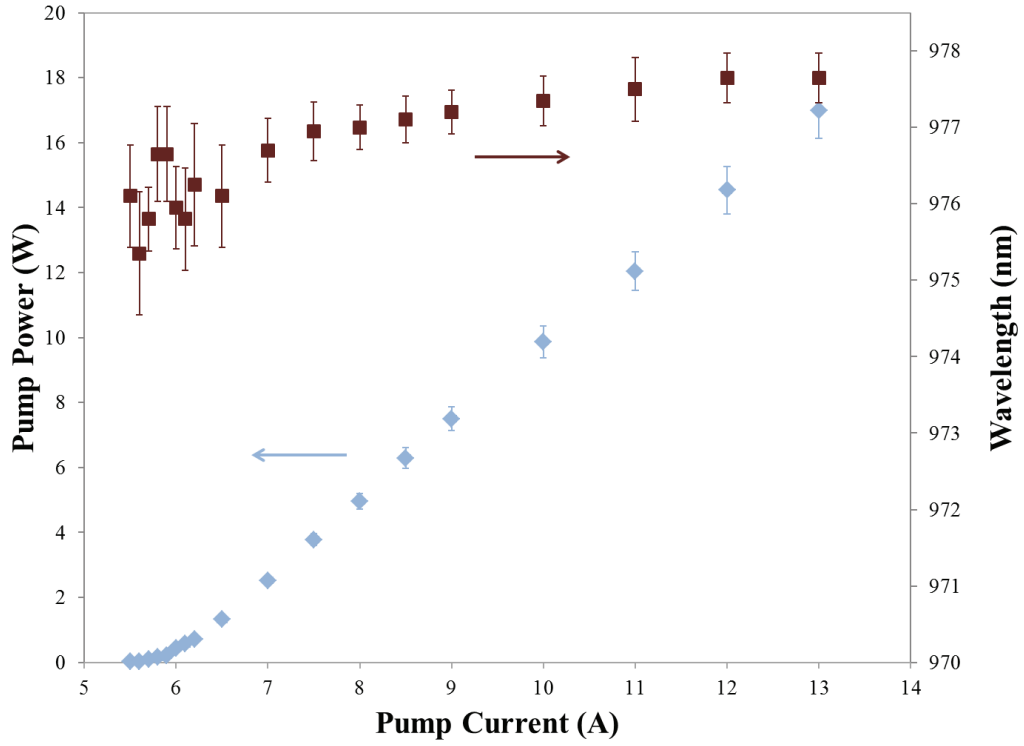


Figure 5.1-1: Changes in pump power and wavelength with pump current inside laser cavity.

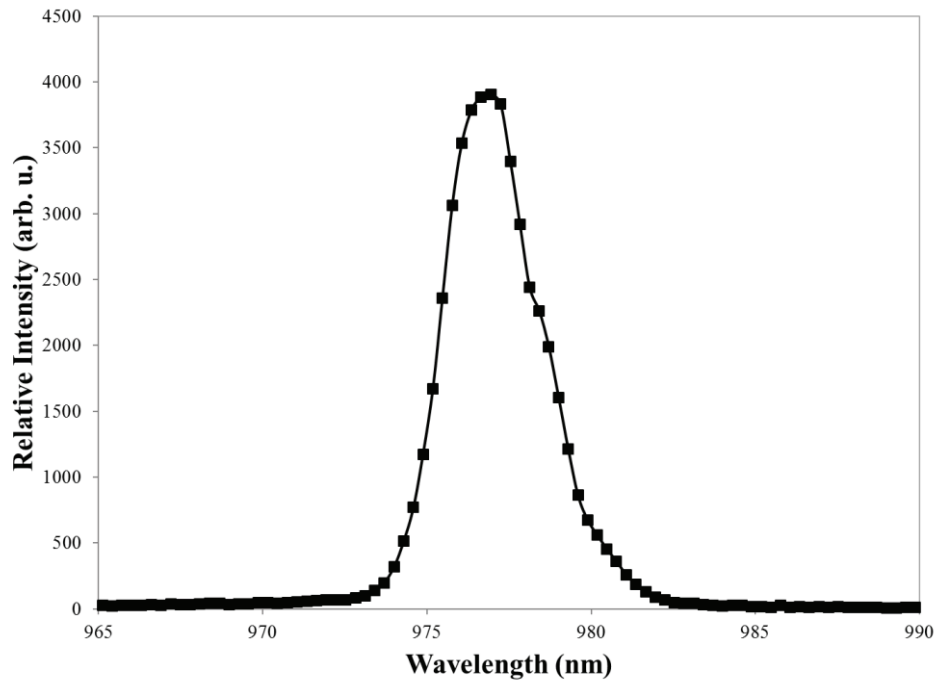


Figure 5.1-2: Typical pump spectrum at 1.2 W output power.

Determination of the pump beam waist and propagation, M^2 , factor was done very similarly to the procedure described in Section 3.1 for the CW output beam. One change made to this procedure was that instead of using a plano-convex lens to focus the fibre output the 50:50 mm achromatic doublet lens pair was used as it was the specific focussing configuration of interest. Due to the limitations in space it was also not possible to take many measurements before the focus as is required for the ISO 11146-1 standard. The measured beam radii are shown in Figure 5.1-3 along with the M^2 fit. M_y^2 and M_z^2 were found to be 50 ± 3 and 54 ± 3 respectively. The beam waist radius in y was $93.6 \mu\text{m} \pm 0.7 \mu\text{m}$ and in z it was $95.0 \mu\text{m} \pm 0.7 \mu\text{m}$. The y and z directions were considered to be horizontal and vertical respectively with reference to the optical table.

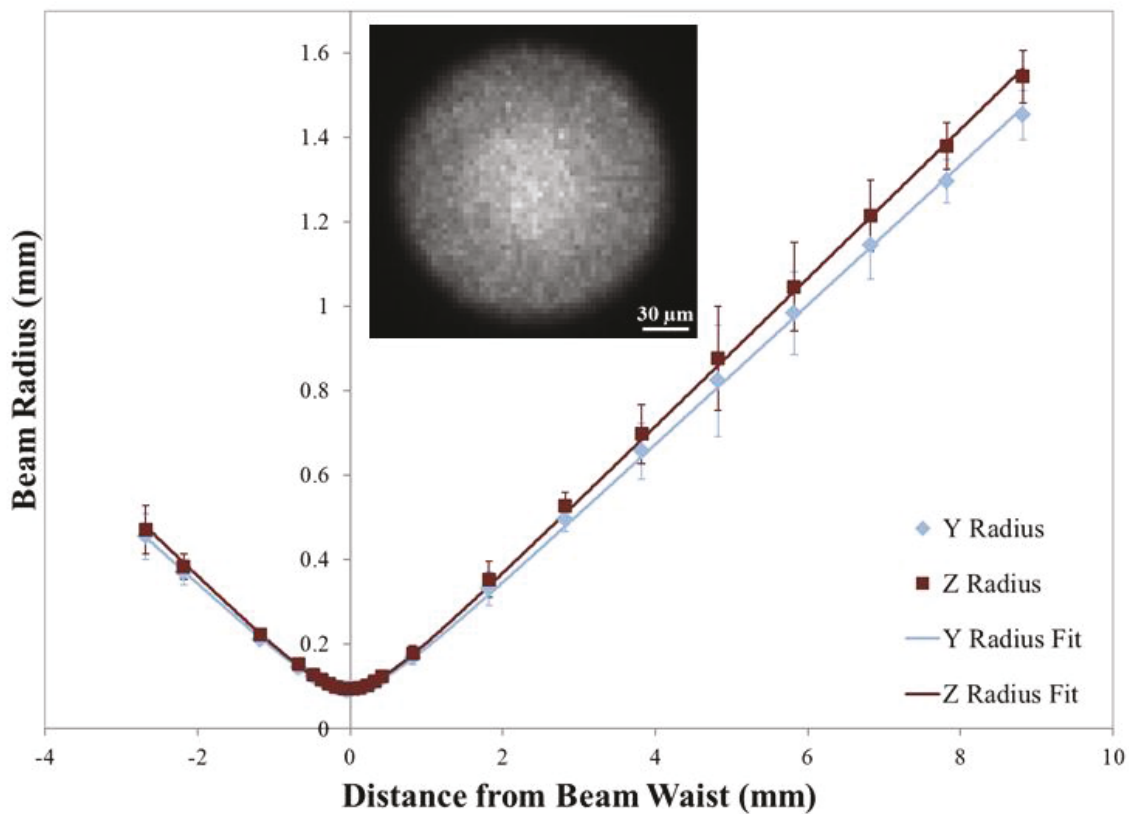


Figure 5.1-3: M^2 fit to the measured pump beam radius in the y and z directions. Inset shows the focussed beam profile at its beam waist.

5.1.2 CW Output Characteristics

During the development of the laser cavity the first steps involved were to determine what cavity size, mode size, and pump size produced the best results. A CW cavity configuration was used for this determination. The initial configuration was done using a 50:75 mm PCX lens pair which caused the diode pump laser fibre output to be reimaged with a magnification of approximately 1.5. The focussed pump waist radius was $187 \mu\text{m} \pm 27 \mu\text{m}$ in y and $191 \mu\text{m} \pm 23 \mu\text{m}$ in z . Directions y and z correspond to horizontal and vertical respectively. Once entering the crystal, the horizontal beam waist was expanded to $267 \mu\text{m}$. The laser crystal was placed in two separate locations within the cavity to determine the effect mode size and pump-mode overlap ratio had on output performance. In the first case the crystal was placed $2.63 \text{ cm} \pm 0.03 \text{ cm}$ from the DM and in the second case it was placed $4.00 \text{ cm} \pm 0.03 \text{ cm}$ from the DM. In both cases the pump beam waist was maintained as a constant value as given above.

The general cavity layout is shown in Figure 3.1-1 for reference. The length of the cavity was not changed and was measured to be $7.66 \text{ cm} \pm 0.02 \text{ cm}$. The laser mode radius inside the crystal for the first case varied from 201 to $205 \mu\text{m}$ in the y and 140 to $146 \mu\text{m}$ in the z , and for the second case from 234 to $240 \mu\text{m}$ in the y and 164 to $172 \mu\text{m}$ in the z based on Gaussian matrix calculations. The slope efficiencies for the first and second cases are $28.5\% \pm 0.2\%$ and $30.4\% \pm 0.3\%$ respectively. The thresholds for the first and second cases are $6.1 \text{ W} \pm 0.4 \text{ W}$ and $7.0 \text{ W} \pm 0.4 \text{ W}$. The slope efficiencies of the two systems are illustrated in Figure 5.1-4. It is also valuable to look at the overall input pump to output laser power efficiency. The efficiency increases with increasing pump power but tends to plateau asymptotically. The input to output efficiency is shown in Figure 5.1-5.

It was of interest to improve the input to output efficiency for the laser cavity and one means to do this was by lowering the threshold, i.e. increasing the small-signal gain. To do this the pump beam waist size was reduced by replacing the focussing PCX lens pair with a

50:50 mm achromatic doublet lens pair. This not only reduced magnification to approximately one but also improved focussing quality with reduced aberrations. The pump beam waist was expected to be $94 \mu\text{m} \pm 2 \mu\text{m}$ and $95 \mu\text{m} \pm 2 \mu\text{m}$ in the y and z directions respectively. Once entering the crystal the horizontal beam waist was expanded to $134 \mu\text{m}$. To also improve pump-mode overlap the cavity length was increased to $9.91 \text{ cm} \pm 0.02 \text{ cm}$ which led to a calculated crystal mode radius that varied from 139 to $145 \mu\text{m}$ in the y and 92 to $106 \mu\text{m}$ in the z . The slope efficiency was found to be $28.3\% \pm 0.2\%$ and the threshold became $3.8 \text{ W} \pm 0.2 \text{ W}$. The plots of slope efficiency and input to output efficiency are shown in Figures 5.1-4 and 5.1-5 respectively.

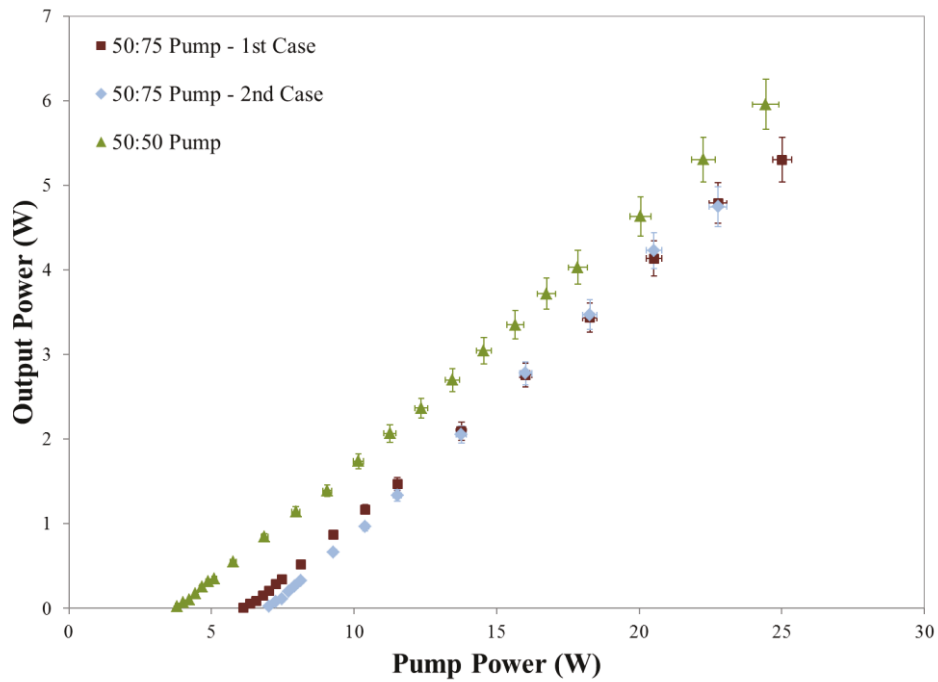


Figure 5.1-4: Output power versus pump power under CW operation.

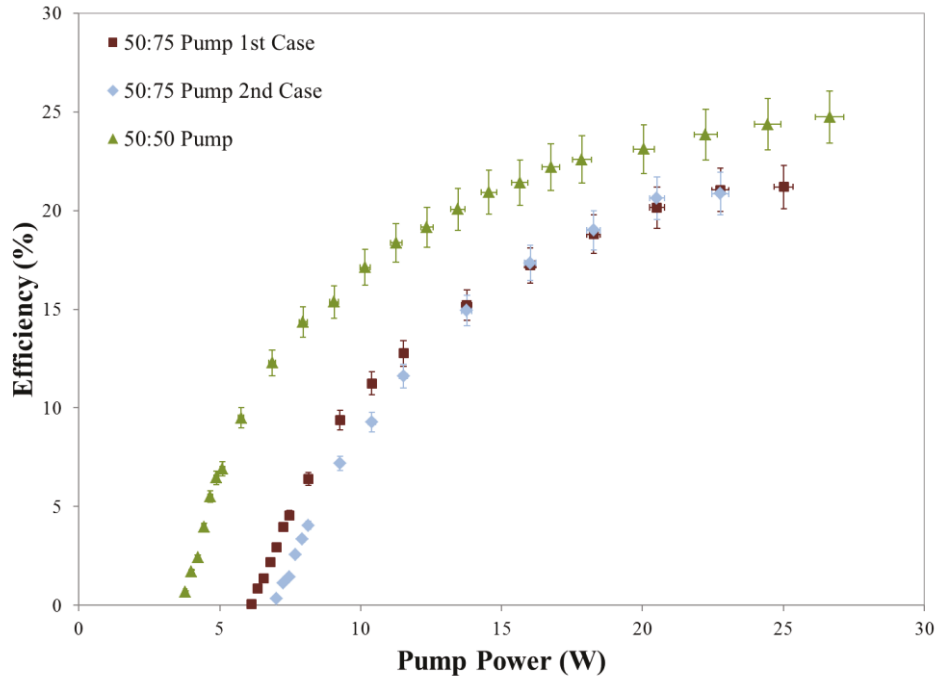


Figure 5.1-5: Optical laser efficiency under CW operation.

The peak wavelength of the CW output laser beam fluctuated somewhat as the output power increased. The majority of the fluctuations occurred near threshold and once output power increased beyond 4 W. In general, the wavelength was well defined and laid near 1050 nm. The peak wavelength variation with changing output power is shown in Figure 5.1-6.

Output stability in CW cavities is also an area of interest. If the output power is fluctuating significantly it can be an indicator of poor cavity conditions. Output fluctuations were measured as shown in Figure 3.1-3b. Stability measurements were taken with a Tektronix DPO2024 oscilloscope using the nanosecond photodiode. Figure 5.1-7 shows the laser output on a time scale of 100 μ s/div while using DC coupling and a 1000 Ω load on the photodiode. The fluctuations in the signal on the time scale of tens of microseconds can be seen to be quite small. At 10.8 W pump power the percent fluctuation peak to peak in output power was 2.2%. In Figure 5.1-8 the output signal was recorded with the sub-nanosecond photodiode into a Tektronix 7104 analog oscilloscope terminated with a 50 Ω load. It was possible to see the fine output structure with this combination and with a 1 ns/div timescale inter-mode

beating could be seen with a period of approximately 696 ps. This corresponds to a frequency of 1.44 GHz which is very close to the 1.47 GHz beat frequency expected from the cavity length. Even though there was evidence of two wavelength modes operating in the cavity the CW resonator was well designed and aligned.

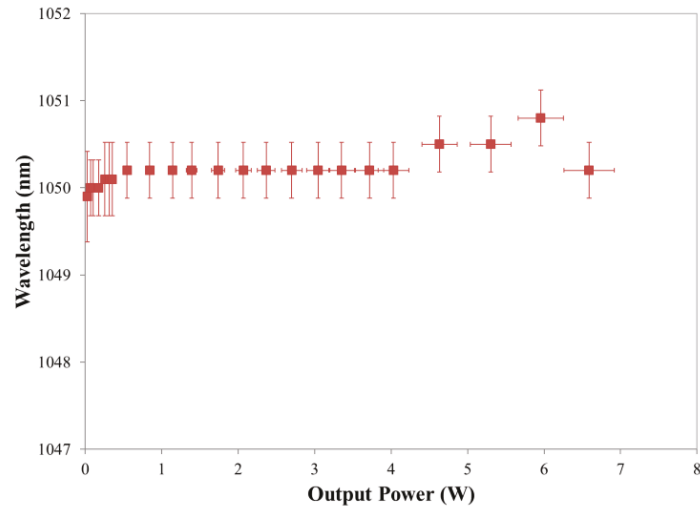


Figure 5.1-6: Change in peak CW output wavelength with changing output power.

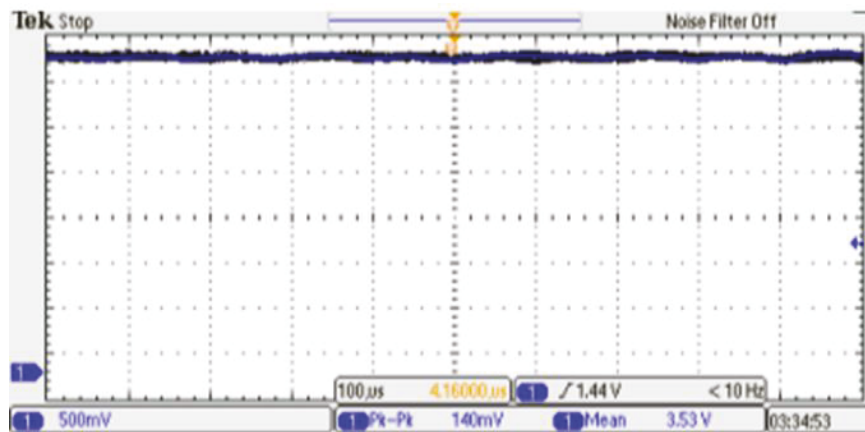


Figure 5.1-7: Photodiode measurement of laser power stability with 1000 Ω termination. Time scale: 100 $\mu\text{s}/\text{div}$. Voltage scale: 500 mV/div. DC coupling.

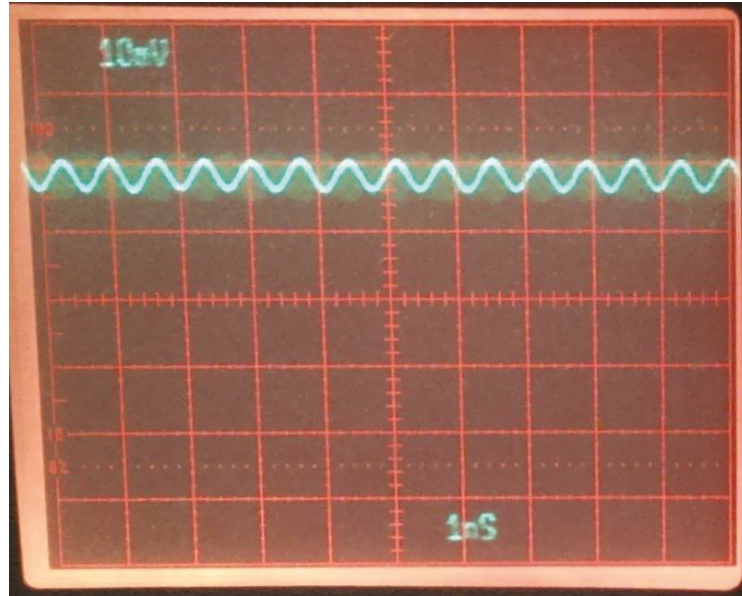


Figure 5.1-8: Sub-nanosecond photodiode measurement of laser power stability with 50 Ω termination. Time scale: 1 ns/div. Voltage scale: 10 mV/div.

The quality of the output beam was analysed by calculating the M^2 factor from the measured beam sizes focussed by a 200 mm focal length lens. Astigmatism was limited and the M^2 factor in the major and minor axes (axes with the widest and narrowest beam waists respectively) was 1.0 ± 0.2 . The plot of experimental data and the fitting functions is shown in Figure 5.1-9. There was some discrepancy between spot sizes before and after the beam waist which caused an increase in the beam radius uncertainty.

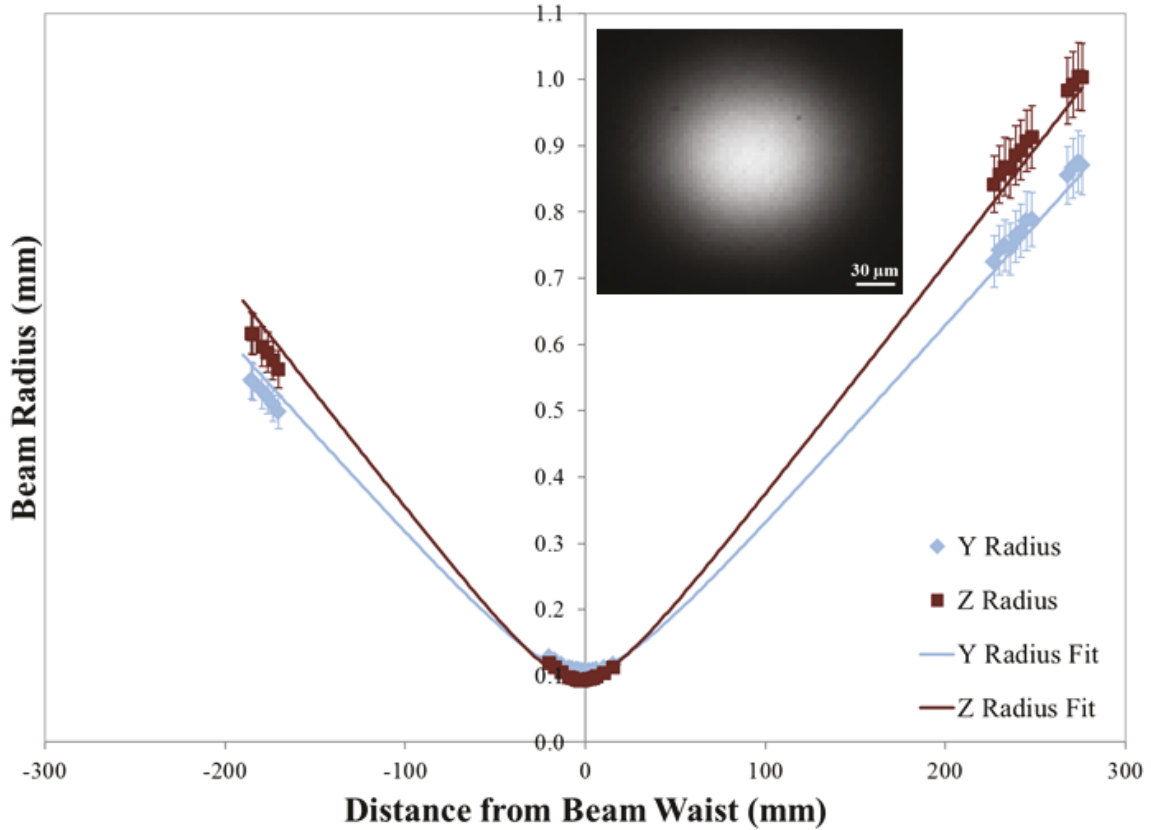


Figure 5.1-9: M^2 fit to the measured CW output beam radius in the y and z directions. Inset shows the focussed beam profile at its beam waist.

5.1.3 Q-switching Output Characteristics

From the CW analysis it was evident that the best configuration for lowering the threshold and obtaining the highest input to output optical efficiency was with the 50:50 mm pump focussing. To produce QS pulses a saturable absorber (SA) was added to the cavity. Initially a 95% saturable transmission Cr:YAG SA was used. This SA was from Altechna and was AR coated in our own facility. The AR coating allowed the SA to be installed at normal incidence which was very convenient for alignment purposes. Unfortunately, the coating was easily damaged by the intracavity laser power during a QS pulse. Repeatable pulsed lasing was only generated for a short time before a weak spot on the coating would damage.

Measurements of pulse width, repetition rate, average power, and pulse energy were taken during the periods of repeatable lasing. The full-width half-maximum (FWHM) pulse width was initially found to be approximately 67 ns with an approximate average output power of 370 mW at a pump power of 13.6 W. This corresponds to an optical to optical efficiency of 3% and a CW to QS conversion efficiency of 15% at equivalent pump power. When taking pulse energy measurements the FWHM pulse width shifted to approximately 86 ns for unclear reasons. It is possible the laser mode shifted from changes in alignment to coincide with an area of higher loss in the gain crystal or SA. If there was a spatially uneven excited state to ground state absorption cross-section ratio in the SA this could explain a shift in pulse width. Changes in SA performance have a significant effect on pulse characteristics. The pulse energy found from the energy measurement ranged from 0.5-0.6 mJ.

The difficulty in achieving stable lasing without component damage and the variability in output parameters required a new configuration. New uncoated SAs were purchased and placed in the cavity at Brewster's angle. With the 95% unsaturated transmission SA from Altechna, optical damage was again an issue. This time, however, the DM damaged rather than the SA and it was impossible to achieve more than a single QS pulse. Finally, the 98% unsaturated transmission SA from Newlight Photonics was installed and repetitive Q-switching was achieved. Burning of the DM was still an issue but an area of higher damage strength was found that enabled complete measurement of output characteristics.

The average output power and repetition rate are plotted in Figure 5.1-10. Both rose sharply with the first 0.7 W of pump power past the threshold of $8.6 \text{ W} \pm 0.4 \text{ W}$ but then settled into more moderate growth and from there continued to increase linearly with pump power. The slope efficiency of average output power over incident pump power was found to be $19.8\% \pm 0.6\%$. The trends of the average power and repetition rate show that both these parameters are intimately linked to one another. It was expected then that the change in energy and pulse width from pulse to pulse be very little. This was true and can be seen in Figure 5.1-11. There was a slight increase in pulse width as the pump power was increased

from threshold but this flattened out about 0.9 W from threshold. The pulse energy saw the reverse trend with a slight decrease as the pump power was increased from threshold to 9.1 W and then flattening from there. The ratio of average QS output power to CW output power at the same pump power was also calculated in order to see how effectively the QS laser could convert the available laser energy to an output pulse. The relationship is shown in Figure 5.1-12.

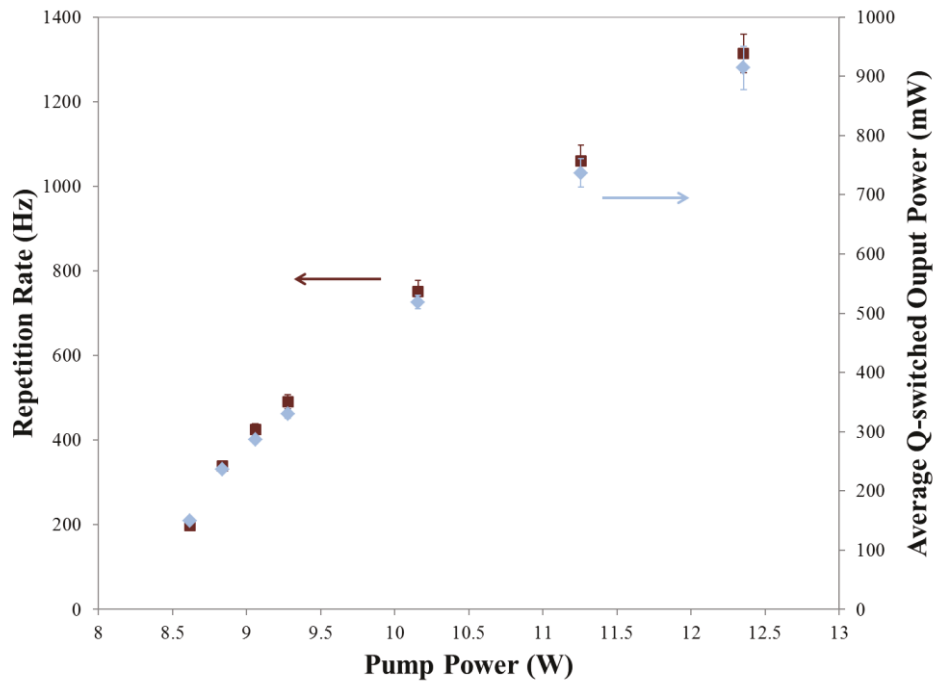


Figure 5.1-10: Repetition rate and average output power for QS operation as a function of pump power.

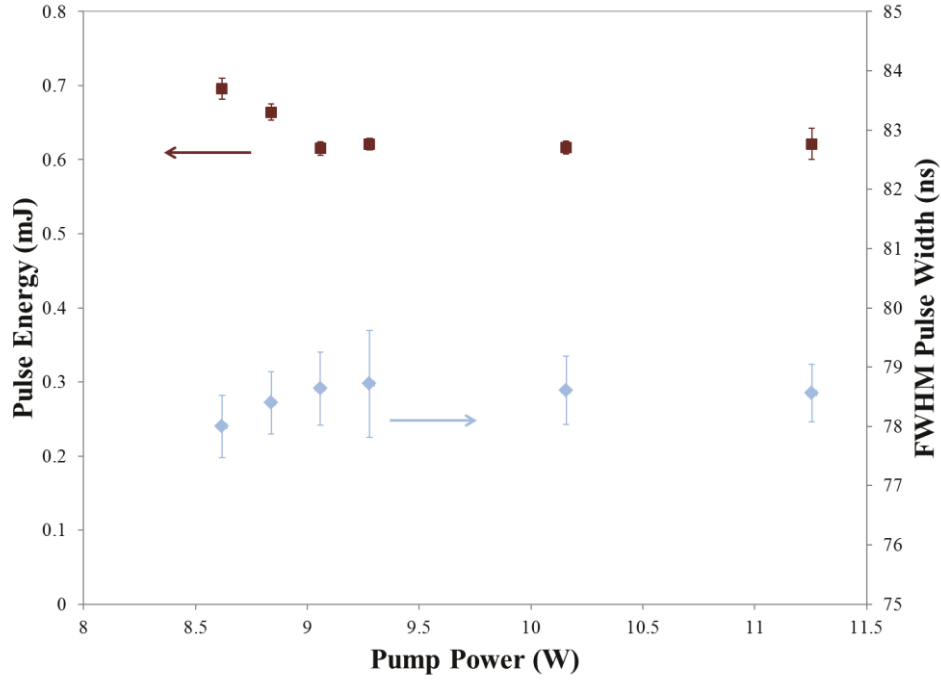


Figure 5.1-11: Pulse energy and FWHM pulse width for QS operation as a function of pump power.

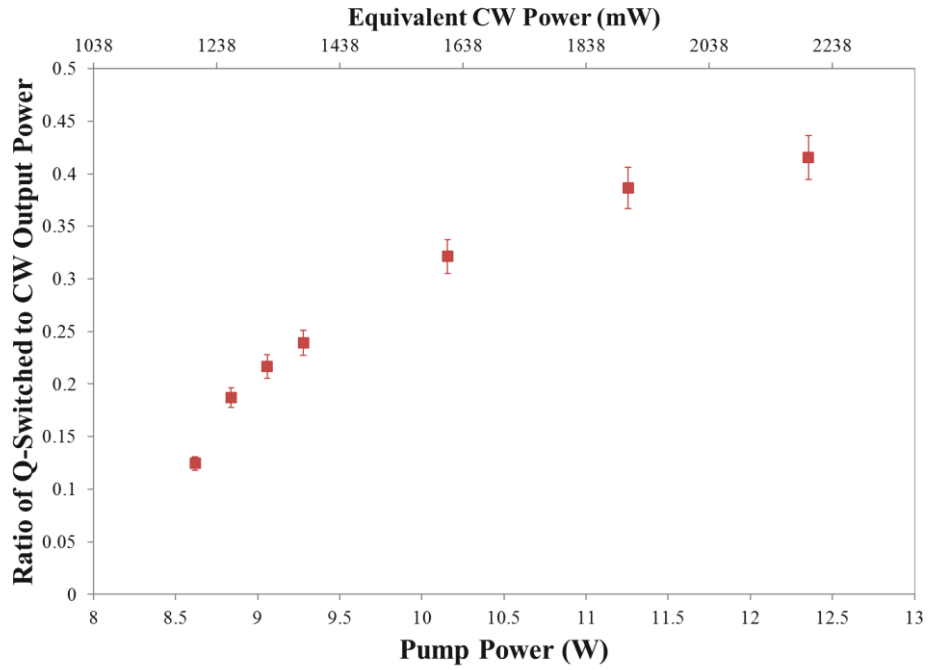


Figure 5.1-12: Ratio of average QS output power to CW output power for the same pump power.

The peak wavelength fluctuated as pump power, and consequently output power, was increased. The change in wavelength over the measurement values can be seen in Figure 5.1-13. Nearer to threshold the peak wavelength varied by around 0.1% from the average value when the pump power was modified. As the output was increased the changes in peak wavelength became a more systematic rise although the values stayed within error of each other. The error in determination of the wavelength grew at higher powers due to increased fluctuation in the output wavelength. A typical wavelength measurement for the QS laser pulse is shown in Figure 5.1-14. This spectrum was taken at 11.3 W pump power with time integration. The time integration likely resulted in a wider spectrum than truly existed due to the peak wavelength shifting with time.

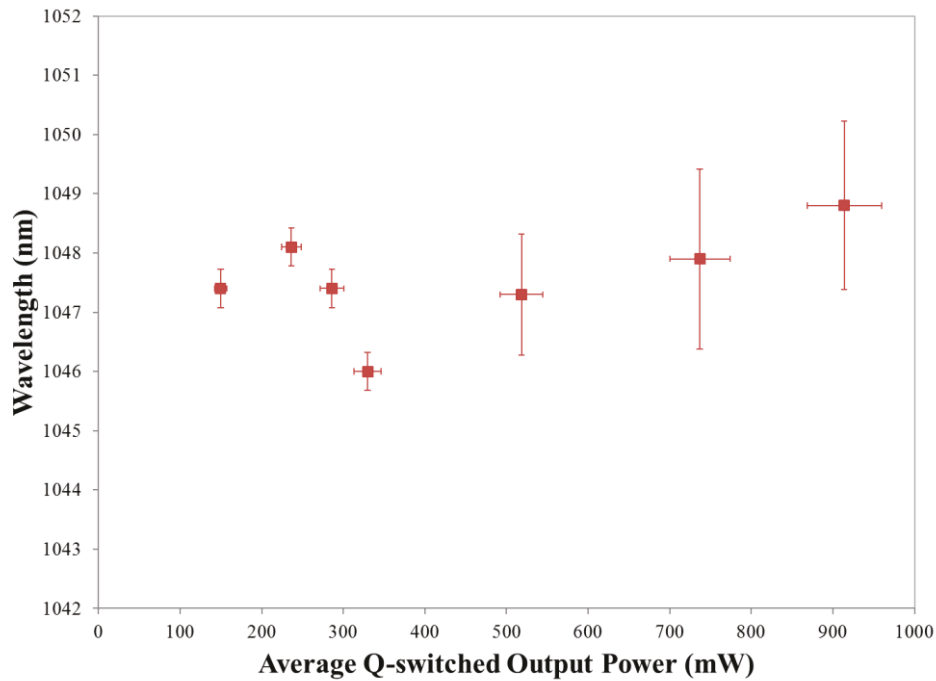


Figure 5.1-13: Change in peak QS output wavelength with changing output power.

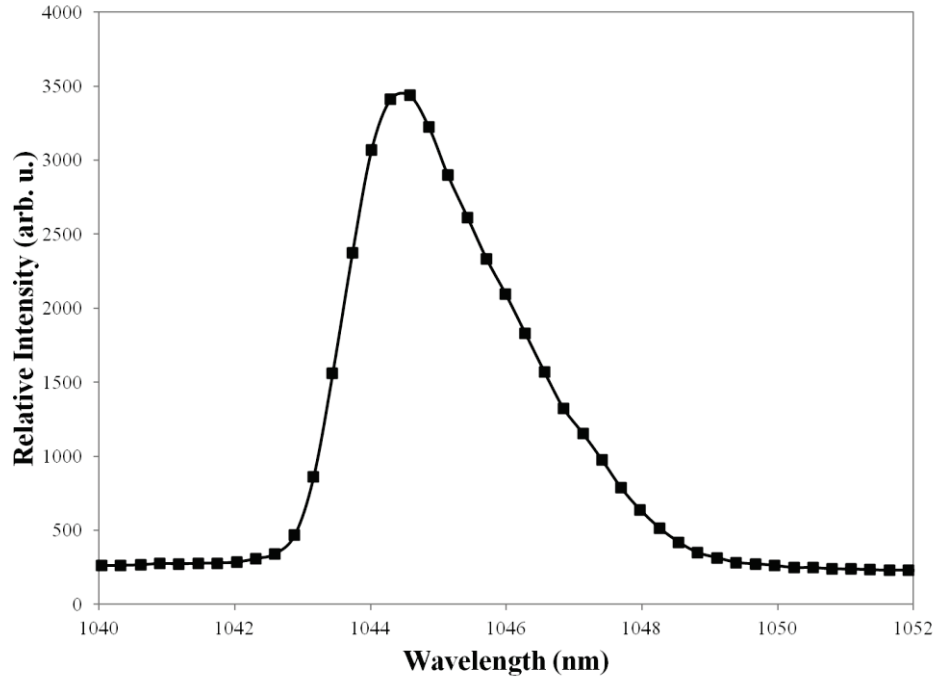


Figure 5.1-14: Typical QS output spectrum at 11.3 W pump current.

The temporal profile of the QS pulse was very consistent over the full range of pump powers. The width changed slightly as described above but the actual shape of the pulses remained constant. A typical pulse is shown in Figure 5.1-15. This measurement was taken at a pump power of 12.0 W.

The M^2 factor was calculated for the QS output beam from the measured beam sizes focussed by a 200 mm focal length lens. Astigmatism was again limited and the M^2 factor in the major and minor axes was 1.1 ± 0.2 . The plot of experimental data and the fitting functions is shown in Figure 5.1-16. The experimental data fit the calculated trend quite well on both sides of the beam waist.

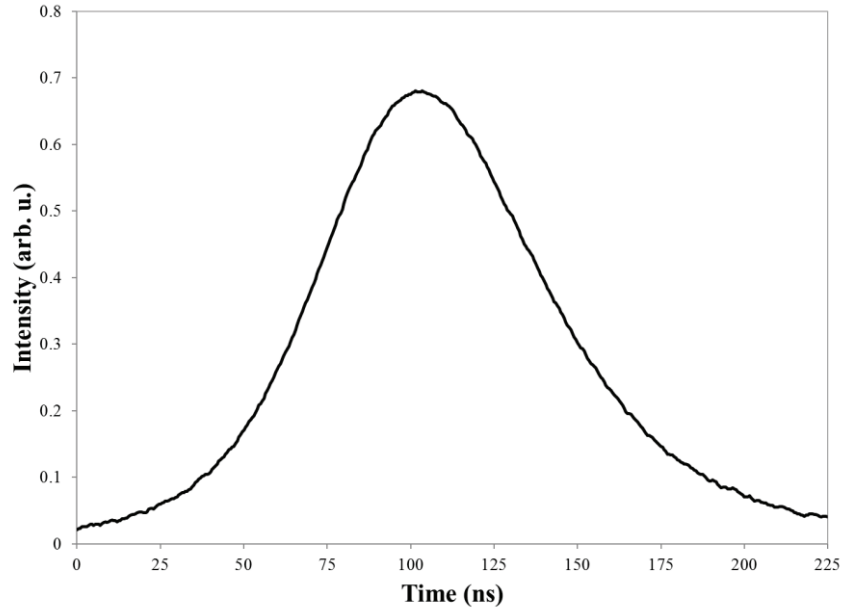


Figure 5.1-15: QS pulse shape at 12.0 W pump power.

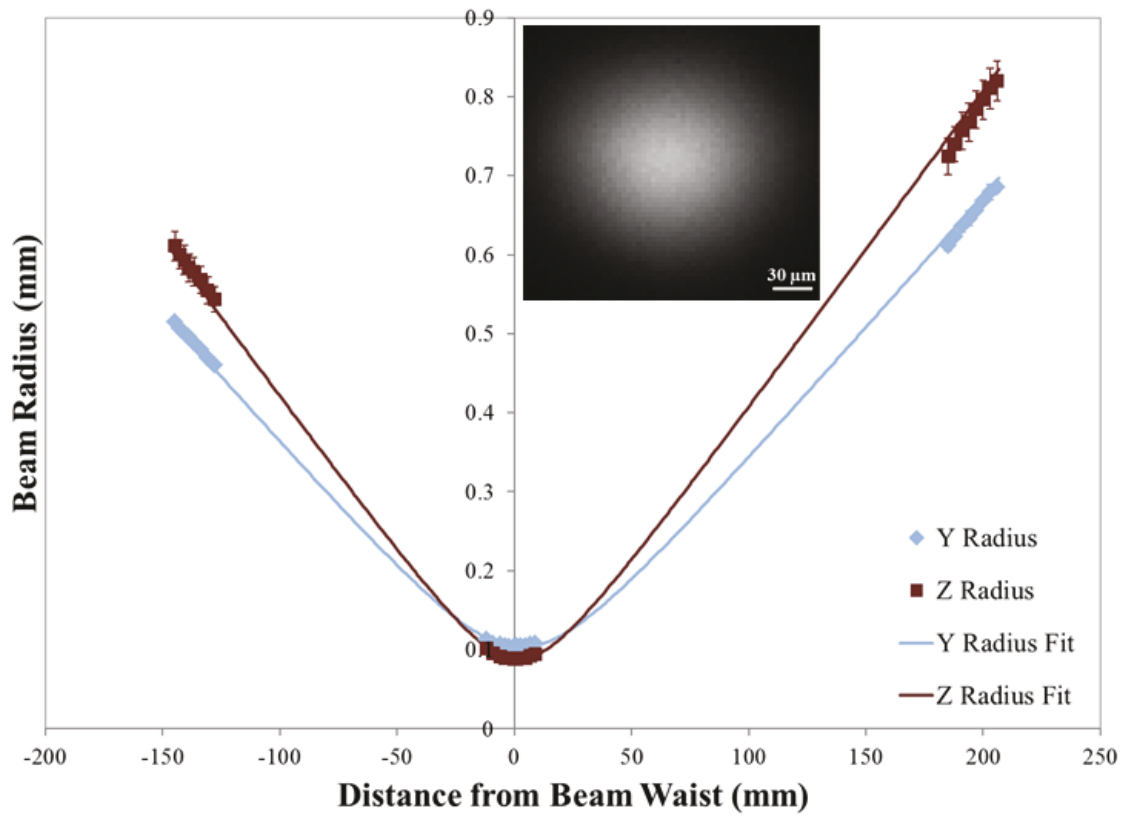


Figure 5.1-16: M^2 fit to the measured QS output beam radius in the y and z directions. Inset shows the focussed beam profile at its beam waist.

5.1.4 CW Thermal Measurement

Thermal images of the laser crystal in the CW resonator were taken with an IR camera in order to map the distribution of temperatures on the pump beam exit face. The thermal images are oriented with the cooled sides to the bottom and left, as shown in Figure 5.1-19. As Figures 5.1-17 and 5.1-18 show, the overall temperature of the crystal increases with increased pump power. The images show the pump power increasing from 0 W up to 19 W. For the thermal measurements the pump was focussed on the crystal using the 50:50 mm achromatic pair in the configuration presented in Figure 3.1-1. The temperature was distributed with the peak temperature occurring at the top-right corner where contact was made with only the mount clamp. The lowest temperatures occurred near the sides of the crystal in contact with the cooled mount as expected. In some images it was possible to see where the pump beam exits the crystal by a slight increase in temperature relative to the surrounding area. While the peak temperature was expected to be located in this area it could not be seen as the spot size was possibly too small to be imaged by the camera. The temperature observed was instead averaged by the camera and does not differ much from the areas lying outside of the pumped region. Radiation trapping may also play a role in diffusing the temperatures near the pump beam.

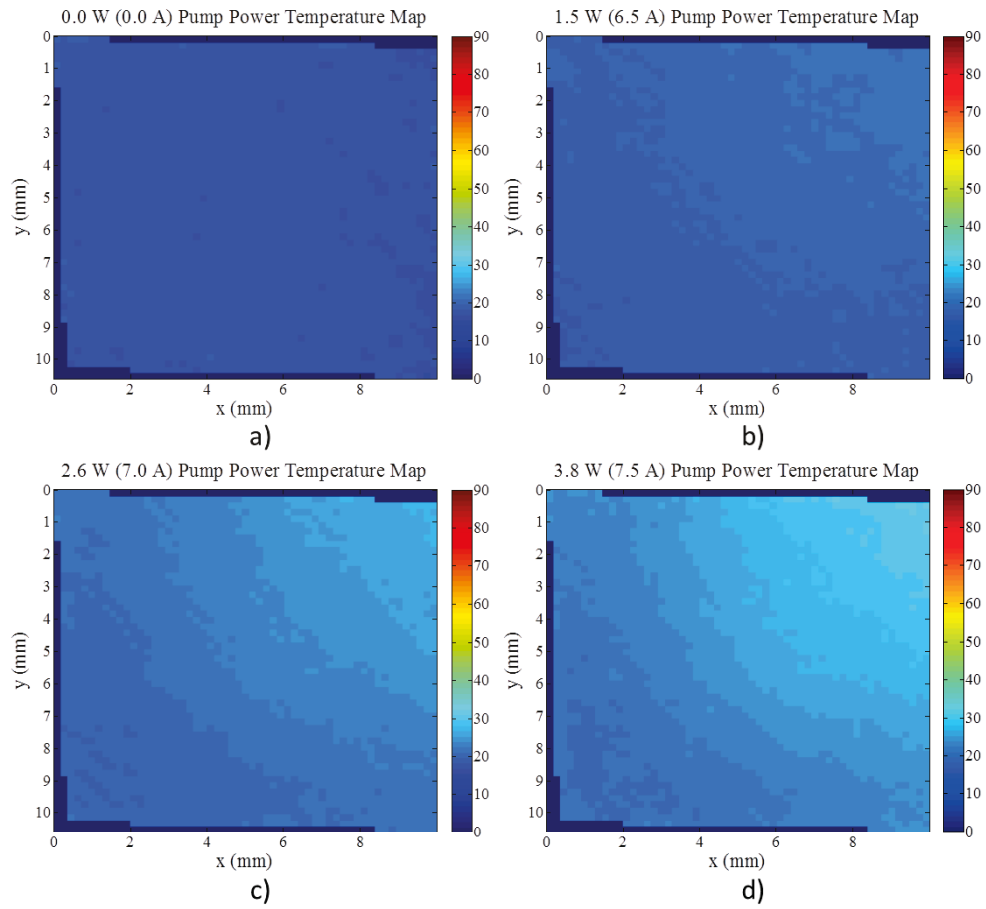


Figure 5.1-17: Thermal images captured at different pump powers below CW threshold. a) 0 W, b) 1.5 W, c) 2.6 W, and d) 3.8 W. Temperature scale is in degrees Celsius.

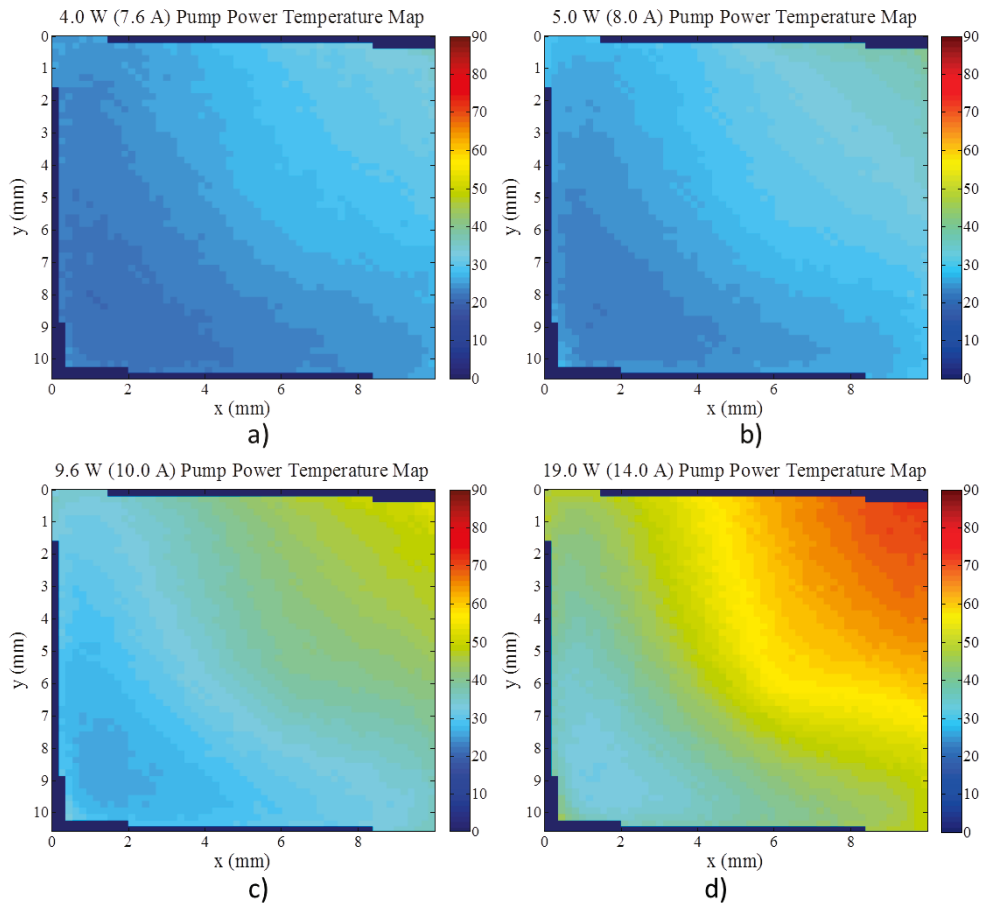


Figure 5.1-18: Thermal images captured at different pump powers at and above CW threshold. a) 4.0 W, b) 5.0 W, c) 9.6 W, and d) 19.0 W. Temperature scale is in degrees Celsius.

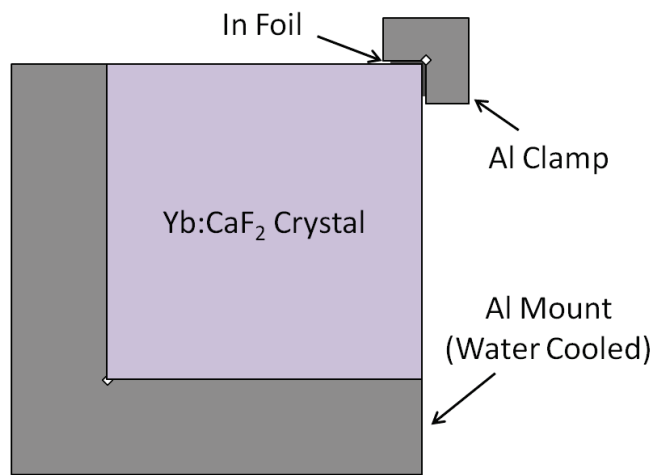


Figure 5.1-19: Crystal orientation as displayed in the thermal images used in the simulations and experiment.

To see how the temperature of the crystal face scales with increasing pump power, in Figure 5.1-20 three pixel location temperatures are plotted over the range of pump powers. The actual locations of those pixels are shown in Figure 5.1-21. The first pixel is located near the peak temperature in the top-right corner, the second pixel is located at the approximate centre of the pump beam, and the third pixel is located in the bottom-left corner where temperature should be close to a minimum. As pump power increases to threshold and after about 1.5 W past threshold the temperatures rise linearly. At threshold and just past threshold there is an obvious non-linear jump increase in temperature, especially for pixel 1.

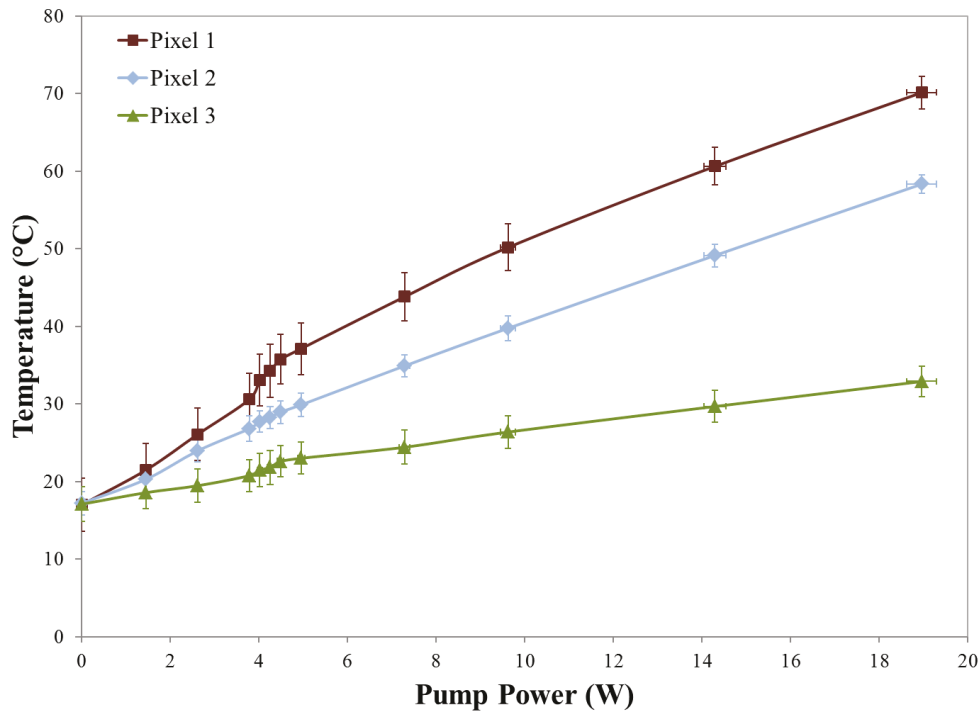


Figure 5.1-20: Experimental evolution of temperatures at specific pixel locations as pump power increases for the CW laser case.

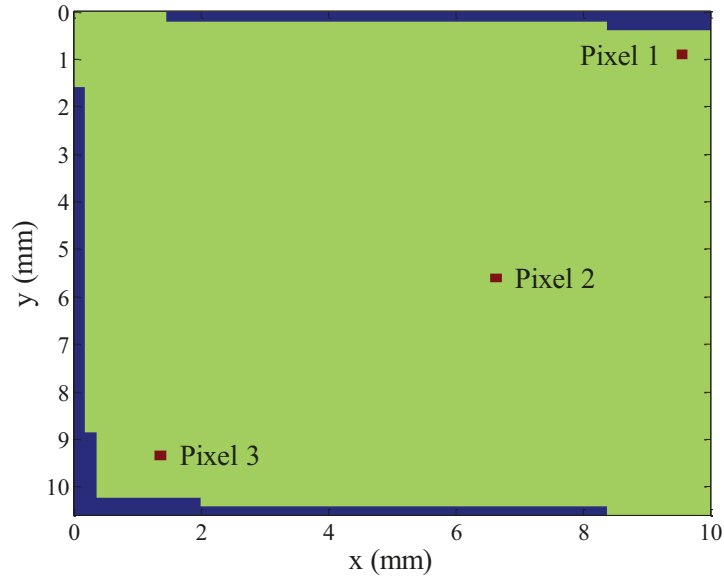


Figure 5.1-21: Pixel locations for plot of experimental CW pixel temperatures.

5.1.5 *Q-switching Thermal Measurement*

Thermal images were again taken of the pump beam exit face of the laser crystal at different pump powers but in the QS cavity configuration rather than CW. The thermal images are oriented as demonstrated in Figure 5.1-19. The pump power is varied from 0 W to 19 W and focussed with the 50:50 mm achromatic pair onto the crystal in the configuration shown in Figure 3.2-1. The un-coated SA used was from Newlight Photonics with an unsaturated transmission of 98%. The temperature maps are shown in Figures 5.1-22 and 5.1-23. The general trend was the same as in the CW case with temperatures increasing with increased pump power, the peak temperature occurring at the top-right corner, and the minimum temperatures occurring along the cooled edges. Resolution was higher for these images than with the CW images and consequently it was possible to see more clearly where the pump beam absorption occurred. The peak temperature still occurs at the top corner rather than the pumped spot and that was again possibly due to limited resolution, an averaging of temperatures in the vicinity of the pump, and radiation trapping. One issue arose from the measurements where the lower temperatures at low pump power were measured as being below the cooling temperature which was not possible. The higher error at low

temperatures may be explained by the addition of the ZnSe lens used to magnify the laser crystal. This lens caused a marked decrease in radiation intensity and introduced a spectral modulation from the AR coating applied to it. This resulted in a flattening of the measured calibration response curve at lower temperatures, and so because temperatures lower than the cooling temperature of 16.0°C had not been calibrated for, any slight drop in pixel intensity could cause the calculated temperature to drop significantly. It is possible that during the calibration the coolant temperature was not given enough time to equalise and therefore the lowest temperature calibrated for was higher than the crystal temperature during the actual thermal measurements.

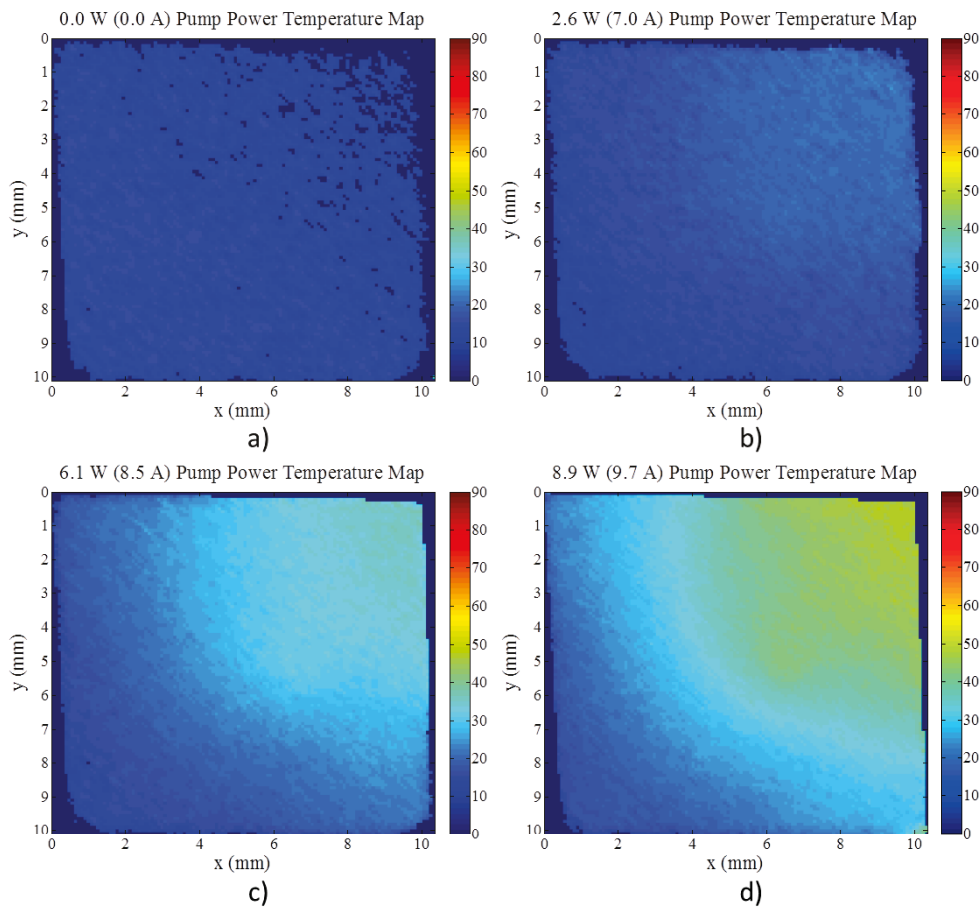


Figure 5.1-22: Thermal images captured at different pump powers below Q-switching threshold. a) 0 W, b) 2.6 W, c) 6.1 W, and d) 8.9 W. Temperature scale is in degrees Celsius.

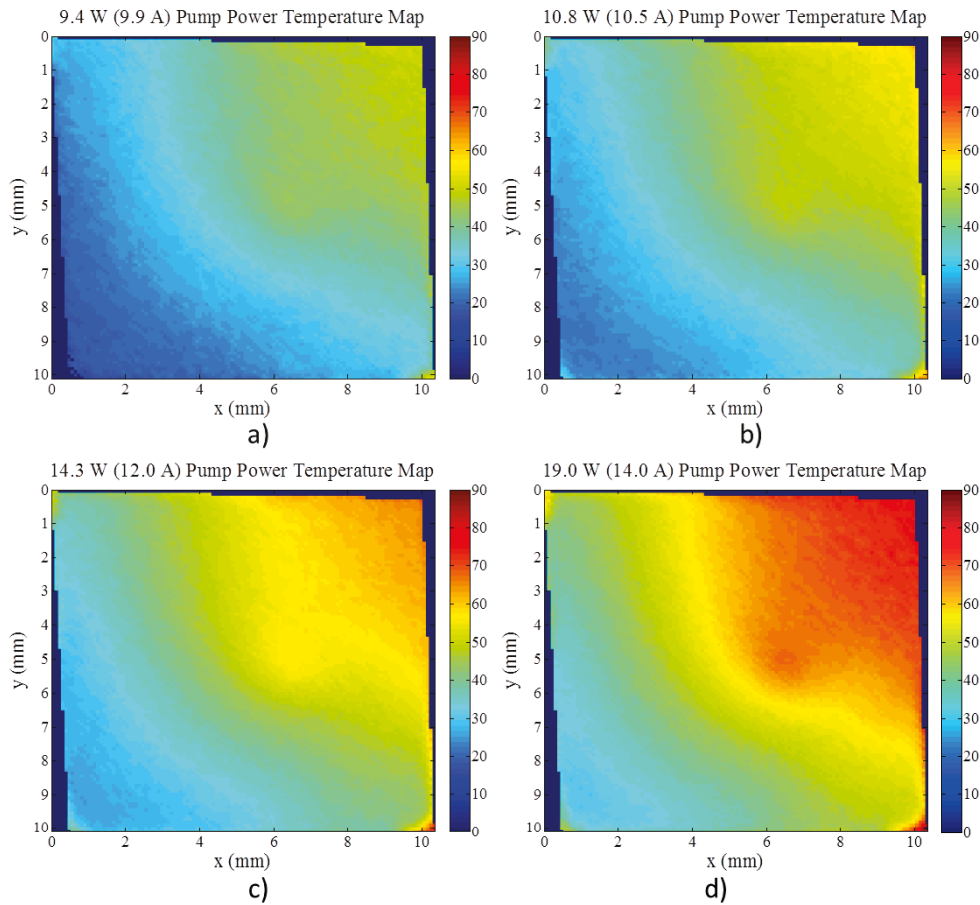


Figure 5.1-23: Thermal images captured at different pump powers at and above Q-switching threshold. a) 9.4 W, b) 10.8 W, c) 14.3 W, and d) 19.0 W. Temperature scale is in degrees Celsius.

To once again see how the temperature of the crystal face scales with increasing pump power, in Figure 5.1-24 three pixel location temperatures are plotted over the range of pump powers. The actual locations of those pixels are shown in Figure 5.1-25. The first pixel is located near the peak temperature in the top-right corner, the second pixel is located at the approximate centre of the pump beam, and the third pixel is located in the bottom-left corner where temperature should be close to a minimum. As pump power increases to threshold and after about 1 W past threshold the temperatures rise approximately linearly. At threshold and just past threshold there is an obvious non-linear jump increase in temperature. The low

temperature non-linearity and the enhanced jump at threshold for pixel 3 were caused by the issues with low temperature calibration as mentioned above.

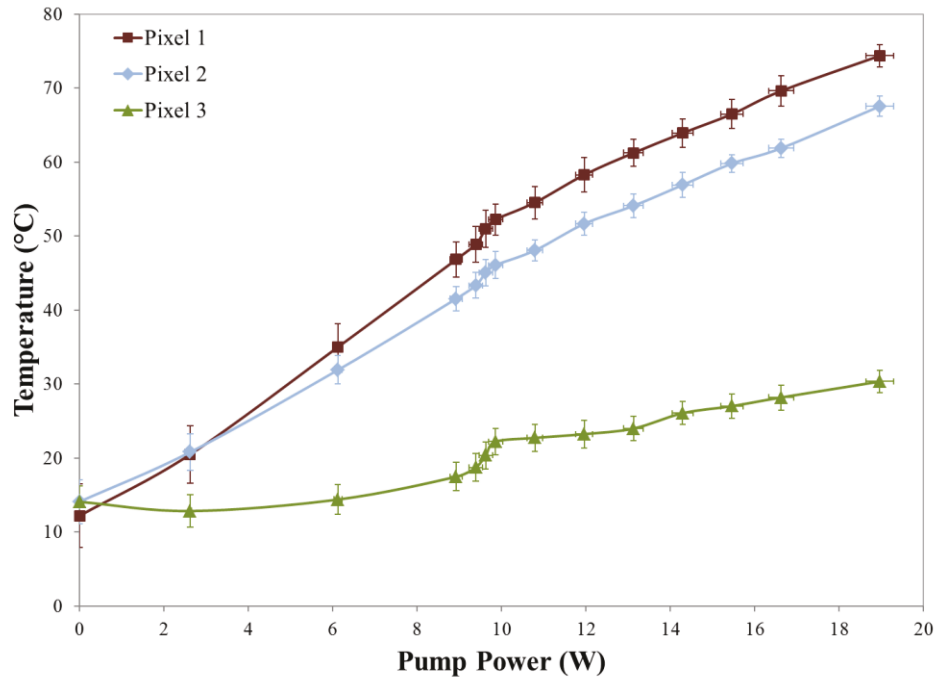


Figure 5.1-24: Experimental evolution of temperatures at specific pixel locations as pump power increases for the QS laser case.

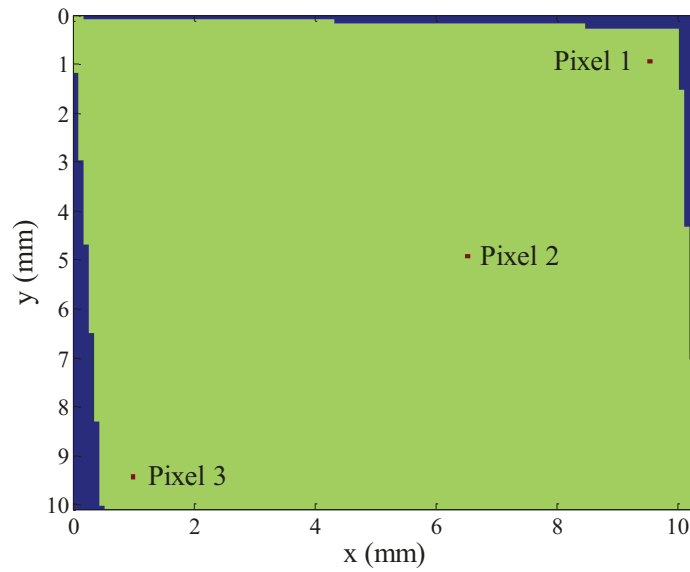


Figure 5.1-25: Pixel locations for plot of experimental QS pixel temperatures.

5.2 Simulation Results

Once the operating point and characteristics of a given laser system have been determined it is unlikely the configuration chosen was the best possible in terms of overall performance. This is where simulations can be used to optimize the laser system and provide the best possible output for the desired application. Rate equation modelling was performed for the QS laser in order to optimize several different parameters of the laser system in a parametric study. To ensure the simulations were accurate the experimental operating point was first modelled and run. Thermal FEA simulations were also undertaken to both provide information for the rate equation modelling and to understand the factors required to properly manage the heat generated in the laser crystal. Again, the thermal model was first matched with experiment to confirm the accuracy of the simulations.

5.2.1 *Q-switching Rate Equation Simulations*

Once the output characteristics, such as pulse energy, pulse width, average output power, and repetition rate, of the Q-switching rate equation model had been matched to within 30%, and generally considerably better than this, of the experimental values the model was deemed to be of sufficient accuracy to be used for parametric studies. Even though the model does not provide completely exact results it can be employed to understand which parameters could be varied to lead to a better optimized laser output. To begin, the model was run for the same pump powers employed in the experiment. The average output power and repetition rate are plotted in Figure 5.2-1 and the output pulse energy and FWHM pulse width are plotted in Figure 5.2-2. The repetition rate and average output power both increase nearly linearly for pump power greater than 13 W and they follow essentially the same trend. Pulse energy shows a slow increase with increased pump power and the pulse width displays a decrease that falls sharply near threshold but slows as the pump power increases. A comparison of the simulation outputs with the experimental results for two pump powers, 9.6 W and 12.0 W is given in Table 5.2-1.

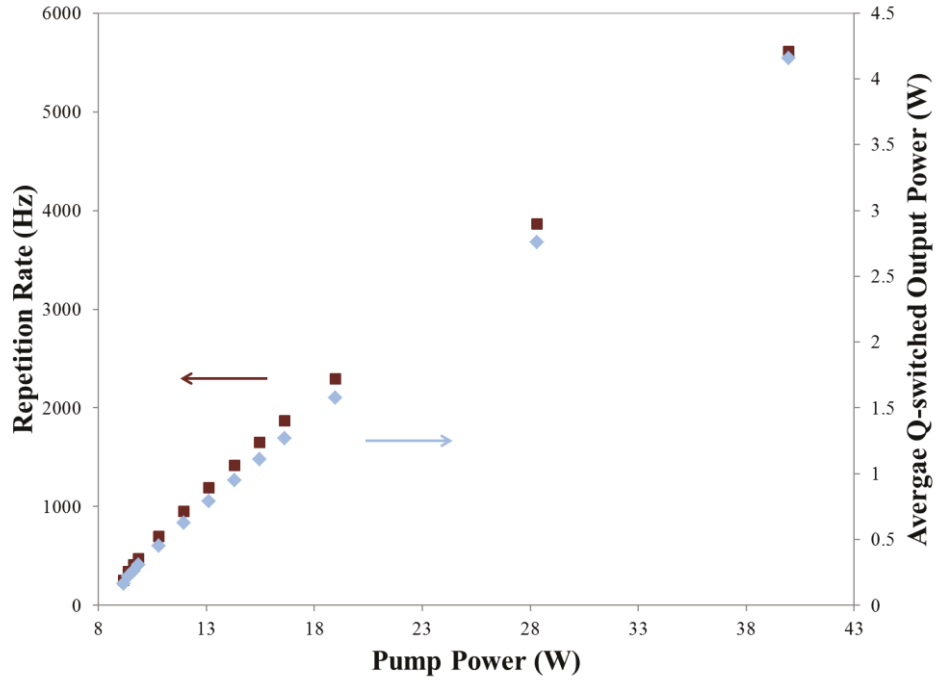


Figure 5.2-1: Repetition rate and average output power for simulated QS operation as a function of pump power.

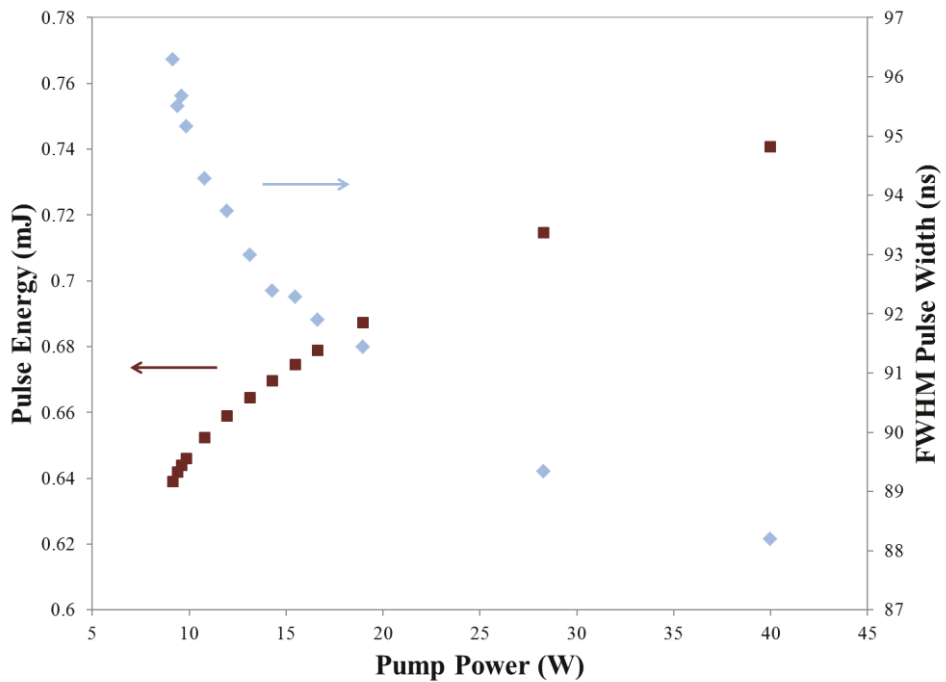


Figure 5.2-2: Pulse energy and FWHM pulse width for simulated QS operation as a function of pump power.

Table 5.2-1: Comparison of experimental and simulated QS output results.

Pump Power	Results	Experimental Value	Simulated Value	Percent Difference
9.6 W	Repetition Rate (Hz)	424	410	3.3%
	Average Output Power (mW)	286	264	7.7%
	Output Pulse Energy (mJ)	0.62	0.64	3.2%
	FWHM Pulse Width (ns)	78.6	95.7	21.8%
12.0 W	Repetition Rate (Hz)	1060	950	10.4%
	Average Output Power (mW)	737	626	15.1%
	Output Pulse Energy (mJ)	0.62	0.66	6.5%
	FWHM Pulse Width (ns)	78.6	93.7	19.2%

To elucidate the laser dynamics occurring over each QS cycle, the internal photon density, the population inversion density, and the SA transmission are plotted with time. A single pulse simulated with 19.0 W pumping is shown in Figure 5.2-3 and the pulse train is displayed in Figure 5.2-4. The photon density can be seen to increase sharply as the population inversion reaches threshold and as the photon density rises the SA transmission approaches a maximum. As the population inversion decreases to the new, lower cavity loss threshold value the photon density peaks and then begins to decrease. Once the photon density drops to a negligible value the population inversion reaches a minimum. The SA can be seen to recover much faster than the laser crystal's population inversion but much slower than the QS pulse. The process then repeats itself.

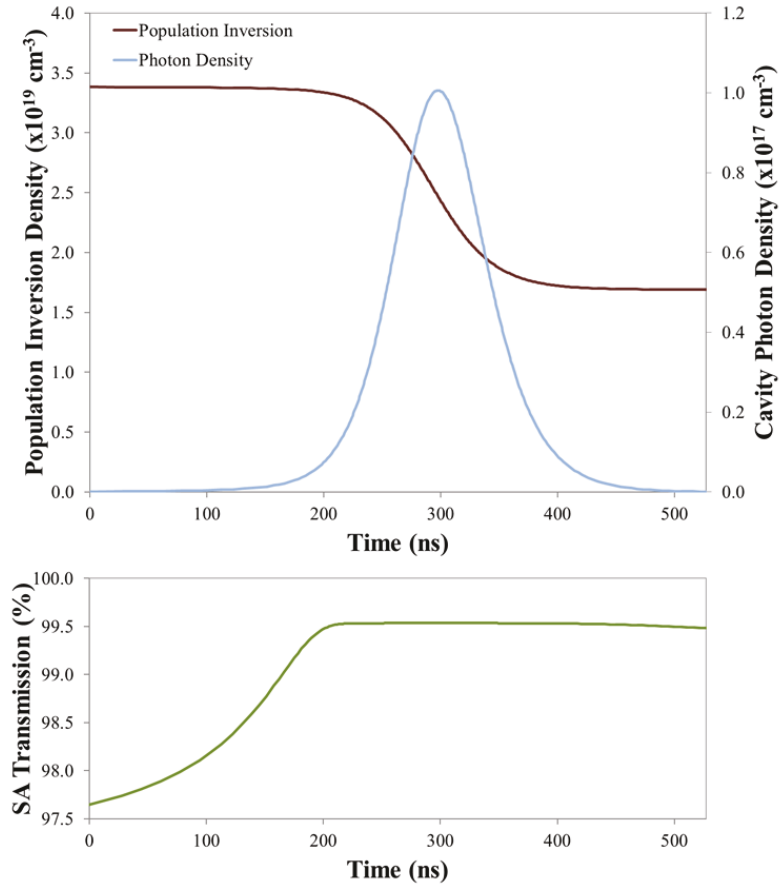


Figure 5.2-3: Population inversion, photon density, and SA transmission dynamics for a single QS pulse with 19.0 W pump power.

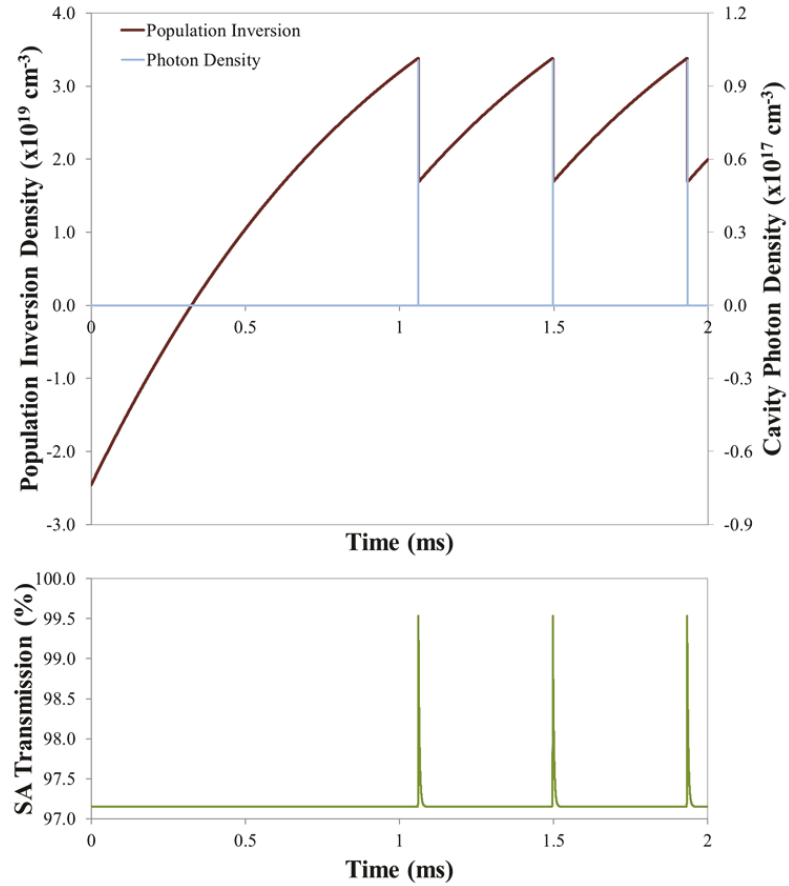


Figure 5.2-4: Population inversion, photon density, and SA transmission dynamics in a QS pulse train.

A parametric study was undertaken to determine optimised parameters for the Q-switching rate equation simulation. There were seven specific parameters chosen to be studied as they were determined to be the most influential components of the simulation that could also, in principle, be modified in the experimental laser and modeled in the simulation. These parameters were the OC reflectivity, SA unsaturated transmission (i.e. the Cr^{4+} dopant density), Yb^{3+} dopant density, length of the laser crystal, length of the laser cavity, size of the laser mode radius, and passive cavity loss. The pump mode area was not independently modified because pump to laser mode coupling was not modelled with complete accuracy in the simulation. The pump to laser mode area ratio cannot drop below 1 as this produces unphysical gain in the system, and additionally the ratio cannot be too large because higher

order transverse modes would likely appear in a real system. For these reasons an area ratio of 1 was used. The range of values solved for in each parameter sweep is shown in Table 5.2-2. The parameters that were held constant for each simulation, unless modified by the parametric sweep, are those used for the original simulations as given in Tables 4.1-1 and 4.1-2. In addition, the pump power was 28.3 W and the temperature was 397.7 K for each simulation. Figures 5.2-5 to 5.2-12 indicate each parameter's effect on average output power, repetition rate, output pulse energy, and FWHM pulse width.

Table 5.2-2: Parameter range for QS optimisation parametric study.

Parameter	Minimum Value	Maximum Value
OC Reflectivity (%)	0.85	0.99
SA Unsaturated Transmission (%)	0.90	0.99
Yb ³⁺ Dopant Density (%)	1.5	5.0
@ Crystal Lengths 0.2 – 0.8 cm		
Laser Crystal Length (cm)	0.3	1.0
Laser Cavity Length (cm)	2.5	25.0
Laser Mode Radius (μm)	50	200
@ Pump to Mode Area Ratio 1.0		
Passive Cavity Loss (%)	0.01	0.07

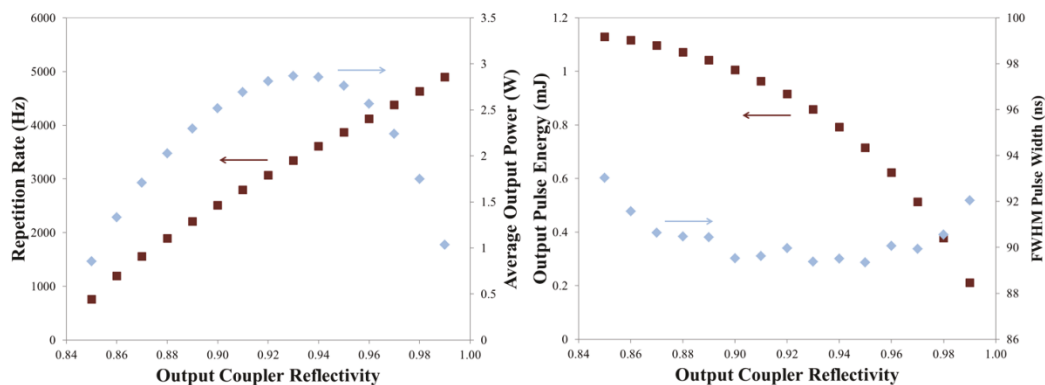


Figure 5.2-5: Change in QS output parameters for changing OC reflectivity.

In Figure 5.2-5 the OC reflectivity is shown to have a strong effect on the laser output. Repetition rate increases with reflectivity because the required population inversion for Q-switching is reduced. The pulse energy does the opposite and decreases with increased reflectivity because less of the energy can be extracted from the cavity. The combination of those two trends causes an optimisation of the average output power to be located at 93% OC reflectivity rather than at either extreme. Pulse width does not change significantly but does show a u-shaped trend likely from the slower extraction of energy at low reflectivities and the difficulty in extracting energy at high reflectivities leading to pulse elongation.

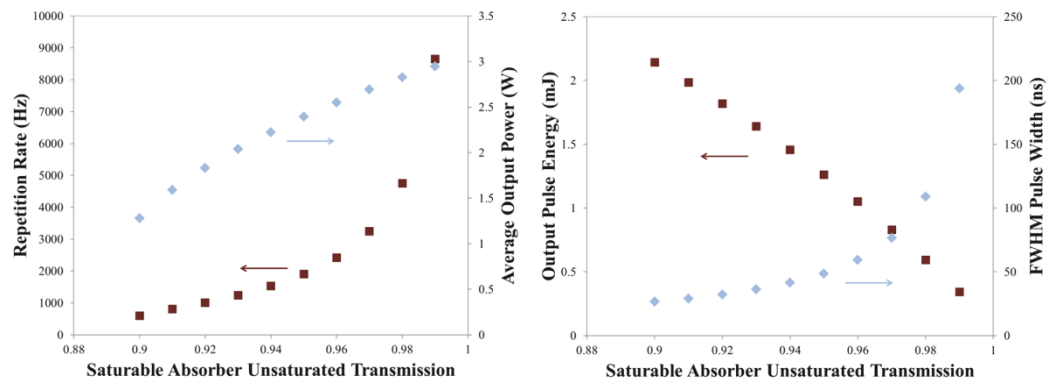


Figure 5.2-6: Change in QS output parameters for changing SA unsaturated transmission.

Figure 5.2-6 displays output characteristics with changing SA unsaturated transmission. The sharp increase in repetition rate at high transmission is from the ease of reaching threshold which then becomes more difficult as transmission is decreased. The pulse energy decreases with increased transmission because the ratio between saturated transmission and unsaturated transmission drops and less stored energy is extracted from the gain medium. The average output power balances the change in energy and repetition rate, and reaches a maximum at high SA transmission. The pulse width is strongly dependent on SA transmission with a large increase at higher transmissions due to a smaller difference between initial gain and loss when the cavity switches from low to high Q.

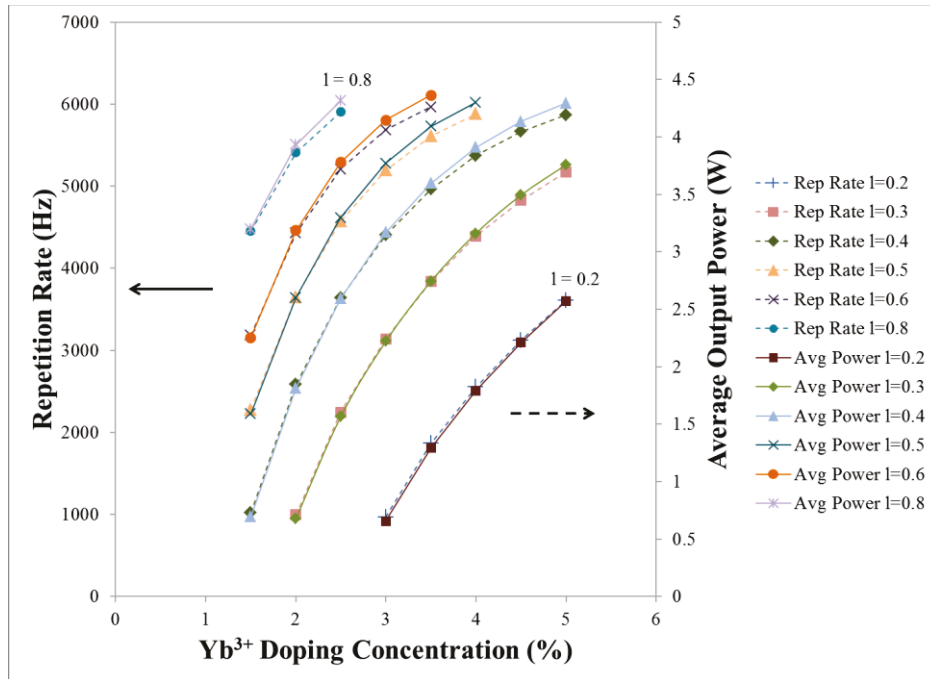


Figure 5.2-7: Change in repetition rate and average output power for changing Yb^{3+} doping concentration. Simulations run for laser crystal lengths (l) of 0.2-0.8 cm as indicated in the legend.

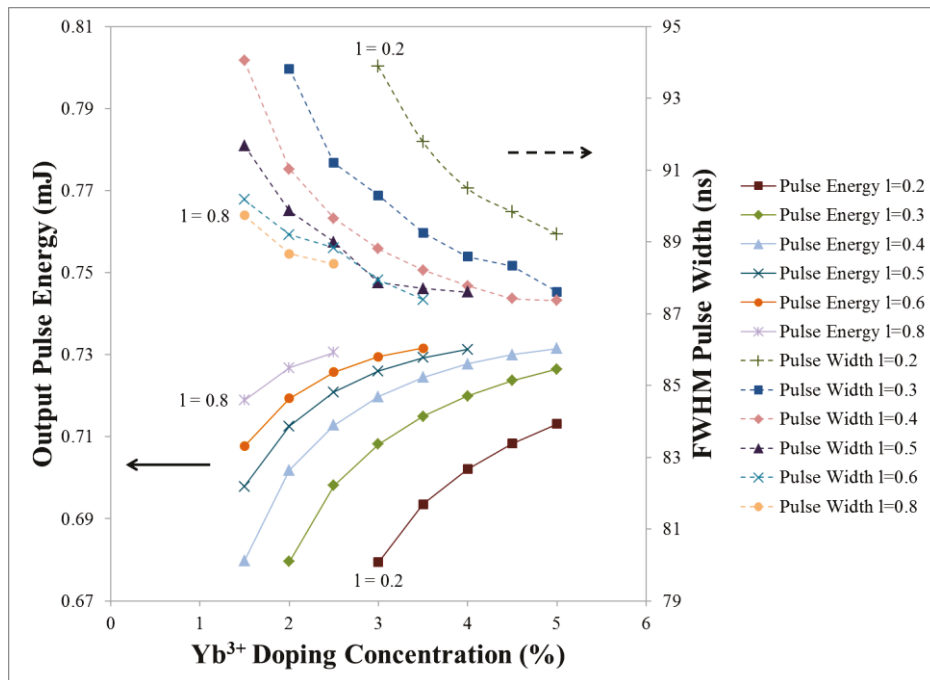


Figure 5.2-8: Change in output pulse energy and FWHM pulse width for changing Yb^{3+} doping concentration. Simulations run for laser crystal lengths (l) of 0.2-0.8 cm as indicated in the legend.

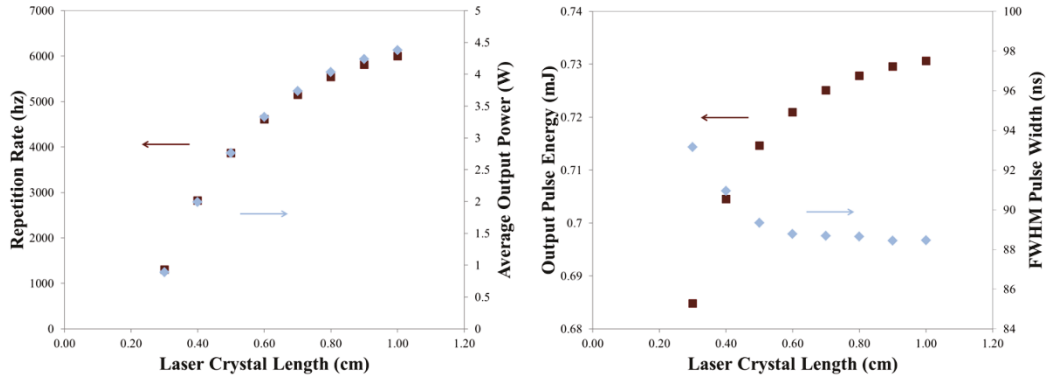


Figure 5.2-9: Change in QS output parameters for changing laser crystal length.

The information presented in Figures 5.2-7 to 5.2-9 should be taken with care. Changes to the crystal length will cause the effects of pump divergence, which were not included in the model, to become more significant. Modification of the doping concentration and crystal length may also lead to a different dynamic between gain and reabsorption along the laser mode which may not be fully represented without modelling of a longitudinally-dependent population inversion. The qualitative trends, however, should still be valid. There is very little change in pulse width and energy with changing length and concentration. There is a small decrease in energy with an increase in both length and concentration because there are a larger number of ions to excite at a specific pump power and the pump does not cause the population inversion to overshoot as much during the transition time of the SA. With a change in initial population inversion when the pulse energy decreases the pulse width increases. The changes in energy and pulse width with population inversion are explained further in Section 6.2.1. The repetition rate and average power both increase with doping concentration and length because the gain is higher in the laser crystal. In reality this would likely be somewhat offset by the increased reabsorption. Figure 5.2-9 indicates the same results as shown in Figures 5.2-7 and 5.2-8 but displayed as only a change in crystal length.

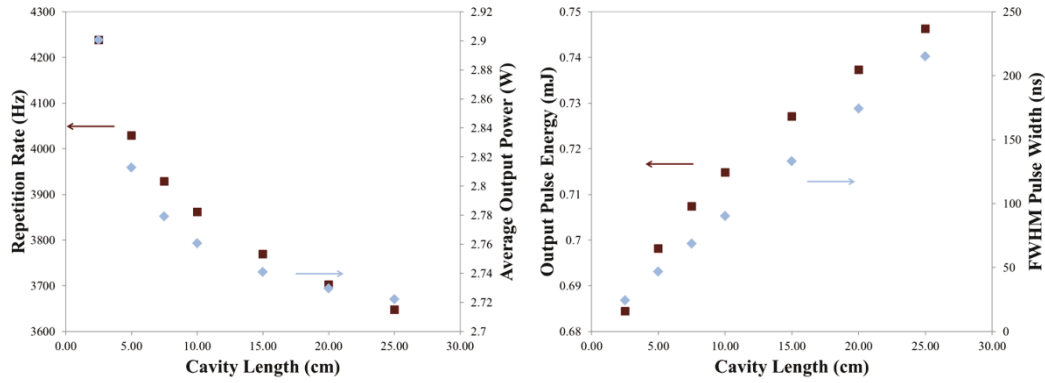


Figure 5.2-10: Change in QS output parameters for changing laser cavity length.

Laser cavity length is an effective parameter to change when pulse width requires modification. In Figure 5.2-10 the pulse width grows with increased cavity length simply due to the increase in cavity round trip time. The change in pulse energy is minimal but tends to increase as cavity length is increased. The additional time it takes the pulse to circulate in the cavity allows the pump to replenish some of the population inversion. Additionally, the extra cavity mode volume causes a decrease in the photon density which leads to a slower rise in photon density per pass, extending the time to remove the population inversion even further. The decrease in repetition rate and average power with cavity length is also a result of the increased photon cavity lifetime.

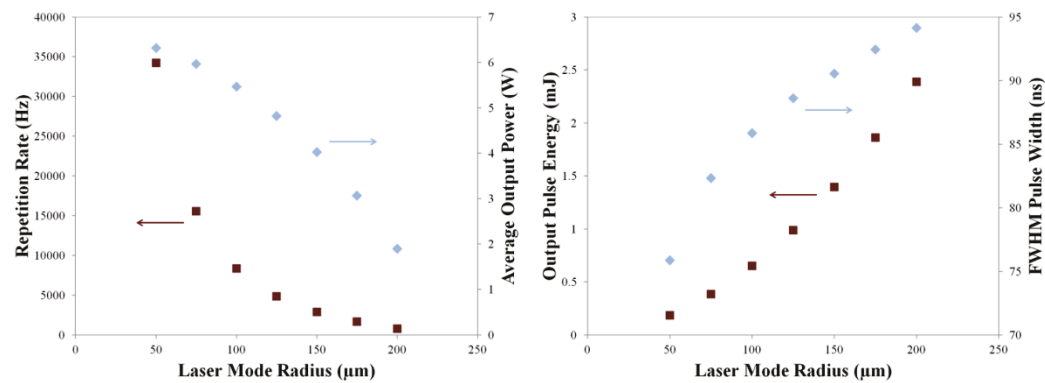


Figure 5.2-11: Change in QS output parameters for changing laser mode radius. Pump to laser mode area ratio was fixed at one.

Figure 5.2-11 displays the output performance with changing laser mode radius. These results are not entirely representative of the true laser because the modelling of pump to laser mode coupling was rudimentary in the simulation and beam divergence was not accounted for. For the same pump to mode area ratio, as the mode radius, and therefore pump radius, decreases the repetition rate increases substantially. This increases because while pump power remains the same the pump fluence is greatly enhanced. With higher pump fluence the threshold inversion is achieved much more rapidly. Average output power increases as well but not as sharply as repetition rate due to the competition between the repetition rate and pulse energy. Pulse energy decreases with the smaller mode and pump volume because there are less inverted ions at lasing threshold within the mode volume and accordingly less photons emitted. The decline in pulse width as mode radius decreases comes from the additional population inversion overshoot that occurs when the pump fluence is increased. X. Zhang et al.⁶⁸ produced a model where the effects of changing pump size and mode size were modeled in detail. Further detail about the relationship between pump to mode size ratio and the pulse energy and pulse width can be found in their paper.

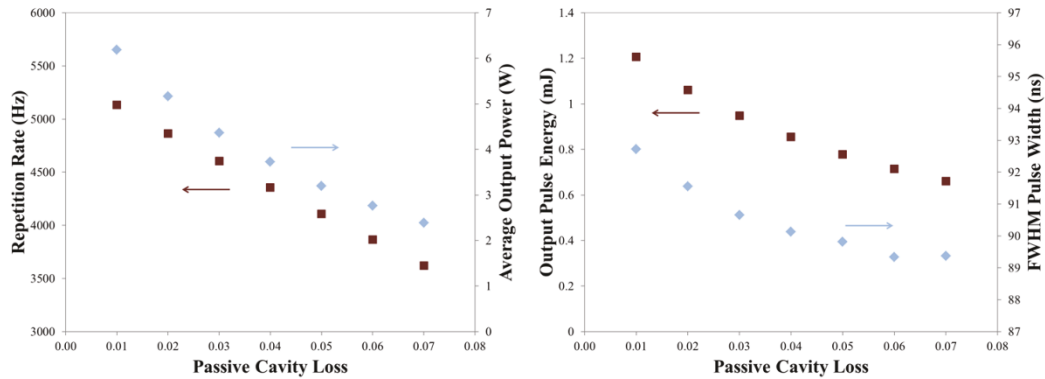


Figure 5.2-12: Change in QS output parameters for changing passive cavity loss.

Finally, the change in output performance with passive cavity loss is shown in Figure 5.2-12. As expected, repetition rate, output power, and output energy all increase with decreased loss. So too does the pulse width which is an unwanted effect. Pulse width

increases because of the change in initial and threshold inversion densities. More detail regarding Figures 5.2-5 to 5.2-12 can be found in Section 6.2.3.

5.2.2 CW Thermal Simulations

The CW thermal imaging experiment produced temperatures with fairly good accuracy and thus this was a good place to start for modelling. Once simulated temperatures matched to within 2% Kelvin of the experimental ones for the non-lasing and lasing cases it satisfied the desired accuracy. To see the similarities between the experiment and simulation, temperature maps, at different pump powers, of the surface at which the pump exits the crystal are displayed in Figures 5.2-13 and 5.2-14 for the cases of below and above CW lasing threshold respectively. The temperature maps are oriented as demonstrated in Figure 5.1-19. The pump power in the simulated images matches to the pump power in the experimental images. There are obvious similarities between the experimental and simulated images as the temperature distribution is essentially the same. However, in the simulations the peak temperatures near the pumped region become clear and show a peak temperature occurring in this area. Greater resolution may lead to this; the resolution of the simulation can be seen by looking at the mesh size, shown in Figure 4.2-4. There was a high density of mesh elements in the pump and laser mode region specifically as this area was critical in the calculation of pump absorption and heat generation.

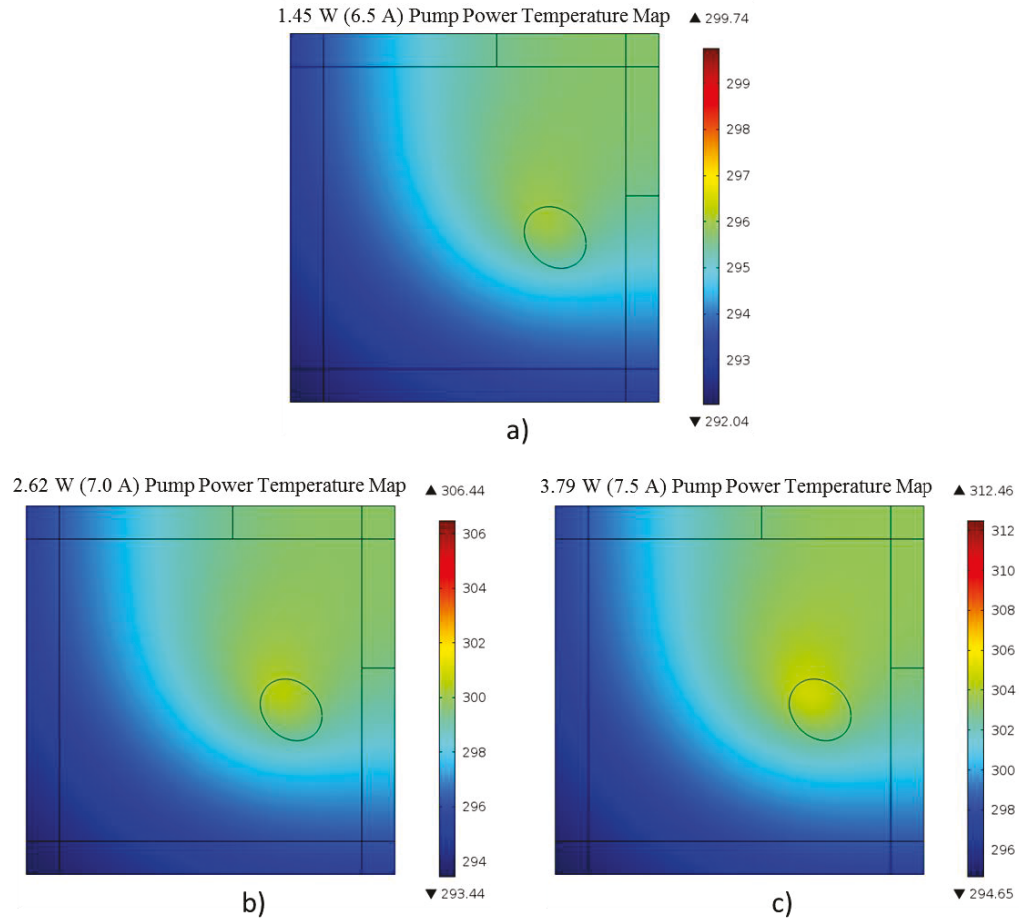


Figure 5.2-13: Thermal images from simulations run at different pump powers below CW threshold. a) 1.45 W, b) 2.62 W, and c) 3.79 W. Temperature scale is in degrees Kelvin.

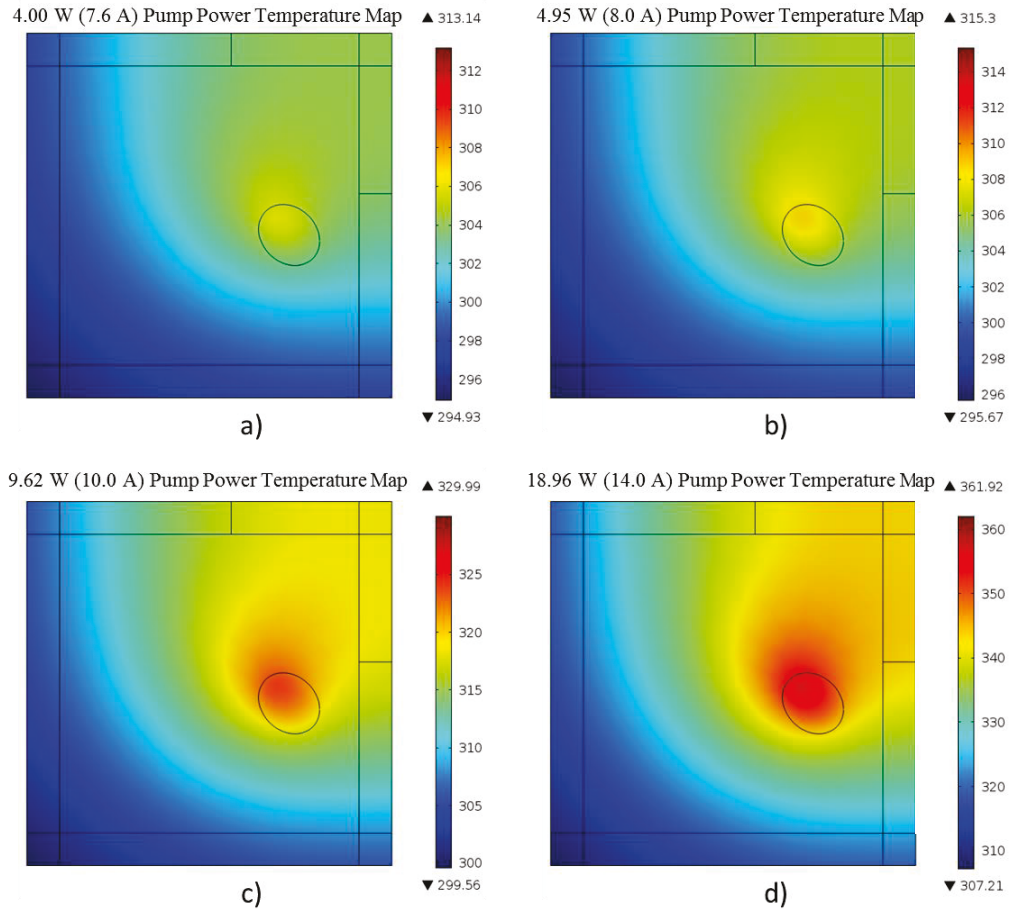


Figure 5.2-14: Thermal images from simulations run at different pump powers at and above CW threshold. a) 4.00 W, b) 4.95 W, c) 9.62 W, and d) 18.96 W. Temperature scale is in degrees Kelvin.

Again to facilitate comparison between experiment and simulation, the temperatures at three points on the pump exit face of the crystal are plotted in Figure 5.2-15. These locations are illustrated in Figure 5.2-16. They roughly correspond to the same locations as in the experimental images; the first pixel is located in the top-right corner, the second pixel is located at the approximate centre of the pump beam, and the third pixel is located in the bottom-left corner where temperature should be a minimum. The temperature trends remain very similar to the experimental results but the sharp increase in temperature at threshold does not materialize in the simulations as can be seen in the inset of Figure 5.2-15. One other major difference is the much larger temperatures at the centre of the pump region and this is

possibly due to the greater spatial accuracy of the simulation versus the experiment and the effects of radiation trapping in the real crystal. This difference can be seen in the inset of Figure 5.2-15. In the experiment, peak temperature occurred at the pixel one location; whereas, in the simulations, pixel two is the location of the highest temperatures.

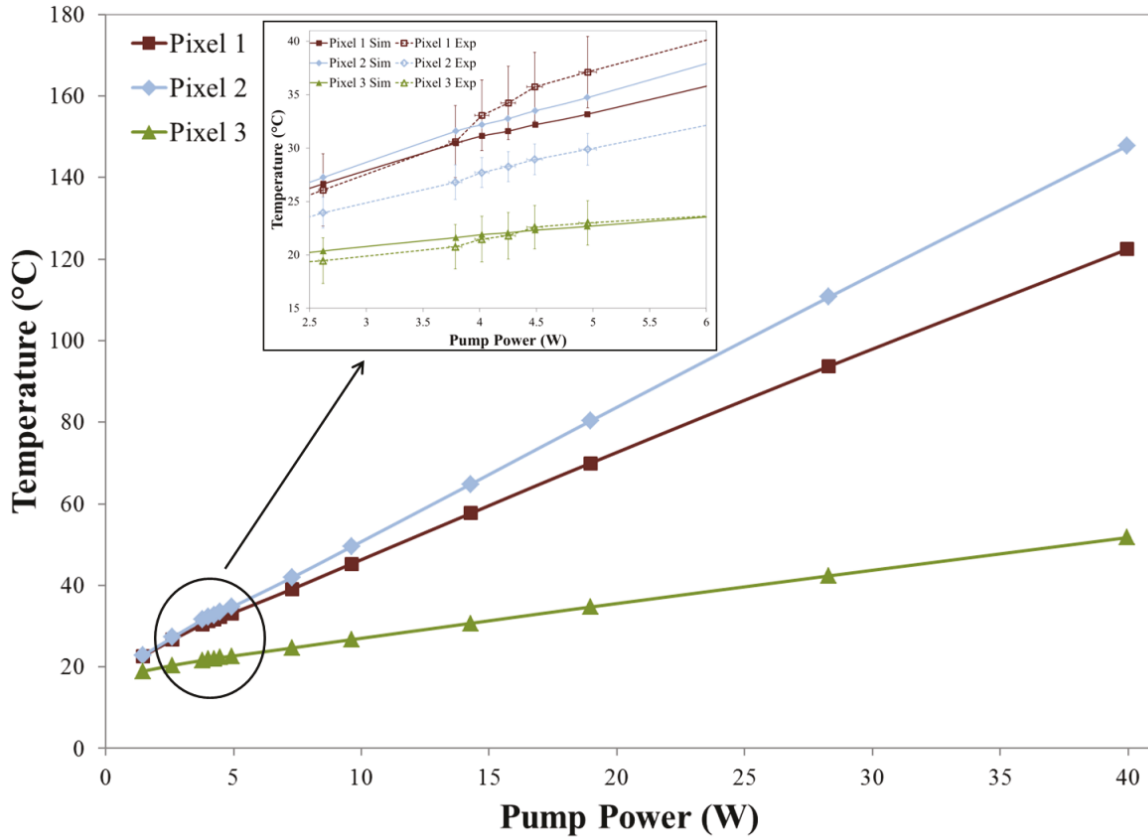


Figure 5.2-15: Simulated evolution of temperatures at specific pixel locations as pump power increases for the CW laser case. Inset detail shows a comparison of simulation and experimental data points from 2.5 to 6 W.

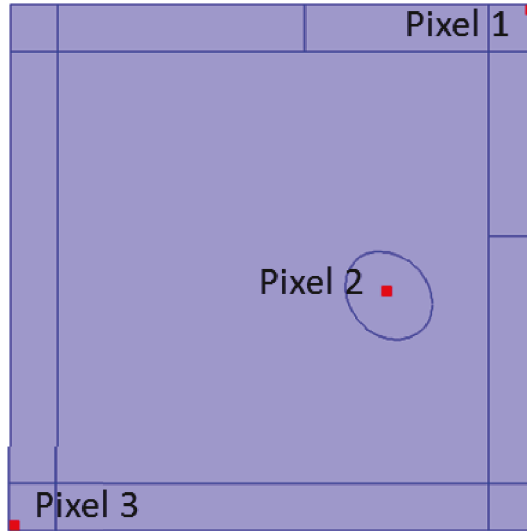


Figure 5.2-16: Pixel locations for plot of simulated CW pixel temperatures.

The ability to simulate the temperature of the entire laser crystal provides information for not only QS output modelling but also allows determination of the peak temperatures in the crystal. The progression of temperatures along the beam propagation axis as pump power increases is shown in Figure 5.2-17. In the images, the location at which the centre of the pump beam exits the crystal is defined as $x' = 0$, and so as x' increases, the position moves towards the front face. The peak temperature occurs at the input face for low pump and laser powers but as the pump and laser power increases the peak temperature shifts backwards towards the pump beam waist and back face. The pump beam waist in the CW configuration was located at $x' = 0.0049$ m and the waist radius was $134 \mu\text{m}$ and $95 \mu\text{m}$ in the y' and z' directions respectively. In Table 5.2-3 the peak temperatures in the crystal are given in reference to the pump power, peak measured back-face temperature, and peak simulated back face temperature. This shows that the peak temperature can be much higher than what is determined by imaging the crystal surface.

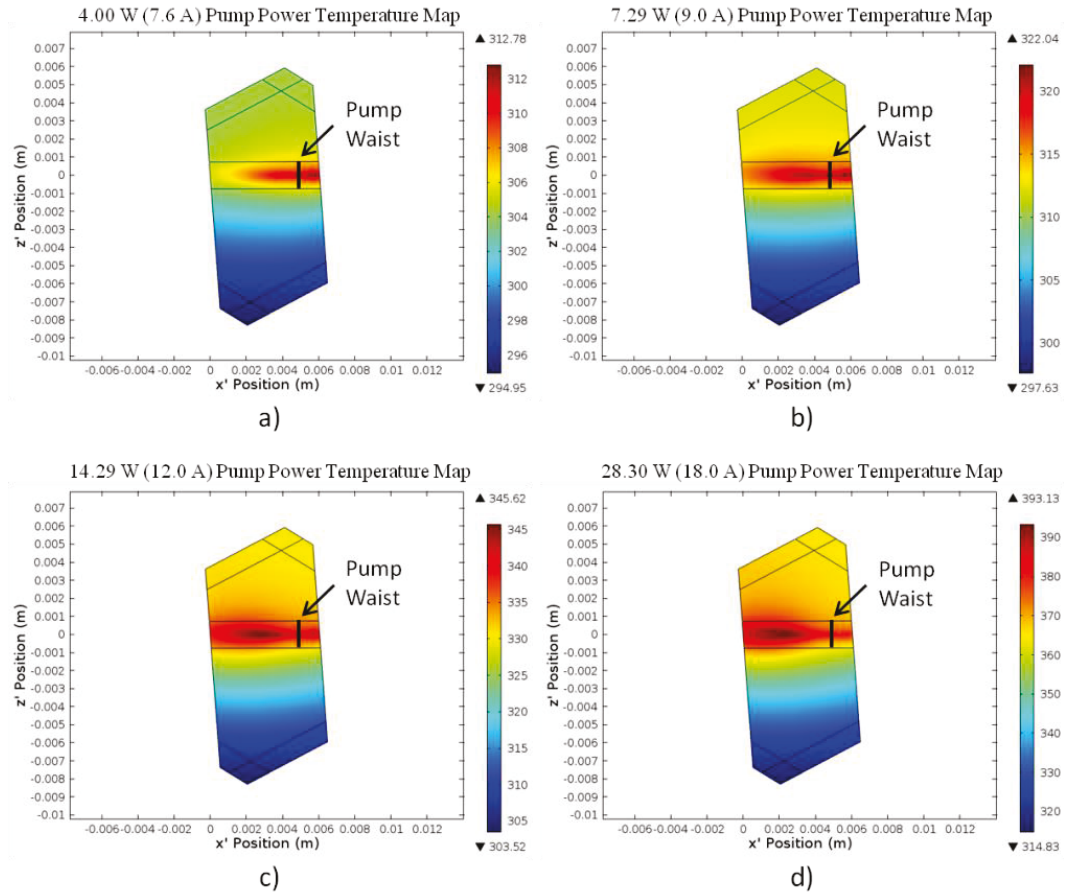


Figure 5.2-17: CW laser simulated distribution of temperature in Kelvin along the pump axis at a) 4.00 W, b) 7.29 W, c) 14.29 W, and d) 28.30 W pump power. The pump enters from the right side and exits the crystal at $x' = 0$, i.e. the back face of the crystal. The pump beam waist location is indicated in each figure.

Table 5.2-3: Comparison of peak temperatures in the measured and simulated CW laser temperature profiles.

Pump Power (W)	Peak Measured Back-Face Temperature (°C)	Peak Simulated Back-Face Temperature (°C)	Peak Simulated Crystal Temperature (°C)
1.45	22.5	23.0	26.6
2.62	28.0	27.5	33.3
3.79	31.7	32.0	39.3
4.02	35.5	32.8	40.0
4.25	37.1	33.4	40.4
4.49	39.4	34.1	41.1
4.95	40.7	35.4	42.2
7.29	47.0	42.9	49.3
9.62	53.2	50.7	56.8
14.29	62.9	66.7	72.6
18.96	72.0	82.8	88.8

While it is useful to predict the crystal temperatures for the current laser system the simulations can also be utilised to see what temperatures develop in a more optimised system. Three aspects of the laser crystal were modified to determine the effect that the changes had on the temperature profile. There were four cases, each of which maintained the exact same parameters as the 18.96 W pump power, CW, thermal simulation except for the parameters relating to the modified aspect. The first temperature profile is shown in Figure 5.2-18a and pertains to the case where the mount temperature adjacent to the cooled crystal edges was maintained at 16.0°C; this would be the situation in an idealized crystal mount that does not increase in temperature as the crystal temperature increases. The second case is shown in Figure 5.2-18b and corresponded to a situation where the thermal contact between the mount and crystal was very good, i.e. a heat transfer coefficient of $1.0 \text{ W}\cdot\text{cm}^{-2}\cdot\text{K}^{-1}$. The third case is given in Figure 5.2-18c and assumed a high crystal quality where the pump and radiative quantum efficiencies were both 0.99 and subsequently the fluorescence lifetime was 1.88 ms. The final case, shown in Figure 5.2-18d, combines all

three previous modifications to construct an ideal cooling configuration. In terms of reduction of crystal temperature the effectiveness is ranked from lowest to highest as cases one to four sequentially. In Table 5.2-4 the changes in peak temperature and average pump beam axis temperature are compared to the original simulation for all four cases.

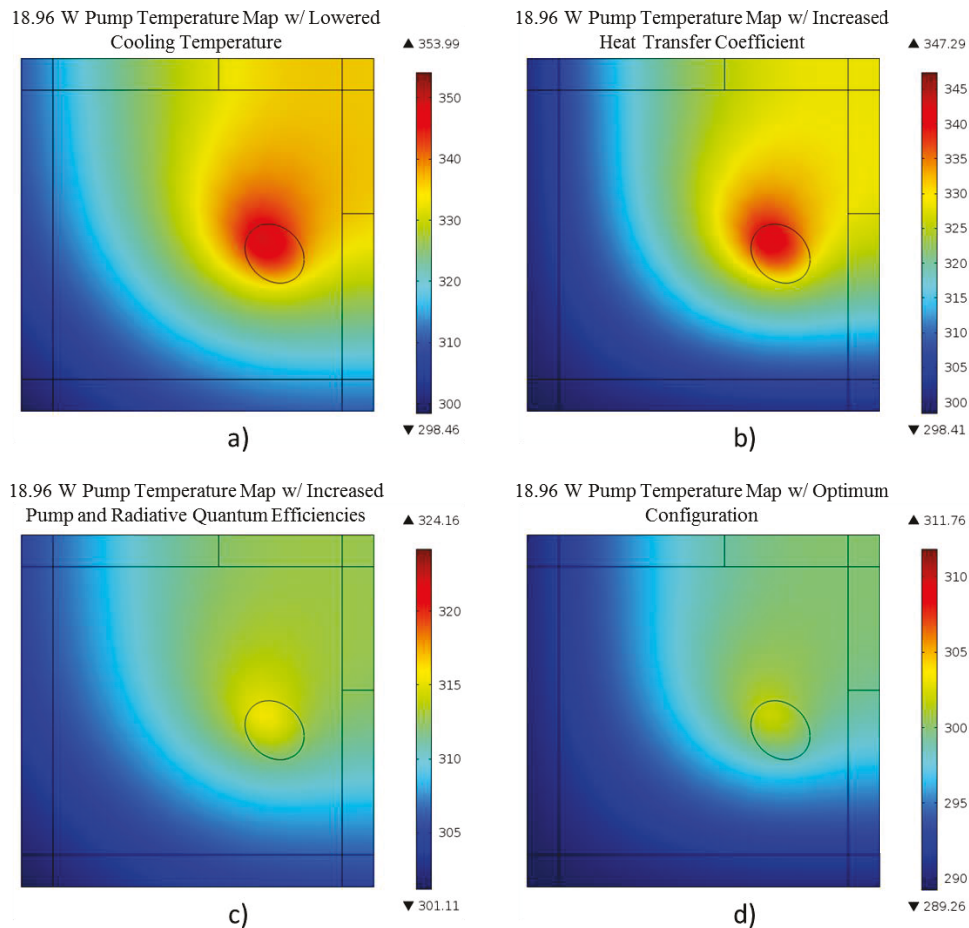


Figure 5.2-18: CW laser thermal images from simulations run with different optimised parameters, all pumped at 18.96 W. a) lowered cooling temperature of 16.0°C, b) increased heat transfer coefficient of $1.0 \text{ W}\cdot\text{cm}^{-2}\cdot\text{K}^{-1}$, c) increased pump and radiative quantum efficiencies of 0.99 respectively, and d) all of the above (a – c). Temperature scale is in degrees Kelvin.

Table 5.2-4: Changes in CW thermal simulation peak and average beam axis temperatures under different simulation configurations.

Configuration	Peak Crystal Temperature (°C)	Average Beam Axis Temperature (°C)
Unaltered	88.8	81.0
Lowered Cooling Temperature	80.8	73.3
Increased Heat Transfer Coefficient	74.1	66.7
Increased Pump and Radiative Quantum Efficiencies	51.0	46.1
Optimum Configuration	38.6	33.2

5.2.3 *Q-switching Thermal Simulations*

The final goal of the thermal model was to compare the QS experimental temperatures with simulated ones. Once simulated temperatures matched to within 4% Kelvin of the experimental ones for the non-lasing and lasing cases the results were accepted as having adequate accuracy. The percent error was larger for the QS laser cases because of the higher experimental error, especially at low temperature. It is anticipated that the QS simulations are more accurate than the experiment because of this. To see the similarities between the experiment and simulation, temperature maps, at different pump powers, of the surface at which the pump exits the crystal are displayed in Figures 5.2-19 and 5.2-20 for the cases of below and above Q-switching lasing threshold respectively. The temperature maps are oriented as demonstrated in Figure 5.1-19. The pump power simulated in the images matches to the pump power in the experimental images except for the 1.45 W (6.5 A), below threshold image. It is included for informational purposes. There are again obvious similarities between the experimental and simulated images as the temperature distribution is essentially the same. With the greater simulation resolution and no radiation trapping modelled, the peak temperatures near the pumped region are clearer than the experimental images and show a significant peak temperature in this area.

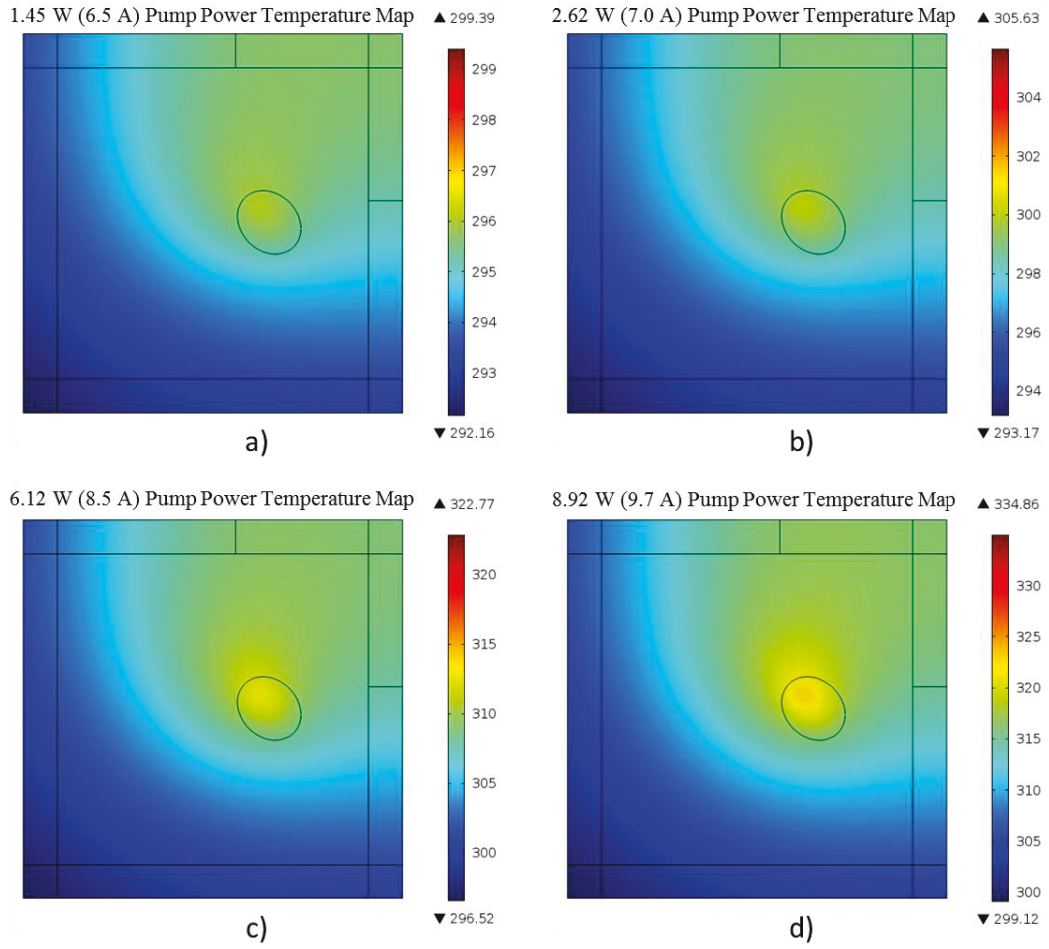


Figure 5.2-19: Thermal images from simulations run at different pump powers below Q-switching threshold. a) 1.45 W, b) 2.62 W, c) 6.12 W, and d) 8.92 W. Temperature scale is in degrees Kelvin.

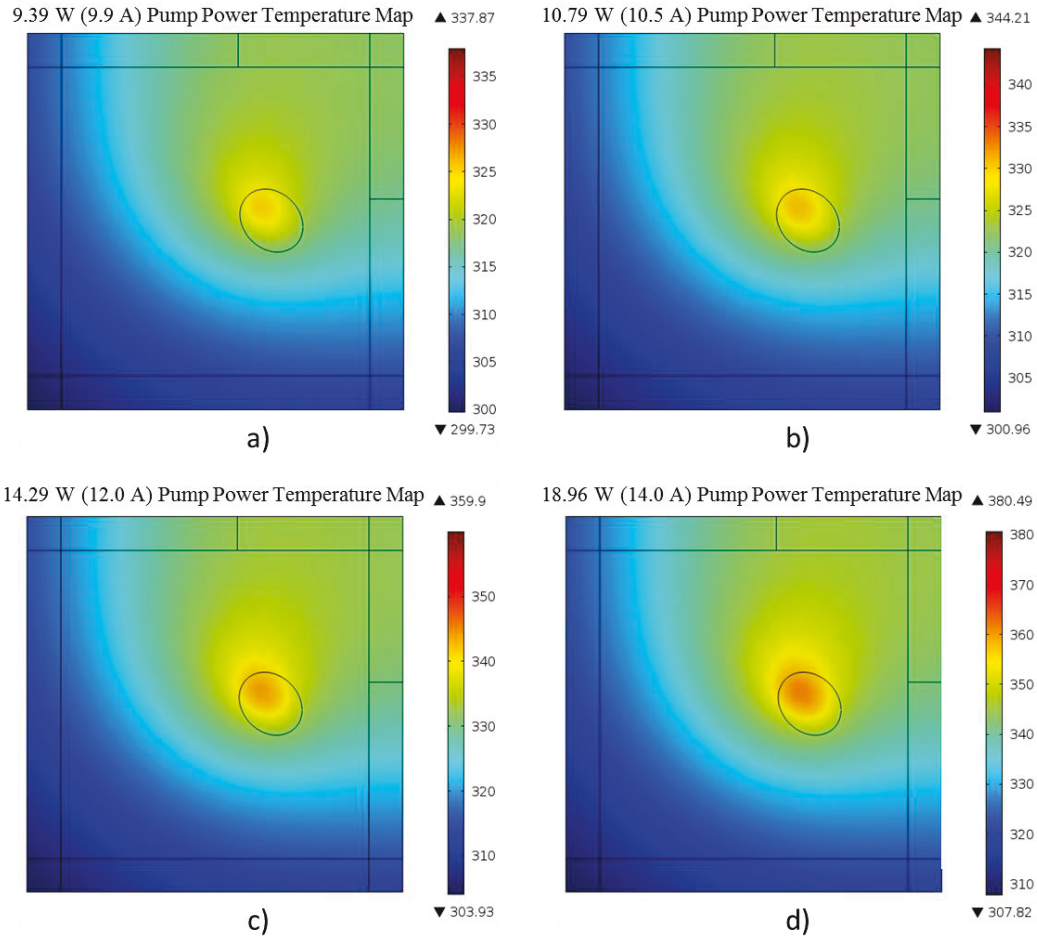


Figure 5.2-20: Thermal images from simulations run at different pump powers at and above Q-switching threshold. a) 9.39 W, b) 10.79 W, c) 14.29 W, and d) 18.96 W. Temperature scale is in degrees Kelvin.

Again to facilitate comparison between experiment and simulation, the temperatures at three points on the pump exit face of the crystal are plotted in Figure 5.2-21. These locations correspond to the same areas as for the CW laser case and are illustrated in Figure 5.2-16. They roughly correspond to the same locations as in the experimental images. The temperature trends remain very similar to the experimental results but the sharp increase in temperature at threshold does not materialize in the simulations as can be seen in the inset of Figure 5.2-21. One major difference is the much larger temperatures at the centre of the pump region and this may be due to the greater spatial accuracy of the simulation versus the experiment and a lack of radiation trapping in the model. This difference can be seen in the

inset of Figure 5.2-15. In the experiment, peak temperature occurred at the pixel one location; whereas, in the simulations, pixel two is the location of the highest temperatures. This difference is not as significant as the CW laser case because the experimental QS images were taken with higher resolution.

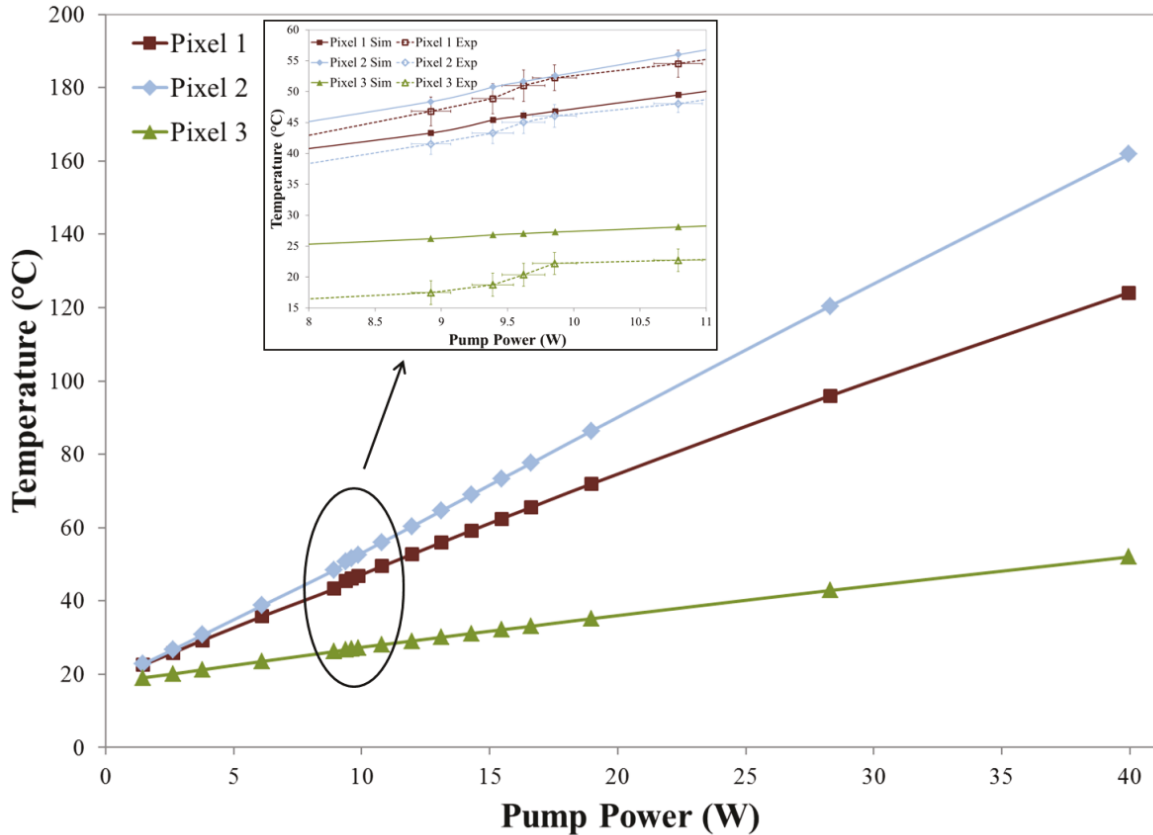


Figure 5.2-21: Simulated evolution of temperatures at specific pixel locations as pump power increases for the QS laser case. Inset detail shows a comparison of simulation and experimental data points from 8 to 11 W.

For the QS case the progression of temperatures along the beam propagation axis as pump power increases is shown in Figure 5.2-22. The temperature in the pumped region is more uniform than the CW case. In the images, the location at which the centre of the pump beam exits the crystal is defined as $x' = 0$, and so as x' increases, the position moves towards the front face. The peak temperature occurs at the input face for low pump and laser powers but as the pump and laser power increases the peak temperature shifts backwards towards the

beam waist and back face. The pump beam waist in the QS configuration was located at $x' = 0.0041$ m and the waist radius was $134 \mu\text{m}$ and $95 \mu\text{m}$ in the y' and z' directions respectively. In Table 5.2-5 the peak temperatures in the crystal are given in reference to the pump power, peak measured back-face temperature, and peak simulated back face temperature. This shows that the peak temperature can be much higher than what is determined by imaging the crystal surface.

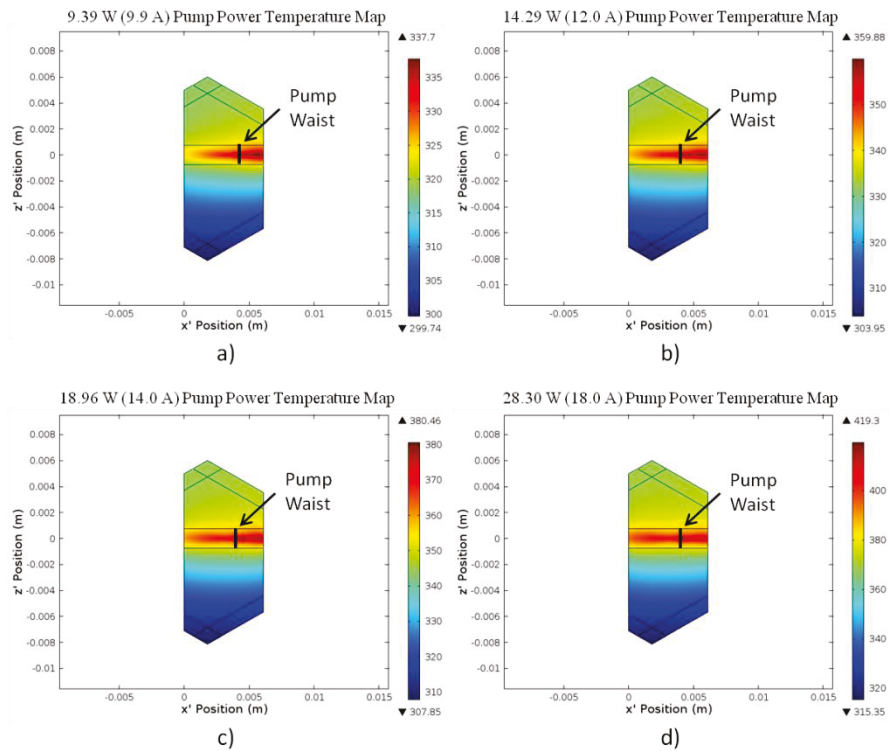


Figure 5.2-22: QS simulated distribution of temperature in Kelvin along the pump axis at a) 9.39W, b) 14.29 W, c) 18.96 W, and d) 28.30 W pump power. The pump enters from the right side and exits the crystal at $x' = 0$, i.e. the back face of the crystal. The pump beam waist location is indicated in each figure.

Table 5.2-5: Comparison of peak temperatures in the measured and simulated QS laser temperature profiles.

Pump Power (W)	Peak Measured Back-Face Temperature (°C)	Peak Simulated Back-Face Temperature (°C)	Peak Simulated Crystal Temperature (°C)
2.62	24.1	27.0	32.5
6.12	37.3	39.5	49.6
8.92	48.4	49.4	61.7
9.39	54.4	51.8	64.7
9.62	55.8	52.7	65.8
9.86	60.3	53.7	66.9
10.79	63.7	57.2	71.1
11.96	66.3	61.6	76.2
13.12	68.3	66.0	81.5
14.29	72.1	70.5	86.8
15.46	76.4	74.9	92.0
16.63	78.7	79.3	97.1
18.96	84.6	88.2	107.3

The QS thermal simulations can be modified in the same way that the CW simulations were to find the effect of optimised parameters on the crystal temperatures. It was also possible to determine the effect the changing temperature had on the QS output performance via the rate equations. In Figure 5.2-23 the temperature profiles for the same four cases as in Section 5.2.2 are shown. In terms of reduction of crystal temperature the effectiveness is ranked from lowest to highest as cases one to four sequentially. In Table 5.2-6 the changes in peak temperature and average pump beam axis temperature are compared to the original simulation for all four cases. In the optimised cooling configuration the peak crystal temperature in degrees Celsius was reduced by 72% from the original configuration. In Table 5.2-7 the comparison of each case's effect on the QS output parameters is shown. As the cooling of the crystal became more effective the output pulse energy decreased. The peak power decreased with this trend as well since the pulse duration only decreased slightly from

91.7 to 90.3 ns. Conversely, the repetition rate rose which caused a rise in average output power.

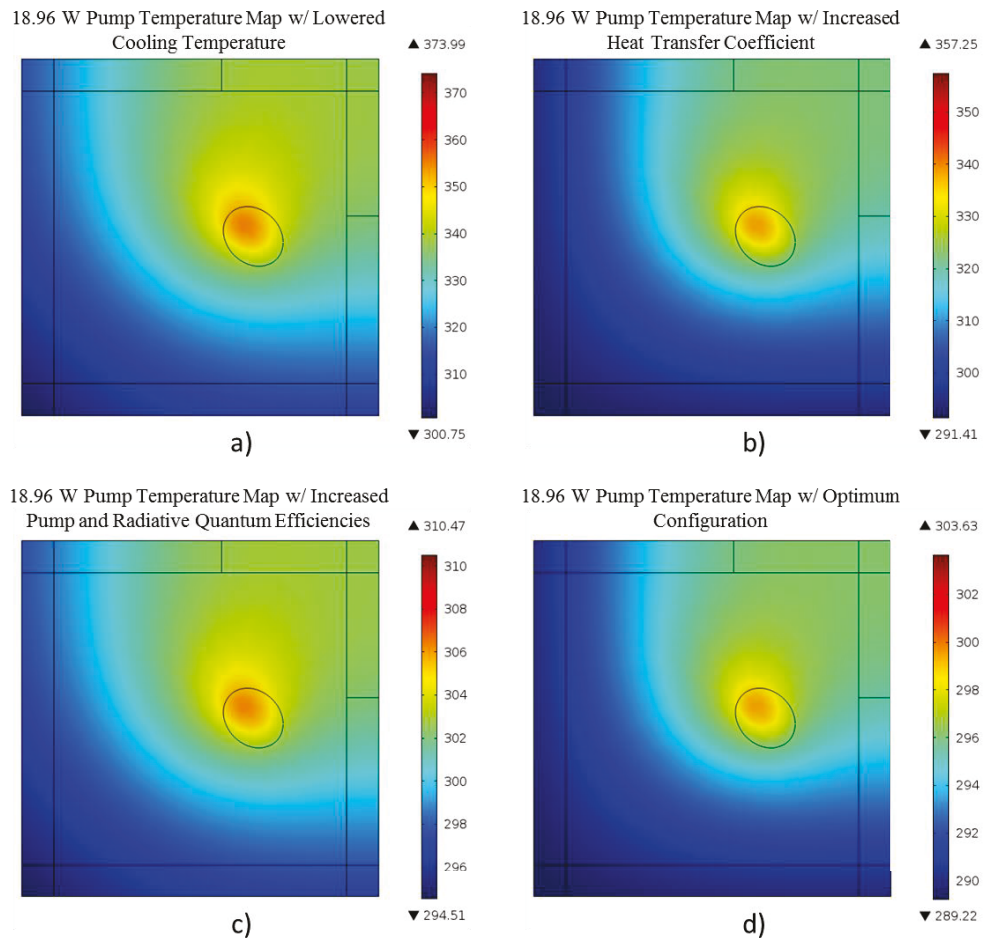


Figure 5.2-23: QS thermal images from simulations run with different optimised parameters, all pumped at 18.96 W. a) lowered cooling temperature of 16.0°C, b) increased heat transfer coefficient of $1.0 \text{ W}\cdot\text{cm}^{-2}\cdot\text{K}^{-1}$, c) increased pump and radiative quantum efficiencies of 0.99 respectively, and d) all of the above (a – c). Temperature scale is in degrees Kelvin.

Table 5.2-6: Changes in QS thermal simulation peak and average beam axis temperatures under different simulation configurations.

Configuration	Peak Crystal Temperature (°C)	Average Beam Axis Temperature (°C)
Unaltered	107.3	97.5
Lowered Cooling Temperature	100.8	90.9
Increased Heat Transfer Coefficient	83.9	73.8
Increased Pump and Radiative Quantum Efficiencies	37.2	34.8
Optimum Configuration	30.5	28.1

Table 5.2-7: QS output performance under different simulation configurations.

Configuration	Output Energy (mJ)	Max Power (kW)	Average Power (W)	Repetition Rate (kHz)
Unaltered	0.69	6.6	1.6	2.3
Lowered Cooling Temperature	0.69	6.6	1.6	2.4
Increased Heat Transfer Coefficient	0.68	6.5	1.7	2.5
Increased Pump and Radiative Quantum Efficiencies	0.67	6.4	2.0	3.0
Optimum Configuration	0.66	6.4	2.1	3.1

It is of some interest to also consider the stresses in the laser crystal induced by the temperature profile. However, the analysis presented here is by no means complete. Proper modelling of internal and external stresses and their application to the likelihood of laser crystal fracture is a complex task. The following is only given for informational purposes on the relative stress distributions inside the crystal under laser operation. The stress is presented as von Mises stress which is a value calculated from the principal stresses simulated within the material and generally gives an indication of the maximum stress at a specific point that could lead to material yielding. Figure 5.2-24 shows the maximum von Mises stresses that occurred along the edges of the crystal where the crystal was in contact with the mount. In

this situation the stress distribution was taken at 100 s and with 18.96 W of incident pump power. The two sides adjacent to the mount had fixed constraints applied to them and the clamped region had a distributed load applied to the face as described in Section 4.2.2. These stresses were exaggerated by the modelling software because the faces were fixed and the stress could concentrate in sharp corners. Since the stress was so high in the corners it is valuable to reduce the scale on the colour bar to show more detail. In Figure 5.2-25 it is seen that the stress on the pumped face of the crystal, inside the edges, transformed radially from the pumped region and increased as it approached the high stress edges. On the un-pumped faces the stress distribution changed mostly along the edge contacting the mount with fairly uniform stress on the other faces.

By removing the fixed constraint on the cooled edges, and the distributed force on the clamped edges, it was possible to see the relative stress generated inside the crystal by the laser heating alone. As can be seen in Figure 5.2-26, the maximum stress magnitude was reduced substantially. The overall distribution of stress was fairly unsymmetrical and tended to concentrate between the pumped region and its nearest crystal edge. Further study is required to completely understand these stress distributions and model them quantitatively.

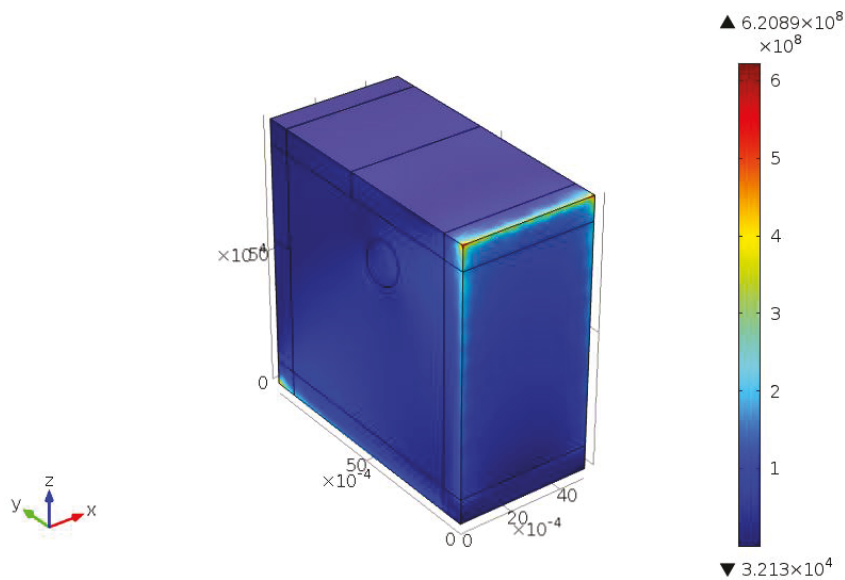


Figure 5.2-24: Stress distribution in constrained QS configuration at 100 s with 18.96 W incident pump power. Stress scale is in units of Pa.

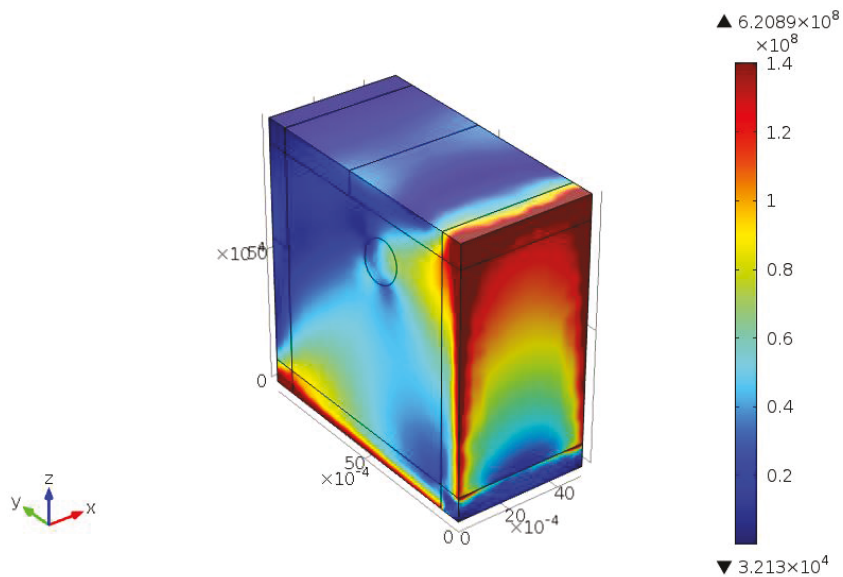


Figure 5.2-25: Stress distribution in constrained QS configuration at 100 s with 18.96 W incident pump power. Colour bar is reduced in scale to show detail. Stress scale is in units of Pa.

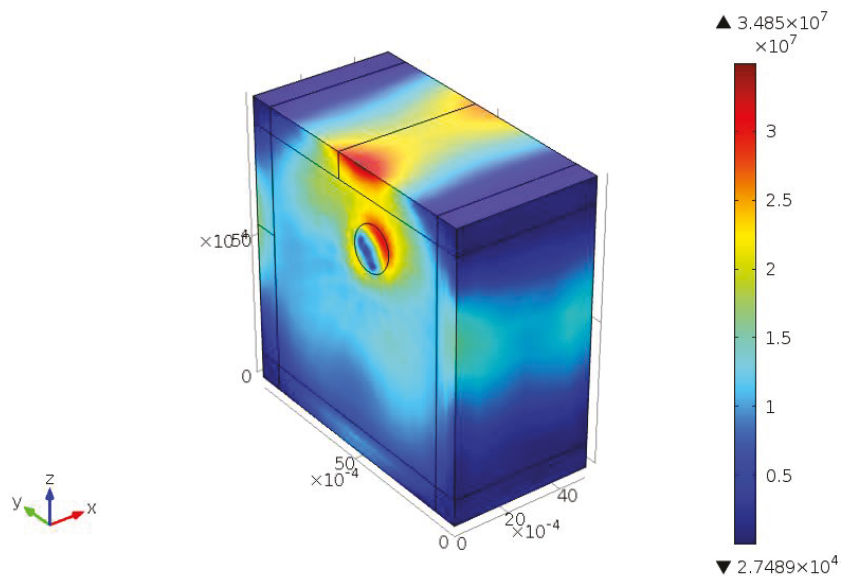


Figure 5.2-26: Stress distribution in unconstrained QS configuration at 100 s with 18.96 W incident pump power. Stress scale is in units of Pa.

Chapter 6

Discussion

The development of a Q-switched (QS) laser requires the proper evaluation of the operating characteristics to determine how well they meet application requirements. After evaluation one can carry out optimisation to create the best possible system. The ability to optimise the QS laser presented here hinges on the development of theoretical or numerical models that accurately describe the real system and the understanding of discrepancies that occur due to modelling assumptions. In the case of both the Q-switching model and the thermal model, there are several assumptions that were necessary in order to develop a model without excessive complexity. The discussion will center on understanding the current laser and how best to optimise it using the modelling. Also the benefit of developing more precise simulations is discussed. Finally, the ability of the current laser to meet the application requirements is examined.

6.1 CW Output Results

6.1.1 Comparison with Theory

With the original development of the QS laser cavity, a CW configuration was used to test and analyse different cavity configurations. The theory summarized and expanded by T. Taira et al.¹¹⁹ showed that the threshold power is strongly dependent on both the laser mode radius and the pump mode radius. Equation (6.1-1) gives the formula for threshold in the case of Gaussian pumping and Equation (6.1-2) is for the case of top-hat pumping.

$$P_{th} = \frac{\pi h \nu_p w_l^2 (1 + a^2)}{4 \eta_p \eta_a (f_1 + f_2) \sigma \tau_l} (L_i + T + 2N_1^0 \sigma l_l) \quad (6.1-1)$$

$$P_{th} = \frac{\pi h \nu_p w_l^2}{4 \eta_p \eta_a (f_1 + f_2) \sigma \tau_l} \left[\frac{2a^2}{1 - e^{(-2a^2)}} \right] (L_i + T + 2N_1^0 \sigma l_l) \quad (6.1-2)$$

$$a = \frac{w_p}{w_l} \quad (6.1-3)$$

Where η_a is the fraction of pump power absorbed in a crystal of length l_l , η_p is the fraction of absorbed pump power that contributes to the upper manifold population, σ is the laser gain cross-section in m^2 , τ_l is the upper manifold fluorescence lifetime in s, T is the transmission of the output coupler (OC), N_1^0 is the un-pumped population inversion density in m^{-3} , h is Planck's constant in $\text{m}^2 \cdot \text{kg} \cdot \text{s}^{-1}$, ν_p is the pump frequency in Hz, w_l is the average laser mode radius in the crystal in m, w_p is the average focussed pump mode radius in m, L_i is the passive cavity loss, and f_1 and f_2 are the lower and upper laser level Boltzmann occupation factors respectively. In the case of astigmatic beams, the equations change slightly with $w_l^2 = w_{l_t} \cdot w_{l_s}$ and $a^2 = \frac{w_{p_t} \cdot w_{p_s}}{w_{l_t} \cdot w_{l_s}}$. Where the subscripts t and s stand for tangential and sagittal.

The laser slope efficiency has a far more complicated relationship but generally is dependent on a , the ratio of pump to laser mode radius. Slope efficiency is directly proportional to the mode matching efficiency. A typical plot of mode matching efficiency, η_m , versus the mode waist ratio for a laser exhibiting significant reabsorption loss under top-hat pumping is shown in Figure 6.1-1. Depending on the ratio of reabsorption loss to passive cavity loss, B , there exists a value of a that produces maximum mode match efficiency, and therefore the highest slope efficiency. In the case of our 2 at.% Yb:CaF₂ laser, the ratio of reabsorption loss to passive cavity loss was approximately 0.3 and so would lie between the plots of $B = 0$ and $B = 0.5$.

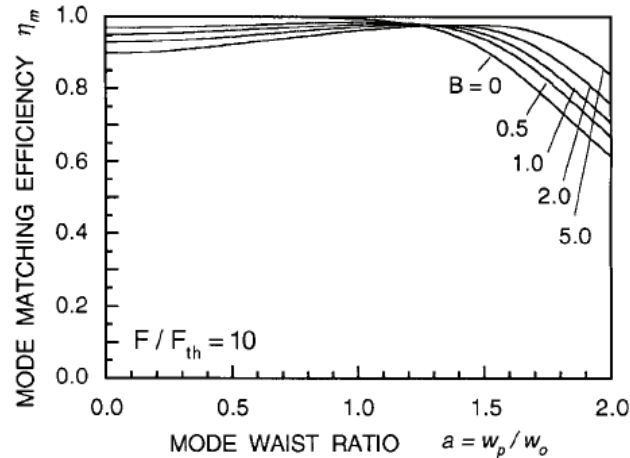


Figure 6.1-1: Mode matching efficiency for a top-hat pump distribution as a function of $a = \frac{w_p}{w_l}$ for different values of reabsorption loss to passive cavity loss ratio, B . Plots are given for pump fluence (F) 10 times greater than threshold.¹¹⁹

Using information such as the above it is possible to determine how well the laser follows the theoretical predictions. The simplest way to do this was to compare the change in CW laser thresholds to the changes in the pump and laser mode radii as was done in the three cavity configurations outlined in Section 5.1.2. These modifications to the laser cavity should also show the correct trend in the slope efficiency. The pump beam from a fibre-coupled diode laser often is approximated as a flat-top beam but in the 75:50 mm focussing configuration, as discussed in Section 5.1.2, a PCX lens was used to focus the beam. This led to a beam shape that was intermediate between Gaussian and flat-top and by using the $D4\sigma$ beam width measurement (discussed in Section 3.1) it was best to use the Gaussian pumping threshold power formula in the calculation. In the first configuration, the average mode radius inside the crystal was 170 μm , the focussed pump beam waist radius was 226 μm , and the threshold was 6.1 W. In the second configuration the average mode radius inside the crystal was 200 μm and the pump beam waist remained the same. By using this information the expected threshold was $P_{th2} = \frac{w_{l2}^2(1+a_2^2)}{w_{l1}^2(1+a_1^2)} P_{th1} = 6.9 \text{ W} \pm 0.3 \text{ W}$. This is very close to the experimental threshold of 7.0 W \pm 0.4 W and agrees within the experimental error. In terms

of slope efficiency it was expected that the efficiency would slightly increase as the laser mode radius was increased. This was anticipated because the peak mode match efficiency for a laser crystal with a $B = 0.5$ is located at a mode radius ratio of 1.1. In the first case the average mode radius ratio was 1.3 and the slope efficiency was measured to be 28.5%. In the second case the average mode radius ratio was 1.1 and the slope efficiency was measured to be 30.4%.

Once it was determined that the laser cavity was following the theory it was expected that the smaller the pump radius, the lower the laser threshold would be. In addition, the small-signal gain increases with a smaller pump radius. The downside to reducing the pump radius was the expected decrease in slope efficiency because the mode radius ratio would drop below one. By minimising the mode radius for the laser cavity this effect could be reduced. All together, the reduction of threshold would benefit the overall output efficiency significantly more than a slight reduction in laser slope would diminish it. The 50:50 mm pump configuration, as described in Sections 3.1 and 5.1.2, was chosen as the best option.

It was not possible to predict the threshold power exactly from the earlier threshold analysis as the new pump configuration maintained a better representation of a flat-top beam than the 75:50 mm configuration but it still did not perfectly represent a flat-top. Instead a range was found from using both Equations (6.1-1) and (6.1-2). By changing the average pump radius in the crystal to $113 \mu\text{m}$ and the average mode radius in the crystal to $119 \mu\text{m}$ the threshold power would become $2.0 \text{ W} \pm 0.3 \text{ W}$ according to the Gaussian prediction and $1.8 \text{ W} \pm 0.4 \text{ W}$ for the top-hat prediction. The measured threshold was found to be $3.8 \text{ W} \pm 0.2 \text{ W}$ which does not agree within error. A decrease in threshold was seen in the calculations and the experiment as was expected for a smaller pump area but the calculation predicts a more significant decrease. Because the calculations were derived from a model that does not include pump divergence, when the divergence becomes more significant it is expected that the experimental threshold would be higher than predicted. The slope efficiency did follow the expected trend and decreased marginally to 28.3%.

The theoretical results only hold if the laser operates in a TEM₀₀ mode. In Section 5.1.2 the M^2 factor was measured to be 1.0 ± 0.2 which indicates a good quality, TEM₀₀ mode beam. Further, the beam stability shown in Figures 5.1-7 and 5.1-8, suggests that there were no major instabilities or sources of noise affecting the laser.

6.1.2 Further Improvements

While the performance of the CW laser, with a slope efficiency of 27% and an optical-to-optical efficiency reaching 22.9%, was reasonable it did not perform as well as Yb:CaF₂ lasers in the literature. M. Jacquemet et al.¹²⁰ have produced a CW laser with a threshold of 2 W, a slope efficiency of 51%, and an optical-to-optical efficiency of 39% using a v-shaped cavity with an OC reflectivity of 95%. The most significant differences between their laser and ours included a shorter, 4 mm long, 5% doped Yb:CaF₂ crystal and a reduced passive cavity loss. Additionally, the pump laser emitted at 979 nm, the cavity was arranged differently, the pump was focussed with a 60:60 mm achromatic doublet pair, and the pump and laser mode radii in the crystal were 100 μm and 95 μm respectively.

The shorter but more densely doped laser crystal would significantly increase pump absorption, increase the small-signal gain, and reduce the threshold. The lower cavity loss along with the longer cavity and the slightly better mode radius ratio would have an effect on the laser slope by increasing it. The ability to pump the laser crystal closer to the absorption peak at 979 nm would increase the amount of pump absorption as well, especially since between 977 and 979 nm the slope of the absorption cross-section is moderately steep at 300 K as can be seen in Figure 1.2-1. All of these effects would have an influence on improving the performance of their laser. On top of this, as has been found in Section 4.2.2 and will be discussed further in Section 6.3.1, the crystal quality in our experiment appears to be somewhat lower than those in many publications. A poor quality crystal can lead to other loss channels for upper state ions, reducing the efficiency and raising the lasing threshold.

When moving to cryogenic temperatures, as discussed by S. Ricaud et al.,²⁶ there tends to be a large improvement in laser operation. The sharpening of the spectral lines, leading to higher peak cross-sections, enables higher gain to be achieved. In addition, the thermal conductivity of the crystal improves leading to better heat removal. With an OC reflectivity of 90% they achieved an efficiency of 65% when considering total output power over absorbed input power. This was with a 2.2% doped, 5 mm long Yb:CaF₂ crystal in a v-shaped cavity pumped at 212 W. The total output power used to calculate the efficiency included the OC extracted power as well as intracavity laser power that reflected from the slightly angled, un-coated laser crystal and escaped from the resonator. In our laser the peak efficiency, if computed using the power emitted from the OC over the assumed absorbed pump power calculated from FEA analysis, becomes 36.3%. Thus a strongly pumped, optimised laser cavity with cryogenic cooling reaches nearly double the efficiency.

With the above stated it is important to understand how we could design a better laser in the future. It is very valuable to optimise the crystal length and doping concentration; ideally pump absorption would be maximised with limited reabsorption of the emitted laser light. The ability to tune the pump wavelength to the exact absorption peak would be beneficial. Ensuring that the laser crystal also has a high pump and radiative quantum efficiency is important for maximising the useful laser power emitted for a given pump power. Mirror and crystal surface cleanliness is very important for reduced cavity loss. Finally, moving to cryogenic temperatures adds complexity to the design but would cause a significant improvement in output performance.

6.2 Q-switching Output Results and Simulations

6.2.1 Comparison of Results and Simulations

Once testing and measurement of the QS laser was complete it was apparent that the results largely fit with expectation. From Figure 5.1-10 the experimental trends of the repetition rate and average output power were essentially identical with both increasing

nearly linearly with incident pump power past threshold. Figure 5.1-11 shows the pulse energy and pulse width and both are nearly constant with changing pump power. This is again the expected result because the amount of energy extracted is related primarily to the difference between the initial and final population inversions. The initial population inversion at the instant of Q-switching is given by achieving a gain which matches the round trip losses at low cavity Q. The final population inversion occurs at the end of the QS pulse when the cavity photon density is too low to reduce the population inversion further; at this point the pump begins to repopulate the upper laser level. To first order these population inversions should not change with increasing pump power at low repetition rates. A low repetition rate in this case is defined as one where the period between pulses is longer than the SA recovery time.

In Figure 5.1-12 the QS to CW output power ratio was plotted and displays a quick increase in the ratio near threshold with what appears to be an asymptotic approach to a maximum value as pump power increases. In the low pump region the repetition rate is so low that there is a large amount of energy dissipated in the laser crystal from spontaneous emission where in the CW laser the energy would be used in the laser field. As the pump power increases the wasted energy is reduced because the population inversion can be extracted faster than it is spontaneously emitted. Once the period between pulses is considerably shorter than the upper laser level fluorescence lifetime the improvement in the QS to CW output power ratio becomes nearly negligible.

The wavelength was also measured and is shown in Figure 5.1-13. The fluctuations, which were larger than those in the CW laser, were likely due to a complex relationship between gain cross-section, population inversion, and temperature. Detailed understanding of this could be achieved through future modelling that takes effects such as temporal hole-burning and reabsorption loss into account.

As in the CW case the beam propagation factor was measured for the QS laser output. The M^2 factor was found to be nearly one which implies very high beam quality. With a high

beam quality it is possible to focus the output of the laser to very small diameters and this is useful when attempting to reach the high laser intensities required for certain applications such as producing a laser plasma for x-ray production.

While the results fit what was expected for the most part there were still discrepancies. There was a small decrease in pulse energy and a small increase in pulse width from threshold to about 1 W pump power above threshold in the experiment. This requires an explanation but first a comparison to the simulations should be made. From the simulation results, the repetition rate and average output power, shown in Figure 5.2-1, display the same, nearly linear, increase with pump power as was present in the experimental results. However, the pulse energy and pulse width, presented in Figure 5.2-2, display a considerably different trend to that produced by the experiment showing a monotonic rise in pulse energy and a monotonic fall in pulse width with increasing pump power. In many QS lasers it has been observed that the pulse energy increases and the pulse width decreases with increasing pump power.^{70,121,122} Several attempts have been made to explain these results through simulation and have achieved reasonable matching with experiment. The pulse energy and peak pulse power are primarily functions of the initial and final population inversions though peak power is also a function of the population inversion at peak photon density (called the threshold population inversion which occurs when gain is equal to the losses at high cavity Q).⁶² The inclusion of the SA recovery time causes the pulse energy to also be a function of the initial SA ground state population.¹²²

From the perspective of the simulation the major changes to the pulse width and pulse energy in the low pump region (less than 20 times threshold) occur because of two factors. First, since the SA does not turn on instantly there is time for the population to overshoot the lasing threshold and therefore increase the initial population inversion. The impact of this would increase with higher pump intensity. Second, as temperature increases with increased pump power the rate at which the inversion is reduced during lasing is modified leading to a change in initial and final population inversions. By comparing to the approximate pulse

energy and pulse width formulas generated by J. Degnan⁶² for the simplified case of fast, i.e. active, Q-switching it is possible to predict the simulated trends. The formulas are given by:

$$E = \frac{1}{f_1 + f_2} V h \nu_l (\Delta N_i - \Delta N_f) \frac{\ln\left(\frac{1}{R_2}\right)}{\ln\left(\frac{1}{R_2}\right) + L_i} \quad (6.2-1)$$

$$t_p = \tau_c \frac{\Delta N_i - \Delta N_f}{\Delta N_i - \Delta N_t \left[1 + \ln\left(\frac{\Delta N_i}{\Delta N_t}\right)\right]} \quad (6.2-2)$$

Where E is the pulse energy in J, ΔN_i is the initial population inversion density before a QS pulse event in m^{-3} . ΔN_f is the final population inversion density after a QS pulse event in m^{-3} , ΔN_t is the threshold population inversion density that occurs at the peak of a QS pulse in m^{-3} , t_p is the FWHM pulse width in s, τ_c is the cavity photon lifetime in s, V is the mode volume in the crystal in m^3 , h is Planck's constant in $\text{m}^2 \cdot \text{kg} \cdot \text{s}^{-1}$, ν_l is the laser frequency in Hz, L_i is the passive cavity loss, and f_1 and f_2 are the lower and upper laser level Boltzmann occupation factors respectively.

As pump power and temperature increase, $\frac{\Delta N_i}{\Delta N_t}$ and $\Delta N_i - \Delta N_f$ both increase leading to an increase in E and a decrease in t_p . These trends can explain the behaviour seen in the simulations but the fact that the experimental results did not exhibit the same response indicates that some aspects of the laser system were not taken into account in the model.

There are myriad small factors that affect the output performance of a laser system and simulation of all of them would be difficult. In an attempt to explain the decrease in pulse energy and increase in pulse width following threshold in the experiment it is possible to look at some of the factors that various groups have already studied. S. Voitikov et al.⁶⁶ discussed the impact that changing the pump to laser mode area ratio has on the output performance. In fact, in many of their results the pulse energy exhibited a decrease with increasing pump power. If the mode area ratio changes so too does the stored inversion, and if the initial inversion is reduced the pulse energy will decrease and the pulse width will

increase just as was seen in the experiment and is shown in Figure 5.1-11. This change in mode and pump size can be small but still lead to a noticeable shift in output. It is possible that thermal lensing (TL) caused this to occur in the experiment. Right at threshold the temperature was seen to jump on the back face of the crystal and this correlates nearly directly with the quick decrease in pulse energy and increase in pulse width. To model this effect properly in the simulations the inclusion of both the thermal lens and the pump and mode distributions would be required. As X. Zhang et al.⁶⁸ showed, by including a Gaussian shape for the mode and pump distributions there can be significant changes in the pulse width and output energy when the pump to mode radius ratio is close to one. This was without even including the impact of pump divergence.

Similar to the change in pump and laser mode area ratio, the ratio of the average crystal laser mode area to average SA laser mode area also plays a part in the initial and final population inversions.¹²¹ This can be modified by TL in both the crystal and the SA. Moreover, the temperature change can affect the losses in both the SA and the crystal. The relative change in both loss and gain within the laser cavity can modify ΔN_i , ΔN_t , and ΔN_f .⁶² If the ratio of gain to loss drops for any reason the performance of the laser will drop. A combination of all these factors could help explain the discrepancies between experiment and simulation.

6.2.2 Further Model Improvements

The subject of model limitations and assumptions has already been discussed in fair detail in Section 4.1. Additionally, in Section 6.2.1 the effects of some of these assumptions have been shown. Here the goal is to make final comments regarding the benefit of further model improvement. Firstly, accurate values for all the key parameters used in the model are required. These include the fluorescence lifetime, absorption and emission cross-section, doping concentration of the laser crystal and SA, and passive cavity loss of the resonator. Accurate values of the laser crystal Stark energy levels are also beneficial. At present these

parameters are known with an accuracy on the order of a few percent up to about 40%. The highest uncertainty occurs in determination of the absorption and emission cross-sections.

The most valuable changes to the laser model would be the addition of extra spatial dimensions. As an intermediate step, a 2D radially symmetric model representing the mode and pump radii with average values along the crystal could be developed. To entirely model the astigmatic pump and laser modes a full 3D model would be required but involves significantly more computational resources. In multi-mode fibre-coupled, laser diode pump configurations the modelling of pump divergence, included in 2D and 3D models, is especially important.¹²³ With the variation of pump and laser mode size it then also becomes possible to model TL.

To properly model the TL, having strong coupling between the thermal model and the rate equation model would be of great value. C. Li et al.⁷² developed a model of a QS laser with a longitudinally varying temperature profile and the output parameters were modified significantly by its inclusion. In general the non-uniform temperature distribution caused a reduction in laser performance and led to modified optimum parameters. With the further addition of SA temperature modelling from laser and pump beam heating, along with changes in mode area at the SA, the changes in the Q-switching performance with pump power would be modelled more accurately.

Until now the spectral component of the laser cross-sections and gain profile has been ignored. A simulation with the ability to model change in frequency with laser operation is possible. To do this it is necessary to include a summation over the wavelength region of interest within the rate equations.¹²⁴ Specifically, the effective population inversion at each wavelength and the photon density, or intracavity laser intensity, for each wavelength must be computed. With this added complexity it is possible to determine the effects that hole-burning and population inversion would have on the frequency of emitted radiation.

Beyond these changes one can then look at a full-wave propagation model of the laser. With these additions the model would be indicative of the major dynamics present in the laser. Because the purpose of the simulation was not to understand every detail about the laser operation, but to give initial predictive capabilities in order to optimise the laser for future development, only the major parameters were considered in the present simulations.

6.2.3 Experimental Optimisation

Before looking at the simulated parametric optimisation it is still possible to make comments about potential improvements to the design of the QS laser. A major issue with QS laser development was the damage of laser cavity elements. The main cause of this was low damage threshold coatings applied to the optics such as AR coatings on the original SAs and the dielectric coating on the dichroic mirror. With any additional dust or hydrocarbons deposited on the surface of these components from operation in air the damage threshold can be reduced even further. To avoid damage it is possible to ensure that components are very clean when placed in the laser cavity, to use optics with higher damage threshold ratings, and to modify the laser mode radius inside the resonator to decrease the laser intensity at sensitive surfaces.

Crystal cracking was also an issue in early laser development. When pumped at high intensity, or with a sudden change in pump intensity, cracks sometimes formed extending from the pumped region of the crystal to the crystal edge. These were certainly a result of thermal stress applied to the crystal. From study of the problem it has become apparent that by using a high quality crystal and a proper cooling configuration the likelihood of damage can be reduced. It has also been found that the use of circular rather than square crystals and crystals with a doping concentration below 3% has improved the damage resistance of Yb:CaF₂.¹²⁵ To further delve into this issue a proper crystal stress and fracture model should be created, and it would improve our understanding of how best to mitigate crystal damage. Recent work with CaF₂ ceramics have shown that the optical properties are near or identical to monocrystalline materials but with improved hardness and fracture strength.¹²⁶ The use of

Yb:CaF₂ ceramic materials as a gain medium may increase the robustness of the laser to thermal effects.

Keeping in mind the issues of component damage, using the simulations in Section 5.2.1 it is possible to improve the overall QS laser design. There are some specific trends in Figures 5.2-5 to 5.2-12 that are worth mentioning. As can be seen from Figure 5.2-11, the average output power and repetition rate were most strongly affected by the pump mode radius. The change in doping concentration and crystal length, shown in Figures 5.2-7 and 5.2-9, also have a significant impact on the average power and repetition rate. These three factors must be taken into account carefully because the magnitude of the changes may not be identical to that shown. As explained previously in Section 5.2.1, this is due to assumptions that were made in the model. Regardless, the figures should be indicative of the qualitative trend. As displayed in Figure 5.2-12, the cavity loss was a significant factor for the average output power, leading to a decrease with increased loss. The repetition rate too was affected by this but not as strongly.

Of interest is the effect the OC reflectivity had on the average output power. In Figure 5.2-5 the combination of shifts in the repetition rate and output pulse energy caused the peak average power to be located at 93% reflectivity rather than at either extreme. Repetition rate, on the other hand, monotonically increased as OC reflectivity increased. Finally, the SA unsaturated transmission modified the repetition rate substantially and the average power somewhat less so, as revealed in Figure 5.2-6. If average output power, and therefore laser efficiency, is the greatest concern then decreasing the mode and pump areas, and the passive cavity loss; increasing the SA unsaturated transmission, the dopant concentration, and the laser crystal length; and optimising the OC reflectivity will produce the best results.

The parameter that had the most impact on the output pulse energy was the laser mode radius, as shown in Figure 5.2-11. Modification of the OC reflectivity and the SA unsaturated transmission also caused significant changes in the pulse energy, as demonstrated in

Figures 5.2-5 and 5.2-6. As with the average power, the pulse energy increases with decreasing passive cavity loss as displayed in Figure 5.2-12. If maximising pulse energy is the primary goal then an increased laser mode area, and a decreased SA unsaturated transmission and passive cavity loss with an optimised OC reflectivity will provide the highest performance.

The pulse duration was more invariant to the operating parameters than the other output properties. From Figures 5.2-6 and 5.2-10 the major influence on the pulse width comes from the SA unsaturated transmission and the laser cavity length. A decrease in the pump mode size also contributes somewhat to a decrease in pulse width as indicated in Figure 5.2-11. To reduce the pulse width it is best to decrease the cavity length, the SA transmission, and the pump radius. Pulse energy and pulse width define the peak pulse power so optimisation of both is required when peak pulse power or peak focussed intensity is of greatest concern. When increasing the size of the laser and pump modes simultaneously, pulse energy increases but so too does the pulse width as can be seen in Figure 5.2-11. With respect to maximised pulse power, when compared, the increase in pulse energy outweighs the increase in pulse width.

The simulation of possible optimised QS laser schemes and comparison of our Yb:CaF₂ QS laser to other similar laser systems in the literature will be presented in Section 6.4.

6.3 Thermal Results and Simulations

6.3.1 *Comparison of Results and Simulations*

The results from the thermal experiments and simulations elucidate some interesting information about the Yb:CaF₂ crystal used in the laser. The most unexpected result was the low values determined for the radiative and pump quantum efficiencies, 0.88 and 0.94 respectively. These values were necessary to replicate in the simulations the high temperatures found in the experiment. Likewise, the low value for the heat transfer coefficient from the crystal to the cooled mount was undesirable but helped to explain the

high crystal temperatures, the elevated cooled crystal edge temperature, and the structure of the thermal gradient. These three findings point to two factors that can be controlled more carefully. The crystal quality is more difficult as it requires the manufacturer to produce an adequate crystal but this is a possibility. The quality of the thermal contact between the crystal and mount is not trivial but it is an aspect of the laser system that is entirely dependent upon the designer and can be significantly improved.

In general, the experimental temperatures determined from the CW lasing configuration followed expected trends. As can be seen from Figure 5.1-20, through the non-lasing phase the temperatures on the pump exit face of the crystal increased relatively linearly until threshold where a jump increase occurred, most noticeably for pixel one in the top-right corner of the crystal. After threshold the slope of the temperature rise flattens to some extent. The relationship between the greater slope pre-threshold and the lesser slope post-threshold may be explained by two effects, pump absorption saturation and laser extraction efficiency.

In the first effect, when lasing does not occur the fractional pump absorption drops as pump power is increased due to saturation, i.e. bleaching, of the crystal. Once lasing threshold is reached, the optical field in the laser cavity reduces the population inversion and causes an overall increase in the lower manifold population. This produces a higher fractional absorption within the laser mode volume. If this were to happen in isolation, the slope of the temperature rise should actually increase once threshold is reached. Counteracting this effect is the increase in laser extraction efficiency as the intracavity laser power increases. Equation (2.2-11) can be used to demonstrate that as the laser extraction efficiency increases, the fractional heat load within the laser mode volume decreases when using our calculated radiative efficiency (η_r) of 0.88. This is because the product of η_r and fluorescence quantum defect $\left(\frac{\lambda_p}{\lambda_f}\right)$ is lower than the value of the lasing quantum defect $\left(\frac{\lambda_p}{\lambda_l}\right)$. The effect of the reduced fractional heat load appears to be stronger than the increased pump absorption and this causes a decrease in the slope of the temperature rise post-threshold. It is possible to see

a slight negative curvature in the temperature rise as well and this may be explained from the laser extraction efficiency continuously increasing as output power increases and the increase of the radiative heat transfer rate at high temperatures. It is interesting to note that if the radiative quantum efficiency was found to be higher, the fractional heat load could increase under laser operation, as was found in Yb:CaF₂ by J. Boudeile et al.³⁰ This would lead to a larger slope post-threshold than pre-threshold but also to an overall decrease in absolute temperature.

In the paper by J. Boudeile et al. they compared the heat generated in a 2.6 at.% doped Yb:CaF₂ crystal under lasing and non-lasing conditions. With 83 W of fibre-coupled diode laser pumping at 980 nm, focussed to a 200 μm radius spot, the peak, front (pump entrance) face temperature reached was 82°C with laser operation and 67°C without laser operation. To explain this result they assumed a pump quantum efficiency of unity and found the radiative quantum efficiency to be 0.993. With current results for our Yb:CaF₂ laser, temperatures substantially greater than this would be expected for a pump power of 83 W. The main difference between J. Boudiele et al.'s procedure and ours is that they measured the front face of their crystal while we measured the back (pump exit) face. However, from the results of our simulations the same temperature trends are present between the front face and back face with increasing pump power.

In the CW laser simulations the decrease in the slope of the temperature rise beyond laser pump threshold can be seen in Figure 5.2-15 and occurs similar to the experimentally measured trends discussed above. The simulation does not show quite as strong a decrease in slope after threshold possibly because in the experiment the radiative heat transfer rate of the crystal was increasing with increased temperature and in the simulation it was constant. In part, the lack of temperature dependent variables in the simulation introduced larger differences between simulated and experimental temperatures as the temperatures rose. These differences are shown in Table 5.2-3 where the measured and simulated temperatures are compared. At threshold (4.03 W pump power) the measured temperatures exceed the

simulated ones but the simulated temperatures rise faster and exceed experimental values at 14.3 W of pump power. A second effect that has the potential to cause this disagreement between experimental and simulated results is fluorescence, or radiation, trapping.

Fluorescence trapping is a significant effect in quasi-three level lasers due to the lower laser level's proximity to the ground state. Fluorescence is emitted from Yb:CaF₂ in all directions when pumped and it can be reabsorbed before it escapes from the crystal. It then either undergoes non-radiative decay or is re-emitted at a longer wavelength. In either case the process adds to the heat load and leads to a dispersive transport of heat. Since the heating of the crystal increases with radiation trapping the determination of the pump and radiative quantum efficiencies in the simulations, as discussed in Section 4.2.3, could be skewed to lower values than were necessary in order to explain the experimental results. This would then produce an inflated value for the fractional heat load, given by Equation (2.2-11), and could be a factor in the disparity between simulated and experimental temperature rises.

Further evidence that fluorescence trapping might be a significant factor can be seen below in Figure 6.3-1 where the simulated and experimental back (pump exit) face temperature maps are compared at a pump power of 19 W. Temperature distributions for the simulations and experiments were found to be similar in both the CW and QS cases but the simulations show an obvious peak temperature in the pumped region of the crystal which is not apparent in the experimental images. Rather, the experimental images show a more diffuse temperature profile near the pumped region. The imaging resolution of the experiment is likely one factor here; illustrated by the QS experiment where imaging resolution was improved and consequently the hot spot became more clearly defined. A second probable explanation for the smearing out of the hot spot in the experiments is radiation trapping. Using the effective absorption cross-section values for a temperature of 333 K from J. Körner et al.⁵⁵ it is possible to calculate the penetration depth of the fluorescence radiation. The spontaneous emission extends from approximately 970 nm to 1044 nm with an average wavelength of 1008 nm. Assuming 2 at.% Yb-doping, the bulk

penetration depth ranges from 0.35 cm at 979 nm to 15.15 cm at 1044 nm. As an example, with considerable fluorescence expected at 979 nm, which has a penetration depth of 0.35 cm, a good portion of this radiation could be trapped in a $1 \times 1 \times 0.5 \text{ cm}^3$ crystal and decay into heat. This has the potential to change the thermal model significantly.

By looking once again at the experimental results, further evidence for radiation trapping can be seen. In a pumped laser crystal, fluorescence increases until lasing threshold is reached at which point it remains constant. Because of this, when pumping below laser threshold the hot spot at the centre of the pumped region would be very difficult to see but above threshold, with a large enough increase in pump power, the hot spot would begin to show up. In the QS laser thermal measurements, displayed in Figures 5.1-22 and 5.1-23, the hot spot becomes more well-defined as pump power increases beyond threshold. The CW images do not show this phenomenon very well due to low image resolution but at the highest pump powers it is possible to see temperature start to peak in the pumped region. If the thermal models were to take this radiative trapping into account the images might resemble experimental ones more closely.

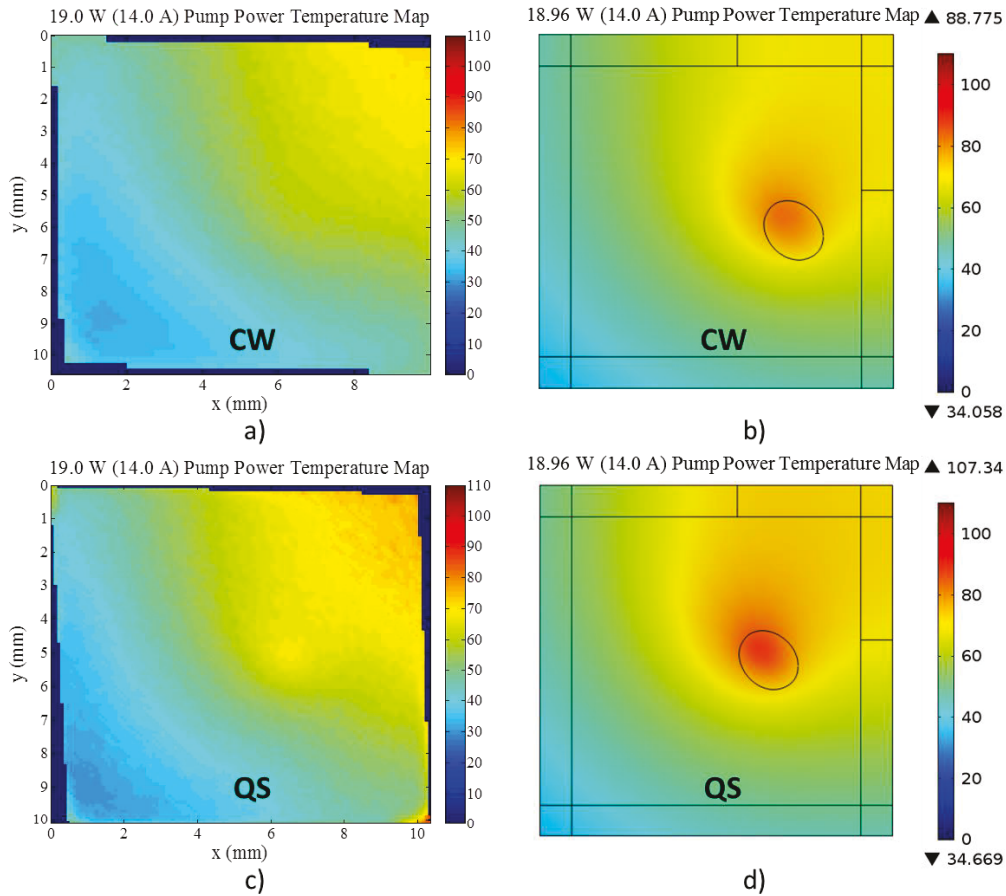


Figure 6.3-1: Comparison of simulated and experimental thermal images at 19 W pumping. a) CW thermal measurement, b) CW thermal simulation, c) QS thermal measurement, and d) QS thermal simulation. Temperatures are in degrees Celsius.

While much of the experimental and simulated results were in reasonable agreement a particularly significant difference between simulated and experimental temperature profiles arose at threshold. The jump increase in temperature on the back (pump exit) face of the crystal right at threshold, noticeable in Figure 5.1-20, did not materialise in the simulations. It is apparent that the simulation did not model the dynamics properly in this region. To more completely model the underlying physics of this situation it would be necessary to both replicate the spatially dependent population inversion that occurs within the laser crystal and to include laser reabsorption. It is expected that this might reproduce most of the temperature increase seen in the experiment.

Laser reabsorption is an effect that causes the stimulated laser radiation to be absorbed in the bulk of the crystal in much the same way as fluorescence trapping. In the presence of a less than unity radiative efficiency, laser reabsorption would increase the thermal load. The effect of reabsorption on the thermal load would be more apparent at low to moderate laser intensities where the laser extraction efficiency is low and therefore the fractional heat load is high. This effect by itself would cause an increase in temperature in the threshold region and to a lesser extent post-threshold. When combined with a longitudinally non-uniform population inversion, laser reabsorption also results in transport of heat from one part of the crystal to another.

The non-uniform population inversion develops because the magnitude of the pump absorbed per unit length drops as it propagates through the crystal which results in a positive population inversion developing near the front of the crystal and a negative population inversion occurring near the back of the crystal. Looking at the simulated pump axis thermal images in Figure 5.2-17, at low pump power, it is possible to see the pump absorption profile directly represented by the temperature magnitudes. As pump power is increased the pump intensity gets very high at the focus and causes the pump absorption to decrease in this region. This results in more pump power absorbed in the crystal towards the back face (where the pump exits) and is indicated by the shift of the peak temperature along the pump axis toward the back face. If laser reabsorption had been modelled in the simulations the heat would be more effectively transported along the pump axis to the back side of the crystal, especially at laser threshold, because reabsorption is much stronger in the negative inversion region. This steep increase in temperature would taper off as the pump power continued to increase because more of the pumped region's population inversion would become positive and heat transport would be reduced just as is indicated by the experimental results plotted in Figure 5.1-20.

In the QS thermal model some reabsorption effects along the pump axis can actually be seen in Figure 5.2-22. Reabsorption during a QS pulse was modelled in the thermal

simulations and even though the pulses occur with a low duty cycle the reabsorption is evident by the uniformity of the temperatures along the pump axis as pump power increases. A comparison between the experimental and simulated pixel temperatures on the back face of the crystal with pump powers at and just above laser threshold is shown in the inset of Figure 5.2-21. A noticeable temperature increase near threshold does occur in the simulation; however, if a spatially dependent population inversion were included in the QS thermal model, as discussed above for the CW model, the temperature rise at the back face of the crystal might more closely resemble the experiment.

Despite some modifications between the CW and QS thermal models, the two results followed similar trends. So too did the experimental results. Both configurations displayed a greater rise in temperature with increased pump power before laser threshold than after. They also both demonstrated a jump increase in temperature right at threshold. The above discussion is as relevant for the QS case as it is for the CW case. One additional, very noticeable, discrepancy between the measured low temperature values and the simulated ones was present in the QS configuration. This was purely an experimental error as the QS and CW experimental results should have been nearly identical at low pump powers. As mentioned in Section 5.1.5, the calibration was not done to a low enough temperature and may have been taken before the coolant temperature equalised causing shifts to the measured temperatures in the experiment.

Instead of only comparing between experimental and simulation results it is also possible to compare between the temperatures reached in the QS model versus the CW model for similar pump powers. From both the simulation and experimental results, the average temperature of the laser crystal under QS operation was higher than under CW operation for pump powers above Q-switching threshold. For example, at 14.29 W pump power the experimental, peak, back face temperature was 72.1°C and 62.9°C for the QS and CW cases respectively. Simulated values were 70.5°C and 66.7°C respectively. The reason for the higher temperature is revealed by looking once again at the pump absorption and fractional

heat load. Firstly, in CW operation the pump absorption stays constant in time. In QS operation the pump absorption is modulated with time. When averaged, the crystal absorbed more pump in QS operation than CW. Secondly, the reduction in fractional heat load from laser action is nearly negligible for QS operation because of the low duty cycle. Therefore, the heat load is higher for the QS laser than the CW laser.

6.3.2 Further Model Improvements

The assumptions used in developing the thermal model and its limitations have been discussed in detail in Section 4.2. If the model were to be further improved to more accurately represent experimental conditions some of these assumptions and limitations would have to be removed. Firstly, a 2D radially symmetric or full 3D rate equation model coupled to the thermal simulation would provide a more accurate description of the laser mode photon density, and the spatially and temporally dependent population inversion. This would allow for proper accounting of the laser reabsorption and longitudinal heat transfer. Secondly, the addition of fluorescence and trapping within the bulk of the laser crystal would provide some additional heating and a spread of the peak temperatures surrounding the pump axis.

There are additional aspects of the model with less impact than the effects above, but still with reasonable influence on the simulation results. The largest of these is the temperature dependence of material parameters and boundary condition coefficients. This has already been described in Section 4.2.5. TL has been ignored entirely from the modelling, mainly due to its very low impact. When modelling very high pump powers, where the temperature elevation in the pump region becomes significant, the TL effect would need to be considered. The TL effect for Yb:CaF₂, from its negative thermo-optic coefficient, would cause the focal spot of the pump beam to be located further from the input face. The mode size would also change within the crystal.

The uncertainty in physical parameters for each individual crystal should also be considered. The most significant parameters are absorption and emission cross-sections, radiative and fluorescence lifetimes, and dopant density. In addition to these parameters one would like an accurate determination of the thermal conductivity, the heat transfer coefficient (HTC) for thermal paste to aluminum, and the exact Stark energy levels.

The mechanical properties have so far been left out of the discussion. Another logical step in the development of the thermal modelling is to accurately model the stresses occurring in the crystal. This requires an accurate model of the mount and clamping conditions including material properties and applied force. The FEA mesh would require refinement to accurately model the stress concentrations in the sharp edges of the crystal. It would also be necessary to understand the mechanisms of crystal fracture in order to classify what magnitude of stress would lead to damage. Potentially the most difficult aspect would be to verify the model in order to obtain confidence in the results. This would be either through comparison with literature or through experimental evaluation.

6.3.3 Experimental Optimisation

Beyond understanding the heating mechanisms of a laser crystal and modelling them accurately, it is important to use this information to suggest improvements to the design of the QS laser. The most relevant information for this comes from Section 5.2.3 where four different cooling configurations were simulated. Figure 5.2-23 shows the simulated temperature maps of the back face of the crystal, and Tables 5.2-6 and 5.2-7 give the temperatures and simulated QS output performance for the different cooling configurations. From this information it appears that using a high quality crystal with near unity pump and radiative efficiencies is the number one way to mitigate high crystal temperatures. If crystal quality is an issue it can be improved by using very high purity Yb^{3+} in the melt which reduces the Tm^{+3} and Er^{3+} impurities. These impurities, when present, can be coupled with the excited state of Yb^{3+} and then lead to radiative and non-radiative losses.⁴⁶ In fact, visible phosphorescence occurs during pumping of the crystals used and this is indicative of excited-

state absorption in the impurity ions. Other factors affecting crystal quality include the presence of crystal defects that might arise during crystal growth and the possibility of Yb^{2+} occurring in the lattice.¹²⁷ The existence of either of these could trap electrons and lead to reduction in efficiencies. In the literature some of the $\text{Yb}:\text{CaF}_2$ crystals utilised have a near unity pump quantum efficiency and a very high (~ 0.99) radiative quantum efficiency.^{30,55} Consequently, the temperatures reached in their crystals would likely have been lower.

In addition to improving the crystal quality, enhancement of the crystal cooling is a very important factor in the laser design. To do this requires care in the design of the mount. If the sides of the mount in contact with the crystal are not parallel with the crystal edges and have appreciable roughness then the surface contact will be poor. To some extent the thermal heat grease should fill the gaps but the grease should be new and applied so that a uniform thickness covers the whole edge of the crystal. It may be beneficial to mount the crystal in a circular enclosure, machined very accurately to match the crystal, to enable cooling on all sides. This would prevent any side of the crystal from being heated unevenly and accordingly avoid concentrating stress in particular areas. In addition to accurate machining, the thermal expansion of the mount would need to be matched to that of the $\text{Yb}:\text{CaF}_2$ crystal.

If proper cooling cannot be obtained with heat grease, or if surface contamination might be an issue, it may be best to use a thin layer of graphite. This will provide more uniform cooling than a bare contact and should have a higher HTC than calculated in the current experiment.⁷⁷ Indium, while maintaining better heat transfer than graphite, requires significant pressure applied to make a high quality contact. With a stress model it would be possible to predict if the improved HTC of indium and higher applied load on the crystal would provide more or less of a benefit in terms of crystal fracture.

Reducing the temperature of the mount, and limiting the length of metal from the cooling water to the crystal itself, would also produce better cooling. This is a minor effect compared to the first two unless moving into low temperature regimes which require the additional effort of using a vacuum chamber to eliminate condensation on the crystal faces. Though it

may be a minor effect, it is also the easiest to implement as long as temperatures do not drop below the dew point.

To determine the value of reducing the temperature to as low as possible the response of the laser must be considered. In Table 5.2-7 the changes in QS laser output are correlated to the change in temperature. If the goal is to produce the highest average output power and repetition rate then reducing the temperature is a good method to optimise this.

6.4 Feasibility for X-ray Generation

Lasers used for generation of soft x-rays need to have pulse intensities in the $10^{11} - 10^{14} \text{ W}\cdot\text{cm}^{-2}$ range.^{89,90} It is also beneficial to have repetition rates on the order of 100 Hz or higher for a faster rate of data accumulation and particularly for imaging. The current experimental Yb:CaF₂ laser produces pulses with a peak power of 7.9 kW and repetition rates that exceed 100 Hz. To use this system to generate x-rays the 1047 nm laser light would have to be focussed to a focal spot of 1.6 μm radius or smaller. This is feasible since the laser beam quality is high for the output beam. Using an f/1.0 lens it would be possible to focus the laser beam to nearly a 1.4 μm radius. However, focussing to such a small spot for 10's of nanoseconds would probably produce a quasi-stationary, spherical ablation plasma on the order of 10's of microns which would act as a significant energy loss and cool the irradiated spot. It is not clear whether the irradiated spot would be hot enough to emit water window (WW) x-rays. It might be expected that such a small spot size would not produce a large amount of x-ray emission and generally in literature the spot sizes have been about 7-10x greater. Accordingly, it is not likely that the current Yb:CaF₂ QS laser would act as an appropriate LPP x-ray source. There is the possibility, however, that with optimisation a more appropriate laser source could be designed.

By using the parametric results from Section 5.2.1 it is possible to optimise the various design aspects of the laser resonator to produce laser pulses with higher peak power. From the discussion in Section 5.2.1 the pump and laser mode volume geometries were not

properly represented since a plane wave without divergence was assumed. Because of this the pump to laser mode area ratio was not modified in the optimisation. In addition, changing the laser crystal doping concentration and length may lead to the effects of beam divergence and reabsorption, which were not fully modelled, becoming more significant, so these parameters were also left unaltered from the experimentally-matched simulations. It was assumed in the optimisation that the laser components can fit into the laser cavity, laser operation would be done in vacuum with very clean optics, and the dichroic mirror (DM) and OC would have a laser damage threshold of at least $10 \text{ J}\cdot\text{cm}^{-2}$. The damage threshold for Yb:CaF₂ is $52 \text{ J}\cdot\text{cm}^{-2}$ and for Cr:YAG it is greater than $5 \text{ J}\cdot\text{cm}^{-2}$.^{29,128} Damage thresholds are given for 10 ns pulse durations at a wavelength of 1064 nm.

The most impact on the output energy and pulse width were the OC reflectivity, SA unsaturated transmission, and cavity length. The change in cavity length and resonator design would lead to changes in laser and pump mode area which also has a major effect on pulse energy. Decreasing both OC reflectivity and SA unsaturated transmission increases the output energy substantially. A decrease in SA transmission is notably more effective at also decreasing the pulse width; therefore, the decrease in SA transmission took precedence over the decrease in OC reflectivity. Conversely, with too large a decrease in SA transmission without a decrease in OC reflectivity, large circulating intracavity energy can build up and damage the laser components. Consideration of these relationships was necessary because as the useful loss of the system increased, at some point the delivered pump power was not enough to reach lasing threshold.

An optimised QS laser was considered and the operating parameters are provided in Table 6.4-1. The same pump to laser mode area ratio as the experimental laser was maintained but the size of the laser mode area was increased through the use of a different resonator layout. A concentric resonator design was developed with a 60 mm radius of curvature DM and OC at either end. The length of the laser cavity was 124.1 mm. This design causes the resonator to be operated very near the stability limit. The OC reflectivity

and SA unsaturated transmission were decreased until an intracavity laser fluence just below the minimum element damage threshold was obtained. The simulated fluence on each element in the cavity is given in Table 6.4-2. The peak circulating energy before damage was 47.7 mJ where the limiting component was the SA. The passive cavity loss also had a noticeable effect on the output performance and so was lowered to 2% which is a reasonable loss for an optimal laser. Pump power was restricted to 85 W because crystal fracture could occur at higher powers with the simulated pump mode radius. The average temperature of the laser crystal was set to 360 K which is possible to achieve under optimised cooling conditions.

It was also of interest to determine the effect thermal lensing (TL) had on cavity stability and output performance. A thermal lens focal length of -100 mm was considered. TL caused a decrease in cavity performance because the cavity mode size decreased. The limiting laser damage threshold was for the DM at an intracavity energy of 22.3 mJ. Thus, for this operating regime TL is to be avoided as much as possible. A comparison of the output performance between the simulation with and without TL is given in Table 6.4-2.

Table 6.4-1: QS rate equation input parameters for peak output power optimisation with and without the effect of thermal lensing.

Input Parameter	No TL	TL
Pump Power (W)	85	85
OC Reflectivity (%)	84.0	80.0
SA Unsaturated Transmission (%)	92.0	94.5
Laser Cavity Length (cm)	12.4	12.4
Avg. Crystal Laser Mode Area ($\times 10^{-4} \text{ cm}^2$)	9.66	7.74
Avg. Crystal Pump Mode Area ($\times 10^{-4} \text{ cm}^2$)	15.7	12.6
Avg. SA Laser Mode Area ($\times 10^{-4} \text{ cm}^2$)	84.0	63.3
Crystal Temperature (K)	360	360
Passive Cavity Loss (%)	0.02	0.02

Table 6.4-2: QS output performance for peak output power optimisation with and without the effect of thermal lensing.

Output Parameter	No TL	TL
Peak Output Power (kW)	187.4	81.3
Output Pulse Energy (mJ)	8.11	4.93
FWHM Pulse Width (ns)	37.9	52.9
Average Output Power (W)	6.33	5.95
Repetition Rate (Hz)	781	1205
Internal Circulating Energy (mJ)	46.5	22.1
Max Crystal Fluence ($\text{J}\cdot\text{cm}^{-2}$)	46.5	26.1
Max SA Fluence ($\text{J}\cdot\text{cm}^{-2}$)	4.9	3.1
Max DM Fluence ($\text{J}\cdot\text{cm}^{-2}$)	9.4	9.9
Max OC Fluence ($\text{J}\cdot\text{cm}^{-2}$)	9.4	5.9

In order to reach focal spot intensities of $2 \times 10^{11} \text{ W}\cdot\text{cm}^{-2}$ the focussed spot radii would have to be $3.6 \mu\text{m}$ if a thermal lens focal length of -100 mm is present in the cavity and $5.5 \mu\text{m}$ if TL is not considered. From this analysis it appears feasible for a QS Yb:CaF₂ laser to generate soft x-rays from a nitrogen-based source. In 2012 M. Crank et al.⁸⁹ showed that they could generate both 2.48 nm and 2.88 nm x-ray emissions from a solid boron-nitride target with laser intensities as low as $2\text{-}3 \times 10^{11} \text{ W}\cdot\text{cm}^{-2}$ at 1064 nm . In their setup an Nd:YAG laser with pulse durations of 6 ns was used and the beam was focussed to a spot size radius of $14 \mu\text{m}$. It is also likely that improved Yb:CaF₂ laser performance could be achieved by using a higher doping concentration or longer crystal length because in the current simulation a large percentage of the pump power was not absorbed as it passed through the crystal. The fraction of absorbed pump was only $0.42\text{-}0.49$ for the optimised laser.

When compared to other actively QS laser systems the achievable pulse power from a Yb:CaF₂ laser under our conditions does not compete very well yet. Yb:CaF₂ has not been a common gain material for QS lasers and only actively QS lasers have been mentioned in the literature to date. The closest passively QS laser was a Na/Yb co-doped CaF₂ laser that reached a peak power of 9.4 W in $1.5 \mu\text{s}$ pulses at a 28 kHz repetition rate.⁴² Peak power

achieved from an actively QS Yb:CaF₂ laser was quoted to be 6.9 MW with 44 mJ of output energy and a pulse duration of 6.4 ns.²⁹ Often actively QS Nd:YAG and Yb:YAG lasers are used for x-ray microscopy applications. These lasers are typically on the order of 100-600 mJ per pulse with 0.6-6 ns pulse widths, i.e. 100-160 MW per pulse.^{13,90,92,96} A more direct comparison would be between passively QS Yb:YAG and Nd:YAG lasers. For example, passively QS Yb:YAG lasers have achieved 1-3 MW of peak power.^{129,130} Nd:YAG has also produced passively QS results with peak powers from 6-24 MW.^{131,132} Generally, the highest of the peak powers quoted here are achieved by reducing the cavity length significantly to decrease pulse width or through the use of high power, pulsed pump sources.

It is possible with significant re-configuration of the Yb:CaF₂ laser that these kinds of powers could be reached. To achieve 2.8 MW of peak power in 3.6 mJ, 1.3 ns pulses at a repetition rate of 20 Hz, M. Tsunekane and T. Taira¹³⁰ used a small micro-chip Yb:YAG/Cr:YAG QS laser cavity near the stability limit with a large mode area. A similar arrangement could be made with a Yb:CaF₂ laser crystal. In unstable resonators the gain of the laser must be high to compensate the large OC loss, which is a problem for Yb:CaF₂, but a move to cryogenic cooling would likely improve the gain as S. Ricaud et al.²⁶ found in 2011. Cryogenic cooling enabled a round-trip laser gain as high as 3.1 but added additional complexity and cost to the laser design. Such round trip gain would be close to the minimum necessary for an unstable resonator configuration. A master oscillator power amplifier (MOPA) design would also be possible. For example, a passively QS Nd:YAG MOPA achieved 42 MW of peak power in 420 mJ, 10 ns pulses at a repetition rate of 30 Hz.¹³³ Again, the low gain per pass of Yb:CaF₂ would necessitate a multi-pass extraction geometry for the amplifier.

Often pulsed laser sources are used to pump the high power QS laser systems and result in improved efficiency and readily controllable Q-switching. We have access to 940 nm pulsed laser diode stacks and utilisation of these pump sources could improve QS peak output power because lasing threshold can be reached with lower reflectivity OCs. Even if the QS

performance is not greatly improved, the study of Yb:CaF₂ under CW and pulsed pumping can enhance our understanding of the crystal for use in short pulse, high power amplifier stages where the broadband emission spectrum is of significant benefit.

Chapter 7

Conclusion

7.1 Summary of Experiments

Demonstration of both the CW and Q-switched (QS) operation of a Yb:CaF₂ laser has been successfully achieved. Three CW operating points were established by modifying the pump and laser mode radii within the cavity. The laser thresholds and slopes were shown to generally follow theoretical expectations. The first operating point was attained with a focussed pump radius of 267 μm horizontally and 191 μm vertically and an average laser mode radius of 203 μm horizontally and 143 μm vertically inside the crystal. The laser slope efficiency was 28.5% and the laser pump threshold was 6.1 W. The second operating point maintained the same pump radius but had a larger average mode radius of 237 μm horizontally and 168 μm vertically inside the crystal. The laser slope efficiency was 30.4% and the laser pump threshold was 7.0 W. The final operating regime was with a pump radius of 134 μm horizontally and 95 μm vertically and an average laser mode radius of 142 μm horizontally and 99 μm vertically. The laser slope efficiency was 28.3% and the laser pump threshold was 3.8 W. The third operating point was shown to be stable with good mode quality. The wavelength was maintained between 1050-1051 nm and the M^2 value was measured to be 1.0 ± 0.2 .

Repetitive passive Q-switching was attained in Yb:CaF₂ for the first time using a 98% unsaturated transmission Cr:YAG saturable absorber (SA). The laser pump threshold was 8.6 W and the highest achieved average output power was 914 mW with a repetition rate of 1314 Hz at an incident pump power of 12.4 W corresponding to 41.6% of the CW laser power for similar conditions. Laser slope efficiency was 19.8%. Well past threshold the output pulse energy was 0.6 mJ and the FWHM pulse width was approximately 79 ns. The

wavelength fluctuated more significantly than in CW operation, from 1046-1049 nm, due to changes in temperature and population inversion with time. An excellent M^2 factor of 1.1 ± 0.2 was determined. From an analysis of possible applications it should be possible to generate soft x-rays from a nitrogen-based plasma using the peak QS power of 7.9 kW focussed to a small 1.6 μm radius spot but the x-ray flux would probably not be high enough for effective x-ray microscopy.

Thermal measurements of both CW and QS laser configurations in lasing and non-lasing operation were taken. Temperatures rose inside the laser crystal for increasing pump power as expected. The highest temperatures occurred near the pumped region of the crystal and the corner of the crystal opposite to the two cooled edges. At high pump power the highest temperatures arose during Q-switching rather than CW operation. The centre of the pumped region did not show a significant temperature rise compared to its surroundings, in part due to fluorescence trapping and the limited camera resolution. A noticeable increase in temperature on the back face of the crystal at, and just past, threshold was measured. This increase is ascribed to reabsorption of laser radiation along the pump axis, transporting heat to the face, and to a small increase to the fractional heat load at threshold from the interaction of the low laser extraction efficiency and increased pump absorption.

7.2 Summary of Simulations

To compare to experimental results and to gain further understanding of the laser system, rate equation modelling was undertaken. The results from the simulations, including output energy, average output power, repetition rate, and pulse width, were found to lie within 30% of experimental values and generally considerably better than this. A parametric study was completed to help suggest improvements to the experimental system. Average power and repetition rate were most strongly affected by pump mode radius, crystal doping concentration, and crystal length, but due to assumptions made in the modelling, the predicted improvements due to optimisation of these factors may not be accurate

quantitatively. In light of this, passive cavity loss, output coupler (OC) reflectivity, and SA unsaturated transmission were instead used to optimise average power and repetition rate. OC reflectivity and SA unsaturated transmission had the most influence on output energy. To optimise the pulse width the SA unsaturated transmission and the cavity length were the most dominant factors.

Using this knowledge, and keeping in mind the damage thresholds of the various laser cavity components, an optimised laser design was simulated. A concentric resonator design with two 60 mm radius of curvature mirrors was utilised. This design increased the laser mode area at all cavity elements compared to the experimental laser. The peak output power achieved was 187 kW with a repetition rate of 781 Hz at a pump power of 85 W. Thermal lensing must be avoided in this resonator design to attain this peak power. In order to reach intensities high enough to generate soft x-rays from a nitrogen-based plasma the laser beam would require a focussed spot radius of approximately 5.5 μm to reach an intensity of $2 \times 10^{11} \text{ W} \cdot \text{cm}^{-2}$.

Thermal simulations were run for the CW and QS laser cases to compare to experiment. Temperatures in Kelvin were found to agree with experiment within 2% for the CW simulations and 4% for the QS simulations. In the simulations, peak temperatures were localised to the pumped region of the crystal. This result may be attributed to increased resolution in the simulation modelling compared to the experiment and the absence of fluorescence trapping in the model. A rapid rise in temperature at threshold was found in the simulation but to a more limited extent compared to the experiment. This was likely due to the lack of laser reabsorption effects in the model.

Optimisation of the heat extraction from the laser crystal was also simulated. With a lower cooling temperature, improved crystal radiative and pump efficiencies, and a higher heat transfer coefficient from crystal to mount the temperature rise in the laser crystal can be drastically reduced. With an improvement in all three factors the simulated peak crystal temperature rise in the QS configuration was reduced by 72%.

7.3 Future Work

The work presented here is not the end of the story. Improvements to the simulations would enable a more accurate model of the laser system. The rate equation modelling can be improved with the inclusion of transverse and longitudinal variations in the pump and laser modes, the population inversion density, and the crystal temperature. There exist models that include many of these effects, sometimes in isolation, and can be modified to fit a Yb:CaF₂ system. A complete combination of rate equation and thermal modelling would be the best method to achieve close agreement to experimental results.

One aid to the modelling process is a complete understanding of crystal properties. Because Yb:CaF₂ is still being actively studied in the literature there exist some uncertainty in many of the physical constants and they tend to vary from crystal to crystal. Examination of the spectroscopic and thermal properties of the laser crystal and comparison to crystals from different manufacturers could help elucidate some of these issues and lead to better modelling.

In Chapter 6 much of the discussion was related to improving the experimental design of the laser. With better modelling an even better optimisation could be obtained to improve Q-switching performance. In either case, experimental confirmation of improved performance is very valuable and should be implemented. With each iteration of modelling and experiment a better understanding could be obtained. This is important not only for improving QS operation for water window (WW) x-ray generation but also for other laser applications such as development of a terawatt level chirped-pulse amplification laser system based on Yb:CaF₂. In order to accomplish high flux WW x-ray generation another possible future direction is to build a master oscillator power amplifier system to increase the pulse energy substantially.

One possible interesting future development would be to determine the feasibility of, and perhaps implement, a self-QS Cr⁴⁺/Yb³⁺ co-doped CaF₂ crystal or ceramic. Self-QS

$\text{Cr}^{4+}/\text{Yb}^{3+}$ co-doped YAG lasers have been successfully shown but to our knowledge this has never been attempted in a CaF_2 host.^{134–137} There has been mention of a $\text{Cr}^{4+}:\text{CaF}_2$ crystal (also containing Cr^+ , Cr^{2+} , and Cr^{3+}) in the literature but not in regards to laser or saturable absorber applications.¹³⁸ If co-doping is not an option perhaps a fusion-bonded $\text{Cr}^{4+}:\text{CaF}_2/\text{Yb}^{3+}:\text{CaF}_2$ monolithic laser could be developed.

In summary, the first Cr:YAG, passively Q-switched, Yb: CaF_2 laser was developed and successfully operated. Modelling of both laser dynamics and heat generation in the laser crystal was also undertaken. This laser potentially could be used in low-flux WW x-ray generation particularly with improvements and optimisation that could raise the peak output power to the level of 100's of kW in power. Future work should include carrying out such experimental optimisation and developing more accurate simulations to build a greater understanding of Yb-doped CaF_2 lasers.

References

- ¹ Fan, T. Y., and Byer, R. L., “Modeling and CW operation of a quasi-three-level 946 nm Nd: YAG laser,” *IEEE Journal of Quantum Electronics*, vol. 23, 1987, pp. 605–612.
- ² Siebold, M., Bock, S., Schramm, U., Xu, B., Doualan, J. L., Camy, P., and Moncorge, R., “Yb:CaF₂: a new old laser crystal,” *Applied Physics B: Lasers and Optics*, vol. 97, Oct. 2009, pp. 327–38.
- ³ Chichkov, B. N., Momma, C., Nolte, S., Alvensleben, F. von, and Tünnermann, A., “Femtosecond, picosecond and nanosecond laser ablation of solids,” *Applied Physics A*, vol. 63, Aug. 1996, pp. 109–115.
- ⁴ Miyaji, G., and Miyazaki, K., “Ultrafast dynamics of periodic nanostructure formation on diamondlike carbon films irradiated with femtosecond laser pulses,” *Applied Physics Letters*, vol. 89, Nov. 2006, p. 191902.
- ⁵ Liao, Y., Cheng, Y., Liu, C., Song, J., He, F., Shen, Y., Chen, D., Xu, Z., Fan, Z., Wei, X., Sugioka, K., and Midorikawa, K., “Direct laser writing of sub-50 nm nanofluidic channels buried in glass for three-dimensional micro-nanofluidic integration,” *Lab on a Chip*, vol. 13, Mar. 2013, pp. 1626–1631.
- ⁶ Banerjee, S. P., Zhijiang Chen, Utkin, I., and Fedosejevs, R., “Detection of buried layers in silicon devices using LIBS during hole drilling with femtosecond laser pulses,” *Applied Physics A: Materials Science & Processing*, vol. 111, Jun. 2013, pp. 791–8.
- ⁷ Tan, D., Li, Y., Qi, F., Yang, H., Gong, Q., Dong, X., and Duan, X., “Reduction in feature size of two-photon polymerization using SCR500,” *Applied Physics Letters*, vol. 90, Feb. 2007, p. 071106.
- ⁸ Osellame, R., Hoekstra, H. j. w. m., Cerullo, G., and Pollnau, M., “Femtosecond laser microstructuring: an enabling tool for optofluidic lab-on-chips,” *Laser & Photonics Reviews*, vol. 5, May 2011, pp. 442–463.
- ⁹ Leahy-Hoppa, M. R., Miragliotta, J., Osiander, R., Burnett, J., Dikmelik, Y., McEnnis, C., and Spicer, J. B., “Ultrafast Laser-Based Spectroscopy and Sensing: Applications in LIBS, CARS, and THz Spectroscopy,” *Sensors (Basel, Switzerland)*, vol. 10, Apr. 2010, pp. 4342–4372.
- ¹⁰ Mo, M. Z., Ali, A., Fourmaux, S., Lassonde, P., Kieffer, J. C., and Fedosejevs, R., “Generation of 500 MeV-1 GeV energy electrons from laser wakefield acceleration via ionization induced injection using CO₂ mixed in He,” *Applied Physics Letters*, vol. 102, 2013.
- ¹¹ Poirier, M., Blenski, T., de Gaufridy de Dortan, F., and Gilleron, F., “Modeling of EUV emission from xenon and tin plasma sources for nanolithography,” *Journal of Quantitative Spectroscopy and Radiative Transfer*, vol. 99, May 2006, pp. 482–492.

- ¹² Makimura, T., Torii, S., Niino, H., and Murakami, K., “Commentary: Nano- and micromachining using laser plasma soft X-rays,” *Journal of Nanophotonics*, vol. 4, 2010, pp. 040305–040305–4.
- ¹³ Berglund, Rymell, Peuker, Wilhein, and Hertz, “Compact water-window transmission X-ray microscopy,” *Journal of Microscopy*, vol. 197, Mar. 2000, pp. 268–273.
- ¹⁴ Payne, S. A., Orth, C. D., and Krupke, W. F., “Diode-pumped Yb-FAP solid-state laser driver for inertial fusion energy power plant,” *IEEE Lasers and Electro-Optics Society Annual Meeting, 1993. LEOS '93 Conference Proceedings, 1993*, pp. 704–705.
- ¹⁵ Chanteloup, J.-C., “HiPER, the European approach to inertial fusion energy, laser driver studies,” *2013 Conference on Lasers and Electro-Optics (CLEO)*, 2013, pp. 1–3.
- ¹⁶ Gonçalves-Novo, T., Albach, D., Vincent, B., Arzakantsyan, M., and Chanteloup, J.-C., “14 J / 2 Hz Yb³⁺:YAG diode pumped solid state laser chain,” *Optics Express*, vol. 21, Jan. 2013, pp. 855–866.
- ¹⁷ Shimogaki, T., Ofuji, T., Tetsuyama, N., Okazaki, K., Higashihata, M., Nakamura, D., Ikenoue, H., Asano, T., and Okada, T., “Applications of nanosecond laser annealing to fabricating p-n homo junction on ZnO nanorods,” 2013, p. 86260V–86260V–7.
- ¹⁸ Amer, M. S., El-Ashry, M. A., Dosser, L. R., Hix, K. E., Maguire, J. F., and Irwin, B., “Femtosecond versus nanosecond laser machining: comparison of induced stresses and structural changes in silicon wafers,” *Applied Surface Science*, vol. 242, Mar. 2005, pp. 162–167.
- ¹⁹ Cheng Luo, L. L., “The application of nanosecond-pulsed laser welding technology in MEMS packaging with a shadow mask,” *Sensors and Actuators A: Physical*, 2002, pp. 398–404.
- ²⁰ Ascari, A., and Fortunato, A., “Nanosecond pulsed laser welding of high carbon steels,” *Optics & Laser Technology*, vol. 56, Mar. 2014, pp. 25–34.
- ²¹ Wood, J. P. M., Plunkett, M., Previn, V., Chidlow, G., and Casson, R. J., “Nanosecond pulse lasers for retinal applications,” *Lasers in Surgery and Medicine*, vol. 43, Aug. 2011, pp. 499–510.
- ²² Yamamoto, Y., and Shinohara, K., “Application of X-ray microscopy in analysis of living hydrated cells,” *The Anatomical Record*, vol. 269, Oct. 2002, pp. 217–223.
- ²³ Petit, V., Doualan, J. L., Camy, P., Ménard, V., and Moncorgé, R., “CW and tunable laser operation of Yb³⁺ doped CaF₂,” *Applied Physics B*, vol. 78, Apr. 2004, pp. 681–684.
- ²⁴ Lucca, A., Jacquemet, M., Druon, F., Balembois, F., Georges, P., Camy, P., Doualan, J. L., and Moncorgé, R., “High-power tunable diode-pumped Yb³⁺:CaF₂ laser,” *Optics Letters*, vol. 29, Aug. 2004, pp. 1879–1881.
- ²⁵ Reagan, B. A., Curtis, A. H., Wernsing, K. A., Furch, F. J., Luther, B. M., and Rocca, J. J., “Development of High Energy Diode-Pumped Thick-Disk Yb:YAG Chirped-Pulse-Amplification Lasers,” *Quantum Electronics, IEEE Journal of*, vol. 48, Jun. 2012, pp. 827–835.

- ²⁶ Ricaud, S., Papadopoulos, D. N., Pellegrina, A., Camy, P., Doualan, J. L., Moncorgé, R., Courjaud, A., Mottay, E., Georges, P., and Druon, F., “Diode-pumped, cryogenically cooled Yb:CaF₂ for high efficient and high power laser,” *Proceedings of SPIE*, vol. 7912, Feb. 2011, p. 79121O–79121O–6.
- ²⁷ Fan, T. Y., Ripin, D. J., Aggarwal, R. L., Ochoa, J. R., Chann, B., Tilleman, M., and Spitzberg, J., “Cryogenic Yb³⁺-Doped Solid-State Lasers,” *Selected Topics in Quantum Electronics, IEEE Journal of*, vol. 13, Jun. 2007, pp. 448–459.
- ²⁸ Ricaud, S., Papadopoulos, D. N., Pellegrina, A., Balembois, F., Georges, P., Courjaud, A., Camy, P., Doualan, J. L., Moncorgé, R., and Druon, F., “High-power diode-pumped cryogenically cooled Yb:CaF₂ laser with extremely low quantum defect,” *Optics Letters*, vol. 36, 2011, pp. 1602–1604.
- ²⁹ Siebold, M., Hornung, M., Bock, S., Hein, J., Kaluza, M. C., Wemans, J., and Uecker, R., “Broad-band regenerative laser amplification in ytterbium-doped calcium fluoride (Yb:CaF₂),” *Applied Physics B*, vol. 89, Nov. 2007, pp. 543–547.
- ³⁰ Boudeile, J., Didierjean, J., Camy, P., Doualan, J. L., Benayad, A., Ménard, V., Moncorgé, R., Druon, F., Balembois, F., and Georges, P., “Thermal behaviour of ytterbium-doped fluorite crystals under high power pumping,” *Optics Express*, vol. 16, Jul. 2008, pp. 10098–10109.
- ³¹ Pirri, A., Alderighi, D., Toci, G., Vannini, M., Nikl, M., and Sato, H., “Direct Comparison of Yb³⁺:CaF₂ and heavily doped Yb³⁺:YLF as laser media at room temperature,” *Optics Express*, vol. 17, Sep. 2009, pp. 18312–18319.
- ³² Lucca, A., Debourg, G., Jacquemet, M., Druon, F., Balembois, F., Georges, P., Camy, P., Doualan, J. L., and Moncorgé, R., “High-power diode-pumped Yb³⁺:CaF₂ femtosecond laser,” *Optics Letters*, vol. 29, Dec. 2004, pp. 2767–2769.
- ³³ Friebel, F., Druon, F., Boudeile, J., Papadopoulos, D. N., Hanna, M., Georges, P., Camy, P., Doualan, J. L., Benayad, A., Moncorgé, R., Cassagne, C., and Boudebs, G., “Diode-pumped 99 fs Yb:CaF₂ oscillator,” *Optics Letters*, vol. 34, May 2009, pp. 1474–1476.
- ³⁴ Machinet, G., Sevillano, P., Guichard, F., Dubrasquet, R., Camy, P., Doualan, J.-L., Moncorgé, R., Georges, P., Druon, F., Descamps, D., and Cormier, E., “High-brightness fiber laser-pumped 68 fs–2.3 W Kerr-lens mode-locked Yb:CaF₂ oscillator,” *Optics Letters*, vol. 38, Oct. 2013, pp. 4008–4010.
- ³⁵ Sevillano, pierre, Machinet, G., Dubrasquet, R., Camy, P., Doualan, J.-L., Moncorgé, R., Georges, P., Druon, F. P., Descamps, D., and Cormier, E., “Sub-50 fs, Kerr-lens mode-locked Yb:CaF₂ laser oscillator delivering up to 2.7 W,” *Advanced Solid-State Lasers Congress*, G. and M. Huber P., ed., Optical Society of America, 2013, p. AF3A.6.
- ³⁶ Ricaud, S., Druon, F., Papadopoulos, D. N., Camy, P., Doualan, J. L., Moncorgé, R., Delaigue, M., Zaouter, Y., Courjaud, A., Georges, P., and others, “Short-pulse and high-repetition-rate diode-pumped Yb:CaF₂ regenerative amplifier,” *Optics letters*, vol. 35, 2010, pp. 2415–2417.
- ³⁷ Ricaud, S., Delaigue, M., Courjaud, A., Druon, F., Georges, P., Camy, P., Doualan, J.-L., Moncorgé, R., and Mottay, E., “Broadband Yb:CaF₂ regenerative amplifier for millijoule range ultrashort pulse amplification,” 2010, p. 75890M–75890M–6.

- ³⁸ Balčiūnas, T., Fan, G. Y., Andriukaitis, G., Pugžlys, A., and Baltuška, A., “High-power top-hat pulses from a Yb master oscillator power amplifier for efficient optical parametric amplifier pumping,” *Optics Letters*, vol. 37, Jul. 2012, pp. 2547–2549.
- ³⁹ Friebel, F., Pellegrina, A., Papadopoulos, D. N., Camy, P., Doualan, J.-L., Moncorgé, R., Georges, P., and Druon, F., “Diode-pumped Yb:CaF₂ multipass amplifier producing 50 mJ with dynamic analysis for high repetition rate operation,” *Applied Physics B*, vol. 117, Nov. 2014, pp. 597–603.
- ⁴⁰ Siebold, M., Hornung, M., Boedefeld, R., Podleska, S., Klingebiel, S., Wandt, C., Krausz, F., Karsch, S., Uecker, R., Jochmann, A., Hein, J., and Kaluza, M. C., “Terawatt diode-pumped Yb:CaF₂ laser,” *Optics Letters*, vol. 33, Dec. 2008, pp. 2770–2772.
- ⁴¹ Kessler, A., Hornung, M., Keppler, S., Schorcht, F., Hellwing, M., Liebetrau, H., Körner, J., Sävert, A., Siebold, M., Schnepf, M., Hein, J., and Kaluza, M. C., “16.6 J chirped femtosecond laser pulses from a diode-pumped Yb:CaF₂ amplifier,” *Optics Letters*, vol. 39, Mar. 2014, pp. 1333–1336.
- ⁴² Su, L., Xu, J., Xue, Y., Wang, C., Chai, L., Xu, X., and Zhao, G., “Low-threshold diode-pumped Yb³⁺,Na⁺:CaF₂ self-Q-switched laser,” *Optics Express*, vol. 13, Jul. 2005, pp. 5635–5640.
- ⁴³ Siebold, M., Jochmann, A., Bock, S., Wandt, C., Hornung, M., Podleska, S., Hellwing, M., Schnepf, M., Bodefeld, R., Hein, J., Kaluza, M. C., and Wemans, J., “Tunable CW and Q-switched operation in Yb:CaF₂ and Yb:SrF₂,” *European Conference on Lasers and Electro-Optics, 2007 and the International Quantum Electronics Conference. CLEOE-IQEC 2007*, 2007, pp. 1–1.
- ⁴⁴ Clet, V., Courjaud, A., Doualan, J., Camy, P., Moncorgé, R., and Mottay, E., “Yb:CaF₂ diode-pumped millijoule nanosecond laser tunable from 1030 to 1065nm,” *2012 Conference on Lasers and Electro-Optics (CLEO)*, 2012, pp. 1–2.
- ⁴⁵ Voron’ko, Y. K., Osiko, V. V., and Shcherbakov, I. A., “Optical Centers and the Interaction of Yb³⁺ Ions in Cubic Fluorite Crystals,” *Soviet Journal of Experimental and Theoretical Physics*, vol. 29, 1969, p. 86.
- ⁴⁶ Ito, M., Goutaudier, C., Guyot, Y., Lebbou, K., Fukuda, T., and Boulon, G., “Crystal growth, Yb³⁺ spectroscopy, concentration quenching analysis and potentiality of laser emission in Ca_{1-x}Yb_xF_{2+x},” *Journal of Physics: Condensed Matter*, vol. 16, Mar. 2004, p. 1501.
- ⁴⁷ Petit, V., Camy, P., Doualan, J.-L., Portier, X., and Moncorgé, R., “Spectroscopy of Yb³⁺:CaF₂: From isolated centers to clusters,” *Physical Review B*, vol. 78, Aug. 2008, p. 085131.
- ⁴⁸ A. E. Nikiforov, A. Y. Z., “Crystal fields of hexameric rare-earth clusters in fluorites,” *Physics of the Solid State*, vol. 47, 2005, pp. 1431–1435.
- ⁴⁹ S. A. Kazanskii, A. I. R., “EPR spectra and crystal field of hexamer rare-earth clusters in fluorites,” *Phys. Rev. B*, vol. 72, 2005.
- ⁵⁰ G. Leniec, S. M. K., “EPR and optical properties of CaF₂:Yb single crystals,” *Proc SPIE*, vol. 5958-82, 2005, pp. 531–540.

- 51 Nikiforov, A. E., Chernyshev, V. A., Volodin, V. P., Avram, N. M., and Avram, C. N., “Ytterbium Clusters in Fluorite CaF₂,” *AIP Conference Proceedings*, vol. 1131, May 2009, pp. 96–101.
- 52 V. A. Chernyshev, A. E. N., “Electronic structure of Yb³⁺ impurity centers in fluorites,” vol. 52, 2010, pp. 1874–1879.
- 53 Lacroix, B., Genevois, C., Doualan, J. L., Brasse, G., Braud, A., Ruterana, P., Camy, P., Talbot, E., Moncorgé, R., and Margerie, J., “Direct imaging of rare-earth ion clusters in Yb:CaF₂,” *Physical Review B*, vol. 90, Sep. 2014, p. 125124.
- 54 Druon, F., Ricaud, S., Papadopoulos, D. N., Pellegrina, A., Camy, P., Doualan, J. L., Moncorgé, R., Courjaud, A., Mottay, E., and Georges, P., “On Yb:CaF₂ and Yb:SrF₂: review of spectroscopic and thermal properties and their impact on femtosecond and high power laser performance [Invited],” *Optical Materials Express*, vol. 1, Jun. 2011, p. 489.
- 55 Koerner, J., Vorholt, C., Liebetrau, H., Kahle, M., Kloepfel, D., Seifert, R., Hein, J., and Kaluza, M. C., “Measurement of temperature-dependent absorption and emission spectra of Yb:YAG, Yb:LuAG, and Yb:CaF₂ between 20 °C and 200 °C and predictions on their influence on laser performance,” *Journal of the Optical Society of America B*, vol. 29, Sep. 2012, pp. 2493–2502.
- 56 Körner, J., Jambunathan, V., Hein, J., Seifert, R., Loeser, M., Siebold, M., Schramm, U., Sikocinski, P., Lucianetti, A., Mocek, T., and Kaluza, M. C., “Spectroscopic characterization of Yb³⁺-doped laser materials at cryogenic temperatures,” *Applied Physics B*, vol. 116, Jul. 2014, pp. 75–81.
- 57 Shcheulin, A. S., Angervaks, A. E., Semenova, T. S., Koryakina, L. F., Petrova, M. A., Fedorov, P. P., Reiterov, V. M., Garibin, E. A., and Ryskin, A. I., “Additive colouring of CaF₂:Yb crystals: determination of Yb²⁺ concentration in CaF₂:Yb crystals and ceramics,” *Applied Physics B*, vol. 111, Jun. 2013, pp. 551–557.
- 58 Wagner, W. G., and Lengyel, B. A., “Evolution of the Giant Pulse in a Laser,” *Journal of Applied Physics*, vol. 34, Jul. 1963, pp. 2040–2046.
- 59 Kay, R. B., and Waldman, G. S., “Complete Solutions to the Rate Equations Describing Q-Spoiled and PTM Laser Operation,” *Journal of Applied Physics*, vol. 36, Apr. 1965, pp. 1319–1323.
- 60 Szabo, A., and Stein, R. A., “Theory of Laser Giant Pulsing by a Saturable Absorber,” *Journal of Applied Physics*, vol. 36, May 1965, pp. 1562–1566.
- 61 Koechner, W., *Solid state laser engineering / Walter Koechner*, New York: Springer-Verlag, 1976., 1976.
- 62 Degnan, J. J., “Theory of the optimally coupled Q-switched laser,” *IEEE Journal of Quantum Electronics*, vol. 25, Feb. 1989, pp. 214–220.
- 63 Nabors, C. D., “Q-switched operation of quasi-three-level lasers,” *IEEE Journal of Quantum Electronics*, vol. 30, Dec. 1994, pp. 2896–2901.
- 64 Degnan, J. J., “Optimization of passively Q-switched lasers,” *IEEE Journal of Quantum Electronics*, vol. 31, Nov. 1995, pp. 1890–1901.

- ⁶⁵ Degnan, J. J., Coyle, D. B., and Kay, R. B., “Effects of thermalization on Q-switched laser properties,” *IEEE Journal of Quantum Electronics*, vol. 34, May 1998, pp. 887–899.
- ⁶⁶ Voitikov, S. V., Demidovich, A. A., Batay, L. E., Kuzmin, A. N., and Danailov, M. B., “Sub-nanosecond pulse dynamics of Nd:LSB microchip laser passively Q-switched by Cr:YAG saturable absorber,” *Optics Communications*, vol. 251, 2005, pp. 154–164.
- ⁶⁷ Xiao, G., and Bass, M., “A generalized model for passively Q-switched lasers including excited state absorption in the saturable absorber,” *IEEE Journal of Quantum Electronics*, vol. 33, Jan. 1997, pp. 41–44.
- ⁶⁸ Zhang, X., Zhao, S., Wang, Q., Ozygus, B., and Weber, H., “Modeling of passively Q-switched lasers,” *Journal of the Optical Society of America B*, vol. 17, Jul. 2000, pp. 1166–1175.
- ⁶⁹ Li, S. T., Zhang, X. Y., Wang, Q. P., Li, P., Chang, J., Zhang, X. L., and Cong, Z. H., “Modeling of Q-switched lasers with top-hat pump beam distribution,” *Applied Physics B*, vol. 88, Jul. 2007, pp. 221–226.
- ⁷⁰ Dong, J., Deng, P., Liu, Y., Zhang, Y., Xu, J., Chen, W., and Xie, X., “Passively Q-Switched Yb:YAG Laser with Cr⁴⁺:YAG as the Saturable Absorber,” *Applied Optics*, vol. 40, Aug. 2001, pp. 4303–4307.
- ⁷¹ Lu, M., Chatwin, C. R., Young, R. C. D., and Birch, P. M., “Numerical simulation of a CW-pumped Cr:YAG passively Q-switched Yb:YAG pulsed laser,” *Optics and Lasers in Engineering*, vol. 47, Jun. 2009, pp. 617–621.
- ⁷² Li, C., Liu, Q., Gong, M., Chen, G., and Yan, P., “Q-switched operation of end-pumped Yb:YAG lasers with non-uniform temperature distribution,” *Optics Communications*, vol. 231, Feb. 2004, pp. 331–341.
- ⁷³ Chenais, S., Balembois, F., Druon, F., Lucas-Leclin, G., and Georges, P., “Thermal lensing in diode-pumped ytterbium Lasers-Part I: theoretical analysis and wavefront measurements,” *IEEE Journal of Quantum Electronics*, vol. 40, Sep. 2004, pp. 1217 – 1234.
- ⁷⁴ Chenais, S., Balembois, F., Druon, F., Lucas-Leclin, G., and Georges, P., “Thermal lensing in diode-pumped ytterbium Lasers-Part II: evaluation of quantum efficiencies and thermo-optic coefficients,” *IEEE Journal of Quantum Electronics*, vol. 40, Sep. 2004, pp. 1235 – 1243.
- ⁷⁵ Auge, F., Druon, F., Balembois, F., Georges, P., Brun, A., Mougél, F., Aka, G., and Vivien, D., “Theoretical and experimental investigations of a diode-pumped quasi-three-level laser: the Yb³⁺-doped Ca₄GdO(BO₃)₃ (Yb:GdCOB) laser,” *IEEE Journal of Quantum Electronics*, vol. 36, 2000, pp. 598–606.
- ⁷⁶ Fan, T. Y., “Heat generation in Nd:YAG and Yb:YAG,” *IEEE Journal of Quantum Electronics*, vol. 29, Jun. 1993, pp. 1457–1459.
- ⁷⁷ Chénais, S., Forget, S., Druon, F., Balembois, F., and Georges, P., “Direct and absolute temperature mapping and heat transfer measurements in diode-end-pumped Yb:YAG,” *Applied Physics B*, vol. 79, Jul. 2004, pp. 221–224.

- ⁷⁸ Didierjean, J., Forget, S., Chenais, S., Druon, F., Balembois, F., Georges, P., Altmann, K., and Pflaum, C., “High-resolution absolute temperature mapping of laser crystals in diode-end-pumped configuration,” H.J. Hoffman and R.K. Shori, eds., 2005, pp. 370–379.
- ⁷⁹ Yu, H., Bourdet, G., and Ferre, S., “Comprehensive modeling of the temperature-related laser performances of the amplifiers of the LUCIA laser,” *Applied Optics*, vol. 44, Oct. 2005, pp. 6412–6418.
- ⁸⁰ Didierjean, J., Herault, E., Balembois, F., and Georges, P., “Thermal conductivity measurements of laser crystals by infrared thermography. Application to Nd:doped crystals,” *Optics Express*, vol. 16, Jun. 2008, pp. 8995–9010.
- ⁸¹ Zhang, S., and Wang, X., “Thermal model of continuous wave end-pumped passively Q-switched laser,” *Optics Communications*, vol. 295, May 2013, pp. 155–160.
- ⁸² Risk, W. P., “Modeling of longitudinally pumped solid-state lasers exhibiting reabsorption losses,” *Journal of the Optical Society of America B*, vol. 5, Jul. 1988, pp. 1412–1423.
- ⁸³ Gupta, M. C., and Ballato, J., *The handbook of photonics [electronic resource] / edited by Mool C. Gupta, John Ballato*, Boca Raton : CRC/Taylor & Francis, c2007., 2007.
- ⁸⁴ Raikonen, E., Buchter, S. C., and Kaivola, M., “Modeling the Time-Dynamics of Miniature Passively Q-switched Lasers,” *IEEE Journal of Quantum Electronics*, vol. 45, Dec. 2009, pp. 1563–1570.
- ⁸⁵ Inguscio, M., Wallenstein, R., North Atlantic Treaty Organization. Scientific Affairs Division, and NATO Advanced Study Institute on Solid State Lasers: New Developments and Applications (1992 : Tuscany, I., *Solid State Lasers : New Developments and Applications*, Plenum Press, 1994.
- ⁸⁶ Li, Q., Feng, B., Zhang, Z., and Zhang, T., “Direct numerical simulation of quasi-three-level passive Q-switched laser,” *Optics Communications*, vol. 284, Jun. 2011, pp. 3391–3398.
- ⁸⁷ Cengel, Y. A., and Ghajar, A. J., *Heat and Mass Transfer: Fundamentals and Applications*, New York, NY: McGraw-Hill, 2011.
- ⁸⁸ Chénais, S., Druon, F., Forget, S., Balembois, F., and Georges, P., “On thermal effects in solid-state lasers: The case of ytterbium-doped materials,” *Progress in Quantum Electronics*, vol. 30, 2006, pp. 89–153.
- ⁸⁹ Crank, M., Harilal, S. S., Hassan, S. M., and Hassanein, A., “Excitation wavelength dependence of water-window line emissions from boron-nitride laser-produced plasmas,” *Journal of Applied Physics*, vol. 111, Feb. 2012, p. 033301.
- ⁹⁰ Legall, H., Blobel, G., Stiel, H., Sandner, W., Seim, C., Takman, P., Martz, D. H., Selin, M., Vogt, U., Hertz, H. M., Esser, D., Sipma, H., Luttmann, J., Höfer, M., Hoffmann, H. D., Yulin, S., Feigl, T., Rehbein, S., Guttman, P., Schneider, G., Wiesemann, U., Wirtz, M., and Diete, W., “Compact x-ray microscope for the water window based on a high brightness laser plasma source,” *Optics Express*, vol. 20, Jul. 2012, pp. 18362–18369.

- ⁹¹ Sakdinawat, A., and Attwood, D., “Nanoscale X-ray imaging,” *Nature Photonics*, vol. 4, Dec. 2010, pp. 840–848.
- ⁹² Seim, C., Baumann, J., Legall, H., Redlich, C., Mantouvalou, I., Blobel, G., Stiel, H., and Kanngießer, B., “Laboratory full-field transmission x-ray microscopy,” *Proceedings of SPIE*, vol. 8678, 2012, pp. 867808–867808–10.
- ⁹³ Zeng, G., Daido, H., Togawa, T., Nakatsuka, M., Nakai, S., and Aritome, H., ““Water window” x-ray source produced by a slab glass laser,” *Journal of Applied Physics*, vol. 69, Jun. 1991, pp. 7460–7464.
- ⁹⁴ Fiedorowicz, H., Bartnik, A., Jarocki, R., Szczurek, M., and Wilhein, T., “X-ray emission in the ‘water window’ from a nitrogen gas puff target irradiated with a nanosecond Nd:glass laser pulse,” *Applied Physics B*, vol. 67, Sep. 1998, pp. 391–393.
- ⁹⁵ Harilal, S. S., Miloshevsky, G. V., Sizyuk, T., and Hassanein, A., “Effects of excitation laser wavelength on Ly- α and He- α line emission from nitrogen plasmas,” *Physics of Plasmas (1994-present)*, vol. 20, Jan. 2013, p. 013105.
- ⁹⁶ Martz, D. H., Selin, M., von Hofsten, O., Fogelqvist, E., Holmberg, A., Vogt, U., Legall, H., Blobel, G., Seim, C., Stiel, H., and Hertz, H. M., “High average brightness water window source for short-exposure cryomicroscopy,” *Optics Letters*, vol. 37, Nov. 2012, pp. 4425–4427.
- ⁹⁷ Siegman, A. E., “How to (Maybe) Measure Laser Beam Quality,” *DPSS (Diode Pumped Solid State) Lasers: Applications and Issues*, M. Dowley, ed., Optical Society of America, 1998, p. MQ1.
- ⁹⁸ Ophir, and Spiricon, “Beam Width Measurement Accuracy.”
- ⁹⁹ Northrop Grumman, “Cr⁴⁺: YAG Absorption Coefficient” Available: http://www.northropgrumman.com/BusinessVentures/SYNOPTICS/Products/SpecialtyCrystals/Documents/pageDocs/Cr4+_YAG_absorption_chart.pdf.
- ¹⁰⁰ Kalisky, Y., “Cr⁴⁺-doped crystals: their use as lasers and passive Q-switches,” *Progress in Quantum Electronics*, vol. 28, 2004, pp. 249–303.
- ¹⁰¹ Ridderbusch, H., and Graf, T., “Saturation of 1047- and 1064-nm Absorption in Cr⁴⁺:YAG Crystals,” *IEEE Journal of Quantum Electronics*, vol. 43, Feb. 2007, pp. 168–173.
- ¹⁰² Wakaki, M., ed., *Physical Properties and Data of Optical Materials*, CRC Press, 2007.
- ¹⁰³ Bezuidenhout, D. F., “Calcium Fluoride (CaF₂),” *Handbook of Optical Constants of Solids*, E.D. Palik, ed., Burlington: Academic Press, 1997, pp. 815–835.
- ¹⁰⁴ Crystran Ltd., “Germanium (Ge),” *Crystran* Available: <http://www.crystran.co.uk/optical-materials/germanium-ge>.
- ¹⁰⁵ Spectrogon AB, “LP-11000 nm Transmission,” May 2014.
- ¹⁰⁶ Gustafsson, B., “Finite Difference Methods,” *Fundamentals of Scientific Computing*, Springer Berlin Heidelberg, 2011, pp. 145–171.

- ¹⁰⁷ Toci, G., Alderighi, D., Pirri, A., and Vannini, M., “Lifetime measurements with the pinhole method in presence of radiation trapping: II—application to Yb³⁺ doped ceramics and crystals,” *Applied Physics B*, vol. 106, Jan. 2012, pp. 73–79.
- ¹⁰⁸ Camy, P., Doualan, J. L., Benayad, A., Von Edlinger, M., Ménard, V., and Moncorgé, R., “Comparative spectroscopic and laser properties of Yb³⁺-doped CaF₂, SrF₂ and BaF₂ single crystals,” *Applied Physics B: Lasers & Optics*, vol. 89, Dec. 2007, pp. 539–542.
- ¹⁰⁹ Petit, V., Doualan, J.-L., Camy, P., Budasca, C., and Moncorgé, R., “Spectroscopy and tunable laser operation of Yb³⁺:CaF₂ single crystals,” *Proceedings of SPIE*, vol. 5460, Sep. 2004, pp. 123–131.
- ¹¹⁰ Su, L., Xu, J., Li, H., Wen, L., Yang, W., Zhao, Z., Si, J., Dong, Y., and Zhou, G., “Crystal growth and spectroscopic characterization of Yb-doped and Yb, Na-codoped CaF₂ laser crystals by TGT,” *Journal of Crystal Growth*, vol. 277, Apr. 2005, pp. 264–268.
- ¹¹¹ Daimon, M., and Masumura, A., “High-accuracy measurements of the refractive index and its temperature coefficient of calcium fluoride in a wide wavelength range from 138 to 2326 nm,” *Applied Optics*, vol. 41, Sep. 2002, pp. 5275–5281.
- ¹¹² Zelmon, D. E., Small, D. L., and Page, R., “Refractive-index measurements of undoped yttrium aluminum garnet from 0.4 to 5.0 μm,” *Applied Optics*, vol. 37, Jul. 1998, pp. 4933–4935.
- ¹¹³ Zhang, X., Brenier, A., Wang, J., and Zhang, H., “Absorption cross-sections of Cr⁴⁺:YAG at 946 and 914 nm,” *Optical Materials*, vol. 26, Aug. 2004, pp. 293–296.
- ¹¹⁴ Gaumé, R., Viana, B., Vivien, D., Roger, J.-P., and Fournier, D., “A simple model for the prediction of thermal conductivity in pure and doped insulating crystals,” *Applied Physics Letters*, vol. 83, Aug. 2003, pp. 1355–1357.
- ¹¹⁵ Petit, J., Viana, B., Goldner, P., Roger, J.-P., and Fournier, D., “Thermomechanical properties of Yb³⁺ doped laser crystals: Experiments and modeling,” *Journal of Applied Physics*, vol. 108, Dec. 2010, pp. 123108–123108–11.
- ¹¹⁶ *ASHRAE handbook. Fundamentals*, Atlanta, Ga.: American Society of Heating, Refrigerating, and Air-Conditioning Engineers, c1981., 1981.
- ¹¹⁷ Pukhonin, V. V., and Chaikin, A. S., “Spectral emissivity of LiF, CaF₂, and NaCl crystals and fused quartz in the range 2–25 μ,” *Journal of Applied Spectroscopy*, vol. 16, Jan. 1972, pp. 106–109.
- ¹¹⁸ Korth Kristalle GmbH, “Calcium Fluoride (CaF₂)” Available: <http://www.korth.de/index.php/162/items/10.html>.
- ¹¹⁹ Taira, T., Tulloch, W. M., and Byer, R. L., “Modeling of quasi-three-level lasers and operation of cw Yb:YAG lasers,” *Applied Optics*, vol. 36, Mar. 1997, pp. 1867–1874.
- ¹²⁰ Jacquemet, M., Lucca, A., Druon, F., Balembois, F., Georges, P. M., Petit, V., Doualan, J.-L., Camy, P., and Moncorgé, R., “High-power CW diode-pumped laser operation of Yb³⁺:CaF₂ crystal,” *Proceedings of SPIE*, vol. 5460, Sep. 2004, pp. 83–90.

- ¹²¹ Liu, J., Ozygus, B., Yang, S., Erhard, J., Seelig, U., Ding, A., Weber, H., Meng, X., Zhu, L., Qin, L., Du, C., Xu, X., and Shao, Z., “Efficient passive Q-switching operation of a diode-pumped Nd:GdVO₄ laser with a Cr⁴⁺:YAG saturable absorber,” *Journal of the Optical Society of America B*, vol. 20, Apr. 2003, pp. 652–661.
- ¹²² Li, J., Ueda, K., Dong, J., Musha, M., and Shirakawa, A., “Maximum value of the pulse energy of a passively Q-switched laser as a function of the pump power,” *Applied Optics*, vol. 45, Jul. 2006, pp. 5377–5384.
- ¹²³ Liu, J., “Oscillation behavior of quasi-three-level lasers with residual resonant absorption losses,” *Optical and Quantum Electronics*, vol. 45, Sep. 2013, pp. 987–997.
- ¹²⁴ Pan, L., *Experiment and modeling of passively Q-switched ytterbium doped double-clad fiber lasers [electronic resource] / by Lei Pan*, 2010., 2010.
- ¹²⁵ Töpfer, T., “Private communication,” Nov. 2013.
- ¹²⁶ Akchurin, M. S., Basiev, T. T., Demidenko, A. A., Doroshenko, M. E., Fedorov, P. P., Garibin, E. A., Gusev, P. E., Kuznetsov, S. V., Krutov, M. A., Mironov, I. A., Osiko, V. V., and Popov, P. A., “CaF₂:Yb laser ceramics,” *Optical Materials*, vol. 35, Jan. 2013, pp. 444–450.
- ¹²⁷ Yang, P., Deng, P., and Yin, Z., “Concentration quenching in Yb:YAG,” *Journal of Luminescence*, vol. 97, Apr. 2002, pp. 51–54.
- ¹²⁸ Crystech Inc., “Basic Properties of Cr:YAG” Available: <http://www.crystech.com.cn/products/crystals/qswitchcrystals/CrYAG.htm>.
- ¹²⁹ Dong, J., Ren, Y., and Cheng, H., “>1 MW peak power, an efficient Yb:YAG/Cr⁴⁺:YAG composite crystal passively Q-switched laser,” *Laser Physics*, vol. 24, May 2014, p. 055801.
- ¹³⁰ Tsunekane, M., and Taira, T., “High Peak Power, Passively Q-Switched Yb:YAG/Cr:YAG Micro-Lasers,” *IEEE Journal of Quantum Electronics*, vol. 49, May 2013, pp. 454–461.
- ¹³¹ Shimony, Y., Kalisky, Y., and Chai, B. H. T., “Quantitative studies of Cr⁴⁺:YAG as a saturable absorber for Nd:YAG laser,” *Optical Materials*, vol. 4, Mar. 1995, pp. 547–551.
- ¹³² Ling, M., Jin, G., Tan, X., Wu, Z., and Liang, Z., “End-pumped Nd:YAG Q-switched laser with high energy and narrow pulse for glass carving,” 2009, p. 72822A–72822A–5.
- ¹³³ Kabanov, V. V., Bezyazychnaya, T. V., Bogdanovich, M. V., Grigor’ev, A. V., Lebiadok, Y. V., Lepchenkov, K. V., Ryabtsev, A. G., Ryabtsev, G. I., and Shchemelev, M. A., “LD-pumped erbium and neodymium lasers with high energy and output beam quality,” 2013, p. 87800K–87800K–8.
- ¹³⁴ Jun, D., Peizhen, D., and Jun, X., “The growth of Cr⁴⁺, Yb³⁺:yttrium aluminum garnet (YAG) crystal and its absorption spectra properties,” *Journal of Crystal Growth*, vol. 203, May 1999, pp. 163–167.
- ¹³⁵ Zhou, Y., Thai, Q., Chen, Y. C., and Zhou, S., “Monolithic Q-switched Cr,Yb:YAG laser,” *Optics Communications*, vol. 219, Apr. 2003, pp. 365–367.

- ¹³⁶ Dong, J., Shirakawa, A., Ueda, K., Yagi, H., Yanagitani, T., and Kaminskii, A. A., “Ytterbium and chromium doped composite $Y_3Al_5O_{12}$ ceramics self-Q-switched laser,” *Applied Physics Letters*, vol. 90, May 2007, p. 191106.
- ¹³⁷ Ma, J., Cheng, Y., Dong, J., Ueda, K., and Kaminskii, A. A., “Enhancement of Cr, Yb:YAG self-Q-switched lasers by bonding Yb:YAG crystal,” *Quantum Electronics Conference Lasers and Electro-Optics (CLEO/IQEC/PACIFIC RIM), 2011*, 2011, pp. 638–640.
- ¹³⁸ Jablonski, R., “Investigations of chromium-doped CaF_2 monocrystals irradiated with gamma rays,” 1975.

Appendix A

Matlab Codes for Rate Equation Simulation

A.1 Main Program

This is the main program that runs the rate equation solver and computes output parameters. It includes a function to evaluate the differential equations.

```
function Qswitchcode_thesis
% Qswitchcode_thesis: solves the Q-switched laser rate equations and
% produces output results.
% LaserRate_thesis(t,yin): solves the coupled rate equations for a
% Q-switched laser using the Matlab RK function ode45. Crystal temperature
% is found from COMSOL FEA simulations. The result is the time evolution
% of a CW-pumped, passively Q-switched laser. Variable names based on
% paper by Qinan Li, 2011. Parametric inputs generated from an Excel file
% and outputs are saved to another Excel file.
%
% (C) Travis Schoepp, 2014

clear all; close all;
% Counter for number of solutions computed
count = 0;
% Determine names and number of sheets in file
[~, Sheets] = xlsfinfo('Q Switching Parametric Model Inputs
R2.xlsx');
param_studies = size(Sheets,2);      % Number of sheets

% Create cell array for writing to excel file
export_char = {'Eout (Degnan) (mJ)';...
               'Eout (calc) (mJ)';...
               'Pmax (calc) (W)';...
               'Pave (W)';...
               'FWHM (ns)';...
               'Approx. FWHM (Degnan) (ns)';...
               'Rep Rate (Hz)';...
               'N_i (cm^-3)';...
               'N_t (cm^-3)';...
               'N_f (cm^-3)';...
               'Avg Abs N2 (m^-3)';...
               'Avg Pump Abs';...
               'Pmax (Degnan)';...
               'Approx. FWHM (calc) (ns)';...
               'Number of Pulses'};

% Loop for each sheet of file except last (number of parametric studies)
for r=1:(param_studies-1)
```

```

% Parameters are ordered as shown in lines 47 to 59
params = xlsread('Q Switching Parametric Model Inputs
R2.xlsx',Sheets{r}); % Read in parameters for each
iteration (column-wise)
num_iter = size(params,2); % Determine number of iterations
for parametric study

% Create vectors to hold variables of interest
export_num = cell(15,num_iter);

% Loop for each combination of parameters in current study
for s=1:num_iter
    % Parametric Variables
    l = params(1,s); % Length of laser crystal in cm
    la = params(2,s); % Length of absorber in cm
    Lc = params(3,s); % Length of cavity in cm (straight-line)
    T = params(4,s); % Approx. operating crystal temperature in K
    wlm = params(5,s); % Pump waist radius multiplier
    w2s = params(6,s); % Saggital laser mode radius in cm
    w2t = params(7,s); % Tangental laser mode radius in cm
    Ta = params(8,s); % Unsaturated absorber transmission
    N0 = params(9,s); % Laser crystal concentration in cm^-3
    R2 = params(10,s); % Output coupler reflectivity
    Wpc = params(11,s); % Incident pump power in W
    C_loss = params(12,s); % Lumped cavity losses
    time = params(13,s); % Time at which to end the computation

    % Universal Constants
    c = 2.998e10; % Speed of light in cm/s
    h = 6.626e-34; % Planck's constant J*s
    Kb = 1.38e-23; % Boltzmann constant m^2*kg/s^2/K

    % Changeable Constants
    nL = 1.42866; % Laser crystal refractive index @1034nm
    nLp = 1.42904; % Pump crystal refractive index @977nm
    na = 1.81523; % Saturable absorber refractive index @1034nm
    theta_L = 55*pi/180; % Angle of incidence laser crystal
    theta_a = 61.15*pi/180; % Angle of incidence saturable absorber
    l_L = 1/cos(asin(sin(theta_L)/nL)); % Laser light path
    length in laser crystal in cm
    l_Lp = 1/cos(asin(sin(theta_L)/nLp)); % Pump light path
    length in laser crystal in cm
    l_a = la/cos(asin(sin(theta_a)/na)); % Light path length in
    absorber in cm
    Lca = Lc-l+l_L-la+l_a; % Length of cavity in cm (laser path)
    L = Lc-l+l_L*nL-la+l_a*na; % Optical length of cavity in cm
    sigLa = 1.77e-21; % Laser absorption transition cross-section
    @1047nm in cm^2 (4<->5)
    sigpa = 1.28e-20; % Pump absorption transition cross-section
    @977nm in cm^2 (1<->5)
    sigLe = 3.76e-21; % Laser emission transition cross-section
    @1047nm in cm^2 (4<->5)
    sigpe = 1.04e-20; % Pump emission transition cross-section
    @977nm in cm^2 (1<->5)
    sigg = 9.55e-19; % Absorber ground state transition cross
    section @1047nm in cm^2

```

```

sigg1 = 3.2e-18;    % Absorber ground state transition cross
  section @1064nm in cm^2
sige = 1.54e-19;    % Absorber excited state transition cross
  section @1047nm in cm^2
E1L = h*c*530;      % Energy of lower laser level (3) in J
E2L = h*c*10199;    % Energy of upper laser level (5) in J
E1p = 0;            % Energy of lower pump level (1) in J
E2p = h*c*10201.1;  % Energy of upper pump level (5) in J
E2 = h*c*50;        % Energy of level 2 in J
E3 = h*c*110;       % Energy of level 3 in J
E6 = h*c*10300;     % Energy of level 6 in J
E7 = h*c*10580;     % Energy of level 7 in J
Ti = 289.35;        % Initial crystal temperature in K
f1L = exp(-E1L/Kb/T) / (exp(-E1p/Kb/T)+exp(-E2/Kb/T)+exp(...
  -E1L/Kb/T)+exp(-E3/Kb/T));    % Lower laser level fractional
  population (4)
f2L = exp(-E2L/Kb/T) / (exp(-E2L/Kb/T)+exp(-E6/Kb/T)+exp(...
  -E7/Kb/T));    % Upper laser level fracitonal population (5)
f1p = exp(-E1p/Kb/T) / (exp(-E1p/Kb/T)+exp(-E2/Kb/T)+exp(...
  -E1L/Kb/T)+exp(-E3/Kb/T));    % Lower pump level fractional
  population (1)
f2p = exp(-E2p/Kb/T) / (exp(-E2p/Kb/T)+exp(-E6/Kb/T)+exp(...
  -E7/Kb/T));    % Upper pump level fracitonal population (5)
tL = 1.66e-3;      % Fluorescence lifetime for upper laser level
  in s
t2 = 3.5e-6;       % Fluorescence lifetime of absorber excited
  state (2) in s
t4 = 0.1e-9;       % Fluorescence lifetime of absorber level 4 in s
w1s = 384.3e-4*w1m;    % Saggital pump mode radius in cm
% Tangential pump mode radius in cm
w1t = 378.8e-4*w1m * cos(asin(sin(theta_L)/nLp))/cos(theta_L);
Ns0 = -log(Ta)/(sigg*la);    % Saturable absorber concentration
  in cm^-3
R1 = 0.999;        % Dichroic mirror reflectivity
lambda_L = 1047e-7; % Laser wavelength in cm
lambda_p = 977e-7; % Pump wavelength in cm
Rc = 0.05863;     % Pump reflectivity at Brewster's angle (55 deg.)
Wp = Wpc*(1-Rc);   % Transmitted incident pump power

% Dependent constants
s1 = pi*w1s*w1t;    % Pump beam area in crystal in cm^2
s2 = pi*w2s*w2t;    % Laser mode area in crystal in cm^2
hv_p = h*c/lambda_p;    % Pump photon energy in J
hv_L = h*c/lambda_L;    % Laser photon energy in J
tr = 2*L/c;         % Cavity round-trip time
tc = tr/(-1*log(R1*R2)+C_loss);    % Photon cavity lifetime in s
A = c/nL;           % Simplifying constants
B = l_Lp*s1*hv_p;
C = l_L*c/(Lca*nL);    % Not positive about use of l_L and Lca
D = l_a*c/(Lca*na);    % Not positive about use of l_a and Lca

% Initial conditions
Nli = N0;           % Lower laser manifold population density in cm^-3
Ngi = Ns0;          % Lower saturable absorber manifold population
  density in cm^-3
Phii = 0;           % Average photon density in cavity in photons/cm^3

```

```

% Simulation parameters
timerange = [0, time];      % Time range for simulation

% RK Solver
[t,y] = ode45(@LaserRate_thesis,timerange,[N1i Ngi Phi]);
count = count+1;           % Keep running tally of number of solutions
assignin('base','count',count); % Export tally to workspace

% Create meaningful variables
N1 = y(:,1); % Lower laser manifold population density in cm^-3
Ng = y(:,2); % Lower saturable absorber manifold population
           density in cm^-3
Phi = y(:,3); % Average photon density in cavity in
           photons/cm^3

% Additional information
Pout = hv_L*s2*Lca*log(1/R2)/tr*Phi; % Instantaneous output
           power in W (Degnan)
Ninv = f2L*(N0-N1)-f1L*N1; % Population inversion density in
           cm^-3

% Find pulses
num_pulses = 20; % Max number of pulses desired
j=zeros(1,2*num_pulses);
jj = 0; % Determines whether or not currently within a
           pulse window
d = 1; % End of search variable
for i=1:length(t)
    if ~jj % If currently less than 10^14 (jj = 0)
        if Phi(i) > 10^14 % If Phi goes above 10^14
            j(2*d-1) = i;
            jj = 1;
        end
    else % If currently above 10^14 (jj = 1)
        if Phi(i) < 10^14 % If Phi goes below 10^14
            j(2*d) = i;
            jj = 0;
            d = d+1; % Increment number of pulses found
            if d > num_pulses % Once number of pulses desired
                are found, end loop
                break
            end
        end
    end
end
end

% Ensure that if the search for pulses ended before num_pulses
% is met then reduce number of pulses for future computation.
if d <= num_pulses
    j = j(1:2*(d-1));
    num_pulses = d-1;
end

% Pump Absorption
Pabs = (1-exp(-((sigpa*f1p+sigpe*f2p)*N1(j(1):length(N1))-...
           sigpe*f2p*N0)*l_Lp)); % Fraction of pump absorbed at each
           time step

```

```

Pabs_avg = sum(Pabs)/length(Pabs);    % Average pump absorption

% Find peak value and location of pulses for repetition rate
% and Ninv determination
maxPhi = zeros(1,num_pulses);    % Maximum value of phi
Phi_indx = zeros(1,num_pulses);    % Location of max value of phi
Pmax_sim = zeros(1, num_pulses);    % Maximum power in interval
for i=1:num_pulses
    [maxPhi(i) Phi_indx(i)] = max(Phi(j(2*i-1):j(2*i)));
    Pmax_sim(i) = max(Pout(j(2*i-1):j(2*i)));
    Phi_indx(i) = Phi_indx(i)+j(2*i-1)-1;    % Set up index from
    time=0
end

% Pulse widths of pulses and population inversions
v=zeros(1,2*num_pulses);
tp_ = zeros(1,2*num_pulses);
tp_FWHM = zeros(1, num_pulses);
Ninv_i = zeros(1, num_pulses); % Initial inversion before pulse
Ninv_f = zeros(1, num_pulses); % Final inversion after pulse
for f = 1:num_pulses
    a = j(2*f-1);
    Ninv_i(f) = Ninv(a-1);
    b = j(2*f);
    Ninv_f(f) = Ninv(b+1);
    P_HM = maxPhi(f)/2;    % Half of the maximum of the interval
    for i=a:b
        if Phi(i)>=P_HM    % Find values larger than 1/2 of the
            peak Phi
                if v(2*f-1) == 0
                    v(2*f-1) = i;
                end
                v(2*f) = i;
            elseif (v(2*f-1)>0) && (Phi(i)<P_HM)
                break
            end
        end
    end
end

% Determine which values give closest FWHM
llH = P_HM-Phi(v(2*f-1)-1);
luH = Phi(v(2*f-1))-P_HM;
ulH = Phi(v(2*f))-P_HM;
uuH = P_HM-Phi(v(2*f)+1);
if llH < luH
    tp_(2*f-1) = t(v(2*f-1)-1);
else
    tp_(2*f-1) = t(v(2*f-1));
end
if ulH < uuH
    tp_(2*f) = t(v(2*f));
else
    tp_(2*f) = t(v(2*f)+1);
end
% Save pulse durations
tp_FWHM(f) = tp_(2*f)-tp_(2*f-1);
end

```

```

% Determine if there are enough pulses to exclude first two
% Purpose of excluding first pulses is that they may not have
% reached steady-state
if num_pulses < 6
    rr = 1;      % Start from first pulse
else
    rr = 3;      % Start from third pulse
end

% Find average pulse duration
tp_ave = mean(tp_FWHM(rr:num_pulses));

% Determine time between pulse peaks
delta_peak = zeros(1,length(Phi_indx)-1);      % Storage of
time differences
for f = 1:length(Phi_indx)-1
    delta_peak(f) = t(Phi_indx(f+1))-t(Phi_indx(f));
end

% Determine repetition rate
rep_rate = 1/mean(delta_peak(rr:length(delta_peak)));

% Use above search to also determine initial, peak pulse, and
% final inversion
Ninv_i_ave = mean(Ninv_i(rr:num_pulses));      % Initial inversion
before pulse
Ninv_t_ave = mean(Ninv(Phi_indx(rr:num_pulses)));      % Peak of
pulse inversion
Ninv_f_ave = mean(Ninv_f(rr:num_pulses));      % Final inversion
after pulse

% Find window for energy in output pulse
p=zeros(1,2*num_pulses);
pp = 0;      % Determines whether or not currently within a
pulse window
e = 1;      % End of search variable
for i=1:length(t)
    if ~pp      % If currently less than 10^14 (jj = 0)
        if Phi(i) > 10^13      % If Phi goes above 10^14
            p(2*e-1) = i;
            pp = 1;
        end
    else      % If currently above 10^14 (jj = 1)
        if Phi(i) < 10^13      % If Phi goes below 10^14
            p(2*e) = i;
            pp = 0;
            e = e+1;      % Increment number of pulses found
            if e > num_pulses      % Once number of pulses desired
                are found, end loop
                break
            end
        end
    end
end
end
if e <= num_pulses
    p = p(1:2*(e-1));
end
end

```

```

% Find Eout from pulse power
Eout_sim = zeros(1,e-1);
for f = 1:e-1
    a = p(2*f-1);
    b = p(2*f)-1;
    for i=a:b
        dt = t(i+1)-t(i);
        Edt = (Pout(i+1)+Pout(i))/2*dt;
        Eout_sim(f) = Eout_sim(f) + Edt;
    end
end

% Average output energy
Eout_sim_ave = mean(Eout_sim(rr:length(Eout_sim)));

% Calculate output and internal energy and peak power (Degnan
and Beach)
gam = sigLa*f1L + sigLe*f2L; % Gamma i.e. inversion
reduction factor
% Peak output pulse power in W
Pmax_theory = hv_L*s2*l_L*log(1/R2)/((f1L+f2L)*tr)*(...
Ninv_i_ave-Ninv_t_ave*(1+log(Ninv_i_ave/Ninv_t_ave)));
Eout_theory = hv_L*s2*l_L*(Ninv_i_ave-Ninv_f_ave)*log(1/R2)/...
(log(1/R2)+C_loss)/(f1L+f2L); % Output pulse energy in J
tp_a_theory = Eout_theory/Pmax_theory; % Approximate pulse
width (numerical solution should be more accurate) in s
Pmax_sim_ave = mean(Pmax_sim); % Average simulated output power
tp_a_sim = Eout_sim_ave/Pmax_sim_ave; % Approximate pulse width in s
Ecirc = Eout_sim_ave/log(1/R2); % Effective circulating energy
in the cavity in J
% Internal peak power at the output coupler in W
Poc_max = Pmax_sim_ave/(1-R2)+R2*Pmax_sim_ave/(1-R2);
Pdm_max = (1+R1)*sqrt(R2)*Pmax_sim_ave/(1-R2); % Approximate
peak power at the dichroic mirror in W
Pave = rep_rate*Eout_sim_ave; % Average power in W

% Display Pulse
figure(1)
subplot(5,1,1)
plot(t_pp,Ninv_p)
str = sprintf('Population Inversion Density at R=%g', R2);
xlabel('t (ns)'), ylabel('Density (cm^-^3)'), title(str)
subplot(5,1,2)
plot(t_pp,Phi_p)
str = sprintf('Photon Density at R=%g', R2);
xlabel('t (ns)'), ylabel('Density (cm^-^3)'), title(str)
subplot(5,1,3)
plot(t_pp,Ng_p,'b',t_pp,Ns0-Ng_p,'r')
str = sprintf('Absorber Level Population Density at R=%g', R2);
xlabel('t (ns)'), ylabel('Density (cm^-^3)'), title(str)
subplot(5,1,4)
plot(t_pp,exp(-sigg*l_a*Ng_p-sige*l_a*(Ns0-Ng_p))*100)
str = sprintf('Saturable Absorber Transmission at R=%g', R2);
xlabel('t (ns)'), ylabel('Transmission (%)'), title(str)
subplot(5,1,5)
plot(t_p,Pout_p)

```

```

str = sprintf('Output Power at R=%g', R2);
xlabel('t (s)'), ylabel('Power (W)'), title(str)

% Display Pulse Train
figure(2)
subplot(4,1,1)
plot(t,Ninv)
str = sprintf('Population Inversion Density at R=%g', R2);
xlabel('t (s)'), ylabel('Density (cm^-^3)'), title(str)
subplot(4,1,2)
plot(t,Phi)
str = sprintf('Photon Density at R=%g', R2);
xlabel('t (s)'), ylabel('Density (cm^-^3)'), title(str)
subplot(4,1,3)
plot(t,Ng, 'b', t, Ns0-Ng, 'r')
str = sprintf('Absorber Level Population Density at R=%g', R2);
xlabel('t (s)'), ylabel('Density (cm^-^3)'), title(str)
subplot(4,1,4)
plot(t,Pout)
str = sprintf('Output Power at R=%g', R2);
xlabel('t (s)'), ylabel('Power (W)'), title(str)

% Calculate the value of N2 that gives the average power
% absorption
N2_ave = QS_N2_function_R8_ParaOpt(N1, t, j, num_pulses, N0,...
T, Wpc);
% Save cell array for writing to excel file
export_num(:,s) = {Eout_theory*1000; Eout_sim_ave*1000;
Pmax_sim_ave; Pave; tp_ave*1e9; tp_a_theory*1e9; rep_rate;...
Ninv_i_ave; Ninv_t_ave; Ninv_f_ave; N2_ave; Pabs_avg;...
Pmax_theory; tp_a_sim*1e9; num_pulses};
end

% Combine cell arrays to get output data for current parametric study
export_data = [export_char, export_num];
% Save cell array to spreadsheet
xlswrite('Q Switching Parametric Model Outputs R1 - ODE45.xlsx',
export_data, Sheets{r});
end

% Nested function in order to share the workspace
function yout = LaserRate_thesis(t,yin)
% LaserRate_thesis: calculates the laser rate system of equations
% yout = LaserRate_thesis(t,yin): evaluates system of
% differential equations from the paper by Qinan Li,
% 2011. It solves the slope for lower laser level
% population density, lower saturable absorber level
% population density, and average photon density in the
% cavity using time and variable values at a specific
% time step. This code is used in conjunction with
% Qswitchcode_thesis.
%
% Input:
% t = the current time value (s)
% yin = vector of current variable values; first value is lower
% laser manifold population density (N1, cm^-3), second is
% lower saturable absorber manifold population density

```

```

%      (Ng, cm^-3), and third is average photon density in cavity
%      (Phi, cm^-3)
% Output:
%      yout = vector of slopes; Column 1 - dN1/dt (cm^-3s^-1),
%      2 - dNg/dt (cm^-3s^-1), 3 - dPhi/dt (cm^-3s^-1)
%      (C) Travis Schoepp, 2014

% Compute slopes for each variable and insert into a column vector
yout = [(A*yin(3)*(sigLe*f2L*(N0-yin(1))-sigLa*f1L*yin(1))+...
(N0-yin(1))/tL-Wp/B*(1-exp(-(sigpa*f1p+sigpe*f2p)*yin(1)-...
sigpe*f2p*N0)*1_Lp)); (-sigg*c/na*yin(3)*yin(2)+(Ns0-yin(2))/...
t2); (C*(sigLe*f2L*(N0-yin(1))*(yin(3)+(1/Lca/s2))-sigLa*f1L*...
yin(1)*yin(3))-D*yin(3)*(sigg*yin(2)+sige*(Ns0-yin(2)))-
yin(3)/tc)];
end
end

```

A.2 Average Upper Manifold Population Density Program

This function calculates the value of the upper manifold population that produces the average pump absorption. It requires inputs from the program 'Qswitchcode_thesis'.

```

function N2_ave = QS_N2_function_thesis(N1, t, j, num_pulses, N0,
T, Pp)
% QS_N2_function_thesis: calculates the value of N2 that gives the
%      average calculated pump absorption.
%      N2_ave = QS_N2_function_thesis(N1, t, j, num_pulses, N0, T, Pp):
%      calculates the value of N2 that gives the average
%      calculated absorption. The average absorption is found
%      from N2 where the values of N2 are determined by a
%      Fourier series of a piecewise fitted polynomial. N2 is
%      used at multiple time steps to find the absorption
%      expected. These are averaged then the proper N2 value
%      is found which gives this average value.
%
% Input:
%      N1 = vector of lower manifold population densities (cm^-3)
%      t = vector of time steps (s)
%      j = location of beginning of first and second (and third)
%      Q-switched pulses
%      num_pulses = gives number of pulses in N1 vector
%      N0 = Dopant concentration (cm^-3)
%      T = Crystal temperature (K)
%      Pp = Pump power (W)
% Output:
%      N2_ave = N2 value that gives average pump absorption (m^-3)
%      (C) Travis Schoepp, 2014

N0_ = N0*(0.01)^-3; % Dopant concentration (m^-3)

% If less than three pulses use first two otherwise use second and third
if num_pulses < 3
    N1_ = N1(j(1):j(3)); % Select beginning of pulse to next pulse N1
    t_ = t(j(1):j(3)); % Select beginning of pulse to next pulse t
else

```

```

    N1_=N1(j(3):j(5)); % Select beginning of pulse to next pulse N1
    t_=t(j(3):j(5)); % Select beginning of pulse to next pulse t
end
[uu,iu]=max(N1_); % Find max value of N1 and make beginning
N1_=N1_(iu:length(N1_));
t_=t_(iu:length(t_));
[l1,il]=min(N1_); % Find min value of N1 and make end
N1_=N1_(1:il);
t_=t_(1:il);
t_=t_-t_(1); % Move plot back to origin

N2_ = N0_-(N1_/0.01^3); % N2 in m^-3

N2_reg = polyfit(t_,N2_,3); % Cubic fit

I1=t_(length(t_))-t_(1); % Duration of rising N2
I2=500e-9; % Approx. pulse duration
I=(I1+I2)/2; % Half the period
max_N2=max(N2_); % Maximum N2
min_N2=min(N2_); % Minimum N2
a1=N2_reg(1); % a1-d1 coefficients for rising N2
b1=N2_reg(2);
c1=N2_reg(3);
d1=N2_reg(4);
a2=(min_N2-max_N2)/I2; % a2-b2 coefficients for falling N2
b2=max_N2-a2*I1;

I3=2*I-I2; % Variable for computation

a0_ = (1/I)*(a1/4*I^4+b1/3*I^3+c1/2*I^2+d1*I+a2/2*(4*I^2-...
I3^2)+b2*I2);

f = 0.5*a0_; % Initialize Fourier series
t__ = 0:100e-9:4*I; % Time variable

% Determine Fourier coefficients and add them to the series
for n=1:10
    e=pi*n/I;
    a_ = (1/(I*e^4))*(e*sin(e*I3)*(e^2*a1*I3^3-6*a1*I3+b1*(e^2*...
I3^2-2)+c1*e^2*I3+e^2*d1)+cos(e*I3)*(3*a1*e^2*I3^2-2)+...
(e^2*(2*b1*I3+c1))-(c1*e^2-6*a1)))+(1/(I*e^2))*(e*(a2*2*I+...
b2)*sin(e*2*I)+a2*(cos(e*2*I)-cos(e*I3))-e*(a2*I3+b2)*...
sin(e*I3));
    b_ = (1/(I*e^4))*(sin(e*I3)*(3*a1*(e^2*I3^2-2)+e^2*(2*b1*I3+...
c1))-e*cos(e*I3)*(e^2*a1*I3^3-6*a1*I3+b1*(e^2*I3^2-2)+c1*...
e^2*I3+e^2*d1)-(2*e*b1-e^3*d1)))+(1/(I*e^2))*(a2*(sin(e*2*...
I)-sin(e*I3))-e*(a2*2*I+b2)*cos(e*2*I)+e*(a2*I3+b2)*...
cos(e*I3));
    f = f+a_*cos(n*pi/I*t__)+b_*sin(n*pi/I*t__);
end

plot(t__,f)

sigpa = 1.28e-24;
sigpe = 1.04e-24;
c = 2.998e10; % Speed of light in cm/s
h = 6.626e-34; % Planck's constant J*s

```

```

Kb = 1.38e-23;      % Boltzmann constant m^2*kg/s^2/K
E1L = h*c*530;     % Energy of lower laser level (3) in J
E2L = h*c*10199;   % Energy of upper laser level (5) in J
E1p = 0;           % Energy of lower pump level (1) in J
E2p = h*c*10201.1; % Energy of upper pump level (5) in J
E2 = h*c*50;       % Energy of level 2 in J
E3 = h*c*110;      % Energy of level 3 in J
E6 = h*c*10300;    % Energy of level 6 in J
E7 = h*c*10580;    % Energy of level 7 in J
% Lower laser level fractional population (4)
f1L = exp(-E1L/Kb/T) / (exp(-E1p/Kb/T)+exp(-E2/Kb/T)+exp(-E1L/...
    Kb/T)+exp(-E3/Kb/T));
% Upper laser level fractional population (5)
f2L = exp(-E2L/Kb/T) / (exp(-E2L/Kb/T)+exp(-E6/Kb/T)+exp(-E7/Kb/T));
% Lower pump level fractional population (1)
f1p = exp(-E1p/Kb/T) / (exp(-E1p/Kb/T)+exp(-E2/Kb/T)+exp(-E1L/...
    Kb/T)+exp(-E3/Kb/T));
% Upper pump level fractional population (5)
f2p = exp(-E2p/Kb/T) / (exp(-E2p/Kb/T)+exp(-E6/Kb/T)+exp(-E7/Kb/T));
Rc = 0.05863;      % Crystal face Brewster reflectivity

% Split N2 into 40 slices
N2_s=f(1:floor(length(f)/40):length(f));
Q = zeros(1,40);   % Initialise absorbed power
% Determine Q for each slice of N2
for i=1:40
    fu = @(x) (sigpa.*f1p.*N0_-(sigpa.*f1p+sigpe.*f2p).*...
        N2_s(i)).*Pp.*(1-Rc).*exp(-(sigpa.*f1p.*N0_-(sigpa.*f1p+...
        sigpe.*f2p).*N2_s(i)).*x);
    Q(i) = integral(@(x) fu(x),0,6.102e-3);
end

mQ = mean(Q);      % average Q
di = 0.1;          % Initialize difference
i = 1;
% Find closest N2 value to give average Q
while(1)
    fu = @(x) (sigpa.*f1p.*N0_-(sigpa.*f1p+sigpe.*f2p).* f(i)).*...
        f(i)).*Pp.*(1-Rc).*exp(-(sigpa.*f1p.*N0_-(sigpa.*f1p+...
        sigpe.*f2p).*f(i)).*x);
    dQ = integral(@(x) fu(x),0,6.102e-3);
    if abs(dQ-mQ) < di
        N2_ave = f(i);
    end
    if i<(length(f)-3)
        i=i+4;
    else
        break
    end
end
end

```

Appendix B

COMSOL Thermal Simulation Parameters

The information presented here is a representative sample of the COMSOL thermal simulations. This report was generated from the lasing, Q-switching thermal simulation. The parameters for the other simulations can be derived from this appendix and from Section 4.2.

B.1 Global Definitions

B.1.1 Parameters

Parameters

Name	Expression	Description
d	0.02[1]	Doping concentration
k0	9.71[W/m/K]	Thermal Conductivity at no doping
norm	1[W/m/K]	Unit for variable calc
sigy	93.6e-6[m]	Beam radius in y
sigz	95.0e-6[m]	Beam radius in z
wly	85.34e-6[m]	Laser mode waist in y
wlz	73.05e-6[m]	laser mode waist in z
P0	14.29 [W]	Incident Power – changes each simulation
Rc	0.05863[1]	Front Face Crystal Reflectivity
Rm	0.0[1]	Dichroic Mirror Reflectivity
Ac	2.71[1/cm]	Pump Absorption Coefficient
Acl	0.028 [1/cm]	Laser absorption coeff
eta_qdf	0.0278[1]	Heat load from fluorescence quantum defect
eta_qdl	0.0693[1]	Heat load from lasing quantum defect
eta	0.23[1]	Heat load calculated
sigabs	1.28e-20[cm ²]	Absorption cross-section at pump wavelength
sigabsl	1.77e-21[cm ²]	Abs cross-section laser
sigem	1.04e-20[cm ²]	Emission cross-section at pump wavelength
sigeml	3.76e-21[cm ²]	Em cross-section laser
tau	1.66[ms]	Emission lifetime

Name	Expression	Description
norm1	$1[\text{m}^2/\text{W}]$	Unit for saturation intensity
hnu	$2.0332\text{e-}19[\text{J}]$	Pump photon energy
hnu1	$1.8973\text{e-}19[\text{J}]$	Laser photon energy
htv	$8.29[\text{W}/\text{m}^2/\text{K}]$	Heat transfer coefficient vertical
ht45	$9.08[\text{W}/\text{m}^2/\text{K}]$	Heat transfer coefficient 45 deg upward
hc	$38.9[\text{W}/\text{m}^2/\text{K}]$	Top corner effective heat transfer coefficient
heff	$0.13[\text{W}/\text{cm}^2/\text{K}]$	Effective H for crystal-copper contact
M2y	50.1	M-squared of pump in "y" axis of ellipse
M2z	53.9	M2 of pump in "z" axis of ellipse
M2l	1	M2 of laser beam averaged
x0	$2.03\text{e-}3 [\text{m}]$	Focal spot in crystal along propagation "x" axis
x0l	$-13.1\text{e-}3 [\text{m}]$	Laser beamwaist along propagation "x" axis
n	1.43 [1]	Refractive index
y0	$4.01\text{e-}3[\text{m}]$	Pump beam center in y
z0	$7.5\text{e-}3[\text{m}]$	Pump beam center in z
c	$299792458[\text{m}/\text{s}]$	Speed of light in vacuum
k_B	$1.3806504\text{e-}23[\text{J}/\text{K}]$	Boltzmann Constant
N0	$5.15\text{e}20[\text{cm}^3]$	Dopant Density
N2	$8.3703\text{e}25[\text{m}^3]$	Average upper state population – changes each simulation
eta_1	1 - 0.878	Non-radiative heat load for reabsorption of laser
Pmax	8501 [W]	Peak output power – changes each simulation
tp	$91.9\text{e-}9 [\text{s}]$	Pulse duration – changes each simulation
RR	1438[Hz]	Repetition rate – changes each simulation
R1	0.95	Output Coupler
Tinit	290.67[K]	Initial Average Crystal Temperature – changes each simulation
Tcool	291.82[K]	Mount Temperature – changes each simulation

B.1.2 Variables

Variables

Name	Expression	Description
k_int	$(573.8*d^2*norm) - (102.6*d*norm) + 8.6902[\text{W}/\text{m}/\text{K}]$	Quadratic interpolation of k

Name	Expression	Description
t_	$0.81935*x + 0.40538*y - 0.40538*z + 0.903997$ [m]	Length of vector in direction of propagation
y_	$\sqrt{(((x - x0_t_)*0.5733 - (y - y0_t_)*0.57937 + (z - z0_t_)*0.57937)*0.5733)^2 + 2*(((x - x0_t_)*0.5733 - (y - y0_t_)*0.57937 + (z - z0_t_)*0.57937)*0.57937)^2}$	Distance of point along the ellipse "y" axis
z_	$\sqrt{2)*0.5*((y - y0_t_)) + (z - z0_t_))}$	Distance of point along the ellipse "z" axis
x_	$\sqrt{(((x - x0_x0)*0.81935 + (y - y0_x0)*0.4053 - (z - z0_x0)*0.4053)*0.81935)^2 + 2*(((x - x0_x0)*0.81935 + (y - y0_x0)*0.4053 - (z - z0_x0)*0.4053)*0.4053)^2}$	Distance of point along the propagation "x" axis from pump beamwaist
x_l	$\sqrt{(((x - x0_x0l)*0.81935 + (y - y0_x0l)*0.4053 - (z - z0_x0l)*0.4053)*0.81935)^2 + 2*(((x - x0_x0l)*0.81935 + (y - y0_x0l)*0.4053 - (z - z0_x0l)*0.4053)*0.4053)^2}$	Distance of point along the propagation "x" axis from mode beamwaist
wp_y	$1.429*sigy*\sqrt{1 + ((M2y*977e-9*x_)/(n*pi*sigy^2))^2}$ [m]	Pump Gaussian beam radius in "y" axis of ellipse (1.429 factor from angle propagation expansion)
wp_z	$sigz*\sqrt{1 + ((M2z*977e-9*x_)/(n*pi*sigz^2))^2}$ [m]	Pump Gaussian beam radius in "z" axis of ellipse
wl_y	$1.429*wly*\sqrt{1 + ((M2l*1047e-9*x_l)/(n*pi*wly^2))^2}$ [m]	Cavity beam radius in "y" axis of ellipse (1.429 factor from angle propagation expansion)
wl_z	$wlz*\sqrt{1 + ((M2l*1047e-9*x_l)/(n*pi*wlz^2))^2}$ [m]	Cavity beam radius in "z" axis of ellipse
Il	$2*Pint*\exp(-2*((y - y0)/wl_y)^2 + ((z - z0)/wl_z)^2)/(pi*wl_y*wl_z)$	Cavity laser intensity
Pint	0 [W]	Internal cavity power (2*circulating power) – requires input each run
x_0	$\sqrt{(((x - x0_0)*0.81935 + (y - y0_0)*0.4053 - (z - z0_0)*0.4053)*0.81935)^2 + 2*(((x - x0_0)*0.81935 + (y - y0_0)*0.4053 - (z - z0_0)*0.4053)*0.4053)^2}$	Distance of point along the propagation "x" axis from crystal face

B.1.3 Functions

B.1.3.1 Rectangle 1

Parameters

Name	Value
Function name	tophat
Lower limit	0
Upper limit	1
Size of transition zone	0.01

B.1.3.2 Analytic 2

Definition

Name	Value	Units
Function name	SGaus	
Expression	$\exp(-2*((y1^2 + z1^2)^{(1/2)}/0.75e-3)^{20})$	
Arguments	{y1, z1}	m

B.1.3.3 Analytic 3

Definition

Name	Value	Units
Function name	SGaus1	
Expression	$\exp(-2*(((y1/wp_y1)^2 + (z1/wp_z1)^2)^{(1/2)})^{40})$	
Arguments	{y1, z1, wp_y1, wp_z1}	m

B.1.3.4 Analytic 4

Definition

Name	Value	Units
Function name	f11	
Expression	$\exp(-h_const*c*530/(0.01*k_B*T1))/(\exp(-h_const*c*0/(0.01*k_B*T1)) + \exp(-h_const*c*50/(0.01*k_B*T1)) + \exp(-h_const*c*110/(0.01*k_B*T1)) + \exp(-h_const*c*530/(0.01*k_B*T1)))$	
Arguments	T1	K

B.1.3.5 Analytic 5

Definition

Name	Value	Units
Function name	fp1	

Name	Value	Units
Expression	$\exp(-h_const*c*0/(0.01*k_B*T1))/(\exp(-h_const*c*0/(0.01*k_B*T1)) + \exp(-h_const*c*50/(0.01*k_B*T1)) + \exp(-h_const*c*110/(0.01*k_B*T1)) + \exp(-h_const*c*530/(0.01*k_B*T1)))$	
Arguments	T1	K

B.1.3.6 Analytic 6

Definition

Name	Value	Units
Function name	f12	
Expression	$\exp(-h_const*c*10199/(0.01*k_B*T1))/(\exp(-h_const*c*10199/(0.01*k_B*T1)) + \exp(-h_const*c*10300/(0.01*k_B*T1)) + \exp(-h_const*c*10580/(0.01*k_B*T1)))$	
Arguments	T1	K

B.1.3.7 Analytic 7

Definition

Name	Value	Units
Function name	fp2	
Expression	$\exp(-h_const*c*10201.1/(0.01*k_B*T1))/(\exp(-h_const*c*10201.1/(0.01*k_B*T1)) + \exp(-h_const*c*10300/(0.01*k_B*T1)) + \exp(-h_const*c*10580/(0.01*k_B*T1)))$	
Arguments	T1	K

B.1.3.8 Analytic 8

Definition

Name	Value	Units
Function name	x0_	
Expression	$t1*0.81935$	m
Arguments	t1	m

B.1.3.9 Analytic 9

Name	Value	Units
Function name	y0_	
Expression	$y0 + t1*0.40538$	m
Arguments	t1	m

B.1.3.10 Analytic 10

Definition

Name	Value	Units
Function name	z0_	
Expression	$z0 - t1 * 0.40538$	m
Arguments	t1	m

B.2 Model 1 (mod1)

B.2.1 Definitions

Variables

Name	Expression	Description
Ilsat	$hnu1 / ((f1(T) * sigabs1 + f2(T) * sigem1) * tau)$	Pump saturation intensity
Ipsat	$hnu / ((fp1(T) * sigabs + fp2(T) * sigem) * tau)$	Laser saturation intensity
Imin	$hnu / ((fp1(T) * sigabs * f2(T) * sigem1 / (f1(T) * sigabs1) - fp2(T) * sigem) * tau)$	Min transparency intensity
Pave_in	$Pmax * tp * RR / (1 - R1)$	Average laser power inside resonator

B.2.2 Geometry

Geometry statistics

Property	Value
Space dimension	3
Number of domains	12
Number of boundaries	58
Number of edges	92
Number of vertices	48

B.2.2.1 Block 1 (blk1)

Size and shape

Name	Value	Units
Axis Type	Cartesian	
Size	{0.005, 0.01, 0.01}	m
Position	{0, 0, 0}	m

Layers

Name	Value
Layer names	Layer 1
Layers	0.0009
Front	On
Back	On
Top	On

B.2.2.2 Block 4 (blk4)**Size and shape**

Name	Value
Axis Type	Cartesian
Size	{0.005, 0.01, 0.01}
Position	{0, 0, 0}

Layers

Name	Value
Layer names	Layer 1
Layers	0.0009
Front	On
Back	On
Top	On

B.2.2.3 Cylinder 1 (cyl1)**Size and Shape**

Name	Value
Axis type	Cartesian
Radius	0.75e-3
Height	0.00769
Position	{0 - 0.81935*1e-3, y0 - 0.40538*1e-3, z0 + 0.40538*1e-3}

B.2.2.4 Block 2 (blk2)**Size and shape**

Name	Value
Axis Type	Cartesian
Size	{0.005, 0.0035, 0.0009}

Name	Value
Position	{0, 0.0056, 0.0091}

B.2.2.5 Block 3 (blk3)

Size and shape

Name	Value
Axis Type	Cartesian
Size	{0.005, 0.0009, 0.0035}
Position	{0, 0.0091, 0.0056}

B.2.3 Materials

B.2.3.1 Yb-doped Calcium Fluoride

Material parameters

Name	Value	Unit
Young's modulus	89.6e9	Pa
Density	3181	kg/m ³
Coefficient of thermal expansion	1.887e-5	1/K
Poisson's ratio	0.21	1
Heat capacity at constant pressure	854	J/(kg*K)
Thermal conductivity	k_int	W/(m*K)

B.2.4 Coefficient Form PDE (c)

Selection

Selection	Domains 1–12
-----------	--------------

Settings

Description	Value
Shape function type	Lagrange
Element order	Quadratic
Compute boundary fluxes	Off
Value type when using splitting of complex variables	Complex
Frame	Spatial
Dependent variable quantity	Power (W)
Source term quantity	Power per unit length (W/m)

B.2.4.1 Coefficient Form PDE 1

Selection

Selection	Domains 1–12
-----------	--------------

Equations

$$e_a \frac{\partial^2 Pp}{\partial t^2} + d_a \frac{\partial Pp}{\partial t} + \nabla \cdot (-c \nabla Pp - \alpha Pp + \gamma) + \beta \cdot \nabla Pp + a Pp = f$$

$$\nabla = \left[\frac{\partial}{\partial x}, \frac{\partial}{\partial y}, \frac{\partial}{\partial z} \right]$$

Settings

Description	Value
Diffusion coefficient	{0, 0, 0}, {0, 0, 0}, {0, 0, 0}
Absorption coefficient	(sigabs*fp1(ts.T)*N0 - (sigabs*fp1(ts.T) + sigem*fp2(ts.T))*N2)
Source term	0
Mass coefficient	0
Damping or mass coefficient	0
Conservative flux convection coefficient	{0, 0, 0}
Convection coefficient	{0.81935, 0.40538, -0.40538}
Conservative flux source	{0, 0, 0}

B.2.4.2 Zero Flux 1

Selection

Selection	Boundaries 47–58
-----------	------------------

Equations

$$-\mathbf{n} \cdot (-c \nabla Pp - \alpha Pp + \gamma) = 0$$

$$\nabla = \left[\frac{\partial}{\partial x}, \frac{\partial}{\partial y}, \frac{\partial}{\partial z} \right]$$

B.2.4.3 Initial Values 1

Selection

Selection	Domains 1–12
-----------	--------------

Settings

Description	Value
Initial value for Pp	0
Initial time derivative of Pp	0

B.2.4.4 Dirichlet Boundary Condition 1

Selection

Selection	Boundaries 14, 21
-----------	-------------------

Equations

$$Pp = r$$

$$g_{\text{reaction}} = -\mu$$

Settings

Description	Value
Value on boundary	$P0*(1 - Rc)*(1 - Rm)*SGaus(y_, z_)$
Prescribed value of Pp	On
Apply reaction terms on	Individual dependent variables
Use weak constraints	Off

B.2.4.5 Dirichlet Boundary Condition 2

Selection

Selection	Boundaries 1–5, 7–8, 10–11, 13, 17, 20, 26, 29–30, 32–33, 36, 39, 42–46
-----------	---

Equations

$$Pp = r$$

$$g_{\text{reaction}} = -\mu$$

Settings

Description	Value
Value on boundary	0
Prescribed value of Pp	On
Apply reaction terms on	Individual dependent variables
Use weak constraints	Off

B.2.5 Coefficient Form PDE 2 (c2)

Selection

Selection	Domains 1–12
-----------	--------------

Settings

Description	Value
Shape function type	Lagrange
Element order	Quadratic
Compute boundary fluxes	Off

Description	Value
Value type when using splitting of complex variables	Complex
Frame	Spatial
Dependent variable quantity	Power (W)
Source term quantity	Power per unit length (W/m)

B.2.5.1 Coefficient Form PDE 1

Selection

Selection	Domains 1–12
-----------	--------------

Equations

$$e_a \frac{\partial^2 P_{p1}}{\partial t^2} + d_a \frac{\partial P_{p1}}{\partial t} + \nabla \cdot (-c \nabla P_{p1} - \alpha P_{p1} + \gamma) + \beta \cdot \nabla P_{p1} + a P_{p1} = f$$

$$\nabla = \left[\frac{\partial}{\partial x}, \frac{\partial}{\partial y}, \frac{\partial}{\partial z} \right]$$

Settings

Description	Value
Diffusion coefficient	{{0, 0, 0}, {0, 0, 0}, {0, 0, 0}}
Absorption coefficient	(Ac*pi*w1_y*w1_z*Imin + Acl*2*Pint*exp(-2*((y_/w1_y)^2 + (z_/w1_z)^2)))*wp_y*wp_z*Ipsat*Ilsat/(pi*wp_y*wp_z*w1_y*w1_z*Ipsat*Ilsat*Imin + w1_y*w1_z*Ilsat*Imin*Pp1 + 2*wp_y*wp_z*Ipsat*Imin*Pint*exp(-2*((y_/w1_y)^2 + (z_/w1_z)^2)))
Source term	0
Mass coefficient	0
Damping or mass coefficient	0
Conservative flux convection coefficient	{0, 0, 0}
Convection coefficient	{0.81935, 0.40538, -0.40538}
Conservative flux source	{0, 0, 0}

B.2.5.2 Zero Flux 1

Selection

Selection	Boundaries 47–58
-----------	------------------

Equations

$$-\mathbf{n} \cdot (-c \nabla P_{p1} - \alpha P_{p1} + \gamma) = 0$$

$$\nabla = \left[\frac{\partial}{\partial x}, \frac{\partial}{\partial y}, \frac{\partial}{\partial z} \right]$$

B.2.5.3 Initial Values 1

Selection

Selection	Domains 1–12
-----------	--------------

Settings

Description	Value
Initial value for Pp1	0
Initial time derivative of Pp1	0

B.2.5.4 Dirichlet Boundary Condition 1

Selection

Selection	Boundaries 14, 21
-----------	-------------------

Equations

$$Pp1 = r$$

$$g_{\text{reaction}} = -\mu$$

Settings

Description	Value
Value on boundary	$P0*(1 - Rc)*(1 - Rm)*SGaus(y_, z_)$
Prescribed value of Pp1	On
Apply reaction terms on	Individual dependent variables
Use weak constraints	Off

B.2.5.5 Dirichlet Boundary Condition 2

Selection

Selection	Boundaries 1–5, 7–8, 10–11, 13, 17, 20, 26, 29–30, 32–33, 36, 39, 42–46
-----------	---

Equations

$$Pp1 = r$$

$$g_{\text{reaction}} = -\mu$$

Settings

Description	Value
Value on boundary	0
Prescribed value of Pp1	On
Apply reaction terms on	Individual dependent variables
Use weak constraints	Off

B.2.6 Thermal Stress (ts)

Settings

Description	Value
Element type	Mixed order
Thermal stress fields	U2 + T1
Surface radiosity	Linear
Value type when using splitting of complex variables	{Complex, Complex, Complex}
Frame	Material
Displacements control spatial frame	On
Reference point for moment computation	{0, 0, 0}
Add mixed form pressure everywhere	Off
Structural transient behavior	Quasi - static
Typical wave speed for perfectly matched layers	ts.cp
Heat transfer in biological tissue	Off
Porous matrix model	0
Surface-to-surface radiation	Off
Radiation in participating media	Off
SmeApplModeID	SolidMechanics
EquationType	smetffs

B.2.6.1 Thermal Linear Elastic 1

Selection

Selection	Domains 1–12
-----------	--------------

Equations

$$-\nabla \cdot \boldsymbol{\sigma} = \mathbf{F}_v, \quad \boldsymbol{\sigma} = \mathbf{s}$$

$$\mathbf{s} - \mathbf{s}_0 = \underline{\underline{\mathbf{C}}} : (\boldsymbol{\epsilon} - \boldsymbol{\epsilon}_0 - \boldsymbol{\epsilon}_{inel}), \quad \boldsymbol{\epsilon}_{inel} = \underline{\underline{\boldsymbol{\alpha}}}(T - T_{ref})$$

$$\boldsymbol{\epsilon} = \frac{1}{2}[(\nabla \mathbf{u})^T + \nabla \mathbf{u}]$$

$$\rho c_p \frac{\partial T}{\partial t} + \rho c_p \mathbf{u} \cdot \nabla T = \nabla \cdot (k \nabla T) + Q$$

Settings

Description	Value
Young's modulus	From material
Poisson's ratio	From material
Elasticity matrix	{{335.3e9, 0, 0, 0, 0, 0}, {0, 113.07e9, 0, 0, 0, 0}, {0, 0, 115e9, 0, 0, 0}, {0, 0, 0, 0, 0, 0}, {0, 0, 0, 0, 0, 0}, {0,

Description	Value
	0, 0, 0, 0, 0}}
Density	From material
Solid model	Isotropic
Specify	Young's modulus and Poisson's ratio Standard (XX, YY, ZZ, XY, YZ, XZ)
Nearly incompressible material	Off
Strain reference temperature	290.15[K]
Material	Domain material
Coefficient of thermal expansion	{{1.16e-5, 0, 0}, {0, 5.4e-6, 0}, {0, 0, 5.9e-6}}
Thermal conductivity	From material
Heat capacity at constant pressure	From material
Energy dissipation	0
Calculate dissipated energy	0

B.2.6.2 Free 1

Selection

Selection	Boundaries 1–4, 7, 10–11, 14, 17, 20–21, 26, 30, 33, 36, 39, 42–44, 46–58
-----------	---

B.2.6.3 Initial Values 1

Selection

Selection	Domains 1–12
-----------	--------------

Settings

Description	Value
Displacement field	{0, 0, 0}
Structural velocity field	{0, 0, 0}
Temperature	Tinit

B.2.6.4 Heat Source 1

Selection

Selection	Domain 7
-----------	----------

Equations

$$\rho c_p \frac{\partial T}{\partial t} + \rho c_p \mathbf{u} \cdot \nabla T = \nabla \cdot (k \nabla T) + \dot{q}$$

Settings

Description	Value
Heat source	General source - User defined
Heat source	$\text{eta} * (-0.81935 * Pp1x + 0.4053 * Pp1y - 0.4053 * Pp1z) + ((0.81935 * Pp1x + 0.4053 * Pp1y - 0.4053 * Pp1z) - (0.81935 * Ppx + 0.4053 * Ppy - 0.4053 * Ppz)) * \text{SGaus1}(y_ , z_ , w1_y, w1_z) / (\text{pi} * w_y * w_z) * \text{SGaus1}(y_ , z_ , w_y, w_z) + \text{eta_1} * P\text{ave_in} * \text{sigabs1} * \text{fl1}(ts.T) * (N0 - N2) * \exp(-\text{sigabs1} * \text{fl1}(ts.T) * (N0 - N2) * x_0) / (\text{pi} * w1_y * w1_z) * \text{SGaus1}(y_ , z_ , w1_y, w1_z)$

B.2.6.5 Fixed Constraint 1**Selection**

Selection	Boundaries 5, 8, 13, 32
-----------	-------------------------

Equations

$$\underline{\mathbf{u}} = \mathbf{0}$$

B.2.6.6 Heat Flux 2**Selection**

Selection	Boundaries 1, 4, 7, 11, 14, 17, 21, 26, 30, 33, 36, 39, 47–58
-----------	---

Equations

$$-\mathbf{n} \cdot (-k \nabla T) = h \cdot (T_{\text{ext}} - T)$$

Settings

Description	Value
Heat flux	Inward heat flux
Heat transfer coefficient	htv
External temperature	295.15[K]

B.2.6.7 Heat Flux 3**Selection**

Selection	Boundaries 10, 20, 43–44
-----------	--------------------------

Equations

$$-\mathbf{n} \cdot (-k \nabla T) = h \cdot (T_{\text{ext}} - T)$$

Settings

Description	Value
Heat flux	Inward heat flux
Heat transfer coefficient	ht45
External temperature	295.15[K]

B.2.6.8 Heat Flux 4

Selection

Selection	Boundaries 2–3, 5, 8, 13, 32
-----------	------------------------------

Equations

$$-\mathbf{n} \cdot (-k\nabla T) = h \cdot (T_{\text{ext}} - T)$$

Settings

Description	Value
Heat flux	Inward heat flux
Heat transfer coefficient	heff
External temperature	Tcool

B.2.6.9 Heat Flux 1

Selection

Selection	Boundaries 29, 42, 45–46
-----------	--------------------------

Equations

$$-\mathbf{n} \cdot (-k\nabla T) = h \cdot (T_{\text{ext}} - T)$$

Settings

Description	Value
Heat flux	Inward heat flux
Heat transfer coefficient	hc
External temperature	295.15[K]

B.2.6.10 Boundary Load 1

Selection

Selection	Boundary 29
-----------	-------------

Equations

$$\boldsymbol{\sigma} \cdot \mathbf{n} = \mathbf{F}_A$$

Settings

Description	Value
Load	User defined, force per unit area
Load	{0, 0, -215.82}

B.2.6.11 Boundary Load 2

Selection

Selection	Boundary 45
-----------	-------------

Equations

$$\sigma \cdot \mathbf{n} = \mathbf{F}_A$$

Settings

Description	Value
Load	User defined, force per unit area
Load	{0, -215.82, 0}

B.2.7 Meshes

B.2.7.1 Free Tetrahedral 1 (ftet1)

Selection

Selection	Domain 7
-----------	----------

Settings

Name	Value
Maximum element size	2.8E-4
Minimum element size	2.0E-6
Curvature factor	0.2
Resolution of narrow regions	Off
Maximum element growth rate	1.3
Predefined size	Extremely fine
Custom element size	Custom

B.2.7.2 Free Tetrahedral 2 (ftet2)

Selection

Selection	Domains 2, 4–6, 8, 10–11
-----------	--------------------------

Settings

Name	Value
Maximum element size	0.0010
Minimum element size	1.8E-4
Curvature factor	0.6
Resolution of narrow regions	0.5
Maximum element growth rate	1.5

B.2.7.3 Free Tetrahedral 3 (ftet3)

Selection

Selection	Domains 1, 3, 9, 12
-----------	---------------------

Settings

Name	Value
Maximum element size	3.5E-4
Minimum element size	1.5E-5
Curvature factor	0.3
Resolution of narrow regions	0.85
Maximum element growth rate	1.35
Predefined size	Extra fine

B.3 Study 1*B.3.1 Solver Configurations***B.3.1.1 Time-Dependent Solver 1 (t1)****General**

Name	Value
Time	{0, 10, 20, 30, 40, 50, 60, 70, 80, 90, 100}
Time Stepping Method	Generalized alpha
Times to store	Steps taken by solver